Understanding the physical processes causing surface creep on faults

Daniel B. Gittins
Exeter College
University of Oxford

A thesis submitted for the degree of
Doctor of Philosophy

"Ooh, you're going to be a doctor. Do you think you can fix my knee?"
– Margaret 'Peggy' Moore, 1936–2021

To Nan.
Thank you for always being my biggest fan. Sorry, I never managed to fix your knee.

Acknowledgements

Personal

This thesis would not have been possible without the support of my supervisor, Jessica Hawthorne. Thank you for your support and guidance and for enabling me to have the freedom to explore new avenues of research. I would also like to thank my second supervisor, Joe Cartwright. Thank you for all the enthusiastic discussions over coffee and your guidance on life beyond this thesis.

Thank you to the earthquake mechanics group at Oxford: Yannick Caniven, Hui Huang, Julien Renou, Robin Sullivan, Shannon Blackbourne, and Chloe Fairhurst. Thank you for all the exciting discussions. A special thank you to Alice Turner and Rebecca Colquhoun for their support throughout the last four years and for putting up with me constantly talking about soil. I am also thankful to other PhD students and postdocs in the Departments of Earth Sciences and Archaeology who were there throughout my PhD journey, for the good and the bad: Hannah R, Matt, Sophie, Toby, Lewis, Lot, Hannah S, Roberta, Tamarah, Simon, and many others. Thank you also to Andrew Walker for his support and guidance on many a Python issue, as well as his enthusiasm and humour, making the long days in the office a little more bearable. I express my deepest gratitude to Conall Mac Niocaill and Karin Sigloch for allowing me to begin my 8-year journey at Oxford. Thank you, Conall, for your continuing support throughout my time in Oxford.

I would also like to thank those outside of Oxford. Thank you to the COMET community for the many fruitful discussions. Thanks also to John Langbein, Josie Nevitt, and others at the USGS for your insight into the workings of creeping faults and to Kathryn Materna for the valuable field experience along the San Andreas Fault System. I would also like to thank Emily Brodsky, Heather Savage, Susan Schwartz, and others at UCSC, as well as Roland Bürgmann and Heather Crume (Shaddox) at UC Berkeley for the lively discussions on creep events. A special thank you should go to Roger Bilham at CU Boulder. Thank you for your invaluable guidance, encouragement, expertise, and field experience. Without you, I would not understand the world of creep events and creepmeters as well as I do today.

I am indebted to my family — Mum, Dad, and sister, Heather for their continued support throughout my education. Thank you also for putting up with all the phone calls while I cook and do other domestic tasks; you are the most enjoyable "podcast." I would also like to thank my grandparents: Bill, Peggy, Betty and Norman. Thank you for supporting me along my crazy journey to Oxford; I hope that wherever you are, I have managed to make you proud.

I thank Marcia Pryce for sharing many a laugh and cups of tea over the last ten years. Thank you for always being there throughout my journey from Teesside to Oxford.

Thank you to Katy Mellor-Jones for being the most supportive friend over the last eight years. Thank you for all the crazy conversations and your constant belief in me, even when I don't believe it myself. You have kept me grounded and reminded me that there is life beyond the Oxford spires.

Finally, thank you to Ellie Wilkinson for your support, encouragement to step out of my comfort zone, and for constantly pushing me to improve as a human. Thank you for all of our adventures and for keeping me sane through the COVID lockdowns. I will always remember the life lessons I learned from you or your constant encouragement to be better as we journeyed out from Teesside 8 years ago.

Funding

This work was primarily funded by UK Research and Innovation through a Natural Environment Research Council (NERC) scholarship. Supplementary funding was received from Exeter College.

Data

The data used in this thesis comes from a variety of open-access datasets: USGS creepmeter and strainmeter data is available from USGS (2005), PBO strainmeter data is available from GAGE (2023) and NOAA rainfall data is available from NOAA (2021).

Software

The majority of the analysis in this thesis was conducted in Python 3 (Rossum and Drake, 2009) and iPython (Pérez and Granger, 2007) using a variety of packages including Cartopy (Met Office, 2010), cmcrameri (Crameri, 2018, 2023; Crameri et al., 2020), Geopandas (Jordahl et al., 2020), Matplotlib (Hunter, 2007), Numpy (Harris et al., 2020), Numba (Lam et al., 2015), ObsPy (Beyreuther et al., 2010), okada wrapper (Thompson, 2015), Pandas (McKinney, 2010; pandas development team, 2023), and Scipy (Virtanen et al., 2020).

Statement of Authorship

The work in Chapter 2 has been accepted for publication in the Journal of Geophysical Research: Solid Earth under the following title:

Gittins, D.B., and Hawthorne J.C. (2022). *Are Creep Events Big? Estimations of Along-Strike Rupture Lengths*

Jessica Hawthorne supervised the project. Daniel Gittins authored the paper and figures (which were improved with comments and suggestions from the authors), wrote the original code, and conducted the analysis.

The work in Chapter 3 has been submitted to and is under review by the Journal of Geophysical Research: Solid Earth under the following title:

Gittins, D.B. and Hawthorne J.C. (in prep). *Scattered M3–4 slip bursts within creep events on the San Andreas Fault*

Jessica Hawthorne supervised the project and provided the original strainmeter cleaning code. Daniel Gittins authored the paper and figures, modified the original codes supplied by Jessica Hawthorne, wrote the supplementary code, and conducted the analysis.

Chapter 4 of this thesis was supervised by Jessica Hawthorne. Daniel Gittins authored the chapter and figures, wrote the original code, and conducted the analysis.

Abstract

Since the 1960s, we have observed creep events along the central San Andreas Fault. Despite this, we still do not know (1) when they occur, (2) where they occur, (3) how they grow spatially, (4) how much moment they release, or (5) the driving physics behind them. To address these questions, I use creepmeter and strainmeter data from along the central San Andreas Fault.

Using a cross-correlation approach, I examine 18 USGS creepmeter records between 1985 and 2020 and identify 2120 creep events. I correlate these events between creepmeters and identify many large ($>$ few km long) creep events.

Next, I combine creepmeter and strainmeter observations at the northern end of the central San Andreas Fault to identify the along-strike location, depth, and magnitude of creep events. Strainmeters record strain offsets associated with creep events, which I reproduce by modelling the strain produced by a rectangular patch of slip at various fault locations and magnitudes. I find that creep events are not the repeated rupture of a single fault patch but arise from a range of along-strike locations at depths $>$4 km, with a magnitude of 3–4.

Finally, I use displacement-time evolution of creep events to discriminate between five rheological models for creep events: (1) rate and state friction at a constant state rate near steady state, (2) rate and state friction above steady state, and (3) rate and state friction below steady state (4) power-law flow, and (5) linear flow. Using a basin-hopping approach, I minimise the misfit between the observed creep event and the predicted displacement from each model. Most creep events have their displacement evolution best described by power-law flow or rate and state friction below steady state. These surprising results suggest that additional work is required to understand the driving physics behind creep events.

Table of Contents

List of Figures **v**

List of Tables **xvii**

Nomenclature **xviii**

1 Introduction **1**

1.1 Initial discovery of creeping faults and creep events through the offset of anthropogenic features . . . 8

1.2 Geodetic instrumentation along the San Andreas Fault over the last 60 years . . . 11

1.2.1 Early instrumentation in the 1970s . . . 11

1.2.2 Expansion of monitoring driven by the predicted 1983–1993 Parkfield earthquake . . . 13

1.2.3 The new geodetic age: airborne and satellite observations . . . 17

1.3 Geodetic estimates of the rate of fault slip on the central San Andreas Fault . . . 18

1.3.1 Along-strike creep rate variations . . . 19

1.3.2 Temporal creep rate changes . . . 23

1.3.3 How do shallow creep rates compare to these estimates of the deep slip rate along the San Andreas Fault? . . . 26

1.4 Estimates of the rupture extent of creep events . . . 27

1.4.1 Scenario A: short and shallow ruptures . . . 28

1.4.2 Scenario B: long and shallow ruptures . . . 29

1.4.3 Scenario C: long and deep ruptures . . . 30

1.5 Physical models for creep events . . . 30

1.5.1 Surface layer models . . . 31

1.5.2 Two-layer models . . . 33

1.5.3 Advanced models for producing creep events 39
1.5.4 Geology of creeping faults 41
1.6 Aims and Objectives 43
1.7 Thesis Outline 44

2 Are Creep Events Big? Estimations of Along-strike Rupture Lengths 45
2.1 Introduction 47
2.2 Creepmeters and Creep Events 53
2.3 Identifying Creep Events at Individual Creepmeters 54
2.3.1 Automated Detections 55
2.3.2 Results 58
2.4 Identifying Correlated Events Between Creepmeters 59
2.4.1 Estimating the Frequency of Multi-creepmeter Ruptures 60
2.4.2 Removing Short-term Rainfall Effects 64
2.4.3 Detecting Long Creep Events by Visual Inspection 67
2.5 Summary of Creep Event Behaviours 68
2.5.1 Isolated Events 69
2.5.2 Small Events (2 km or Less) Recorded at Two Creepmeters . . . 72
2.5.3 Medium-sized Events (3-6 km) Recorded at Two or Three Creepmeters 73
2.5.4 Large Events (10 km or more), Sometimes Skipping Creepmeters 77
2.5.5 Multi-strand Ruptures? 80
2.6 Short-term Rainfall Influence on Creep Events 82
2.6.1 Percentage of Correlated Events Decreases 83
2.6.2 Percentage of Correlated Events Remains Unchanged 85
2.6.3 Percentage of Correlated Events Increases 85
2.7 Discussion 85
2.7.1 What Drives Creep Events? 86
2.7.2 Moment Accommodated by Creep Events? 88
2.8 Conclusion 89

3 Are Creep Events Big 2? Estimations of Rupture Location, Depth, and Magnitude 91
3.1 Introduction 93
3.2 Data 95
3.2.1 Processing and correcting the strainmeter data 97
3.3 Identifying strain offsets associated with creep events 98
3.4 Identifying the location and magnitude of slip 100
3.4.1 Forward model 100
3.4.2 Matching the observed strain data 101
3.4.3 Location of the slip creating creep-event associated strain offsets 105
3.4.4 Propagation of the slip creating creep-event associated strain offsets 111
3.4.5 Depth of the slip creating creep-event associated strain offsets . 111
3.4.6 Magnitude of the slip creating creep-event associated strain offsets 114
3.5 Discussion 115

3.5.1 How many locations produce creep events? 116
3.5.2 What are the implications of patches at depth? 116
3.5.3 What is the role of creep events in accommodating the moment budget of the region? 117
3.6 Conclusion 119

4 Determining the rheology of creep events using their temporal evolution 121
4.1 Introduction 123
4.2 Data 124
4.3 Rheological Laws 126
4.3.1 Spring-Block slider model 128
4.3.2 Rate and state models 129
4.3.3 Power-law and Linear Flow 133
4.4 Fitting the shape of the events 135
4.4.1 Forward Model 135
4.4.2 Noise Estimates 136
4.4.3 Parameter Search 137
4.5 Results 138
4.5.1 Power-law flow 138
4.5.2 Rate and state friction below steady state: the healing regime ($\dot{\theta} \approx 1$) 139
4.5.3 Rate and state friction above steady state: decreasing state regime ($\dot{\theta} < 0$) 139
4.5.4 Linear flow model 139
4.5.5 Rate and state friction at constant state rate near steady state ($\dot{\theta} \approx 0$) 140
4.5.6 Fit parameters 140
4.6 Discussion 141
4.6.1 Option 1: Power-law flow 142
4.6.2 Option 2: Rate and state friction below steady state in a velocity-weakening regime (the healing regime, $\dot{\theta} \approx 1$ 143
4.6.3 Option 3: More complex model required? 143
4.7 Conclusion 145

5 General conclusions and perspectives 149
5.1 Chapter aims 150
5.1.1 Chapter 2: Are Creep Events Big? Estimations of Along-strike Rupture Lengths 150
5.1.2 Chapter 3: Are Creep Events Big 2? Estimations of Rupture Location, Depth, and Magnitude 152
5.1.3 Chapter 4: Rheology of creep events 154
5.2 Future Work 155
5.3 Broader Outlook 157
5.4 Concluding remarks 159

A Supporting Material for 'Are Creep Events Big? Estimations of Along-strike Rupture Lengths' 161

A.1 Supplementary Text S1 162
A.2 Creep Catalog 166
A.3 Creep Booklets 168
A.4 Supplementary Figures 169

B Supporting Material for 'Are Creep Events Big 2? Estimations of Rupture Location, Depth, and Magnitude' 192

B.1 Supplementary Figures 192

References 195

List of Figures

1.1 Creepmeter record from CWC showing multiple creep events. Inset shows an example of a creep event in November 1994. 3

1.2 Distribution of geodetic instruments in the 1960s. The location of instruments are from: Schulz (1989) (creepmeters), Burford and Harsh (1980) (alignment arrays and some anthropogenic structures), Brown and Wallace (1968) (anthropogenic structures) and Wallace and Roth (1967) (anthropogenic structures). The locations of faults (grey lines) are from USGS and CGS (2020), with the San Andreas Fault highlighted (as the black line). 4

1.3 Distribution of geodetic instruments in the 1970s. The location of instruments are from: Schulz (1989) (creepmeters), Burford and Harsh (1980) (alignment arrays and some anthropogenic structures), Lisowski and Prescott (1981) (short-range network survey) and the USGS (1991) (geodolites). The locations of faults (grey lines) are from USGS and CGS (2020), with the San Andreas Fault highlighted (as the black line). . . . 5

1.4 Distribution of geodetic instruments in the 1980s. The location of instruments are from: Schulz (1989) (creepmeters), USGS (1991) (geodolites) USGS (2005) (EDM) and USGS (2023) (tensor borehole strainmeters). The locations of faults (grey lines) are from USGS and CGS (2020), with the San Andreas Fault highlighted (as the black line). 6

1.5 Distribution of geodetic instruments in the 1990s. The location of instruments are from: Schulz (1989) (creepmeters), USGS (1991) (geodolites) USGS (2005) (EDM), USGS (2023) (tensor borehole strainmeters), GAGE (2023) (tensor borehole strainmeters) and Murray and Svarc (2017) (GNSS). The locations of faults (grey lines) are from USGS and CGS (2020), with the San Andreas Fault highlighted (as the black line). 7

1.6 Scaling relationships of slow- and regular earthquakes, modified from Gombert and Hawthorne (2023). Values are taken from (1) Shelly (2017); Thomas et al. (2016); Hawthorne et al. (2019), (2) Farge et al. (2020), (3) Huang and Hawthorne (2022), (4) Supino et al. (2020), (5) Bostock et al. (2015), (6) Ito et al. (2007), (7) Matsuzawa et al. (2009), (8) Maury et al. (2016), (9) Yabe et al. (2021), (10) Takeo et al. (2010), (11) Ide et al. (2008), (12) Royer et al. (2015); Hawthorne et al. (2016a), (13) Itaba and Ando (2011), (14) Kitagawa et al. (2011), (15) Itaba et al. (2013); Ochi et al. (2016), (16) Sekine et al. (2010), (17) Rousset et al. (2017), (18) Michel et al. (2019), (19) Tu and Heki (2017). 8
1.7 Damaged drainage gully and wall at the Cienega Winery, Cienega Rd, Hollister, CA. a), b) & c) Drainage gully offset by right lateral creep. d) Damage to the NW wall of the winery building due to right lateral creep. 9
1.8 Fence offset by right lateral creep at Nyland Ranch, San Juan Bautista, CA. View taken looking down Road D. 10
1.9 Offset pavement (a)) and curb (b)) along 6$^{\text{th}}$ Street, Hollister, CA by right lateral creep. 10
1.10 Schematic illustration of a creepmeter. Modified from Bilham et al. (2004). 12
1.11 Installation set up for the B065 strainmeter used in Chapter 3. Shown are the borehole structure, original gauge orientations and installation geology. Figure from the Plate Boundary Observatory notes on B065, available from https://www.unavco.org/data/strain-seismic/bsm-data/bsm-data.html. 16
1.12 Distribution of geodetic instruments in the 2000s. The location of instruments are from: Schulz (1989) (creepmeters), USGS (2005) (EDM), USGS (2023) (tensor borehole strainmeters and dilatometers), GAGE (2023) (tensor borehole strainmeters) and Murray and Svarc (2017) (GNSS). The locations of faults (grey lines) are from USGS and CGS (2020), with the San Andreas Fault highlighted (as the black line). 19
1.13 Distribution of geodetic instruments in the 2010s. The location of instruments are from: Schulz (1989) (creepmeters), USGS (2023) (tensor borehole strainmeters and dilatometers), GAGE (2023) (tensor borehole strainmeters) and Murray and Svarc (2017) (GNSS). The locations of faults (grey lines) are from USGS and CGS (2020), with the San Andreas Fault highlighted (as the black line). 20
1.14 Distribution of geodetic instruments in the 2020s. The location of instruments are from: Schulz (1989) (creepmeters), USGS (2023) (tensor borehole strainmeters and dilatometers), GAGE (2023) (tensor borehole strainmeters) and Murray and Svarc (2017) (GNSS). 21

1.15 a) Schematic diagram illustrating the fault slip rate and depth that different instruments can record. b) Schematic diagram showing the depths of different events recorded along the creeping section of the San Andreas Fault. Depths are approximated but based upon creep event depths from Gladwin et al. (1994), McHugh and Johnston (1978) and Mortensen et al. (1977), repeating earthquake depths from Waldhauser and Schaff (2008), background seismicity depths from Waldhauser and Schaff (2021), slow slip and tremor depths from Rousset et al. (2019a) and rupture extent of the Parkfield earthquake depths are based upon creepmeter observations and the epicentre of the 2004 Parkfield earthquake described in Langbein et al. (2005). c) Plot of slip rate with distance along the San Andreas Fault. The orange line represents the instruments with a short aperture (<10 m), the dark blue striped line represents the instruments with an intermediate aperture (10 m – 1 km), and the light blue dashed line represents the instruments with a large aperture (>1 km). Panel c) is modified from Burford and Harsh (1980), Lisowski and Prescott (1981) and Titus (2006) and is based upon creepmeter data from Schulz et al. (1982) and Schulz (1989); 10-year alignment array data from Burford and Harsh (1980); short-range networks and geodolite data from Lisowski and Prescott (1981); 35-year alignment array data and continuous GPS data from Titus et al. (2005) and Titus (2006) and a plate motion rate from Argus and Gordon (2001). 24
1.16 Surface creepmeter displacement measurements five years after the 2004 M_w 6 Parkfield earthquake. The vertical line represents the time of the earthquake. 25
1.17 Three scenarios for creep events. a) small and shallow, b) long and shallow and c) long and deep. 28
1.18 Model for the spatial growth of creep events through an expanding circular slip patch. Modified from King et al. (1973). 31
1.19 Two layer model for creep events proposed by Bilham and Behr (1992). Modified from Bilham and Behr (1992). 35
1.20 Two layer model for creep events proposed by Scholz (1998). Modified from Wei et al. (2013). 37
1.21 Three layer model for aseismic slip proposed by Wei et al. (2013) to explain stable creep, creep events and afterslip. Modified from Wei et al. (2013). 38

2.1 Map of the creeping section of the central San Andreas Fault (black) and other faults in central California (grey). The creepmeters are shown as coloured triangles. National Oceanic and Atmospheric Administration (NOAA) stations are shown as black circles. Faults plotted are from the United States Geological Survey (USGS)/California Geological Survey (CGS) Quaternary faults and folds database (USGS and CGS, 2020). . 49

2.2 10 years of slip at two creepmeter locations that show creep events of different characters: a) Cienega Winery (CWN), showing a multi-step creep event, and b) Middle Mountain (XMM), showing a single step creep event. 50
2.3 Three creep event size scenarios. a) Short, shallow ruptures. b) Long, shallow ruptures. c) Long, deep ruptures. 52
2.4 Processing stages of the automated detection. a) Raw creepmeter data from Cienega Winery (CWN) showing a creep event on 11th February 1994. b) The same creep event bandpass filtered between 2 h and 5 d (black line), along with the template creep event (green line). The template has been aligned with the data according to the peak of the cross-correlation time series shown in panel (c). The red cross in all panels indicates the estimated creep event start time, taken as the time of the trough in the filtered data in panel b). 56
2.5 Properties of the creep events at each creepmeter. a) Number of detected events. b) Median creep event slip. c) Median creep event duration. d) Percentage of total fault slip accommodated in creep events. Note XRSW, XHSW, and X46 do not have values. This is due to a large amount of left-lateral slip, making calculating the total amount of slip for these creepmeters not easily quantifiable. e) Median slip divided by median recurrence interval. 60
2.6 Creep records for the 21 to 26th May 2016 at (a) Cienega Winery (CWN), (b) Harris Ranch (XHR), and (c) San Juan Bautista (XSJ). The figure illustrates our approach to detecting closely timed events. For each event at Cienega Winery (panel a), we search for events at (b) Harris Ranch and (c) San Juan Bautista that occur within 24 hours of the Cienega Winery event (grey regions in panels b and c). 61
2.7 a) Probability distributions of the percentage of CWN creep events observed at XHR (orange) and XSJ (green) within 24 hours, based on bootstrapping. b) Probability distributions that a CWN event would coincide with an XHR or XSJ event by chance: if events were randomly timed. c) The distributions in (a) minus the distributions in (b): probability distributions on the percentage of CWN events that were observed at XHR and XSJ within 24 hours for a physical reason. 63
2.8 (a-c) Probability distributions on the percentage of XMM events observed at XMD. Panels a-c are as in Figure 2.7, with the observed, by chance, and real percentages, but the three histograms in each panel illustrate the effect of removing rainy intervals. The blue histograms use all XMM events in the comparison, while the orange and red histograms use only XMM events that follow 7 or 14-day periods without rain. d) The percentage of XMM events observed at XMD by chance, as in panel b, but when XMD events preceded by rainfall are removed. The reduced percentage suggests that XMD events are more common in rainy intervals. 68

2.9 Maps of the creeping section of the central San Andreas Fault (black) showing the location of different creep event behaviours. The creepmeters are shown as coloured triangles, and greyed-out triangles are creepmeters not involved in events. a) Location of isolated events. b) Location of (<2 km) events recorded at two creepmeters. c) Location of 5 km events recorded at multiple creepmeters. d) Location of long (10 to 30 km) propagating events. 69
2.10 Creep events and percentage of events observed at other creepmeters for isolated creep events at XSJ, XMR, and XGH. a) Creep event at XSJ on 15th June 1993. c) Creep event at XMR on 18th May 1993. e) Creep event at XGH on 8th July 1991. b), d) and f) indicate the percentage of events XSJ, XMR, and XGH events found at other creepmeters, with 70% confidence intervals. Vertical coloured lines in b), d) and f) mark the location of the creepmeter. 71
2.11 Small creep events from the XMM - XMD and Highway 46 (X46 & C46) areas and percentage of events observed at other creepmeters for XMM and X46. a) Creep event at XMM and XMD on 26th July 1991. c) Creep event at X46 and C46 on 22st June 2015.b) and d) indicate the percentage of XMM and X46 events found at other creepmeters, with 70% confidence intervals. Vertical coloured lines in b) and d) mark the location of the creepmeters in a) and c). 74
2.12 Medium-sized creep events from the XHR - CWN, XMM - XVA, XVA - XTA areas and the Southwest trace (XRSW - XHSW) and percentage of events observed at other creepmeters for XHR, XMD, XVA, and XRSW. a) Creep event at XHR and CWN on 11th–12th February 1994. c) Creep event at XMM, XMD and XVA on 29th–30th June 2014. e) Creep event at XVA, XPK and XTA on 21st–22st April 2008. g) Creep event at XRSW and XHSW on 16th January 1993. b), d), f), and h) indicate the percentage of XHR, XMD, XVA, and XRSW events found at other creepmeters, with 70% confidence intervals. Vertical coloured lines in b), d), f), and h) mark the location of the creepmeters in a), c), e) and g) respectively. 78
2.13 Potential large creep events from XSC - WKR section and percentage of events observed at other creepmeters for XPK and XSC. a) Creep event on the XMM - XTA section on 23st–25th September 2000. c) Creep event along the XSC - WKR section on 3st–4th March 1991. b) and d) indicate the percentage of XPK and XSC events found at other creepmeters, with 70% confidence intervals. Vertical coloured lines in b) and d) mark the location of the creepmeters in a) and c). 81
2.14 Scatter plots of the median percentage of creep events found at XHSW. In panel (a), all XHSW events are included. In panel (b), XHSW events with rainfall in the 7 days prior are removed. 83

2.15 Percentage of creep events observed at pairs of creepmeters accounting for rainfall. a) Percentage of XSC events observed at WKR. b) Percentage of XMM events observed at XMD. c) Percentage of CWN events observed at XHR. In a), b), and c), the original percentages are in blue, and the percentage of events after accounting for rainfall in the previous 7- or 14-days are orange and red, respectively. 84

3.1 Map of the northern end of the creeping section of the San Andreas Fault (black). Other faults in central California are shown in grey. The USGS creepmeters are coloured triangles (XSJ: dark blue, XHR: medium blue, CWN: light blue), and the USGS (green) and PBO (orange) strainmeters are coloured circles. Faults plotted are from the USGS/California Geological Survey Quaternary Faults and Folds database (USGS and CGS, 2020). 94

3.2 Strain offsets associated with creep events. a) & d) XHR082, b) & e) CWN080 and c) & f) XHR084. In a) to c), the orange and brown lines represent the ϵ_{E-N}-na and ϵ_{2EN}-na components at B065, respectively. The dark green and medium green lines represent the ϵ_{E-N} and ϵ_{2EN} components at SJT when it was operational. In d) to f), creep records from XSJ (dark blue dashed line), XHR (medium blue solid line), and CWN (light blue dot-dashed line) are plotted. The grey vertical bar represents the time shown in the corresponding panel above for the strain offset, with the orange vertical bar representing the duration and timing of the associated strain offset. 96

3.3 Histograms showing the size of the observed strain offsets on the non-atmospheric components of a) ϵ_{E-N}-na, and b) ϵ_{2EN}-na, as well as c) their duration and d) onset time difference to creep events recorded on creepmeters. 99

3.4 Green's functions of a) ϵ_{E-N}-na and d) ϵ_{2EN}-na components showing how strain changes at the surface as a result of displacements in different locations. The shaded region of panels a) & d) represent regions that produce positive strain offsets. In contrast, the unshaded represent the regions that produce a negative strain offset. The contours in both the shaded and unshaded regions illustrate how the strain offsets change within the regions, with locations further away from the boundary between shaded and unshaded having larger strain offsets. The vertical dashed blue line is the depth cross-section in b) or e). The horizontal dashed green line is the along-strike cross-section in c) & f). b) & e) show the effects of varying depth at one location (blue crosses) compared to the observed offset and associated uncertainty (black shifted histogram) for the ϵ_{E-N}-na and ϵ_{2EN}-na respectively. c) & f) show the effects of varying along-strike location at one depth (green circles) compared to the observed offset and associated uncertainty (black shifted histogram) for the ϵ_{E-N}-na and ϵ_{2EN}-na respectively. 102

3.5 XHR094 observed at B065 and associated with a creep event at XHR. a) Magnitude of the best fitting scenarios for each 500×500m grid square. b) Strain records of B065 (ϵ_{E-N}-na orange line and ϵ_{2EN}-na brown line). The vertical orange bar shows the duration of the strain offset. c) Relative probability of the best fitting scenarios for each 500×500m grid square. d) Creepmeter record of XSJ (dark blue dashed line), XHR (medium blue solid line), and CWN (light blue dot-dashed line). The grey vertical bar represents the time shown in b), with the orange vertical bar representing the duration and timing of the associated strain offset. In a) & c), the grey dots are seismicity from the Northern California Earthquake Data Center catalogue (NCEDC, 2014), the brown and orange lines are contours of the Green's function of the ϵ_{2EN}-na and ϵ_{E-N}-na components of strain respectively. The hatching shows where the Green's function is positive. 106
3.6 XHR083 observed at B065 and associated with a creep event at XHR, panels as in 3.5. 107
3.7 XHR084 observed at B065, associated with a creep event at XHR, panels as in 3.5. 107
3.8 CWN094_2 observed at B065 and associated with a creep event at CWN, panels as in 3.5. 108
3.9 a) Distance from XHR horizontally of the five best-fitting scenarios for each strain event, ordered by the distance of each event's best-fitting scenario and coloured by each scenario's relative probability. The vertical dashed blue lines represent the location of XHR (dark blue) and CWN (light blue). b) The depth of the five best-fitting scenarios for each strain event, ordered by the depth of each event's best-fitting scenario and coloured by each scenario's relative probability. The vertical dashed orange line represents 2 km depth, and the vertical dashed brown line represents 4 km depth. 109
3.10 a) Location of the five best-fitting scenarios for slip location creating strain offsets when data is available from SJT. b) Location of the five best-fitting scenarios for all slip locations creating strain offsets. The grey dots are seismicity from the Northern California Earthquake Data Center catalogue (NCEDC, 2014). 110
3.11 a) Strainmeter record spanning XHR084, XHR084_2, and CWN081, with ϵ_{E-N}-na shown as the orange line and ϵ_{2EN}-na as the brown line. b) Creepmeter record of the same time as in a), showing the creepmeter records of XSJ (dashed dark blue), XHR (solid medium blue), and CWN (dot-dashed light blue). In both a) and b), the durations of strain offsets XHR084, XHR084_2, and CWN081 are shown as dark, medium, and light green vertical bands, respectively. c), d) & e) Probability distributions for XHR084, XHR084_2 and CWN081 respectively. c), d) & e) are as in 3.5 c). 112

3.12 Histograms of the percentage of slip locations in each depth range following bootstrapping. The blue histogram shows the 0 - 2 km depth range, the orange histogram shows the 2 - 4 km depth range, and the green histogram shows the 4+ km range. The grey histogram represents the slip location group with an inconclusive depth range. 113
3.13 Magnitude of the top five scenarios for each strain event. Each square is coloured based on the top 5 events and their relative probability. The blue and orange vertical lines represent M_w 3 and 4 respectively. 114
3.14 Histograms of the percentage of creep events in each M_w range following bootstrapping. The blue histogram shows the creep events with M_w <3.0, the orange histogram shows creep events with M_w 3.0 - 4.0, and the green histogram shows events with M_w >4.0. 115

4.1 Map of the northern end of the creeping section of the central San Andreas Fault (black). Other faults in central California are shown in grey. The USGS creepmeter XHR is the grey triangle. Faults plotted are from the USGS/California Geological Survey Quaternary faults and folds database (USGS and CGS, 2020). 125
4.2 Example creep event recorded at XHR2 on 15th December 1997. Key features of the creep events recorded at XHR are highlighted. 126
4.3 Spring block slider model. 128
4.4 a) The covariance matrix of the earlier XHR2 creepmeter (1992 to 2005). b) The covariance matrix of the later XHR3 creepmeter (2009 to 2019). Note that XHR3 has lower noise than XHR2. 137
4.5 Six example events showing the five rheological fits. a) XHR 004, b) XHR 030, c) XHR 064, d) XHR 072, e) XHR 088 & f) XHR 105. Note that event codes refer to the events in the catalogue of Gittins and Hawthorne (2022a). The observed creepmeter data are grey circles. Linear flow and power-law flow are in light and dark blue, respectively. For the rate and state friction laws, the constant state rate near the steady state ($\dot{\theta} \approx 0$) is in red, the above steady state (decreasing state) is in orange, and the below steady state (healing regime) is in yellow. 146
4.6 Histograms showing the percentage of events best fit by each rheology. Linear flow and power-law flow are in light and dark blue, respectively. For the rate and state friction laws, the constant state rate near steady state ($\dot{\theta} \approx 0$) is in red, the above steady state (decreasing state) is in orange, and the below steady state (healing regime) is in yellow. . . . 147

4.7 Distributions of the fitting parameters. a) & b) are the initial slip rate and time constant of the linear flow law. c), d), and e) are the power-law flow law's initial slip rate, time constant, and power-law exponent. f) & g) are the initial slip rate and time constant of the rate and state friction at a constant state rate near steady state ($\dot{\theta} \approx 0$). h), i) & j) are the initial slip rate, time constant, and time of tectonic loading in the rate and state friction law above steady state (decreasing state). k), l), and m) are the initial slip rate, time constant, and the ratio of the rate and state coefficients B/A of the rate and state friction law below the steady state (healing regime). 148

A.1 Examples of creep event and non-creep event-related signals at both CWN and XMM. The blue vertical dashed lines indicate the start of the event, and the orange dashed line is the end of the event. a) Example of creep event at CWN. b) Example of a non-creep event-related step at CWN. c) Example of creep event at XMM. d) Example of a non-creep event-related step at XMM. 169
A.2 Scatter plots plotting slip, duration and number of events against one another. a) Median slip vs. number of events at each creepmeter. b) Median duration vs. number of events at each creepmeter. c) Median slip vs. medium duration of events at each creepmeter. 170
A.3 Recurrence intervals of creep events at the 18 USGS creepmeters used in this study. 171
A.4 Recurrence intervals of creep events at southern creepmeters before and after the 2004 Parkfield earthquake. 172
A.5 Creep records from 18 USGS creepmeters showing the timing of creep events. The inter-event slip has been set to 0. The grey vertical band shows the times when creep events were removed from our analysis of southern creepmeters due to the 2004 Parkfield Earthquake. 173
A.6 Spatio-temporal plot of the number of creep events per month at each of the 18 USGS creepmeters, ordered by distance from San Juan Bautista. 28/Sep/2004 - 01/Jan/2006 excluded for southern creepmeters. 174
A.7 Propagation velocities of all creep events found within 24 hours of a creep event at any other creepmeter. The vertical coloured lines below 0 indicate the propagation velocities reported by Evans et al. (1981) (dark purple), King et al. (1973) (light purple) and Mortensen et al. (1977) (light green). 175
A.8 Percentage of XSJ events observed at all other creepmeters, scaled with distance. 175
A.9 Percentage of XHR events observed at all other creepmeters, scaled with distance. 176
A.10 Percentage of CWN events observed at all other creepmeters, scaled with distance. 176
A.11 Percentage of XMR events observed at all other creepmeters, scaled with distance. 177

A.12 Percentage of XSC events observed at all other creepmeters, scaled with distance. 177
A.13 Percentage of XMM events observed at all other creepmeters, scaled with distance. 178
A.14 Percentage of XMD events observed at all other creepmeters, scaled with distance. 178
A.15 Percentage of XVA events observed at all other creepmeters, scaled with distance. 179
A.16 Percentage of XRSW events observed at all other creepmeters, scaled with distance. 179
A.17 Percentage of XPK events observed at all other creepmeters, scaled with distance. 180
A.18 Percentage of XTA events observed at all other creepmeters, scaled with distance. 180
A.19 Percentage of XHSW events observed at all other creepmeters, scaled with distance. 181
A.20 Percentage of WKR events observed at all other creepmeters, scaled with distance. 181
A.21 Percentage of CRR events observed at all other creepmeters, scaled with distance. 182
A.22 Percentage of XGH events observed at all other creepmeters, scaled with distance. 182
A.23 Percentage of C46 events observed at all other creepmeters, scaled with distance. 183
A.24 Percentage of X46 events observed at all other creepmeters, scaled with distance. 183
A.25 Percentage of creep events remaining when events with rainfall in the 3- (light blue), 7- (orange), and 14-days (red) before the event are removed. 184
A.26 Rainfall analysis histograms for Middle Mountain (XMM) and Middle Ridge (XMD). Blue histograms are the original analysis before rainfall was removed, and orange and red histograms are for when events with rainfall in the 7 or 14 days prior are removed, respectively. a) and b) are the bootstrapped distributions of the percentage of events with different amounts of rainfall accounted for. c) and d) show the percentage of time-correlated events that are occurring by chance. e) and f) are the percentage of events that are detected at both creepmeters when by chance occurrences are removed. g) and h) show the percentage of events that are observed at one creepmeter given seasonality and rain at the other. 185

A.27 Rainfall analysis histograms for Highway 46 (X46/C46). Blue histograms are the original analysis before rainfall was removed, and orange and red histograms are for when events with rainfall in the 7 or 14 days prior are removed, respectively. a) and b) are the bootstrapped distributions of the percentage of events with different amounts of rainfall accounted for. c) and d) show the percentage of time-correlated events that are occurring by chance. e) and f) are the percentage of events that are detected at both creepmeters when by chance occurrences are removed. g) and h) show the percentage of events that are observed at one creepmeter given seasonality and rain at the other. 186
A.28 Rainfall analysis histograms for Harris Ranch (XHR) and Cienega Winery (CWN). Blue histograms are the original analysis before rainfall was removed, and orange and red histograms are for when events with rainfall in the 7 or 14 days prior are removed, respectively. a) and b) are the bootstrapped distributions of the percentage of events with different amounts of rainfall accounted for. c) and d) show the percentage of time-correlated events that are occurring by chance. e) and f) are the percentage of events that are detected at both creepmeters when by chance occurrences are removed. g) and h) show the percentage of events that are observed at one creepmeter given seasonality and rain at the other. 187
A.29 Rainfall analysis histograms for Slacks Canyon (XSC) and Work Ranch (WKR). Blue histograms are the original analysis before rainfall was removed, and orange and red histograms are for when events with rainfall in the 7 or 14 days prior are removed, respectively. a) and b) are the bootstrapped distributions of the percentage of events with different amounts of rainfall accounted for. c) and d) show the percentage of time-correlated events that are occurring by chance. e) and f) are the percentage of events that are detected at both creepmeters when by chance occurrences are removed. g) and h) show the percentage of events that are observed at one creepmeter given seasonality and rain at the other. 188
A.30 Rainfall analysis histograms for Roberson Southwest (XRSW) and Hearst Southwest (XHSW). Blue histograms are the original analysis before rainfall was removed, and orange and red histograms are for when events with rainfall in the 7 or 14 days prior are removed, respectively. a) and b) are the bootstrapped distributions of the percentage of events with different amounts of rainfall accounted for. c) and d) show the percentage of time-correlated events that are occurring by chance. e) and f) are the percentage of events that are detected at both creepmeters when by chance occurrences are removed. g) and h) show the percentage of events that are observed at one creepmeter given seasonality and rain at the other. 189

A.31 Rainfall analysis histograms for Hearst Southwest (XHSW) and Varian (XVA). Blue histograms are the original analysis before rainfall was removed, and orange and red histograms are for when events with rainfall in the 7 or 14 days prior are removed, respectively. a) and b) are the bootstrapped distributions of the percentage of events with different amounts of rainfall accounted for. c) and d) show the percentage of time-correlated events that are occurring by chance. e) and f) are the percentage of events that are detected at both creepmeters when by chance occurrences are removed. g) and h) show the percentage of events that are observed at one creepmeter given seasonality and rain at the other. 190
A.32 Rainfall analysis histograms for Hearst Southwest (XHSW) and Parkfield (XPK). Blue histograms are the original analysis before rainfall was removed, and orange and red histograms are for when events with rainfall in the 7 or 14 days prior are removed, respectively. a) and b) are the bootstrapped distributions of the percentage of events with different amounts of rainfall accounted for. c) and d) show the percentage of time-correlated events that are occurring by chance. e) and f) are the percentage of events that are detected at both creepmeters when by chance occurrences are removed. g) and h) show the percentage of events that are observed at one creepmeter given seasonality and rain at the other. 191

B.1 How ϵ_{E-N} strain offsets changes for a 500×500 m patch of fault slipping at different depths (panels a) - c)), having different magnitudes (panels d) - f)) or changing along-strike location (panels g) - i)). The orange horizontal line represents the fault plane, and the orange circle is the location of a hypothetical strainmeter. 193
B.2 Affect of changing the magnitude of the rectangular patch in the grid search on both the ϵ_{E-N} (a)) and ϵ_{2EN} (b)) components of strain. . . . 193
B.3 CWN080 observed at B065, associated with a creep event at CWN, panels as in 3.5. 194
B.4 Seismicity at the northern end of the creeping section of the San Andreas Fault (grey circles). Creepmeter locations are plotted at the surface (XSJ, dark blue; XHR, medium blue; and CWN, light blue). Horizontal orange and brown lines represent 2 and 4 km depths, respectively, and mark the depths used for categorising the depth of the slip patches producing strain offsets. 194

List of Tables

1.1 Pros and Cons of creepmeters. 13
1.2 Pros and Cons of strainmeters. 17

2.1 Some previous estimates of the spatial extent of creep events. 51

Nomenclature

List of symbols

Arabic

A	Coefficient of rate-and-state direct effect
B	Coefficient of the rate-and-state evolution effect
C	Data covariance matrix
D_c	Characteristic slip distance
k, k_B	Spring stiffness, characteristic-
n	Power-law exponent
Q	Fitting Constant
T_{01}	Timing of the start of the rheological fit
$t, t_0, t_1, t_a, t_c, t_{ss}$	Time, initial-, -constant for displacement decay, -characteristic of loading, -constant for displacement decay (flow laws), -constant for displacement decay (at steady state)
V, V_0, V_b, V^*	Sliding velocity, initial-, background-, reference-

Greek

$\delta, \delta_0, \delta_{obs}, \delta_{pred}, \delta_r$	Displacement, initial-, observed-, predicted-, -for a given rheology
$\epsilon, \epsilon_{E+N}, \epsilon_{E-N}, \epsilon_{2EN}$	Strain, areal-, differential, engineering-
θ, θ_0	State variable, Characteristic time
μ, μ_{ss}, μ^*	Friction coefficient, -at steady state, reference value of friction
σ	Normal stress
τ, τ_d	Frictional strength, driving stress
$\dot{\tau}_l$	Loading rate from the surrounding material

List of Abbreviations

B065	PBO strainmeter near Harris Ranch & Cienega Winery
C46	Highway 46 creepmeter (newer)
CGS	California Geological Survey
CRR	Carr Ranch creepmeter
CWC	Cienega Winery Central creepmeter
CWN	Cienega Winery North creepmeter
LFEs	Low-Frequency Earthqaukes
PBO	Plate Boundary Observatory
SJT	USGS strainmeter near San Juan Bautista
SSEs	Slow Slip Events
USGS	United States Geological Survey
VLFEs	Very Low-Frequency Earthquakes
WKR	Work Ranch creepmeter
X46	Highway 46 creepmeter (older)
XGH	Gold Hill creepmeter
XHR	Harris Ranch creepmeter
XHSW	Hearst Southwest creepmeter
XMD	Middle Ridge creepmeter
XMM	Middle Mountain creepmeter
XMR	Melendy Ranch creepmeter
XPK	Parkfield creepmeter
XRSW	Roberson Southwest creepmeter
XSC	Slacks Canyon creepmeter
XSJ	San Juan Bautista creepmeter
XTA	Taylor Ranch creepmeter
XVA	Varian creepmeter

1

Introduction

1.1 Initial discovery of creeping faults and creep events through the offset of anthropogenic features . . . 8
1.2 Geodetic instrumentation along the San Andreas Fault over the last 60 years . . . 11
1.2.1 Early instrumentation in the 1970s . . . 11
1.2.2 Expansion of monitoring driven by the predicted 1983–1993 Parkfield earthquake . . . 13
1.2.3 The new geodetic age: airborne and satellite observations . . . 17
1.3 Geodetic estimates of the rate of fault slip on the central San Andreas Fault . . . 18
1.3.1 Along-strike creep rate variations . . . 19
1.3.2 Temporal creep rate changes . . . 23
1.3.3 How do shallow creep rates compare to these estimates of the deep slip rate along the San Andreas Fault? . . . 26
1.4 Estimates of the rupture extent of creep events . . . 27
1.4.1 Scenario A: short and shallow ruptures . . . 28
1.4.2 Scenario B: long and shallow ruptures . . . 29
1.4.3 Scenario C: long and deep ruptures . . . 30
1.5 Physical models for creep events . . . 30
1.5.1 Surface layer models . . . 31
1.5.2 Two-layer models . . . 33
1.5.3 Advanced models for producing creep events . . . 39
1.5.4 Geology of creeping faults . . . 41
1.6 Aims and Objectives . . . 43
1.7 Thesis Outline . . . 44

Aseismic fault creep was discovered in the middle of the 20th-century (e.g., Steinbrugge and Zacher, 1960), making it a relatively new area of research when compared to earthquakes which have been known about since antiquity (e.g., Stiros, 2021). We first observed aseismic fault creep using the offset of anthropogenic features such as walls and fences (e.g., Ambraseys, 1970; Steinbrugge and Zacher, 1960), and later on using a variety of geodetic instruments (e.g., Gladwin et al., 1994; Huggett et al., 1977; Jolivet et al., 2012; Lyons et al., 2002; Mchugh and Johnston, 1976; Savage and Prescott, 1973; Schulz, 1989; Scott et al., 2020a).

One of the most interesting properties of aseismic creep is that it does not always occur at a steady rate but may occur in bursts of slip, known as creep events. These creep events were first observed in the mid-20$^{\mathrm{th}}$ century along the San Andreas Fault (Tocher, 1960). Figure 1.1 shows examples of creep events recorded on a creepmeter at Cienega Winery, CA. Creep events became the focus of study on aseismic fault creep throughout much of the 1970s–1990s (e.g., Burford, 1977; Evans et al., 1981; Gladwin et al., 1994; Schulz, 1989). To monitor these events, specialist equipment known as creepmeters (see Box 1 for details) were developed and installed all along the central San Andreas Fault in the 1960s & 1970s (e.g., Schulz, 1989), as shown in Figures 1.2 & 1.3. Through these creepmeters, we were able to determine that these creep events had slip amplitudes of a few millimetres, lasted for a few hours to days and occurred every few weeks to months (e.g., Burford, 1977; Gladwin et al., 1994; Schulz, 1989).

In the early 1980s, Schulz et al. (1983) noticed that creep events were closely associated with rainfall, often occurring in the 24 hours following rainfall (Roeloffs, 2001; Schulz et al., 1983). Since these creep events appeared to be small, rainfall-associated events, interest in them began to wane, as is indicated by the number of instruments that ceased to operate in the late 1980s and early 1990s (see Figures 1.4 & 1.5).

As interest in shallow creep events was subsiding, Linde et al. (1996) discovered a new form of aseismic transient that was larger and deeper than shallow creep events. Although this large aseismic transient was of note, work on aseismic creep largely remained focused on investigating the relationship between earthquakes and triggered slip (e.g., Behr et al., 1997).

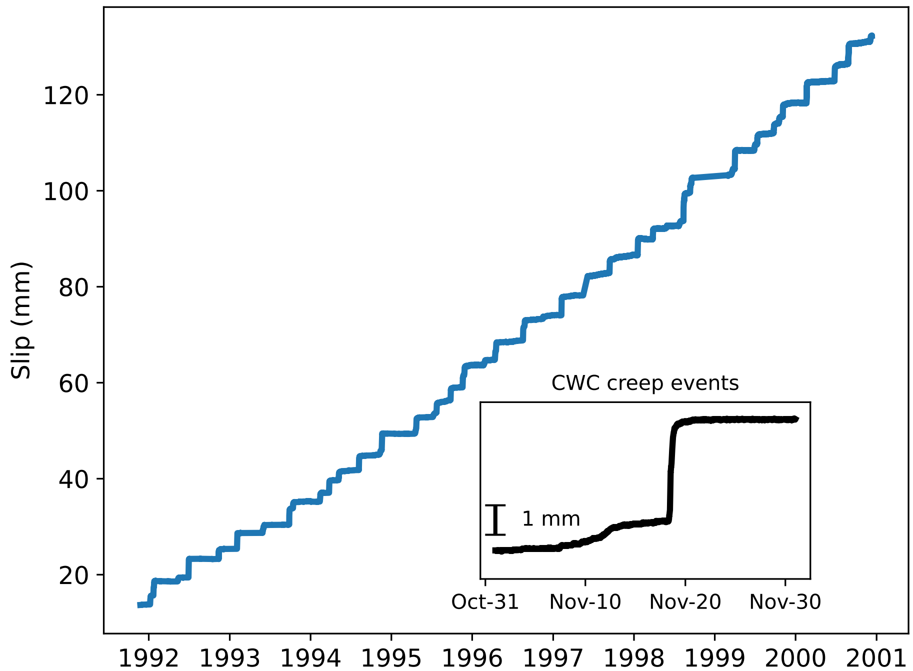

Figure 1.1: Creepmeter record from CWC showing multiple creep events. Inset shows an example of a creep event in November 1994.

In the early 2000s, a new set of fault phenomena was identified, which included: Slow Slip Events (SSEs) (e.g., Dragert et al., 2001; Rogers and Dragert, 2003; Rousset et al., 2019b), tremor (e.g., Rogers and Dragert, 2003; Shelly et al., 2007b), Low-Frequency Earthquakes (LFEs) (e.g., Shelly et al., 2006) and Very Low-Frequency Earthquakes (VLFEs) (e.g., Ide and Yabe, 2014). This caused the focus to shift from small shallow aseismic transients on a few strike-slip faults globally to large aseismic transients that lasted weeks to months and have been found on subduction zones around the world including Cascadia (e.g., Ghosh et al., 2010; Hawthorne and Rubin, 2013; Rogers and Dragert, 2003; Rubin and Armbruster, 2013), Japan (e.g., Shelly et al., 2007a, 2006), Mexico (e.g., Peng and Rubin, 2017; Tymofyeyeva et al., 2019), Costa Rica (e.g., Walter et al., 2011), Alaska (e.g., Rousset et al., 2019b), and New Zealand (e.g., Shreedharan et al., 2022; Warren-Smith et al., 2019). These events were also observed along strike-slip faults, such as along the San Andreas Fault near Parkfield, CA (e.g., Huang and Hawthorne, 2022; Rousset et al., 2019a). This new set of fault phenomena is now

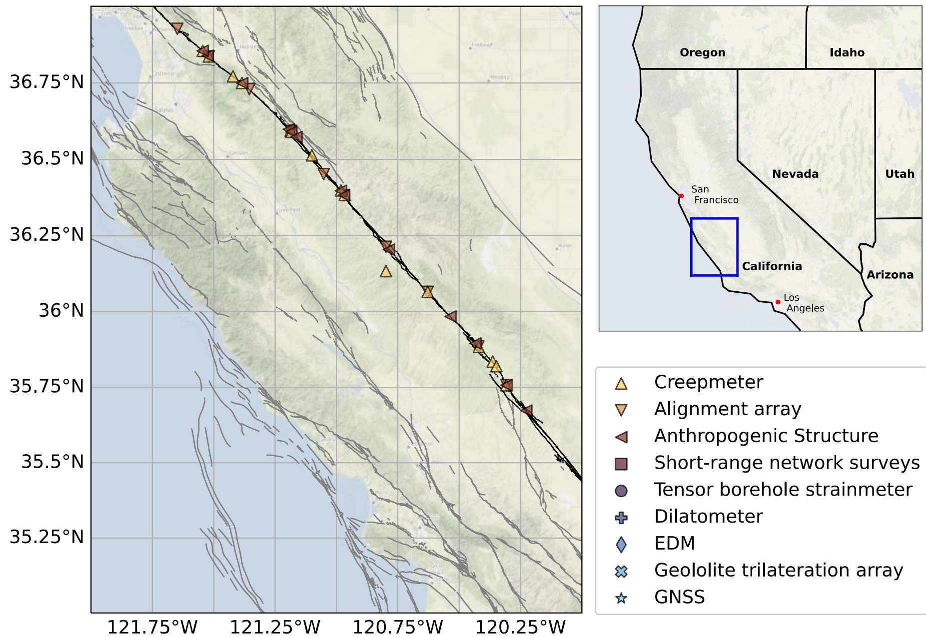

Figure 1.2: Distribution of geodetic instruments in the 1960s. The location of instruments are from: Schulz (1989) (creepmeters), Burford and Harsh (1980) (alignment arrays and some anthropogenic structures), Brown and Wallace (1968) (anthropogenic structures) and Wallace and Roth (1967) (anthropogenic structures). The locations of faults (grey lines) are from USGS and CGS (2020), with the San Andreas Fault highlighted (as the black line).

collectively known as the slow earthquake family.

To try and understand what is causing the slow earthquake family, Ide et al. (2007) investigated how their duration and moment scaled with one another (Figure 1.6). The slow earthquake family scaled with moment $\propto$ duration. This scaling differed notably from regular earthquakes, which scale with moment $\propto$ duration^3 (Ide et al., 2007; Peng and Gomberg, 2010). The two scaling laws for slow and regular earthquakes suggest that a different fault zone process creates each family of events. More recent evaluations of the scaling laws of individual members of this slow earthquake family have shown that events within each member of the family may scale with moment $\propto$ duration^3 (Michel et al., 2019), but the overall scaling across the family of events remains (compare events within groups to all groups in Figure 1.6).

The similar scaling for the slow earthquake family suggests that perhaps one mech-

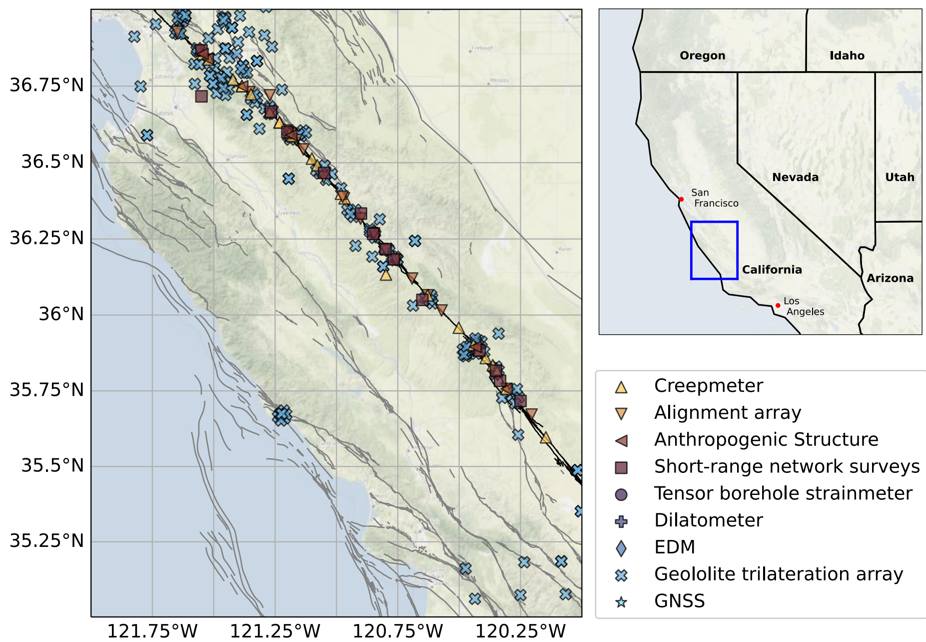

Figure 1.3: Distribution of geodetic instruments in the 1970s. The location of instruments are from: Schulz (1989) (creepmeters), Burford and Harsh (1980) (alignment arrays and some anthropogenic structures), Lisowski and Prescott (1981) (short-range network survey) and the USGS (1991) (geodolites). The locations of faults (grey lines) are from USGS and CGS (2020), with the San Andreas Fault highlighted (as the black line).

anism is creating all these events. Several mechanisms have been proposed for creating slow slip events, including classical rate and state frictional models (e.g., Liu and Rice, 2005; Luo and Ampuero, 2018; Rubin, 2008; Skarbek et al., 2012; Yabe and Ide, 2017), mixed brittle-viscous rheologies (e.g., Lavier et al., 2013, 2021) and shear-induced dilatancy (e.g., Iverson, 2005; Leeman et al., 2018; Segall and Rice, 1995; Segall et al., 2010; Shibazaki and Iio, 2003). Which mechanism controls the slow earthquake family, however, is still up for debate.

We encounter difficulties when discriminating between models for the slow earthquake family. Firstly, these events are typically deep within subduction zones (e.g., Bartlow et al., 2011), meaning they are inaccessible for direct sampling and measurements. Secondly, the recurrence time for these events is months to years (e.g., Wallace et al., 2016), which prohibits long-term studies of these events. Suppose we are to un-

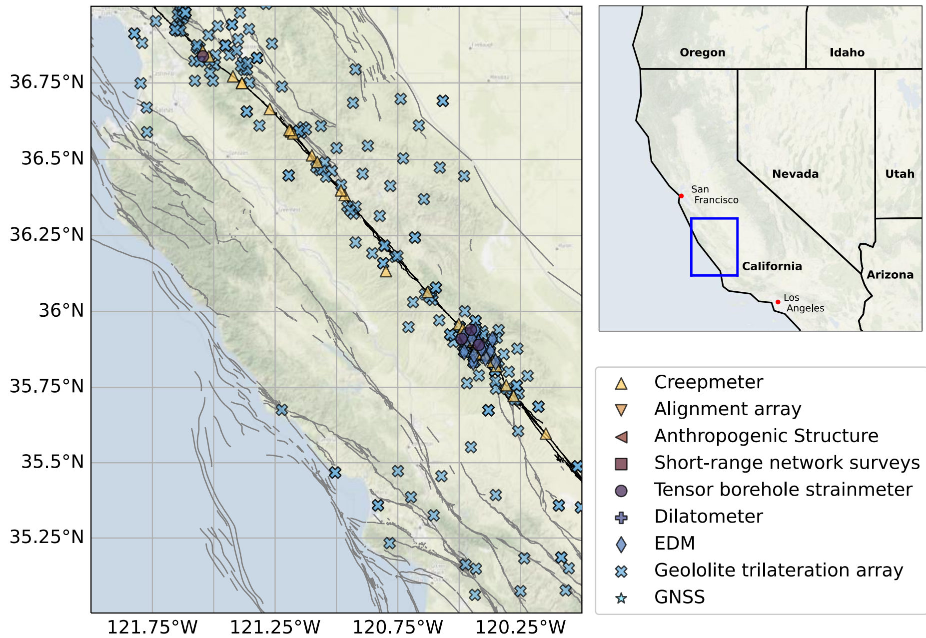

Figure 1.4: Distribution of geodetic instruments in the 1980s. The location of instruments are from: Schulz (1989) (creepmeters), USGS (1991) (geodolites) USGS (2005) (EDM) and USGS (2023) (tensor borehole strainmeters). The locations of faults (grey lines) are from USGS and CGS (2020), with the San Andreas Fault highlighted (as the black line).

derstand these events better. In that case, we must aim to study a regularly recurring aseismic slip transient that occurs close to the Earth's surface. Observations such as these can constrain the physical models driving these events better.

Are shallow aseismic creep events the answer? We have known about and monitored near-surface, regularly repeating aseismic slip transients since the 1960s. These aseismic slip transients are, in fact, the same ones first observed by Tocher (1960) — the shallow creep event along the central San Andreas Fault. Suppose these events are indeed shallow analogues to deeper and larger SSEs. In that case, they could provide an opportunity to discriminate between different driving models for SSEs, given that they recur regularly along faults easily accessible at the surface.

To use these events to discriminate between driving models of slow slip events, we first need to understand shallow creep events comprehensively. Despite knowing

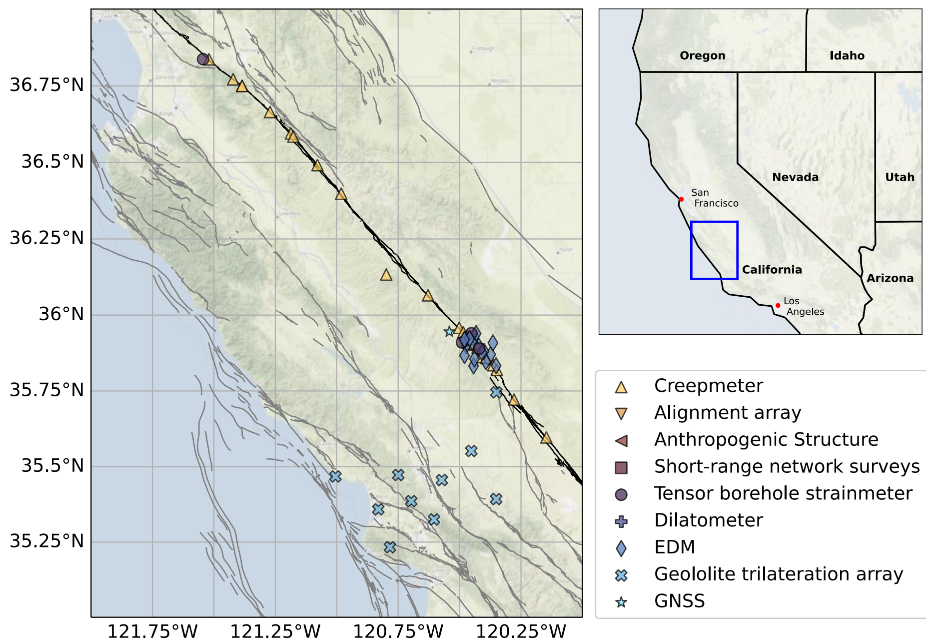

Figure 1.5: Distribution of geodetic instruments in the 1990s. The location of instruments are from: Schulz (1989) (creepmeters), USGS (1991) (geodolites) USGS (2005) (EDM), USGS (2023) (tensor borehole strainmeters), GAGE (2023) (tensor borehole strainmeters) and Murray and Svarc (2017) (GNSS). The locations of faults (grey lines) are from USGS and CGS (2020), with the San Andreas Fault highlighted (as the black line).

about creep events for over 60 years, we still do not know some fundamental features of these events: (1) when and where creep events have occurred, (2) their rupture extent, (3) their moment release or (4) the physical mechanisms behind them. Before determining these, we must revisit the previous work conducted on these events to assess our understanding of these events and provide a baseline from which to answer these fundamental questions about shallow creep events.

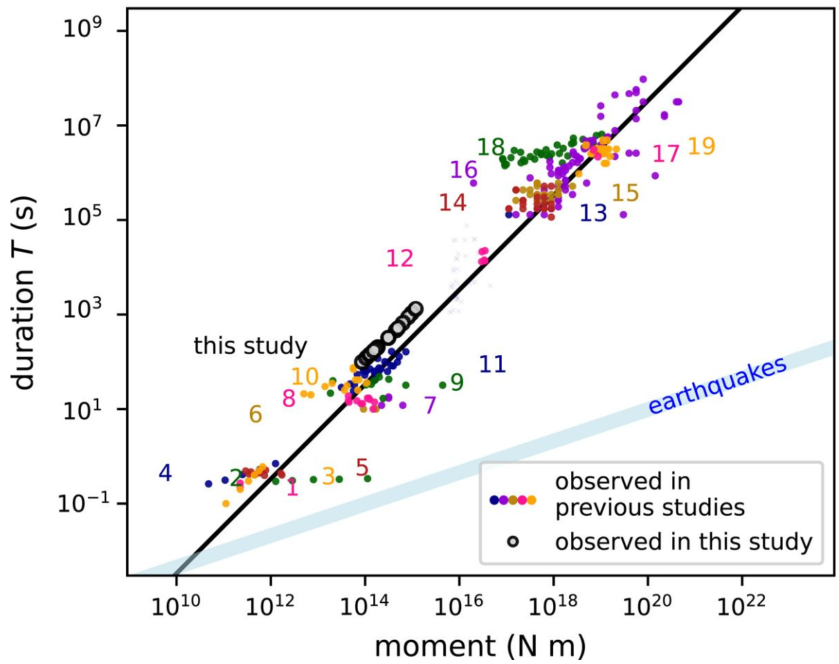

Figure 1.6: Scaling relationships of slow- and regular earthquakes, modified from Gombert and Hawthorne (2023). Values are taken from (1) Shelly (2017); Thomas et al. (2016); Hawthorne et al. (2019), (2) Farge et al. (2020), (3) Huang and Hawthorne (2022), (4) Supino et al. (2020), (5) Bostock et al. (2015), (6) Ito et al. (2007), (7) Matsuzawa et al. (2009), (8) Maury et al. (2016), (9) Yabe et al. (2021), (10) Takeo et al. (2010), (11) Ide et al. (2008), (12) Royer et al. (2015); Hawthorne et al. (2016a), (13) Itaba and Ando (2011), (14) Kitagawa et al. (2011), (15) Itaba et al. (2013); Ochi et al. (2016), (16) Sekine et al. (2010), (17) Rousset et al. (2017), (18) Michel et al. (2019), (19) Tu and Heki (2017).

1.1 Initial discovery of creeping faults and creep events through the offset of anthropogenic features

Aseismic fault creep was observed along the San Andreas Fault following the offset of anthropogenic features, notably the walls of the Cienega Winery (Figure 1.7), which is approximately 11 km south of Hollister, CA (Steinbrugge and Zacher, 1960; Tocher, 1960; Whitten and Claire, 1960).

Having noted that creep was occurring, various observations were made using the offset of resurveyed monuments, seismographs, and three 'creep recorders' (Tocher, 1960). These creep recorders (a predecessor to the creepmeter) each had a different design but allowed for the continuous monitoring of creep (Tocher, 1960). Creep recorded by these creep recorders accumulated mostly in bursts on the order of a week, separated by weeks to months of little to no slip (Tocher, 1960). These bursts are the first reported occurrence of what we now know as creep events.

More surface creep observations were made using the offset of anthropogenic features such as fences (Figure 1.8 from Nyland Ranch, San Juan Bautista, CA), walls (Figure 1.7d)), pavements (Figure 1.9, from Hollister, CA) and bridges, particularly following the 1966 Parkfield earthquake (e.g., Brown and Wallace, 1968; Wallace and Roth, 1967). These observations paved the way for many new geodetic instruments in the late 1960s–early 1970s, as shown in Figures 1.2 & 1.3 (e.g., Nason et al., 1974; Yamashita and Burford, 1973).

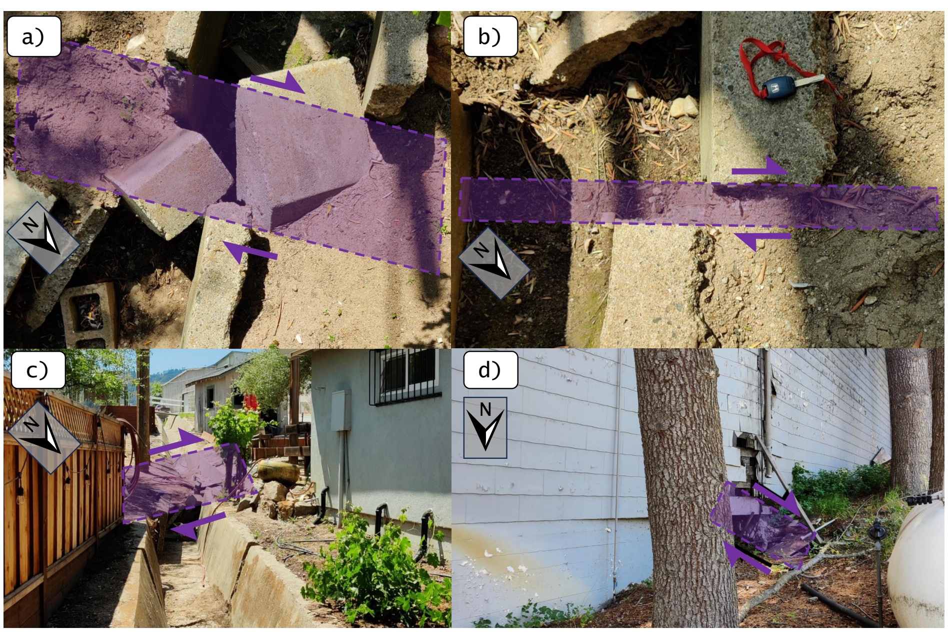

Figure 1.7: Damaged drainage gully and wall at the Cienega Winery, Cienega Rd, Hollister, CA. a), b) & c) Drainage gully offset by right lateral creep. d) Damage to the NW wall of the winery building due to right lateral creep.

Away from California, surface fault creep was observed along the North Anatolian Fault, Turkey, at the beginning of the 1970s (Ambraseys, 1970). Again, much like along

Figure 1.8: Fence offset by right lateral creep at Nyland Ranch, San Juan Bautista, CA. View taken looking down Road D.

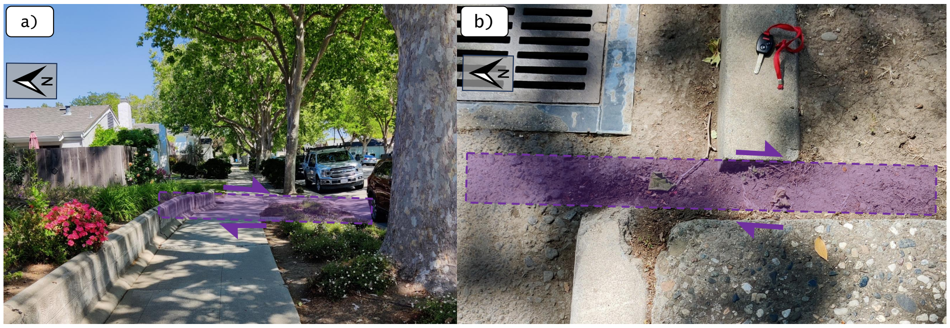

Figure 1.9: Offset pavement (a)) and curb (b)) along 6th Street, Hollister, CA by right lateral creep.

the San Andreas Fault in the decade before, this creep was observed through the offset of anthropogenic features during earthquake afterslip. The most notable anthropogenic features were along the Ismetpasa section of the North Anatolian Fault, where railway tracks and walls were offset by 24 cm between 1957 –1969 (Ambraseys, 1970). The offset of the wall at Ismetpasa was of particular interest. It was resurveyed multiple times in the following decades, e.g., (Allen, 1982; Aytun, 1982; Bilham et al., 2016), even following the installation of creepmeters at the Ismetpasa site in the 1980s (Altay and Sav, 1991; Bilham et al., 2016).

In the following decades, our ability to identify and characterise creeping faults has greatly increased through new geodetic techniques such as GNSS, InSAR, and LiDAR. These instrumental improvements have allowed us to find that creep is widespread globally, being identified in Afghanistan and Pakistan (e.g., Barnhart, 2017; Fattahi and Amelung, 2016; Furuya and Satyabala, 2008), Japan (e.g., Ohzono et al., 2011), China (e.g., Jolivet et al., 2012, 2013; Li et al., 2021; Qiao and Zhou, 2021), Taiwan (e.g., Thomas et al., 2014), Jordan (e.g., Hamiel et al., 2016), the Philippines (e.g., Duquesnoy et al., 1994; Dianala et al., 2020; Fukushima et al., 2019), Ecuador (e.g., Mariniere et al., 2020), Trinidad & Tobago (e.g., Weber et al., 2020), Italy (e.g., Anderlini et al., 2016; Hreinsdottir and Bennett, 2009), Venezuela (e.g., Jouanne et al., 2011; Pousse Beltran et al., 2016; Reinoza et al., 2015) and Tajikistan (e.g., Wilkinson et al., 2021). Despite the improvements in our ability to measure creep, there has not been a corresponding increase in our knowledge of the underlying physics.

1.2 Geodetic instrumentation along the San Andreas Fault over the last 60 years

Since the first discovery of creep and creep events from the offset of anthropogenic features, the central San Andreas Fault has become densely instrumented with various geodetic instruments. Here, we discuss how those geodetic instruments have changed over the last 60 years.

1.2.1 Early instrumentation in the 1970s

During the 1970s, the monitoring of aseismic fault creep in California increased dramatically with the installation of tens of new instruments, including tiltmeters (e.g., Mchugh and Johnston, 1976; McHugh and Johnston, 1978), multi-wavelength distance measurements (e.g., Huggett et al., 1977; Slater and Burford, 1979), and creepmeters, which are described in Box 1 (e.g., Duffield and Burford, 1973; Schulz and Burford, 1978; Schulz et al., 1976; Yamashita and Burford, 1973). Figure 1.3 shows the distribution of active instruments in the 1970s along the central San Andreas Fault.

Using these new instruments, we were able to begin to determine features of aseismic creep along the central San Andreas Fault. We began to (1) understand how creep rate varied along-strike (Section 1.3.1), (2) determine how creep rate varied over time

(Section 1.3.2), (3) estimate the size of creep events (Section 1.4) and (4) decipher possible driving mechanisms behind creep events (Section 1.5).

Box 1: Creepmeters

Creepmeters have been around in some form since the end of the 1950s (Tocher, 1960) and were designed to measure the relative motion of two sides of a fault (Duffield and Burford, 1973; Schulz and Burford, 1978). Figure 1.10 shows the set-up of a creepmeter crossing an active fault. A creepmeter consists of a rod with a low coefficient of thermal expansion anchored on one side of the fault and allowed to move freely on the other side through a sensor (Bilham et al., 2004; Bilham and Castillo, 2020; Duffield and Burford, 1973; Schulz, 1989; Schulz and Burford, 1978). This rod is buried at ≈ 30cm depth (Bilham and Castillo, 2020), while the piers at either end are driven into the ground until they will go no further (Bilham et al., 2004). Creepmeters are installed at 22–45° to the fault strike (Schulz, 1989) and are typically able to measure up to ≈ 1–3 m of displacement across their lifetime before failure (Bilham et al., 2004; Bilham and Castillo, 2020). This large dynamic range comes with a measurement penalty caused by friction between the rod and the conduit as the fault displacement increases. This results in small stick-slip instrumental artefacts (Bilham and Castillo, 2020).

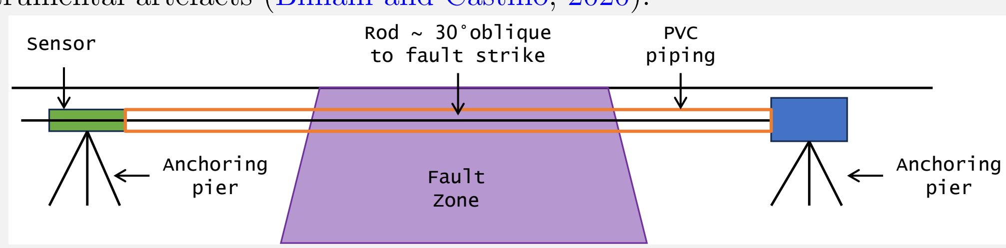

Figure 1.10: Schematic illustration of a creepmeter. Modified from Bilham et al. (2004).

Creepmeters used to take a measurement every 10 minutes, but with advances in data logging and storage, it is now possible to record every minute (Bilham and Castillo, 2020; Schulz, 1989). The resolution of these instruments is between 0.01 and 0.5 mm depending on the age of the instrument (Bilham et al., 2004; Bilham and Castillo, 2020; Schulz, 1989).

Creepmeters are by no means a perfect instrument. However, given their high sampling rate and resolution, they are well suited to monitoring creep events. Given their shallow installation depth, creepmeters are susceptible to rainfall perturbations, and their relatively short lengths lead them to underestimate the full extent of surface slip. A list of the pros and cons of creepmeters is described in Table 1.1.

Pros	**Cons**
Direct on fault measurement of displacement.	Not able to sample all associated deformation as creepmeters do not cross the entire deformation zone (e.g., Aslan et al., 2019) (i.e., too short to measure distributed deformation).
A 1-10 minute sampling frequency is short enough to observe details of slip evolution during creep events.	Affected by site locations and rainfall (e.g., Roeloffs, 2001).
The sub-millimetre resolution of creepmeters allows monitoring of very small creep events.	No longer frictionless instruments and record stick-slip events caused by the instrument and not of tectonic origin (Bilham et al., 2004)).
It is relatively cheap to maintain as it can run for a year on six D cell alkaline batteries (Bilham and Castillo, 2020).	Underestimate slip on the fault compared to instruments with wider apertures.

Table 1.1: Pros and Cons of creepmeters.

1.2.2 Expansion of monitoring driven by the predicted 1983–1993 Parkfield earthquake

In the 1980s, the increase in instrumentation along the creeping faults in California (Figure 1.4) was part of an effort to try and capture both the coseismic and postseismic deformation of the next magnitude 6 Parkfield earthquake, which was predicted to occur between 1983 and 1993 (Bakun and Lindh, 1985; Bakun and McEvilly, 1984; Langbein et al., 2005). This prediction was based upon the observation of a regular sequence of magnitude 6 earthquakes that occurred at Parkfield in 1881, 1901, 1922, 1934 and 1966 (Bakun and Lindh, 1985; Bakun and McEvilly, 1984; Langbein et al., 2005). However, the predicted earthquake would not occur until over a decade later on the 28$^{\text{th}}$ September 2004 (Langbein et al., 2005).

Between 1968 and 1982, the USGS network of creepmeters grew from one instrument at the Cienega Winery to 44 instruments spanning the length of the plate boundary, from Hayward to Palmdale (Schulz et al., 1982). Within this period, a special strong motion creepmeter was developed and installed in 1986-87 at seven sites around Parkfield. The hope was that this instrument could measure the coseismic and postseismic deformation of the earthquake (Schulz, 1989). By 1989, however, the number of creepmeters would begin to decline. This decline is visible when comparing the distribution of instruments between the 1980s (Figure 1.4) and 1990s (Figure 1.5).

During this period, the USGS vastly expanded their alignment array network, with 33 new arrays installed between 1983 and 1986, taking the total to 37 instruments across six faults in California (Wilmesher and Baker, 1987).

In late 1983, a tensor strainmeter (see Box 2 for a description of tensor strainmeters) was installed 1.6 km southwest of the San Andreas Fault at San Juan Bautista at 150 m depth (Gladwin, 1984; Gladwin et al., 1987, 1994). Using data from creepmeters and strainmeters, Gladwin et al. (1994) identified correlated offsets on both instruments. The strain offsets typically preceded the creep event by an hour but could be up to 3 days prior.

Box 2: Tensor Borehole Strainmeters

Borehole strainmeters have been installed to study deformation since the 1970s (Gladwin, 1984). Figure 1.11 shows the installation set-up for a borehole Gladwin Tensor Strainmeter (the type used in Chapter 3). Borehole strainmeters are installed at 120–250 m depth and sealed in place using expansive grout (Gladwin, 1984; Hodgkinson et al., 2013).

Each strainmeter consists of three of four separate gauges that are stacked on top of one another ($\approx$ 20 cm apart) within a borehole (Gladwin, 1984; Mencin, 2018). These gauges are oriented at varying angles (see orientation of CH1–CH4 in Figure 1.11) often at 60° from one another (Gladwin, 1984; Gladwin et al., 1987; Hodgkinson et al., 2013; Mencin, 2018). Each of these gauges consists of three parallel capacitance plates, two of which are fixed in position and one that is free to move as the borehole deforms (Gladwin, 1984; Gladwin et al., 1987; Hodgkinson et al., 2013; Mencin, 2018). The elongation of the gauge is calculated by comparing the distance between the two fixed plates and the middle plate to the free plate (Gladwin, 1984; Hodgkinson et al., 2013).

Through this instrumental design, the position of the moving plate can be monitored to 30 picometres (Gladwin, 1984), giving the instrument a sub-nanostrain resolution (Gladwin, 1984; Gladwin et al., 1987; Hodgkinson et al., 2013; Roeloffs, 2010). The sampling frequency of strainmeters has improved over time, with the older USGS strainmeters taking a sample every 18 minutes (Hawthorne et al., 2016b) compared to the more modern PBO instrument's sampling frequencies of up to 20 Hz, with data also available at 1 Hz and 10-minute intervals (Anderson et al., 2006; Hodgkinson et al., 2013).

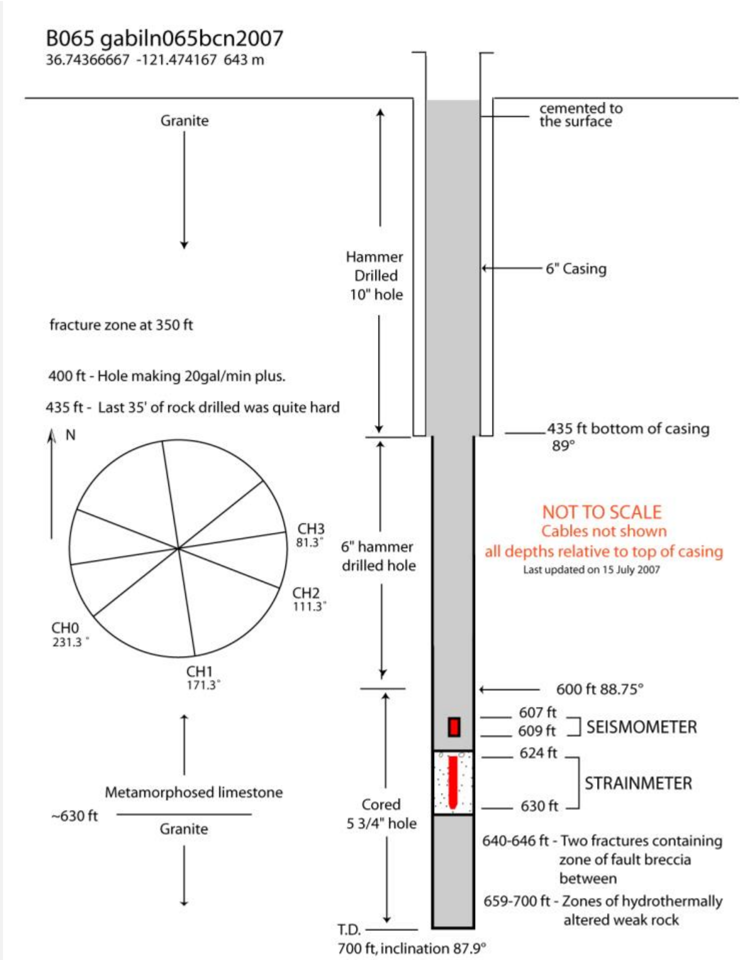

Figure 1.11: Installation set up for the B065 strainmeter used in Chapter 3. Shown are the borehole structure, original gauge orientations and installation geology. Figure from the Plate Boundary Observatory notes on B065, available from https://www.unavco.org/data/strain-seismic/bsm-data/bsm-data.html.

Like creepmeters, borehole strainmeters are useful for observing small aseismic slip events due to their high resolution and quick sampling rate. However, due to this, they are also susceptible to recording large noise signals from non-tectonic sources. They are also expensive instruments to install, given that a borehole must be drilled to a few hundred metres depth for their installation. Table 1.2 describes a list of the pros and cons of borehole strainmeters.

Pros	**Cons**

High-resolution recordings (sub-nanostrain) of deformation signals: able to detect strain offsets associated with small aseismic creep events (e.g., Gladwin et al., 1994).	High-resolution recordings, easily contaminated by non-tectonic signals such as tides and atmospheric pressure (e.g., Hodgkinson et al., 2013).
Sensitive to deformation at greater depths than other geodetic instruments.	Older instruments (i.e., USGS) are generally quite noisy even after removing tides and atmospheric effects.
	installation of instruments is costly (e.g., \$100,000+).
	Not ideally located along the San Andreas Fault (i.e., very few sparsely located instruments).

Table 1.2: Pros and Cons of strainmeters.

1.2.3 The new geodetic age: airborne and satellite observations

One disadvantage of previous studies of creeping faults is that you must first identify that the fault is creeping before you can install instruments like creepmeters. Traditionally, this was done by identifying offsets in anthropogenic features (e.g., Ambraseys, 1970; Steinbrugge and Zacher, 1960). However, with the advent of GNSS, InSAR and LiDAR, as well as a demonstration of the ability of these new techniques to monitor and detect fault displacement (e.g., Massonnet et al., 1993), the way we geodetically monitor faults changed forever.

InSAR and GNSS have allowed us to expand our knowledge of where fault creep occurs. They have led to the identification of creeping faults worldwide, including on the Chaman fault in Afghanistan and Pakistan (e.g., Barnhart, 2017; Fattahi and Amelung, 2016; Furuya and Satyabala, 2008), the Atotsugawa Fault in Japan (e.g., Ohzono et al., 2011), the Haiyuan Fault in China (e.g., Jolivet et al., 2012, 2013; Li et al., 2021), the Longitudinal Valley Fault in Taiwan (e.g., Thomas et al., 2014), the Dead Sea Fault in Jordan (e.g., Hamiel et al., 2016), the Philippine Fault on Leyte Island, Philippines (e.g., Duquesnoy et al., 1994; Dianala et al., 2020; Fukushima et al., 2019), the Quito Fault in Ecuador (e.g., Mariniere et al., 2020), the Central Range Fault in Trinidad &

Tobago (e.g., Weber et al., 2020), the Xianshuihe Fault in China (e.g., Qiao and Zhou, 2021) and the Alto Tiberina Fault in Italy (e.g., Anderlini et al., 2016; Hreinsdottir and Bennett, 2009). A summary of creeping faults globally, including some of those mentioned above, has recently been compiled by Harris (2017).

InSAR, GNSS and LiDAR have also been used to study well-known creeping faults, such as the North and East Anatolian Faults in Turkey (e.g., Aslan et al., 2019; Cetin et al., 2014; Hussain et al., 2016; Kaduri et al., 2017; Karabacak et al., 2011; Rousset et al., 2016) as well as several faults throughout California (e.g., Funning et al., 2007; Khoshmanesh et al., 2015; Lyons et al., 2002; Murray et al., 2014; Scott et al., 2020b; Tiampo et al., 2013)

Although GNSS, InSAR and LiDAR are presenting a new golden age for fault monitoring, their surge in popularity has led to the further decline of the older geodetic networks, with a continual decline during the 21st-century (Figures 1.12 & 1.13), with now only ≈ a dozen creepmeter instruments still in operation along the creeping section of the San Andreas Fault (Figure 1.14).

1.3 Geodetic estimates of the rate of fault slip on the central San Andreas Fault

Given the density and availability of geodetic data along the creeping section of the San Andreas Fault, it is possible to characterise the shallow creep rate and deep slip rate using ground-based and satellite observations. In Section 1.3.1, we discuss how the shallow creep rate varies along strike; in Section 1.3.2, we discuss the temporal variations of shallow creep rate, and in Section 1.3.3 we discuss how these shallow creep rates compare to estimates of deep slip rates.

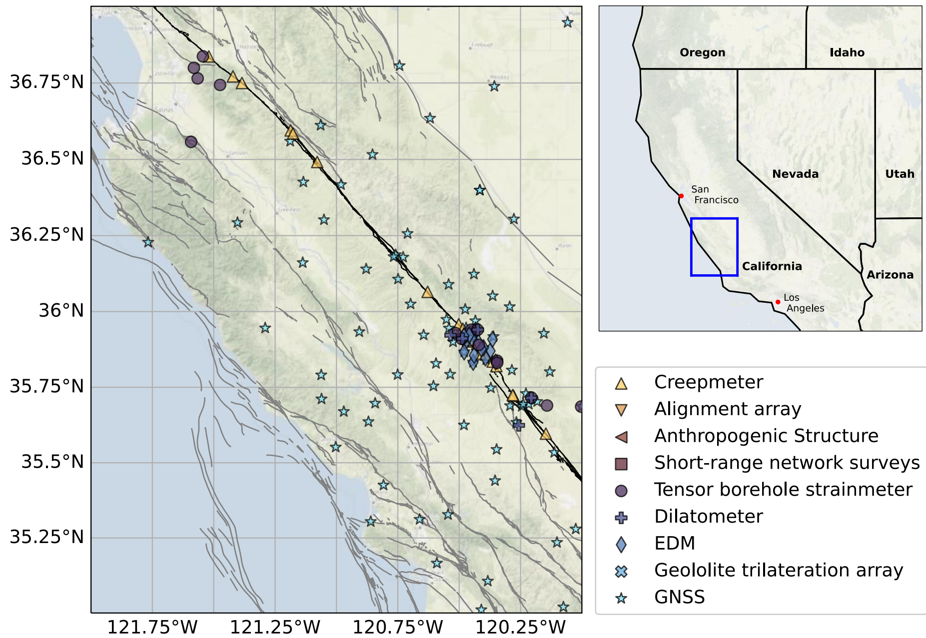

Figure 1.12: Distribution of geodetic instruments in the 2000s. The location of instruments are from: Schulz (1989) (creepmeters), USGS (2005) (EDM), USGS (2023) (tensor borehole strainmeters and dilatometers), GAGE (2023) (tensor borehole strainmeters) and Murray and Svarc (2017) (GNSS). The locations of faults (grey lines) are from USGS and CGS (2020), with the San Andreas Fault highlighted (as the black line).

1.3.1 Along-strike creep rate variations

Using various instruments with differing observations apparatuses, the San Andreas Fault was observed to have a varying creep rate along strike (e.g., Burford and Harsh, 1980; Lisowski and Prescott, 1981; Prescott et al., 1981) as shown in Figure 1.15 c).

Using alignment arrays installed between 1966 and 1968, Burford and Harsh (1980) split the San Andreas Fault into three sections, characterised by their shallow creep rates, seismicity rates and earthquake magnitudes. A central section about 55 km long between Bitterwater and Slack Canyon shows the highest rate of slip ($\approx$ 30 mmyr^{-1}), a relatively low level of seismicity and few earthquakes larger than magnitude 4 (Burford and Harsh, 1980). The two sections on either side show a gradually decreasing shallow creep rate towards the ends of the creeping section. These sections also host high levels of minor seismicity and the occasional moderate earthquake (Burford, 1988).

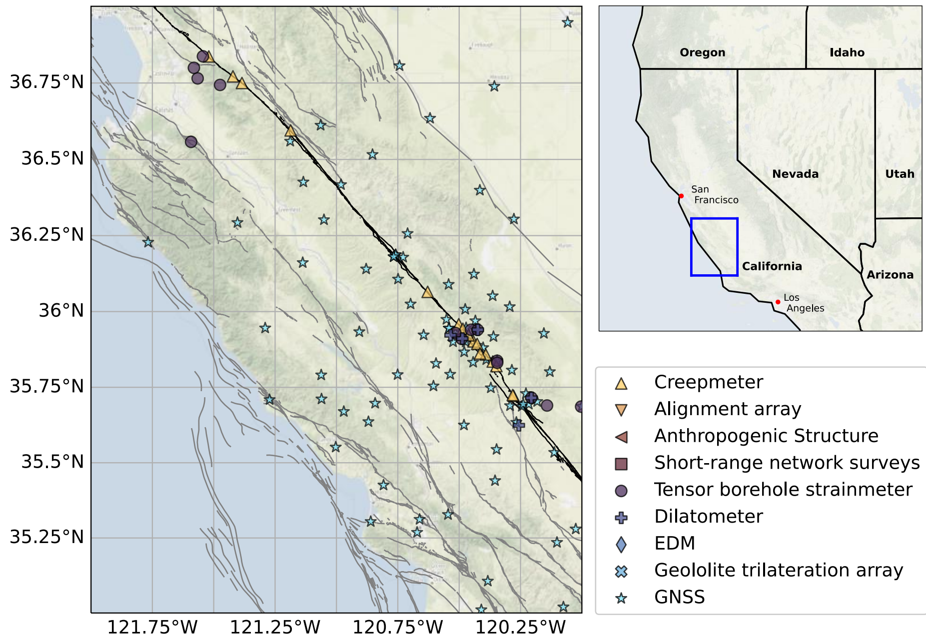

Figure 1.13: Distribution of geodetic instruments in the 2010s. The location of instruments are from: Schulz (1989) (creepmeters), USGS (2023) (tensor borehole strainmeters and dilatometers), GAGE (2023) (tensor borehole strainmeters) and Murray and Svarc (2017) (GNSS). The locations of faults (grey lines) are from USGS and CGS (2020), with the San Andreas Fault highlighted (as the black line).

Using a denser trilateration array, Prescott et al. (1981) and Lisowski and Prescott (1981) identified variations in the creep rate. The shallow fault creep rates calculated using a 100–300 m wide array were shown to increase in a step-wise fashion between San Juan Bautista and Bitterwater from 0–32 mmyr^{-1} and to vary between 26–32 mmyr^{-1} between Bitterwater and Slack Canyon, before decreasing to 3 mmyr^{-1} at Cholame (Lisowski and Prescott, 1981), similar to that of the alignment arrays (Burford and Harsh, 1980). The along-strike variations in creep rate for these short and intermediate-length observational apertures are shown in Figure 1.15 c) as the orange and dark blue lines, respectively.

However, using arrays of geodetic instruments that have a longer observational length/wider aperture (i.e., 20 km long) shows a different pattern (light blue line in Figure 1.15 c)), with the creep rate along the section from San Juan Bautista and Slack Canyon being a constant 32 ±2 mmyr^{-1} (Lisowski and Prescott, 1981).

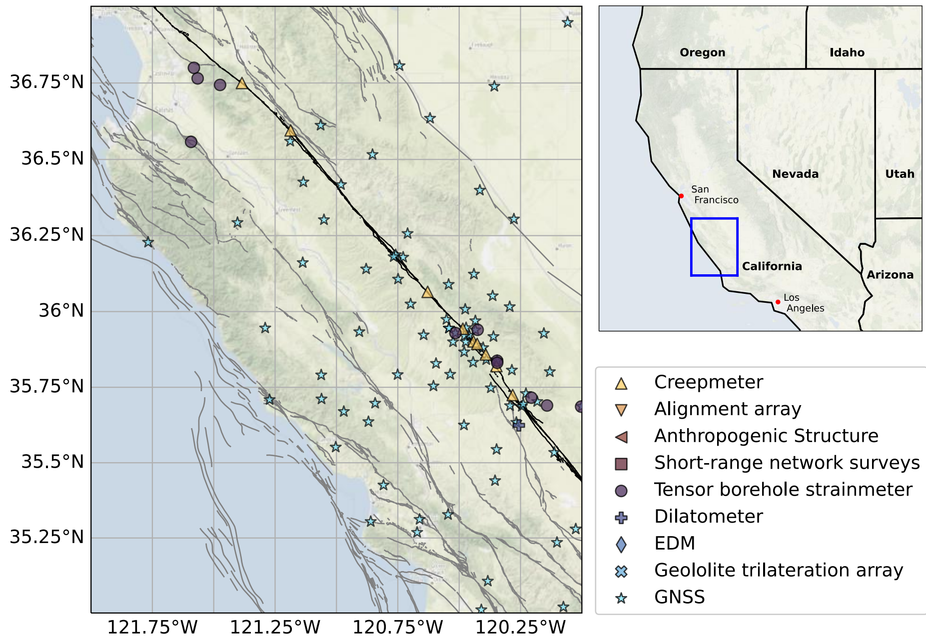

Figure 1.14: Distribution of geodetic instruments in the 2020s. The location of instruments are from: Schulz (1989) (creepmeters), USGS (2023) (tensor borehole strainmeters and dilatometers), GAGE (2023) (tensor borehole strainmeters) and Murray and Svarc (2017) (GNSS).

The width of the deforming zone for the San Andreas Fault is thought to be less than a couple of kilometres (Ryder and Bürgmann, 2008) potentially only a few hundred metres wide (Lisowski and Prescott, 1981). This narrow width may explain why the creep rate estimated by 100–300 m wide alignment arrays captures the majority of the creep rate signal of geodetic instruments with wider apertures (Figure 1.15 c)). The higher slip rate recorded by the wide aperture instruments compared to the shorter aperture instruments near San Juan Bautista (compare orange and light blue lines in Figure 1.15 c)) is likely explained by the presence of the Calaveras Fault in the wider aperture measurement (Lisowski and Prescott, 1981).

Recent InSAR, GNSS, and LiDAR estimates show similar shallow creep rates along the fault. Current InSAR and GNSS estimates for the shallow creep rate on the creeping section of the San Andreas Fault show along strike variations with a peak of 30–33 mmyr^{-1} near the centre, decreasing to 10 mmyr^{-1} at the northern and southern ends (Jolivet et al., 2015; Ryder and Bürgmann, 2008; Titus, 2006; Titus et al., 2011). These estimates are lower than those from far-field slip relating to the plate boundary movement of the Pacific and North American plates, whose angular velocities of ≈ 39 mmyr^{-1} are accommodated by motion on the San Andreas Fault system and the central California Coast Ranges (Argus and Gordon, 2001). This far-field rate is illustrated by the grey bar at the top of Figure 1.15 c). The discrepancy between this far-field plate rate and the motion recorded on the San Andreas Fault is thought to be accounted for by inelastic deformation within the central California Coast Ranges through convergence and fold development (Argus and Gordon, 2001).

A similar creep rate pattern was observed from differential LiDAR (Scott et al., 2020b). The creep rates measured by InSAR, GNSS and LiDAR are 3–4 mmyr^{-1} higher than that of creepmeters and alignment arrays (Figure 1.15 c)), mostly due to the larger apertures of these instruments (Scott et al., 2020b; Titus et al., 2011). Faults are not single planer structures but more zones of deformation that may include several cracks. Currently installed creepmeters are less than 33 m long (Bilham et al., 2004) and may not cross the entirety of the zone of deformation. By failing to cross the entire zone of deformation, creepmeters underestimate the shallow creep rate. In contrast, InSAR, GNSS, and LiDAR have apertures of several km and are able to measure the shallow creep rate across the entire zone of deformation, which leads to slightly higher values. This variation of slip rate with aperture is shown in Figure 1.15 c).

Geodetic instruments also have different depths at which they are able to observe slip. Creepmeters, for example, are only able to detect slip in the upper few-hundred metres (Bilham and Behr, 1992), whereas InSAR and GNSS are able to detect slip from several kilometres depth (e.g., Jolivet et al., 2015). Figure 1.15 a) shows the depths that different instruments are able to detect. The central San Andreas Fault also hosts different types of slip events at different depths with slow slip events and tremor at the base (e.g., Rousset et al., 2019a; Shelly, 2017), repeating earthquakes in the middle (e.g., Waldhauser and Schaff, 2021), the regular M_w 6 Parkfield earthquakes (e.g., Bakun and Lindh, 1985) and its associated afterslip (e.g., Langbein, 2006) extending from depth to the surface, and the shallow aseismic creep events, that form the basis of this thesis, at the top (e.g., Schulz, 1989) (Figure 1.15 b)). This variable depth at which slip is detectable, and the type of events at these depths indicates how we need different instruments to monitor each fault phenomenon, as some are better at monitoring certain types of events than others.

1.3.2 Temporal creep rate changes

Given that we have known about aseismic creep along the creeping section of the San Andreas for over 60 years, it provides a unique opportunity to observe how the shallow creep rate of the fault changes over time.

On short time scales on the order of years, there appear to be fluctuations in creep rate due to earthquakes and bursts of aseismic slip. Following the 2003 M_w 6.5 San Simeon earthquake, the shallow creep rate on the San Andreas Fault increased threefold at the San Juan Bautista creepmeter from 10 mmyr^{-1} to 30 mmyr^{-1} before returning to 10 mmyr^{-1} following the 2004 M_w 6.0 Parkfield earthquake (Hirao et al., 2021). The creep rate before the 2003 M_w 6.5 San Simeon earthquake and after 2004 M_w 6.0 Parkfield earthquake is similar to estimates of the shallow creep rate in San Juan Bautista for several decades prior and post these two earthquakes (e.g., Brown and Wallace, 1968; Burford and Harsh, 1980; Jolivet et al., 2015; Lisowski and Prescott, 1981; Schulz et al., 1982; Schulz, 1989; Titus et al., 2005; Titus, 2006).

At the southern end of the creeping section, the 2004 M_w 6.0 Parkfield earthquake had a dramatic effect on the creep rate at the surface as shown in Figure 1.16 (Langbein, 2006; Langbein et al., 2005). The 1989 Loma Prieta earthquake also affected the shallow creep rate at the creepmeter in San Juan Bautista (Behr et al., 1997). Here, the shallow creep rate increased, yet the creep rate at the nearby Nyland Ranch alignment array remained unchanged (Behr et al., 1997).

By combining InSAR and GNSS with observations of characteristically repeating earthquakes, it is possible to identify changes in background creep rates (Khoshmanesh

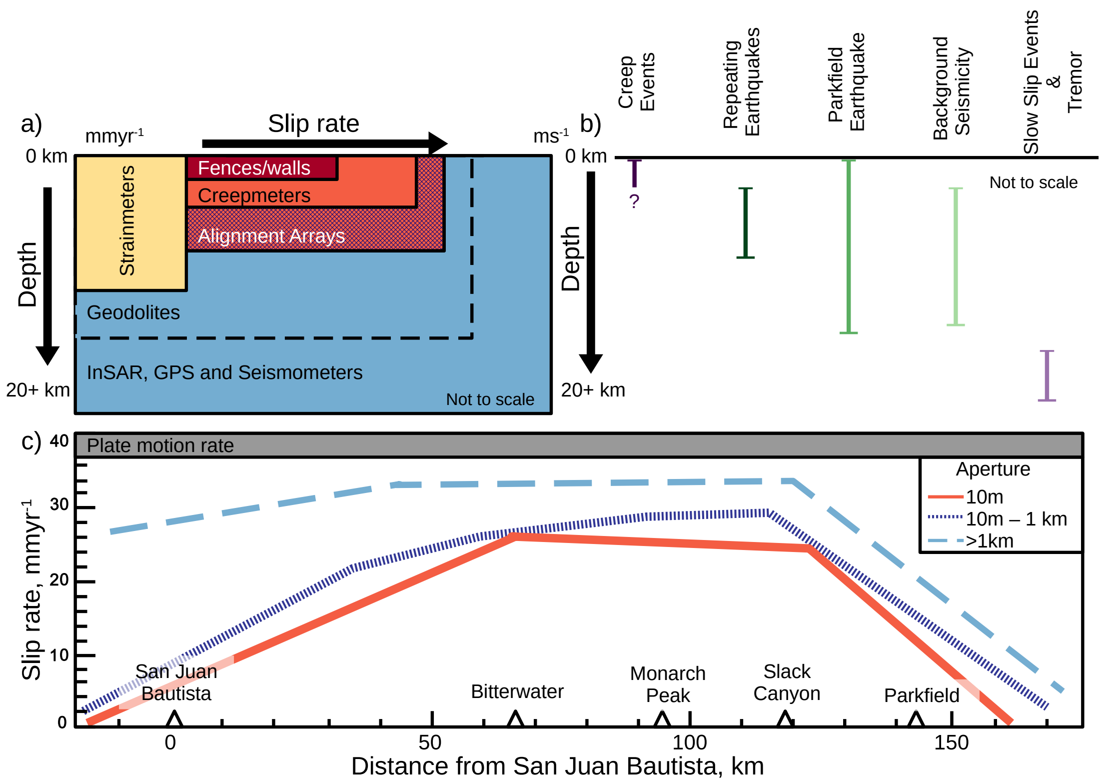

Figure 1.15: a) Schematic diagram illustrating the fault slip rate and depth that different instruments can record. b) Schematic diagram showing the depths of different events recorded along the creeping section of the San Andreas Fault. Depths are approximated but based upon creep event depths from Gladwin et al. (1994), McHugh and Johnston (1978) and Mortensen et al. (1977), repeating earthquake depths from Waldhauser and Schaff (2008), background seismicity depths from Waldhauser and Schaff (2021), slow slip and tremor depths from Rousset et al. (2019a) and rupture extent of the Parkfield earthquake depths are based upon creepmeter observations and the epicentre of the 2004 Parkfield earthquake described in Langbein et al. (2005). c) Plot of slip rate with distance along the San Andreas Fault. The orange line represents the instruments with a short aperture (<10 m), the dark blue striped line represents the instruments with an intermediate aperture (10 m – 1 km), and the light blue dashed line represents the instruments with a large aperture (>1 km). Panel c) is modified from Burford and Harsh (1980), Lisowski and Prescott (1981) and Titus (2006) and is based upon creepmeter data from Schulz et al. (1982) and Schulz (1989); 10-year alignment array data from Burford and Harsh (1980); short-range networks and geodolite data from Lisowski and Prescott (1981); 35-year alignment array data and continuous GPS data from Titus et al. (2005) and Titus (2006) and a plate motion rate from Argus and Gordon (2001).

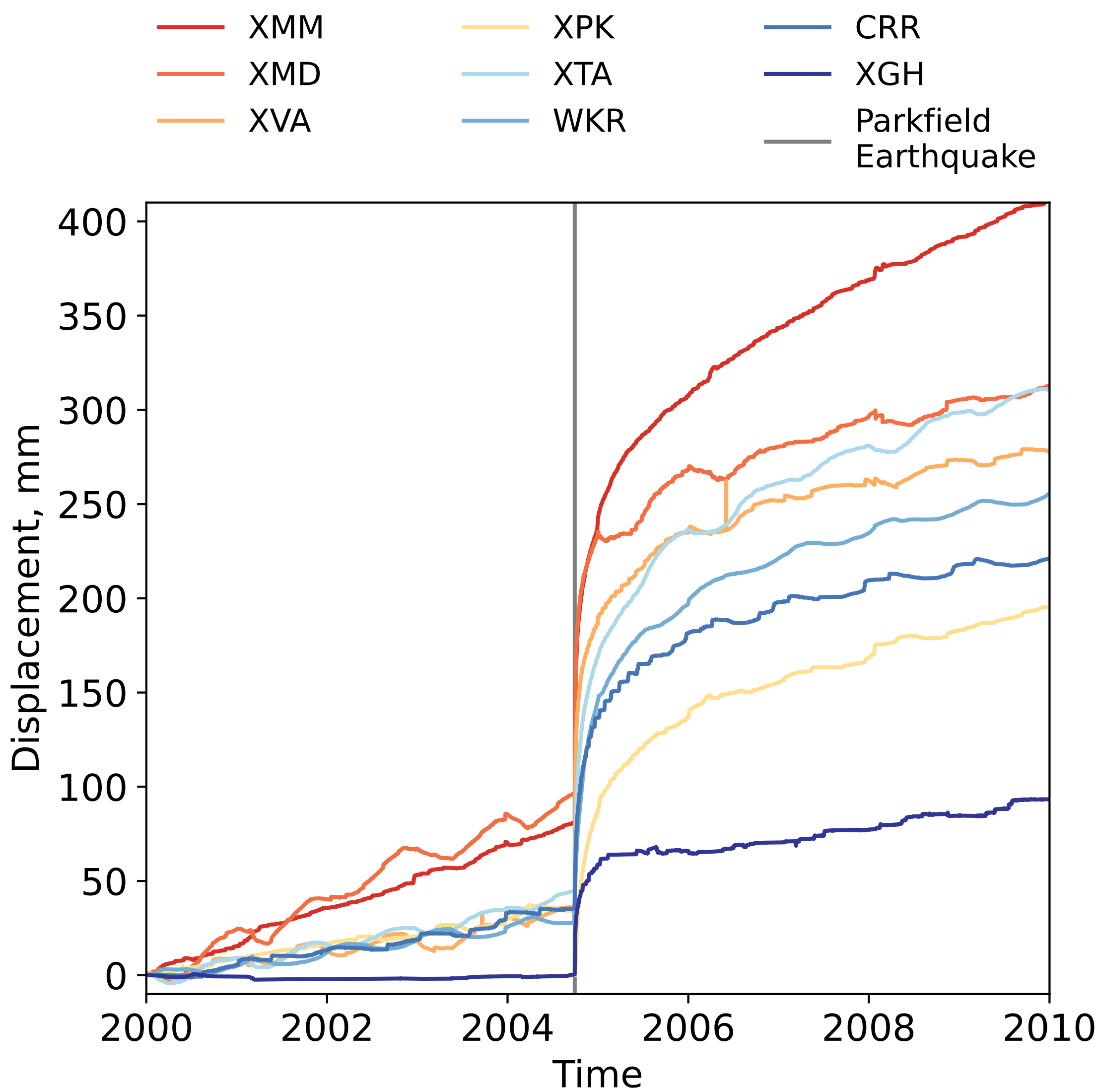

Figure 1.16: Surface creepmeter displacement measurements five years after the 2004 M_w 6 Parkfield earthquake. The vertical line represents the time of the earthquake.

and Shirzaei, 2018a,b; Khoshmanesh et al., 2015), akin to the deeper slow slip event observed along the San Andreas Fault in 1996 (Linde et al., 1996). These 'creep avalanches' indicate that creep rates oscillate around a background rate periodically (Khoshmanesh et al., 2015). This 'creep avalanche' hypothesis assumes deformation occurs only on a planar fault plane, but we know this is not the case in natural fault systems. In particular, deformation often occurs over a broad fault zone of 100 m–2 km width (e.g., Lisowski and Prescott, 1981; Ryder and Bürgmann, 2008), and the fault system may be made up of several parallel strands that work together to accommodate all the deformation.

a planar fault plane, which may not be valid because we know that natural faults are not planar surfaces but instead have a roughness that affects their ability to slip (e.g., Brodsky et al., 2016; Candela et al., 2012; Fang and Dunham, 2013; Thom et al., 2017).

On long timescales, however, the creep rate appears relatively constant. Along the Bitterwater–Slack Canyon section of the San Andreas Fault, the fault creep rate is 28 $\pm$ 2mmyr^{-1} (Titus, 2006). This rate appears to be constant over time with measurements on timescales of 100 years (Swanson et al., 2004) and 1000 years (Hay et al., 1989) agreeing well with modern surficial estimates.

1.3.3 How do shallow creep rates compare to these estimates of the deep slip rate along the San Andreas Fault?

To compare the rate of shallow creep to deep slip, we need to use different instruments depending on the depth at which we want to know the fault movement. Figure 1.15 a) is a schematic diagram that shows how different instruments can measure the rate of fault motion at different depths. Some instruments, such as creepmeters, are only able to measure the creep rates of the upper few hundred metres of the fault (e.g., Evans et al., 1981). In contrast, instruments with wider apertures, such as InSAR and GNSS, can measure both the shallow creep rate and deeper slip rate (e.g., Jolivet et al., 2015; Ryder and Bürgmann, 2008). The ability of InSAR and GNSS to observe both shallow creep rates and deeper slip rates has enabled us to identify that the San Andreas Fault is not moving at the same rate near the surface and at depth. Estimates of shallow creep rates peak at $\approx$ 30 mmyr^{-1} whereas deep slip rates below the seismogenic zone are $\approx$ 33 mmyr^{-1}.

The difference between the shallow creep rate and deep slip rate leads to a moment deficit between the shallow and deep layers of the crust (Maurer and Johnson, 2014; Michel et al., 2018; Ryder and Bürgmann, 2008). This moment deficit could be accommodated by a M_w 5.2–7.2 earthquake every 150 years, on average (Maurer and Johnson, 2014; Michel et al., 2018; Ryder and Bürgmann, 2008). This moment deficit is based upon the assumption that an 80 km long stretch of the creeping section of the San Andreas Fault ruptures to a depth of 10 km (Ryder and Bürgmann, 2008). Alternatively, the moment deficit could be reduced through occasional bursts of creep events (e.g., Khoshmanesh and Shirzaei, 2018b). If we assume a moderate value for the moment deficit, such that it requires a M_w 6.2 earthquake every 150 years, then this moment deficit would be able to be accommodated by a burst of 200 M_w 4.0 creep events every 30 years or a burst of 800 M_w 3.4 creep events every 15 years. Given that moment depends on the area of the fault that has slipped, determining the along-strike and along-depth rupture extents of creep events and, thus, their moment is vital in understanding how much more moment a burst of creep events would release.

1.4 Estimates of the rupture extent of creep events

Since they were first discovered in the 1960s, there have been many attempts to determine the amplitude and rupture extent of creep events. Determining the rupture size of a creep event is one of the first steps into understanding both the physical process that causes them to occur and assessing their importance in the overall seismic cycle. Previous estimates have tended to fall into one of three categories: small and shallow (Figure 1.17 a), long and shallow (Figure 1.17 b) or long and deep (Figure 1.17 c). It should be noted that the depth of the long and deep creep events is still relatively shallow when compared to the depth of the seismogenic zone, which for this region of the San Andreas Fault is between 12–15 km (Jolivet et al., 2015; Ryder and Bürgmann, 2008).

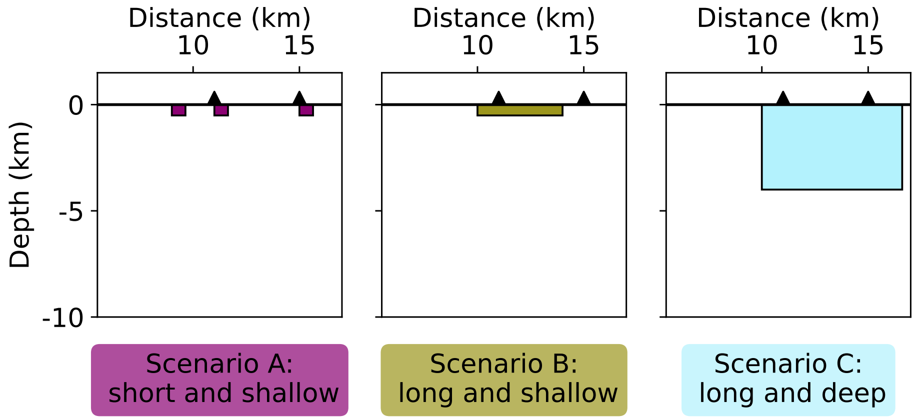

Figure 1.17: Three scenarios for creep events. a) small and shallow, b) long and shallow and c) long and deep.

1.4.1 Scenario A: short and shallow ruptures

Using tilt, strain and water level changes, Mortensen et al. (1977) estimated the rupture length and depth of a pair of creep events along the Harris Ranch–Cienega Winery stretch of the San Andreas Fault that occurred on the 16$^{\text{th}}$ February and 17$^{\text{th}}$ September 1975. These events were modelled as migrating dislocations, with the patch geometry chosen to fit the observed data best. The two events propagate from northwest to southeast; however, the regions involved were not the same length or depth (Mortensen et al., 1977). The creep event in February was approximately 2 km long and extended to 400 m depth, classifying it as a relatively short and shallow event. In contrast, Mortensen et al. (1977) suggested the September event was double the length at 4 km and extended to 2 km depth, classifying it as a long and deep event (see Section 1.4.3 for other long and deep events). As these events occurred in the same stretch of fault, they suggest that creep events along this stretch of fault may not all arise from the same patch.

At the opposite end of the creeping section of the San Andreas Fault, Goulty and Gilman (1978) observed a repeating creep event using strainmeters and creepmeters. The strain signals on the four instruments were similar across four creep events between 1976 and 1977, indicating that the same patch of fault repeatedly ruptured. Goulty and Gilman (1978) used dislocation modelling to identify a slip zone 640 m long that extended between 30–510 m in depth. This repeating event is small and shallow, but unlike the observations by Mortensen et al. (1977), it does not rupture the surface.

Using these correlated strain offsets and creep events, Gladwin et al. (1994) estimated the rupture size of the creep events in the San Juan Bautista region of the San Andreas Fault. Gladwin et al. (1994) found these creep events were roughly 200–500m deep and a few km long, classifying them as small and shallow events. Much like Goulty and Gilman (1978), Gladwin et al. (1994) suggested that these events originated from the same patch of fault that slipped repeatedly.

These shallow creep events reported by Gladwin et al. (1994) are on the same section of the fault that saw the depth of creep shallow following the 1989 Loma Prieta earthquake Behr et al. (1997). Here, the depth of the creeping zone shallowed from 1500 m to 500m following the earthquake, suggesting that a longer observational period may reveal that creep events can arise from two patches in this area similar to the observations of Mortensen et al. (1977) for the Harris Ranch–Cienega Winery section of the San Andreas Fault.

1.4.2 Scenario B: long and shallow ruptures

To explain creep-related tiltmeter observations at the northern end of the creeping section of the San Andreas Fault, 30 km south of Hollister, CA, McHugh and Johnston (1978) used vertically oriented dislocation loops (a loop of dislocations where horizontal motion is accommodated by edge dislocations and vertical motion is accommodated by screw dislocations (Nason and Weertman, 1973)) within an elastic half-space to calculate the expected creep-related tilt observations. Using a generalised elastic model, where slip is allowed to vary both spatially and temporally, McHugh and Johnston (1978) constrained the rupture extent of aseismic creep events that propagated through the region where the tiltmeters were installed on three occasions in 1976: 30$^{\text{th}}$ March, 20$^{\text{th}}$ April and 8$^{\text{th}}$ August. The March and August 1976 events were constrained to the upper 1 km of the fault and were 1.25–2 km long. In contrast, the event in April 1976 was estimated to be 3 km deep and 3.06 km long, classifying it as long and deep (McHugh and Johnston, 1978).

Long and shallow creep events have also been observed along the Calaveras Fault around Hollister, CA, by Evans et al. (1981). Using creepmeters, strainmeters and multi-wavelength distance measurements, Evans et al. (1981) identified two propagating creep events in 1977: 26$^{\text{th}}$–27$^{\text{th}}$ May and 26$^{\text{th}}$ July. Using a similar approach to McHugh and Johnston (1978), Evans et al. (1981) estimated the rupture extent of these two creep events to be between 500–1400 m deep and have an along-strike length of over 6km.

1.4.3 Scenario C: long and deep ruptures

As was discussed earlier, Mortensen et al. (1977) modelled migrating dislocations for two creep events in 1975, the latter of which on the 17$^{\text{th}}$ September 1975 was found to be 4 km long and 2 km deep.

King et al. (1973) used the theoretical fault model of King (1972) to reproduce creepmeter observations. Using a propagating circular slip front, they explained observations of closely timed creep events at four different creepmeters over 6 km apart. However, for this circular slip front to reach creepmeters 6 km away, it needed to extend to 3 km depth (King, 2019; King et al., 1973).

1.5 Physical models for creep events

Since their discovery in the 1960s, various models have been proposed to explain the driving mechanism behind creep events. These models can be grouped into those that suggest creep events originate in an upper surface layer and those that suggest that creep events originate from a layer at depth.

1.5.1 Surface layer models

There have been a couple of proposed models for creep events originating close to the surface. Here, we detail a kinematic model for creep events originating at the surface and how rainfall could drive creep events at shallow depths.

1.5.1.1 Expanding circular cracks

Using the theoretical faulting model of King (1972), King et al. (1973) explained the observation of creep events occurring at different times along the San Andreas Fault using an elastodynamic model (Figure 1.18). This model proposed that slip starts at a shallow depth (the guiding centre) and spreads out within a circular slip patch (King, 1972; King et al., 1973). Finally, the guiding centre of the circle is allowed to propagate along the strike of the fault, with the rupture expanding unilaterally in the horizontal direction. King et al. (1973) also noted that some creep events are preceded by a

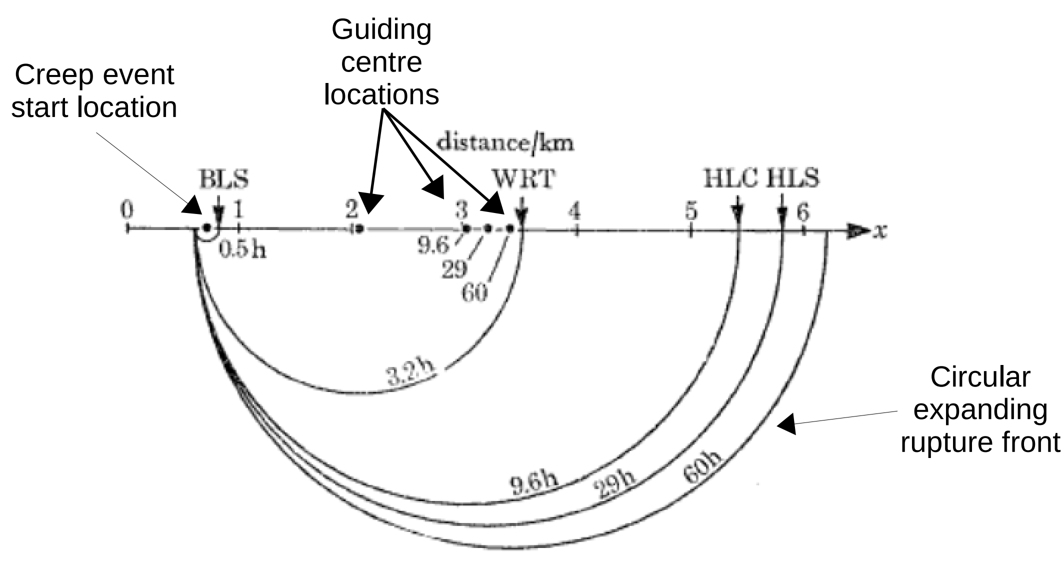

Figure 1.18: Model for the spatial growth of creep events through an expanding circular slip patch. Modified from King et al. (1973).

precursory signal, potentially associated with strain changes linked to the propagation of the circular rupture front. Precursory strain signals associated with the surface recording of creep events would be later identified on borehole strainmeters by Gladwin et al. (1994).

1.5.1.2 Rainfall triggering of creep events

Hydrological signals appear in the recording of creepmeters on two different time scales, with both long- and short-term effects manifesting differently (Roeloffs, 2001; Schulz et al., 1983).

The long-term response usually manifests as a seasonal variation that affects the number of creep events occurring in the wet and dry seasons and the background creep rate (Roeloffs, 2001). Shorter-term effects are more closely related to the weather. During wet weather, there is a tendency for the fault to slip quicker, with accelerated creep during rainfall, which leads to a greater number of creep events (Schulz et al., 1983).

The upper few kilometres of the Earth's crust are thought to be made up of velocity-strengthening material (Marone et al., 1991). The fault will accelerate if this stable region experiences a 'kick' in stress due to increased pore pressure associated with rainfall. The fault will then strengthen, and this will cause the fault to slow down (Helmstetter and Shaw, 2009; Kanu and Johnson, 2011; Perfettini and Ampuero, 2008). This process, known as the 'kick' hypothesis, may explain why the creep events accelerate and subsequently stall and is discussed in greater detail in Chapter 4.

The main drawbacks of this rainfall-induced model relate to two poorly constrained properties of the system: (1) we do not have a quantifiable value for water infiltration rate into the ground to the site of creep event nucleation (Schulz et al., 1983) and (2) we do not know the exact amount of rainfall required to trigger a creep (Schulz et al., 1983), with some estimates stating the requirement for >30 cm of rainfall across 12 months (Roeloffs, 2001).

1.5.2 Two-layer models

In contrast to the shallow models for creep events, several models propose that creep events arise from slip at depth and are later recorded on creepmeters after a surface layer has responded to this. Here, we discuss these so-called 'two-layer models'

1.5.2.1 Dislocation loops

In contrast to the model of King et al. (1973), Slater and Burford (1979) proposed that creep events nucleated at depth and propagated towards the surface. To explain observations of creep events on creepmeters preceded by line length changes on multi-wavelength distance measurements, Slater and Burford (1979) proposed a two-layer model for producing creep events, whereby a thin, soft layer sits atop a very thick elastic layer. Each layer contains a vertical dislocation loop that matches its thickness, but each possesses its own displacement amplitude (Slater and Burford, 1979). Geological evidence for this soft layer is well documented, with an unconsolidated sedimentary layer 2–3 km thick deposited in the Hollister region since the Early Pliocene (Allen et al., 1946; Rogers, 1980; Slater and Burford, 1979).

This model for creep events implies that episodic fault creep behaviour extends to a considerable depth, with deeper portions having accelerated slip periods that last several weeks, in contrast to the shorter duration (several days) of shallow creep events (Slater and Burford, 1979). The deep fault slip may occur weeks before the shallow episodes, meaning several clusters of events along the fault may be related to a single long-term episode of deep seismic slip (Slater and Burford, 1979).

1.5.2.2 Creep events as a yield point process

One of the first models for creep events was the yield point process proposed by Nason and Weertman (1973) as part of a dislocation model for creep events. Nason and Weertman (1973) modelled creep events using a plastic fault gouge embedded between two elastic blocks and proposed that creep events arose from a yield point process whereby the plastic fault gouge would have a finite yield strength. Stress on the fault would be continuously increasing due to the constant production of screw dislocations at depth. A creep event would nucleate when the stress is built up enough and the yield strength is reached. Once the built-up stress is released, the fault undergoes self-healing, restoring the upper yield point, leading to the 'eventfulness' of creep events (Nason and Weertman, 1973).

Using a similar model set up to Nason and Weertman (1973) (i.e., quasi-plastic fault gouge between two elastic blocks), Wesson (1988) proposed that creep events arose from a fault zone which has a power-law rheology. Once an externally applied stress reaches a yield stress at a certain location, a creep event would occur, thus explaining the secular and episodic nature of creep events and their shape and propagation. An important implication of this model is that neighbouring regions may have different yield stresses and not slip simultaneously. Neighbouring patches may load one another and slip in sequence, creating the multi-phase creep events often observed at creepmeters (Wesson, 1988). Wesson (1988) also reconciled the observations of background slip and creep events by suggesting that the shallow fault has a yield stress approaching zero in the upper kilometre, except for a region of the fault at 0.5 km depth, which extends for 5 km along strike, where creep events would originate from (Wesson, 1988).

Advacing on the model of Wesson (1988), Bilham and Behr (1992) propose a two-layer model for aseismic slip, which accounted for both background slip and creep events (Figure 1.19). In this model, stable sliding occurs from the surface to some transition depth, below which episodic creep occurs. These episodic creep events can propagate through the stable sliding layer (Bilham and Behr, 1992). Bilham and Behr (1992) also provides a simplification of the "yield stress patches" of Wesson (1988), whereby the upper layer is at near-zero yield stress and below some transition depth, the slip becomes episodic due to an upper yield point process. This transition from stable sliding to episodic creep may reflect an increase in normal stress with depth; however, the transition depth will also be influenced by pore fluid pressure and tectonic stresses

(Bilham and Behr, 1992)

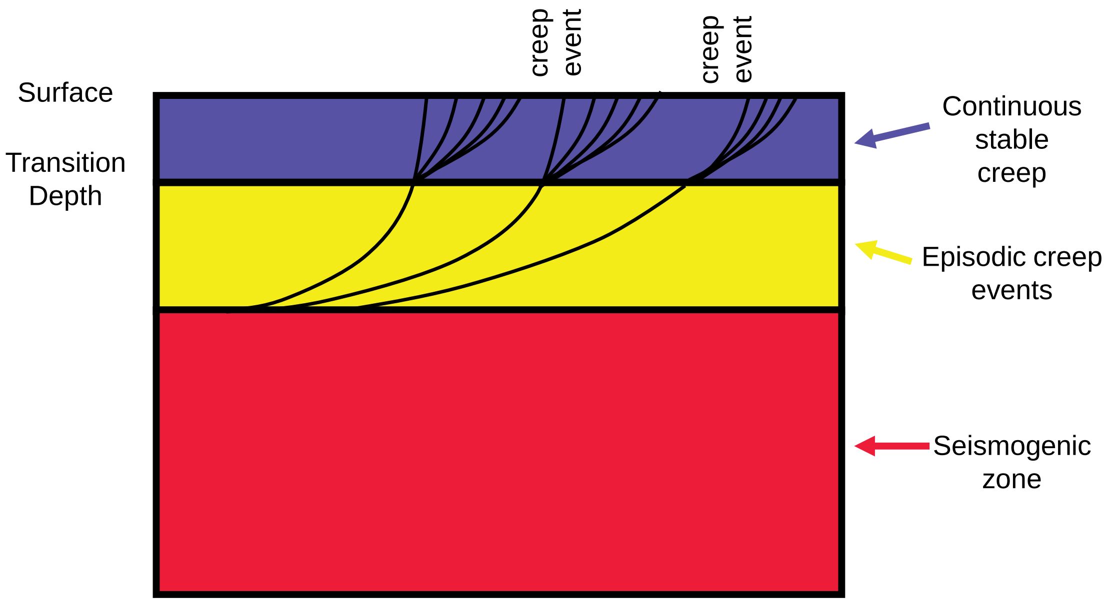

Figure 1.19: Two layer model for creep events proposed by Bilham and Behr (1992). Modified from Bilham and Behr (1992).

1.5.2.3 Frictional models for creep events

The yield point process may be regarded to be the transition from static to dynamic friction as shear stress increases, which may only occur once the fault has slipped a certain distance, i.e., a critical slip distance (Bilham and Behr, 1992; Scholz, 1990). This leads to the assertion that the background creep between creep events measures the critical slip distance associated with creep event nucleation (Bilham and Behr, 1992).

The concept of a critical slip distance is fundamental in the theory of rate and state friction (see Box 3 for details on rate and state friction). Although not always directly studying shallow creep events, many rate-and-state studies of slow-slip events have some transferable inferences to creep event mechanics.

Box 3: Rate and State Friction

Rate and state friction was developed to model and explain laboratory observations of rock friction (Dieterich, 1979; Ruina, 1983). The most common and successful rate and state constitutive law can explain how frictional strength (τ) changes as both velocity (V) and state (θ) change:

$$\tau = \sigma(\mu^* + Aln\frac{V}{V^*} + Bln\frac{V^*\theta}{D_c}), \tag{1.1}$$

where τ is the frictional strength of the fault, σ is the normal stress, V is the sliding velocity, D_c is the characteristic sliding distance, μ^* and V^* are reference values of friction and velocity, and A and B are the coefficients of the direct and evolution effect respectively and θ is the state variable as a function of time.

Ruina (1983) defined state as evolving depending on V and D_c. They proposed this evolution either followed the aging law

$$\dot{\theta} = 1 - \frac{V\theta}{D_c}, \tag{1.2}$$

or the slip law

$$\dot{\theta} = -\frac{V\theta}{D_c}ln\frac{V\theta}{D_c}. \tag{1.3}$$

Both the aging law (Equation 1.2) and slip law (Equation 1.3) can explain different laboratory observations and are typically used in different scenarios. The aging law (Equation 1.2) can explain how fault surfaces strengthen on stationary contact (Marone et al., 1991), and is used to model afterslip, aftershocks and slow earthquakes (e.g., Helmstetter and Shaw, 2009; Liu and Rice, 2005, 2007; Marone et al., 1991). In contrast the slip law (Equation 1.3) can explain large changes in slipping velocity (Beeler et al., 1994) and is often used to explain slip nucleation (Ampuero and Rubin, 2008).

From A and B in Equation 1.1, we can determine how the fault will react to a change in slip rate at steady state. If $A >$B, the fault will get stronger as sliding velocity increases and is deemed velocity-strengthening. The opposite is true if $B > A$ as the fault will weaken with sliding velocity increases and is deemed velocity-weakening.

Creep event specific models typically transition from velocity-strengthening to velocity-weakening as depth increases (Scholz, 1998; Wei et al., 2013). Scholz (1998) proposed that creep events appear to be the same process as an oscillatory behaviour observed at a stability boundary, suggesting that they may arise from a conditionally stable region (Figure 1.20) around the depth where compaction and diagenesis transform sediments into lithified rock. Above this conditionally stable region, a shallow velocity-strengthening region is responsible for the continuous stable creep observed along the San Andreas Fault, possibly associated with unconsolidated sediments (Marone et al., 1991) or the presence of weak minerals (Moore and Rymer, 2007).

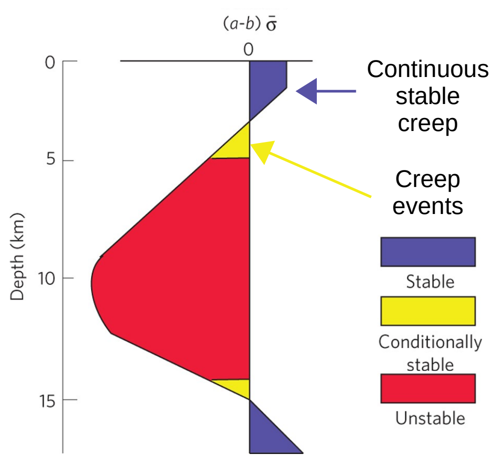

Figure 1.20: Two layer model for creep events proposed by Scholz (1998). Modified from Wei et al. (2013).

Although relatively successful, this set-up cannot explain co-occurring afterslip and creep events (Wei et al., 2013). Suppose the surface velocity-strengthening layer is too thick or is too strongly velocity-strengthening. In that case, the creep events produced in the conditionally stable transition will be arrested before they reach the

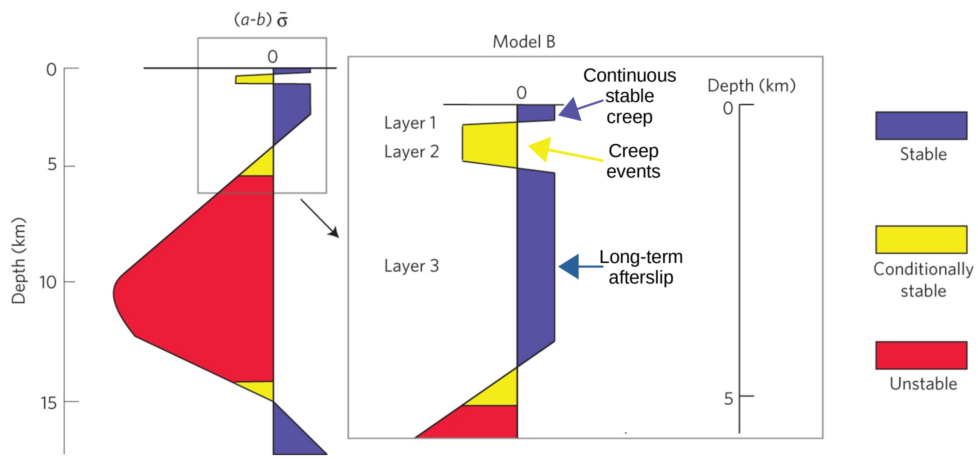

Figure 1.21: Three layer model for aseismic slip proposed by Wei et al. (2013) to explain stable creep, creep events and afterslip. Modified from Wei et al. (2013).

surface (Wei et al., 2013). Inversely, a thin velocity-strengthening layer or a weakly velocity-strengthening layer would prevent multi-year afterslip and inter-creep event stable sliding (Wei et al., 2013). To reconcile the observations of creep events, stable background slip and multi-year afterslip, Wei et al. (2013) proposed adding another shallower conditionally stable region within the upper velocity-strengthening layer, creating a three-layer model for shallow aseismic slip (Figure 1.21). In their model Wei et al. (2013), assume that the effective normal stress increases linearly with depth at a gradient of 13 MPakm^{-1}, the difference between the lithostatic and hydrostatic pressure. The three-layer model of Wei et al. (2013) also has some geological evidence supporting this frictional heterogeneity, with the stratigraphy around the Salton Trough consisting of a three-layer structure of sediments (Pacheco et al., 2006), namely a poorly consolidated sand in Layer 1, a sequence of mudstones, siltstones and sandstones in Layer 2 and a marine shale unit in Layer 3 (Wei et al., 2013).

Despite being able to reproduce all three aseismic behaviours of the Superstition Hills Fault, the Wei et al. (2013) model of creep events does have some slight drawbacks. Their model is only able to produce single-phase creep events as opposed to the multi-phase creep events regularly observed on creepmeter recordings (e.g., Schulz, 1989). Multi-phase creep events most likely require greater complexity along strike/depth, something which is not built into their model by design (Wei et al., 2013).

To produce multi-phase creep events, we need to consider along-strike variability. One might then imagine creep events to be driven by localised slip on a velocity-weakening patch (Belardinelli, 1997; Liu and Rice, 2005, 2007; Rubin, 2008), as opposed to layers (Scholz, 1998; Wei et al., 2013). The presence of neighbouring conditionally stable or velocity-weakening patches that rupture in sequence, similar to the neighbouring slip patches proposed by Wesson (1988), could explain the observations of multiple slip phases recorded on creepmeters, with each phase of slip representing slip on a different patch. These patches must be of a certain size and spacing that allows slip to accelerate and for neighbouring patches to load one another while also preventing dynamic rupture (Ando et al., 2010; Liu and Rice, 2005, 2007; Luo and Ampuero, 2018; Rubin, 2008; Skarbek et al., 2012; Yabe and Ide, 2017). This creates a scenario whereby many parameters need to be tuned correctly in order for creep events to occur.

1.5.3 Advanced models for producing creep events

More complex driving mechanisms should be considered to overcome the requirements for specific conditions for creep events, such as mixed brittle-viscous rheologies, pressure solution creep and shear-induced dilatancy.

1.5.3.1 Mixed brittle viscous rheologies

Adding heterogeneity in the form of a mixed brittle viscous rheology can produce slow aseismic transients (Lavier et al., 2013, 2021). Using a rate-and-state formulation, Lavier et al. (2021) investigated how varying proportions of brittle velocity-weakening and ductile velocity-strengthening materials affected the characteristics of fault slip. Lavier et al. (2021) created a full suite of fault behaviours, including earthquakes, stable creep and slow slip events. Mixtures containing a large proportion of velocity-weakening material did not generate slow slip events, whereas weakly brittle mixtures were able to produce slow slip events (Lavier et al., 2021).

1.5.3.2 Pressure solution creep

At diagenetic to low-grade metamorphic conditions, slow aseismic movement can be accommodated by pressure solution creep (Passchier and Trouw, 2005). Pressure solution creep is a stress-driven fluid-assisted mass transfer process in which variations in chemical potential related to localised stress heterogeneities cause soluble minerals to be progressively dissolved at sites of high solubility and precipitated at sites with low solubility (Gratier et al., 2013; Passchier and Trouw, 2005; Richard et al., 2014). This process accommodates aseismic slip through grain-boundary sliding by diffusion creep (Gratier et al., 2011).

Evidence for this process has been observed in the microstructures of rock samples from the San Andreas Fault Observatory at Depth (SAFOD) (Gratier et al., 2011; Richard et al., 2014). Here, quartz and feldspars are preferentially dissolved at quartz-feldspar grain impingements along pressure solution seams (Gratier et al., 2011), a process which concentrates phyllosilicate minerals such as saponite along the pressure solution seams (Richard et al., 2014). These weak minerals can help to explain the low frictional coefficient often inferred for the San Andreas Fault (Lockner et al., 2011; Moore and Rymer, 2012).

At the SAFOD site, pressure solution creep is able to accommodate the 20 mmyr^{-1} creep rate (Gratier et al., 2011). At higher slip speeds ($\approx >1$ μms^{-1}), pressure solution creep will have to compete with other deformation mechanisms, such as dilation due to granular flow (Niemeijer and Spiers, 2006). Creep events have a maximum creep rate of $\approx$ 0.1–1μms^{-1}. The creep rates during creep events are close to the boundary where pressure solution creep and dilation due to granular flow compete; therefore, we need to consider how other fault zone mechanisms interact with pressure solution creep to understand the driving physics behind creep events.

1.5.3.3 Shear-induced dilatancy

Shear-induced dilatancy is another concept invoked to explain slow aseismic slip (Iverson, 2005; Segall and Rice, 1995; Segall et al., 2010). As a fault slips and accelerates, it may dilate and become undrained, which in turn will reduce pore fluid pressure within the fault zone, stabilising the fault slip and favouring stable sliding (Segall and Rice, 1995; Segall et al., 2010). The combination of low effective stresses, dilatant fault zone material and steady-state velocity-strengthening friction may play a role in the production of creeping zones along faults (Segall and Rice, 1995).

There is some evidence for fault zone dilation during creep events in the form of pore pressure changes during creep events (Roeloffs et al., 1989; Rudnicki et al., 1993), fault zone dilation measured through a set of orthogonal creepmeters (Bilham, 2022) as well as field observations of lens-shaped clay clasts within the core of the creeping faults at the surface. These lens-shaped clasts are thought to rotate during creep events, dilating the fault zone (Bilham, 2022). This dilation should not be surprising given that shear strain results in dilatancy of granular materials (Kruyt and Rothenburg, 2016).

1.5.4 Geology of creeping faults

No matter the physical model proposed for aseismic creep, a determining factor between models is whether the geology present along the fault can creep.

Creeping faults are known to occur in a variety of different geological materials, including in many weak assemblages containing silicate minerals (e.g., Moore et al., 2018; Moore and Rymer, 2007), carbonate minerals (e.g., Carpenter et al., 2015; Oohashi et al., 2012, 2011) and salts (e.g., Hamiel et al., 2016). Here, we discuss the fault rocks present along the creeping section of the San Andreas Fault, focusing on their rate-and-state parameters A & B and their friction coefficients.

1.5.4.1 Geology responsible for aseismic fault creep along the San Andreas Fault

The San Andreas Fault Observatory at Depth (SAFOD) drill hole gave a unique opportunity to investigate the structure of the San Andreas Fault when it crossed the fault at ≈ 3 km depth (Moore and Rymer, 2007). Within this drill core, a suite of weak minerals was observed, including serpentinite (e.g., Moore and Lockner, 2013; Moore and Rymer, 2012), talc (e.g., Moore and Rymer, 2007), smectite clay (saponite) (e.g., Lockner et al., 2011; Moore and Rymer, 2012; Schleicher et al., 2012) and chlorite (e.g., Schleicher et al., 2012).

The frictional properties of these minerals depend on their crystal structure, with frictionally weak phyllosilicate minerals displaying velocity-strengthening behaviour and frictionally strong framework silicates displaying velocity-weakening behaviours (Ikari et al., 2011). The apparent weakness of phyllosilicate minerals is related to two factors: (1) the type of inter-layer bonds they have, and (2) their ability to adsorb water (Morrow et al., 2000).

Weak minerals along the San Andreas Fault are significant as they affect the fault's strength and response to velocity changes. Talc, a velocity-strengthening mineral that is frictionally weak (Ikari et al., 2011), has been observed along the San Andreas Fault and is the only weak mineral able to explain the observed weak frictional strength of the fault (e.g., d'Alessio et al., 2006) over its entire depth range (Moore and Rymer, 2007).

Serpentinite is also found along the central San Andreas Fault (Moore and Rymer, 2012). The frictional strength of serpentinite varies depending on which mineral is present. Lizardite and antigorite have a high coefficient of friction (0.5-0.6), whereas chrysotile has a low coefficient of friction of 0.2, often attributed to the adsorption of water (Moore and Lockner, 2013; Moore et al., 1997). Serpentinites appear to be velocity-strengthening at slow slip rates and velocity-weakening at high slip rates, which may be important in the creeping section's behaviour (Moore et al., 1997).

A clayey gouge along the San Andreas Fault also correlates to the location of serpentinite outcrops in the vicinity of the fault (Moore and Rymer, 2012). The rock formations surrounding these serpentinite outcrops are the Etchegoin Formation (Pliocene–Upper Miocene sandstones, siltstones and conglomerates (Sims, 1990)) and the Franciscan Complex (Cretaceous and Jurassic sandstones and mudstones (Sims, 1990)), along with many other unnamed sandstones and siltstones (Moore and Rymer, 2012). These quartz-feldspar-rich sandstones have implications for the frictional strength of the serpentinites on the fault. When sheared against quartz-rich rocks, serpentinite minerals weaken by forming metasomatic mineral assemblages, including weak minerals such as talc and saponite (Moore and Lockner, 2013).

1.5.4.2 Are similar weak minerals observed on other creeping faults?

Away from California, the association of weak clay minerals and aseismic creep has also been observed (Kaduri et al., 2017). Along the North Anatolian Fault in Turkey, locked sections of the fault correspond to areas of massive limestone deposits with a clay gouge. In contrast, the creeping sections correspond to areas of clay gouge with weak mineral assemblages such as smectite and other phyllosilicates such as micas (Kaduri et al., 2017). These phyllosilicate-rich gouges are found where volcanic rocks have undergone changes during deformation, with soluble minerals such as quartz and feldspar removed through fluid advection, concentrating the phyllosilicates in the gouge (Kaduri et al., 2017).

1.6 Aims and Objectives

This thesis aims to identify when and where shallow creep events are occurring along the San Andreas Fault between 1985 and 2020 and in doing so create the first open-access catalogue of creep events which the wider community can then use to understand better these events and how they interact with the overall slip dynamics of the creeping section of the San Andreas Fault. This thesis also aims to determine how spatially large they are, identify their physical characteristics and determine an appropriate rheological model that explains the displacement-time evolution of creep events.

Objective 1 — Identify creep events in the creepmeter record from the central San Andreas Fault and produce the first open-access catalogue of creep events.

Objective 2 — Determine the along-strike length of creep events along the San Andreas Fault.

Objective 3 — Estimate the along-strike rupture location and depth extent of creep events.

Objective 4 — Estimate the M_w of creep event.

Objective 5 — Determine the rheological model best capable of describing the displacement evolution of a creep event.

1.7 Thesis Outline

The remainder of this thesis is organised as follows:

Chapter 2 — Identification of creep events within the creepmeter record and estimates of their along strike rupture lengths.

Chapter 3 — Constraining the rupture location, depth and M_w of slip creating creep-associated strain offsets.

Chapter 4 — Determining the best-fitting rheological model for creep events.

Chapter 5 — Concluding remarks.

2

Are Creep Events Big? Estimations of Along-strike Rupture Lengths

2.1 Introduction 47
2.2 Creepmeters and Creep Events 53
2.3 Identifying Creep Events at Individual Creepmeters 54
2.3.1 Automated Detections 55
2.3.2 Results 58
2.4 Identifying Correlated Events Between Creepmeters 59
2.4.1 Estimating the Frequency of Multi-creepmeter Ruptures 60
2.4.2 Removing Short-term Rainfall Effects 64
2.4.3 Detecting Long Creep Events by Visual Inspection 67
2.5 Summary of Creep Event Behaviours 68
2.5.1 Isolated Events 69
2.5.2 Small Events (2 km or Less) Recorded at Two Creepmeters . . . 72
2.5.3 Medium-sized Events (3-6 km) Recorded at Two or Three Creepmeters 73
2.5.4 Large Events (10 km or more), Sometimes Skipping Creepmeters 77
2.5.5 Multi-strand Ruptures? 80
2.6 Short-term Rainfall Influence on Creep Events 82
2.6.1 Percentage of Correlated Events Decreases 83
2.6.2 Percentage of Correlated Events Remains Unchanged 85
2.6.3 Percentage of Correlated Events Increases 85
2.7 Discussion 85
2.7.1 What Drives Creep Events? 86
2.7.2 Moment Accommodated by Creep Events? 88
2.8 Conclusion 89

Abstract

Segments of many faults are observed to slip aseismically at the surface. On the central segment of the San Andreas Fault, aseismic slip accumulates largely in creep events: few-mm bursts of slip, which occur every few weeks to months. But even though we have observed creep events worldwide since the 1960s, we still do not know how big most events are or which forces drive them. To address this uncertainty, we systematically identify creep events along the central San Andreas Fault and determine their along-strike rupture extents. We first use cross-correlation and visual inspection to identify events at individual creepmeters. With data from 18 USGS creepmeters, we identify 2120 records of creep events between 1985 and 2020. We then search for slip that is closely timed across multiple creepmeters. We identify 306 instances of closely timed slip, which could indicate 306 creep events that rupture multiple creepmeter locations. Through visual inspection and statistical analysis of timing, we identify a variety of creep event types, including single-creepmeter events, small (<2 km) events, medium-sized (3-6 km) events, large (>10 km) events, and events that rupture multiple fault strands. The existence of many large (>few km) events suggests that creep events are not produced by small, rainfall-associated perturbations; they are more likely driven by complex or heterogeneous frictional weakening, and they may provide a window into the dynamics of larger-scale slip on the San Andreas Fault.

Plain Language Summary

The San Andreas Fault, CA, slips at the surface between San Juan Bautista and Cholame. This slip accumulates slowly or in bursts, known as creep events. Despite observations of creep events since 1966, we still do not know how large they are or what causes them to occur. Here, we determine the length of creep events, as this helps us understand more about how these events are created. If creep events are small, they may be caused by rainfall; however, if they are large, then they are likely self-driven.

Using 18 USGS creepmeters, we identify the timing of creep events and determine their length. Between 1985 and 2020, we have identified 2120 creep events, some of which are recorded at multiple creepmeters, allowing us to determine their along strike-length. We identify five size ranges of our creep events: isolated events, small (<2 km) events, medium-sized (3-6 km) events, large events (>10 km), and events that occur on multiple fault strands events. These larger events are difficult to explain using conventional frictional theory and do not appear to result from rainfall. Therefore, understanding these events is important for determining the process that creates aseismic creep on faults.

Key Points

- Identify 2120 creep events on the central San Andreas Fault and estimate their along-strike lengths
- Creep event lengths range from sub-km to >10 km
- Existence of large events makes it likely that slip is driven by large-scale frictional weakening

2.1 Introduction

Some faults have been observed to creep at the surface since at least the 1960s. Detailed observations of creep were made following the 1966 Parkfield, CA earthquake and the 1968 Coachella Valley, CA earthquake (Bilham and Castillo, 2020; Titus, 2006). Since then, creep has been observed on many additional faults, including the San Andreas, Calaveras, and Hayward Faults in California (Evans et al., 1981; Lienkaemper et al., 2012; Steinbrugge et al., 1960); the North Anatolian Fault in Turkey (Ambraseys, 1970; Bilham et al., 2016); the Philippines Fault on the Island of Leyte (Duquesnoy et al., 1994); the Chihshang Fault, Taiwan (Lee et al., 2005; Thomas et al., 2014); the El

Pilar Fault, Venezuela (Pousse Beltran et al., 2016); and the Chaman Fault, Pakistan (Fattahi and Amelung, 2016). Here, we focus on the central creeping section of the San Andreas Fault in California. This 175 km-long segment between San Juan Bautista and Cholame (Figure 2.1) accumulates most of its slip aseismically (Titus et al., 2011). Two >100 km-long locked sections bound the creeping section. The locked section to the north of San Juan Bautista last ruptured in the 1906 M_w 7.9 San Francisco and 1989 M_w 6.9 Loma Prieta earthquakes, while the southern locked section south of Cholame last ruptured in the 1857 M_w 7.9 Fort Tejon earthquake (Ryder and Bürgmann, 2008; Titus et al., 2011). Smaller ($M \approx 6$) earthquakes also occur near the edges of the creeping section (Langbein et al., 2005). Yet, no major ($M \geq 7$) earthquake has ever been reported within this 175 km-long region (Toppozada et al., 2002). But the long-term aseismic creep rate does vary along strike. The slip rate in the shallow portion of the fault decreases from 30-33 mmyr^{-1} near the centre to 10 mmyr^{-1} near Parkfield and Cholame (Jolivet et al., 2015; Ryder and Bürgmann, 2008; Titus, 2006; Titus et al., 2011). Many spatial and temporal variations of creep are well recorded along the San Andreas Fault's creeping section. Following the 1966 Parkfield earthquake, the region was heavily instrumented with creepmeters (e.g., Schulz, 1989), alignment arrays (e.g., Lienkaemper, 2006), GPS (e.g., Titus et al., 2011), trilateration networks (e.g., Lisowski and Prescott, 1981), and strainmeters (e.g., Gladwin et al., 1994).

The instrumental data revealed that creep on the central San Andreas Fault and other faults does not accumulate at a steady rate (Jolivet et al., 2013; Linde et al., 1996; Roeloffs, 2001; Rousset et al., 2016, 2019b). On the central San Andreas Fault, creep accumulates mostly in small bursts of accelerated slip known as creep events (Figure 2.2). These creep events appear small and repetitive. They display mm to cm of slip, last hours to days, and recur at intervals of weeks to months (Gladwin et al., 1994; Schulz, 1989; Wei et al., 2013; Wesson, 1988). There are larger creep events as well, with durations of weeks to years, but these larger events either accommodate small fractions of the surface slip or contain smaller bursts within them (e.g., Linde et al.,

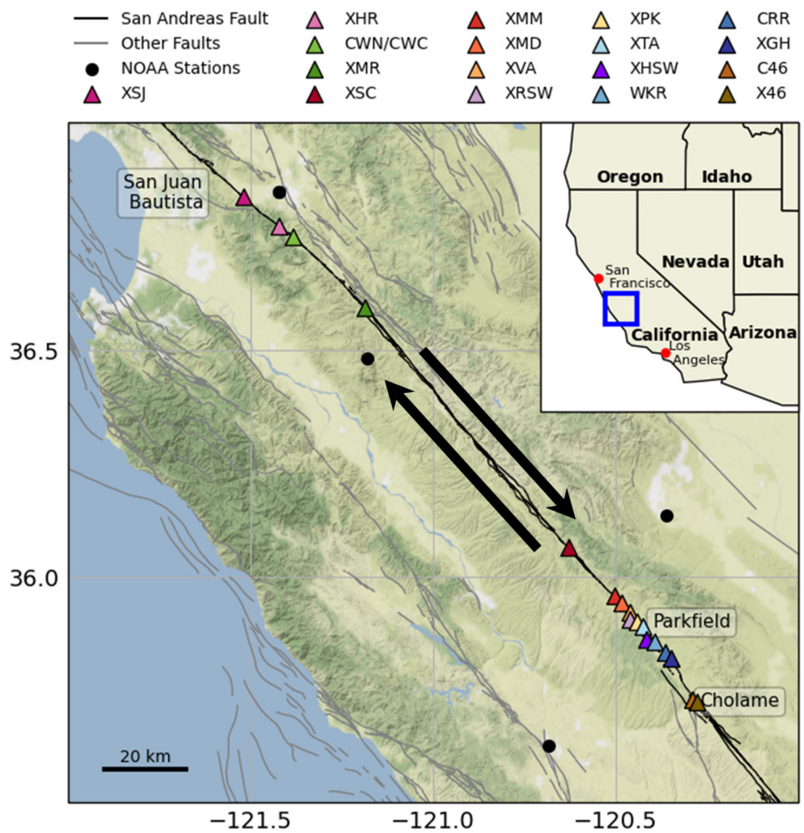

Figure 2.1: Map of the creeping section of the central San Andreas Fault (black) and other faults in central California (grey). The creepmeters are shown as coloured triangles. National Oceanic and Atmospheric Administration (NOAA) stations are shown as black circles. Faults plotted are from the United States Geological Survey (USGS)/California Geological Survey (CGS) Quaternary faults and folds database (USGS and CGS, 2020).

1996; Roeloffs, 2001). It appears that the small repetitive creep events play a dominant role in accommodating surface slip. But even though we know that small creep events are abundant and accommodate more surface slip on the 175 km creeping section, we do not know which fault zone processes cause creep events. We do not even know how *spatially* large most creep events are: how far the ruptures extend along strike or along depth.

We do not know the spatial extent of most creep events because previous work has focused on a handful of larger events or repeated events at an individual creepmeter (e.g., Bilham and Behr, 1992; Evans et al., 1981; Gladwin et al., 1994; Goulty and Gilman, 1978; King, 2019; King et al., 1973; Mchugh and Johnston, 1976; Mortensen

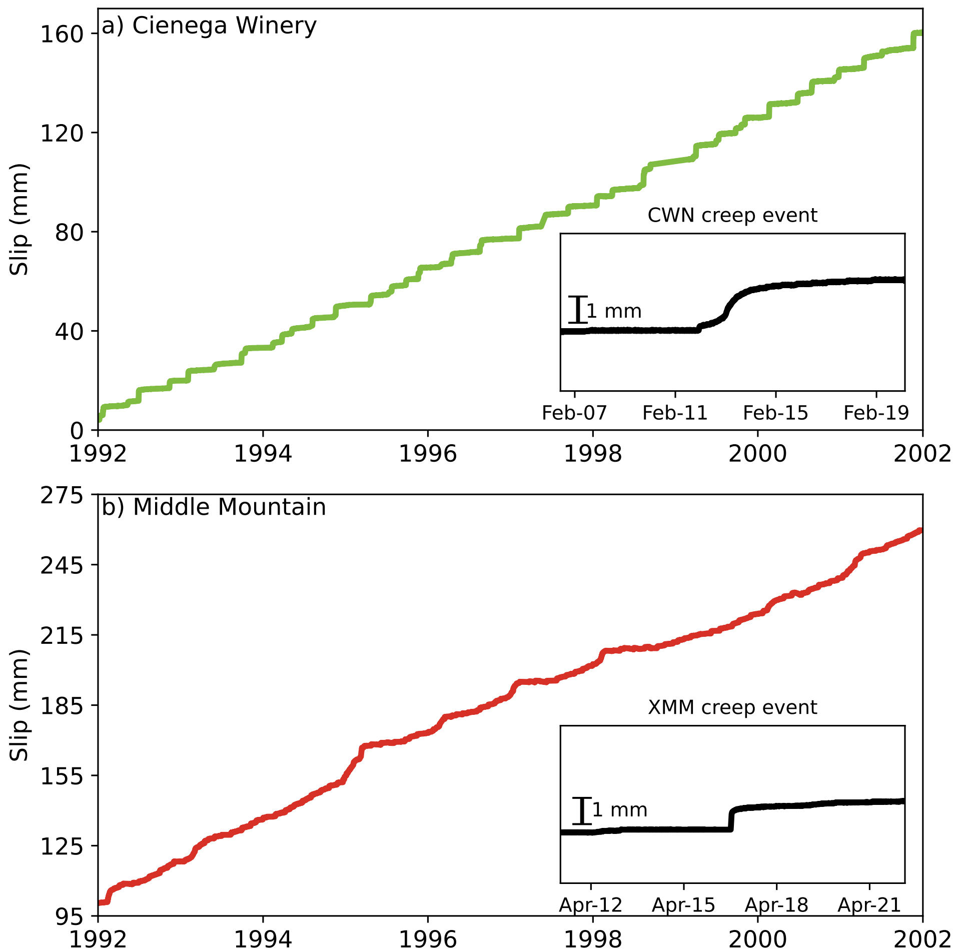

Figure 2.2: 10 years of slip at two creepmeter locations that show creep events of different characters: a) Cienega Winery (CWN), showing a multi-step creep event, and b) Middle Mountain (XMM), showing a single step creep event.

et al., 1977; Nason and Weertman, 1973; Slater and Burford, 1979). Furthermore, slip at an individual creepmeter tells us only about the slip at a particular location; it does not tell how much of the fault is slipping. Previous estimates of the size of creep events vary widely and are summarised in Table 2.1. Some analyses have implied creep events are just short (640m), shallow ruptures (30-510m depth) (Figure 2.3a) (e.g., Gladwin et al., 1994; Goulty and Gilman, 1978; Mortensen et al., 1977) or long (6.6 km), shallow ruptures (510-1400m depth) (Figure 2.3b) (e.g., Evans et al., 1981; Mchugh and Johnston, 1976). However, other evidence implies that creep events could be long and deep, rupturing to depths of 4km, perhaps all the way to the seismogenic zone (Figure 2.3c) (e.g., Bilham et al., 2016; King et al., 1973; King, 2019; Mortensen et al., 1977). Despite all the previous estimates of the rupture extent of creep events, we are still unable to determine which of these scenarios is most common. This is due to the total number of events for which the rupture extent has been calculated lies in the few 10s of events as opposed to the 100s or 1000s of events that occur.

Instrument	**Location**	**Along-strike Length**	**Depth Extent**	**Scenario**	**Reference**
Tiltmeter	SAF near Hollister	couple of km	>0.5–2km	b	Mchugh and Johnston (1976)
Strainmeter	SAF near San Juan Bautista	few km	200–500 m	a	Gladwin et al. (1994)
Strainmeter	Cholame Valley	640 m	30–510 m	a	Goulty and Gilman (1978)
Strainmeter	Calaveras Fault	6.6 km	510–1400 m	b	Evans et al. (1981)
Kinematic modelling	Calaveras Fault	5.6 km	2.8 km	c	King et al. (1973); King (2019)
Multi-wavelength Distance Measuring	Calaveras Fault	—	approx 1 km	b	Slater and Burford (1979)
Tiltmeter, Strainmeter and Water-level Fluctuations	Cienega Winery	0.8 km–4 km	0.4–2 km	a & c	Mortensen et al. (1977)
Strainmeters and Creepmeters	NAF near Ismetpasa	—	4 km	c	Bilham et al. (2016)
Dislocation modeling	—	0.1–5 km	—	—	Nason and Weertman (1973)
Creepmeters	Superstition Hills	—	0.3–3 km	a, b & c	Bilham and Behr (1992)
Creepmeters	SAF near Melendy Ranch	1.2 km	—	—	Burford (1977)

Table 2.1: Some previous estimates of the spatial extent of creep events.

It is essential to know how large creep events are if we are to understand why they happen. For instance, if creep events are small and shallow, one might imagine that the creeping San Andreas Fault is slip rate-strengthening with a stable frictional rheology. Creep events could occur on a nominally stable fault if the fault receives some "kicks" in stress or pore pressure, perhaps from the stress perturbations by rainfall and

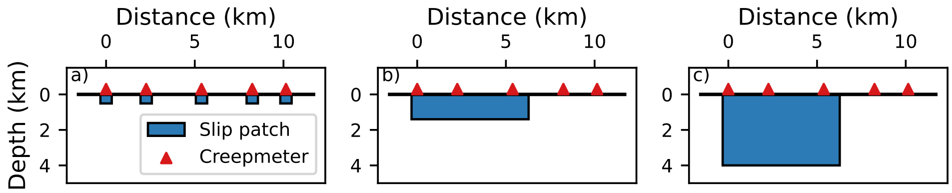

Figure 2.3: Three creep event size scenarios. a) Short, shallow ruptures. b) Long, shallow ruptures. c) Long, deep ruptures.

atmospheric pressure (Helmstetter and Shaw, 2009; Kanu and Johnson, 2011). However, the "kick" hypothesis only seems plausible if creep events are shallow, occurring in a region with low normal stress that provides only modest resistance to acceleration. If creep events are large and deep, it seems more plausible to imagine that they are self-driven: driven by local frictional weakening. However, self-driven creep events are challenging to explain with conventional rate-strengthening or rate-weakening rheologies. To display the episodic but aseismic slip seen in creep events, a fault may require particularly-sized patches of rate-weakening material (e.g., Liu and Rice, 2005; Luo and Ampuero, 2018; Rubin, 2008; Skarbek et al., 2012; Wei et al., 2013; Yabe and Ide, 2017) or a more complex fault zone process such as shear-induced dilatancy (e.g., Iverson, 2005; Leeman et al., 2018; Segall et al., 2010; Segall and Rice, 1995; Shibazaki and Iio, 2003).

The different creep event sizes presented in Figure 2.3 also have different implications for the release of the strain that accumulates along the central creeping section. Geodetic observations suggest that the central San Andreas Fault is creeping slower than the long-term deep slip rate, accumulating a moment deficit (Maurer and Johnson, 2014; Michel et al., 2018; Ryder and Bürgmann, 2008). That moment deficit could be accommodated by a M_w 5.2 – 7.2 earthquake occurring every 150 years, on average (Maurer and Johnson, 2014; Michel et al., 2018; Ryder and Bürgmann, 2008). Or the moment deficit could be accommodated by occasional bursts of creep events (e.g., Khoshmanesh and Shirzaei, 2018b). A moment deficit that requires a M_w 6.2 earthquake per 150 years could be accommodated by a burst of 200 1 mm creep events that are 10 km along strike and 4 km deep occurring every 30 years. But if creep events are much smaller and shallower, say 5 km long and 1 km deep, the observed moment deficit could be accommodated only by a burst of 800 1 mm creep events every 15 years.

In this study, we thus aim to take an important next step in unravelling the origin and role of creep events in the slip dynamics of the creeping section. We aim to determine the typical along-strike extent of creep events on the central San Andreas Fault. We first systematically identify creep events within the remarkable, decades-long USGS creepmeter record. Then, we compare records from multiple creepmeters to characterise the ruptures' along-strike extents and determine if they are small, localised phenomena or large, segment-rupturing events.

2.2 Creepmeters and Creep Events

We use data from 18 USGS creepmeters along the creeping section of the San Andreas Fault (Figure 2.1) to investigate the along-strike length of creep events. Each creepmeter operated for at least nine years between 1985-2020. All creepmeters have sampling intervals of 10 minutes except for Melendy Ranch (XMR), which was upgraded to 1 minute sampling on 6$^{\text{th}}$ September 2018 by the USGS and R.Bilham. Detailed descriptions of each creepmeter and its site location can be found in Schulz (1989).

The creep events we analyse are mostly well recorded. They appear in the data as accelerated bursts of slip (Figure 2.2). Typical creep events last from hours to days and slip on the order of less than a millimetre to several millimetres (Bilham et al., 2004; Wesson, 1988). Creep events may be simple and have a sharp onset (Figure 2.2b) or have multiple steps (Figure 2.2a) that could reflect a migrating slip location (Bilham and Behr, 1992; Gladwin et al., 1994; Schulz, 1989; Wesson, 1988). Creep events may also have a smaller initial step or increased slip rate (sometimes referred to as preamble) preceding the main slip period (Bilham et al., 2004; Wesson, 1988). Occasionally, there is a slight plateau between the first and second phases of slip in multi-step events, where the slip rate is above the background rate but slower than both steps on either side. The length of this plateau is not the same between events, so it is unlikely to be an instrumental artefact (Gladwin et al., 1994). Despite all the possible variations in creep events, whether single or multi-step, sharp or gradual onset, creep events appear to be self-similar at each creepmeter. However, creep events do not have a similar form across creepmeters, giving each creepmeter its own characteristic creep event (Wesson, 1988).

Creep events are not the only signal present in the creepmeter data. There are also many steps in the data. Some steps result from small nearby earthquakes, while others arise because of friction within the creepmeter instrumentation (Bilham and Castillo, 2020). These steps are usually distinguishable from creep events because they occur abruptly, while creep events typically have a longer duration and asymptotically approach a lower slip rate (Figure A.1).

2.3 Identifying Creep Events at Individual Creepmeters

In order to constrain creep events' spatial extent and timing, we first needed to find the events in the data. The creep events we are interested in are readily identifiable via visual inspection. Through visual inspection alone, it is possible to characterise the slip and duration of creep events and develop an understanding of the typical shape that a creep event has at each creepmeter. Yet despite the ease of which detecting creepmeters manually can be achieved, visually examining decades of creepmeter records would be time-consuming. So, we identified the creep events at each creepmeter using an automated approach to obtain initial potential detections. Then, we used visual inspection to refine the catalogue.

The aim of this automated detection was to find the creep events that we already knew were there, as well as those at other creepmeters that, at the time, we had not examined. Before beginning the process of building the automated detection, we manually picked creep events at creepmeters XSJ, XHR, and CWN. We tested our automated detection against these manual picks in order to ensure that our detection was not missing events that we had observed by inspecting the creep record by eye. We find that for these creepmeters, we were able to detect >90% of creep events detected through manual inspection, only missing either very small events or events that have a more surge-like shape, i.e., slip events that have no sharp onsets but rather a slow increase in creep rate over several days–weeks before slowly decreasing in creep rate over the preceding months. The onset and end times of these surge-like events are often ambiguous onsets and end times. These surge-like creep events are much less frequent than the step-like creep events that make up the vast majority of the creep record.

2.3.1 Automated Detections

A full, in-depth description of our automated detections is presented in Supplementary Text A.1. Here, we detail the main processing steps undertaken by our detection scheme.

We began by identifying times of potential creep events: times when the creepmeter record is similar to a template creep event and when there is a significant slip.

For this analysis, we first prepared the data. We interpolated the creepmeter record to ensure that the data were spaced evenly at 10 minute intervals, removed a long-term trend, and bandpass filtered to focus on variations between 2 h and 5 d: the dominant periods of the creep events (Bilham et al., 2004; Gladwin et al., 1994; Wesson, 1988). The black curves in Figure 2.4 a & b illustrate a creep event record before and after filtering. We then picked one template creep event for each creepmeter (green curve in Figure 2.4 b). One creepmeter is an exception; we used two templates for the Melendy Ranch (XMR) creepmeter, as the data's sampling frequency increased after it was updated. We tried using different template events for detecting creep events, which all performed very similarly to one another, varying only in the start time that they detected. As we eventually correct for the discrepancy in start time manually, the choice of template event for each creepmeter was less crucial as long as it was representative of the vast majority of events.

Next, we conducted a rough automated detection by cross-correlating the template creep events with the creepmeter records. The length of the time window for our cross-correlation was the length of the template event and was calculated as a sliding window. We identified peaks in the cross-correlation that exceeded a creepmeter-dependent threshold between 0.05 and 0.2, allowing only one peak per 40 minute interval (Figure 2.4 c). The thresholds for detection were set relatively low, allowing for many false positives so that we could identify creep events with shapes that varied from the template.

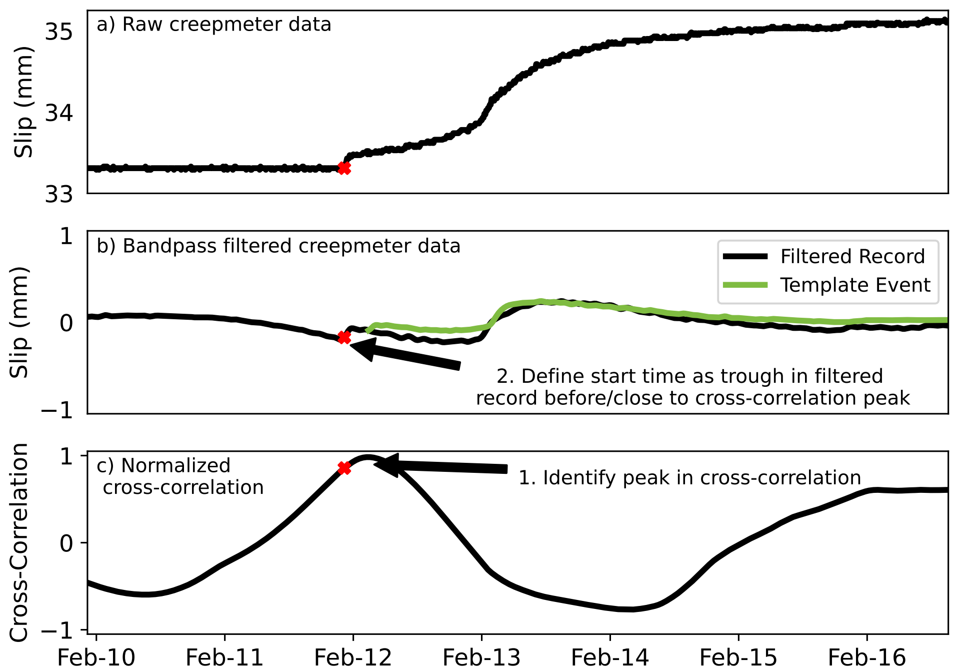

Figure 2.4: Processing stages of the automated detection. a) Raw creepmeter data from Cienega Winery (CWN) showing a creep event on 11$^{\text{th}}$ February 1994. b) The same creep event bandpass filtered between 2 h and 5 d (black line), along with the template creep event (green line). The template has been aligned with the data according to the peak of the cross-correlation time series shown in panel (c). The red cross in all panels indicates the estimated creep event start time, taken as the time of the trough in the filtered data in panel b).

After identifying the potential creep events, we estimated their start times by examining the running average of the slip in hourly windows just before and after the cross-correlation peak. We identified the potential event start as the time when this hourly slip first appears significant: when it exceeds a noise-based threshold value. Then, we refined the start times using a feature of the filtered creep record: a distinct trough at the start of creep events (Figure 2.4 b). This trough has no physical meaning and is purely an artefact of the detrending and filtering processes we used. Despite this, the trough before creep events proved useful to more accurately determine the start time of creep events. We used the time of the nearest trough to the start time we had determined using hourly slip as our automated estimate of the potential creep events' start times (red cross in Figure 2.4).

To estimate the potential creep events' end times, we examined the running average of the slip in overlapping daily windows following the start time. End times were estimated as the first time after the event began, where this daily slip fell below a noise-based threshold.

Once we had end-time estimates, we could calculate the slip in each potential creep event. We subtracted the slip at the start time from the end time. This simple difference provides the best estimate of the slip in the identified time period, given that the noise in the creepmeter record has a random walk character at periods longer than 1 hr (e.g., Langbein et al. (1993); Langbein and Johnson (1997)).

The slip estimates provided a useful way of removing tiny events, most of which result from instrumental resolution or friction within the creepmeters. We removed detections when they had slip less than 1% of the median slip from the largest 10% of creep event detections at each creepmeter.

In our last automated step, we merged events as necessary. Some creep events include multiple accelerations, and those can be detected as multiple creep events. We merged the detections if the start and end times of two potential creep events were the same or overlapped. After completing this step, our catalogue of potential creep events includes 15,180 events.

Finally, we visually inspected all of the potential creep events to ensure no false positives are carried forward into further work. This process removes roughly 13,000 detections, which mainly constitute duplicate detections of multi-phase events, stick-slip instrumental artefacts, and detections that occur in particularly noisy section of the time-series. We manually corrected each start time based on a visual inspection of the data.

2.3.2 Results

With our automated and manual analysis, we identified 2120 creep events at 18 creepmeters. This event catalogue is provided in Supplementary Section A.2. Figure 2.5 shows some of the patterns evident in this catalogue: the number of events at each creepmeter, as well as the events' median slip and duration. There is an anti-correlation between the number of creep events at each creepmeter (Figure 2.5a) and the slip (Figure 2.5b) and duration (Figure 2.5c) of those events. These properties are plotted against one another in Figure A.2. This summary confirms our inferences from visually examining the record: that some fault sections slip in numerous creep events, each with small slip (e.g., Middle Mountain, XMM (Figure 2.2b)), while others slip less frequently, in creep events with large slip (e.g., Cienega Winery, CWN (Figure 2.2a)). Despite the varying sizes and number of creep events, most creepmeters see over 50 % of their total slip accommodated in creep events, with the rest accommodated by stable creep (Figure 2.5d). The exception to this are creepmeters with a surge-like slip that is not detected as a creep event under our detection scheme or creepmeters that suffer from a large amount of left-lateral slip, meaning that the percentage of slip accommodated in creep events is less clear. These percentages show that creep events play an important role in accommodating fault slip at the surface. To remove some of the bias created by the available record, we have also plotted the median slip per event normalised by the median recurrence interval (Figure 2.5e). This proxy for slip rate shows a similar pattern to the percentage of slip accommodated by creep events in Figure 2.5d. The total slip accommodated in creep events at the surface does not account for the total slip observed at depth along the creeping section as the values of median slip per median recurrence interval (Figure 2.5e) are lower than 30-33 mmyr^{-1} leading to a slip deficit (Maurer and Johnson, 2014; Michel et al., 2018; Ryder and Bürgmann, 2008)

We find that creep events along the San Andreas Fault have a recurrence time of weeks to months and vary along the fault (Figure A.3). Furthermore, the creepmeters with fewer, larger creep events appear to have longer recurrence intervals than those with more frequent smaller events. The frequency of creep events is not consistent through time and is affected by seismicity. For instance, the recurrence interval of creep events at creepmeters affected by the 2004 Parkfield Earthquake (XSC–XGH) is shorter in the ten years after the earthquake than in the ten years before it (Figure A.4).

Using our creep event catalogue, we have produced a booklet (Supplementary Section A.3) displaying all the creep events we observe and the creep recorded on other creepmeters at the time of the event. This booklet was useful in identifying creep events that may rupture the surface at more than one creepmeter (Section 2.4.3).

2.4 Identifying Correlated Events Between Creepmeters

An initial visual analysis of the creep event records suggested that some of the creep events span relatively long distances along strike (Figures A.5 & A.6). Both Figures show creep events through time, allowing for the correlation of creep events across different creepmeters. In this section, we describe how we used the closely timed event detections to determine the spatial extent of creep events. We describe how we determined the frequency of multi-creepmeter events, accounted for rainfall-induced coincidences, and visually examined identified ruptures. We summarise the common creep event behaviours identified with this analysis in Section 2.5.

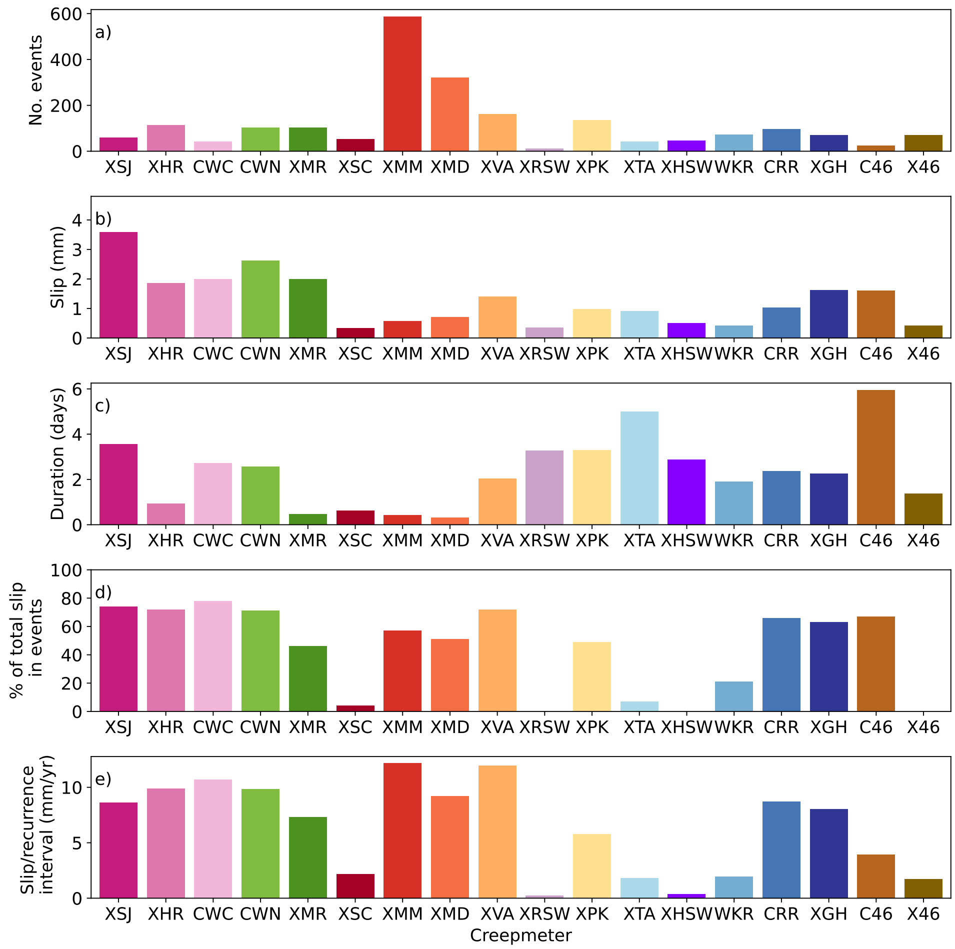

Figure 2.5: Properties of the creep events at each creepmeter. a) Number of detected events. b) Median creep event slip. c) Median creep event duration. d) Percentage of total fault slip accommodated in creep events. Note XRSW, XHSW, and X46 do not have values. This is due to a large amount of left-lateral slip, making calculating the total amount of slip for these creepmeters not easily quantifiable. e) Median slip divided by median recurrence interval.

2.4.1 Estimating the Frequency of Multi-creepmeter Ruptures

It is clear from the records in Figure 2.6 that, during this period, creepmeters 4 km apart display creep events at close times, and it would seem plausible that the events result from a single, >4 km-long creep event. However, it is also possible that the closely timed events are just a coincidence or just a rare large creep event. Our next task, then, was to determine the fraction of creep events observed at one creepmeter that has a closely timed event at another.

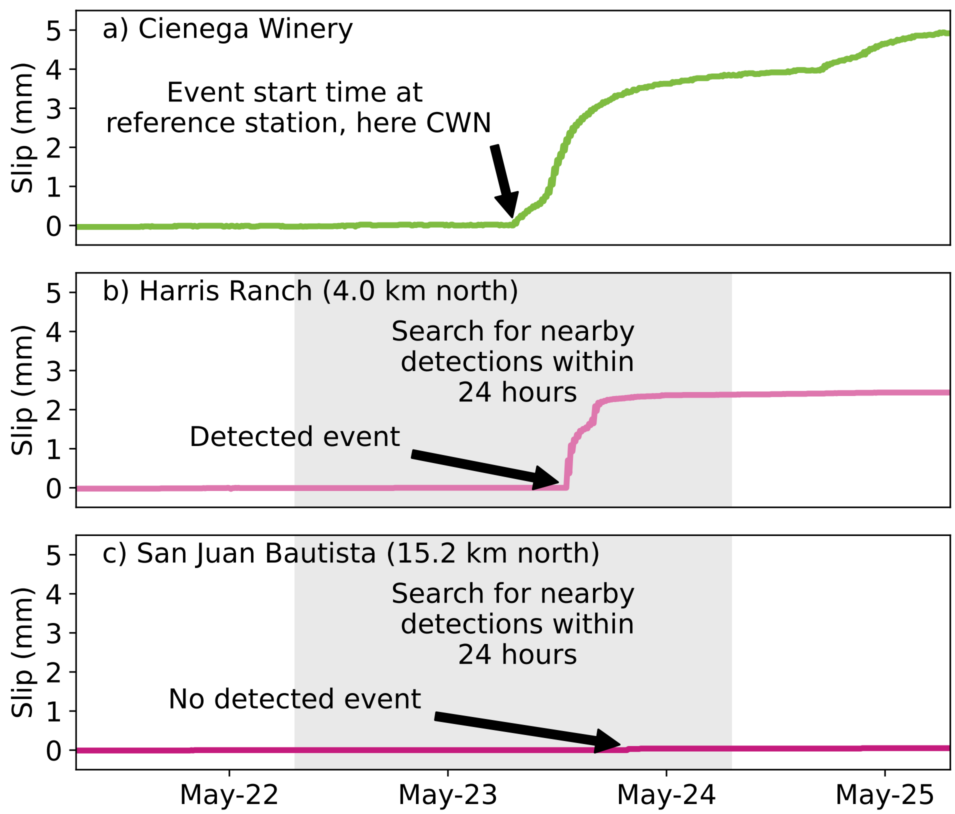

Figure 2.6: Creep records for the 21 to 26$^{\text{th}}$ May 2016 at (a) Cienega Winery (CWN), (b) Harris Ranch (XHR), and (c) San Juan Bautista (XSJ). The figure illustrates our approach to detecting closely timed events. For each event at Cienega Winery (panel a), we search for events at (b) Harris Ranch and (c) San Juan Bautista that occur within 24 hours of the Cienega Winery event (grey regions in panels b and c).

We examined the frequency of closely timed creep events at all pairs of creepmeters. We first isolated the period in which both creepmeters were operational, excluding the period between 28$^{\text{th}}$ September 2004 and 1$^{\text{st}}$ January 2006 on southern creepmeters because this interval is affected by the 2004 $M6$ Parkfield earthquake. We defined one creepmeter in each pair as the main creepmeter. For each creep event on this main creepmeter, we identified the closest event on the second creepmeter and noted the time between the two. Since creep events typically last hours to days, we were particularly interested in when the time between creep events was less than 24 hours. We calculated the percentage of creep events observed at the main creepmeter that occur within 24 hours of a creep event at the second creepmeter.

We selected 24 hours as the threshold value as it provides a balance between detecting slow propagating events and conducting robust statistics. Previously reported propagation velocities for creep event range from 960 m/day to 82.32 km/day (e.g., Evans et al., 1981; King et al., 1973; Mortensen et al., 1977). We have calculated the theoretical propagation velocities (Figure A.7) for any event at one creepmeter that occurs within 24 hours of another event at a different creepmeter regardless of distance along the fault. We find that 60.5% of these possible propagating events have a propagation velocity within the range of those previously reported (Figure A.7). Only 1% of these possible propagating events have a propagation velocity of less than 960m/day. This suggests that we are only missing the very slowest propagating events. We, therefore, choose not to use a time window shorter than 24 hours as this reduces the possibility of detecting slower propagating events.

Using a window longer than 24 hours adds additional unwanted complexity to the statistics and interpretation. For instance, if we consider a window of three days before or after an event, the total time window we need to search for another event is six days. At these timescales, it is possible that two events have occurred at one creepmeter, and both events would correlate with the target event at the main creepmeter. These double correlations are particularly troublesome in the years following the 2004 Parkfield earthquake, when the recurrence interval of creep events is reduced (Figure A.4). Interpretation of these double correlations is also problematic. It becomes unclear whether all three of these detections are one event that propagates back on itself, two events where one is detected at more than one creepmeter or three separate unrelated events. For simplicity of understanding, we, therefore, chose to use a correlation window of 24 hours as this provides both a long enough window to find events that have propagation velocities in the range of those previously reported while also allowing us to conduct more robust statistics without double correlations.

Next, we calculated the uncertainty on this percentage of closely timed creep events. We bootstrapped the data and recomputed the percentage using various subsets of the creepmeter records. We divided the main creepmeter record into years, and in each recomputation, we picked the same number of years as in the original record, but with replacement, and calculated the percentage of these creep events within 24 hours of events at the second creepmeter. This bootstrapping allowed us to estimate a probability distribution on the percentage of events at the main creepmeter that occurs within 24 hours of an event at the second creepmeter. The 15th to 85th percentiles of the orange histogram in Figure 2.7a tells us, with 70% probability, that 24.3 to 31.5% of CWN events are within 24 hours of an event at XHR.

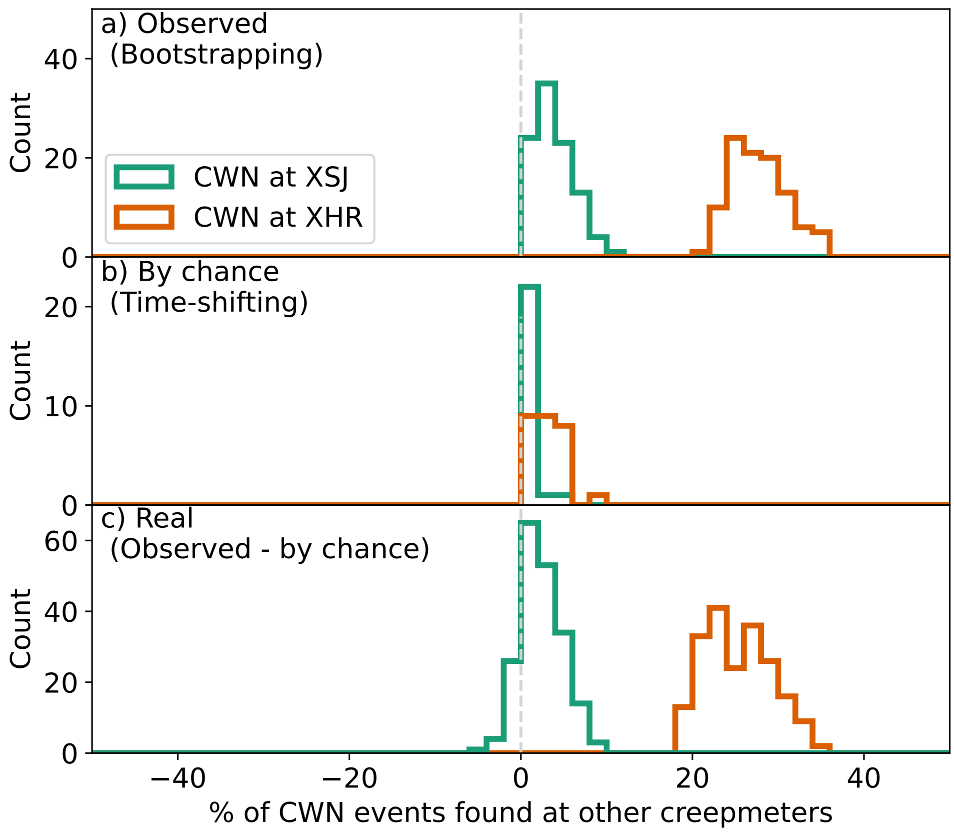

Figure 2.7: a) Probability distributions of the percentage of CWN creep events observed at XHR (orange) and XSJ (green) within 24 hours, based on bootstrapping. b) Probability distributions that a CWN event would coincide with an XHR or XSJ event by chance: if events were randomly timed. c) The distributions in (a) minus the distributions in (b): probability distributions on the percentage of CWN events that were observed at XHR and XSJ within 24 hours for a physical reason.

However, closely timed events are not necessarily physically meaningful; some of the XHR events could occur just before or after CWN events by chance. To determine how many events could be closely timed by chance, we redo our analysis after randomly shifting the times of creep events at the main creepmeter by 1 to 35 years. In each reanalysis, we shifted all of the creep event times by the same amount, looping the times of events shifted beyond the end of the record back through the start. With this constant shift, we were able to maintain the temporal spacing and, thus, the recurrence statistics of the creep events. Further, we use time shifts that are multiples of 1 year to preserve the seasonality of the creep event timing. This time-shifting creates a distribution (Figure 2.7b) that encompasses the percentage of creep events recorded on two creepmeters by chance and unrelated.

To estimate the number of ”real” closely timed events – those that are not by chance, we subtracted the by chance distribution (Figure 2.7b) from the bootstrapped observed distribution (Figure 2.7a). The probability distribution of these real closely timed events is shown in Figure 2.7c, in green for the CWN-XSJ pair and orange for the CWN-XHR pair. In Figure 2.7c, the CWN-XSJ distribution crosses 0% (vertical dashed grey line) and has a 70% confidence interval of 0 to 5.1%, meaning that coincidentally timed events are likely to be unrelated. In contrast, the CWN-XHR distribution is well above 0%, with a 70% confidence interval of 21.3 to 29.1%, indicating that coincidentally timed events are related.

The percentages of events for each creepmeter pair are presented in Figures A.8-A.24. Certain pairs are discussed in more detail in Section 2.5.

2.4.2 Removing Short-term Rainfall Effects

Our results suggest that for many pairs of creepmeters, events are closely timed more often than one would expect by chance. However, these temporal coincidences do not necessarily imply that a single creep event ruptures from one creepmeter to the other; there could be two small events, one near each creepmeter (e.g., Figure 2.3a). These two small events could be closely timed because they both respond to atmospheric or hydrological signals.

Hydrological signals can appear in the creepmeter record on both short and long timescales (Bilham et al., 2004; Roeloffs, 2001; Schulz et al., 1983). The long-timescale hydrological signals are the result of seasonal variations. These seasonal variations manifest in the number of creep events that occur during the wet and dry seasons as well as the overall creep rate (Roeloffs, 2001). The long-timescale components of seasonal hydrological signals are already accounted for in our by-chance distributions, as we used only time shifts that were multiples of a year.

On short timescales, rainfall can influence creep rate as well as creep events. Given that fault zone material of creeping faults are generally rich in clays (e.g., Kaduri et al., 2017; Moore and Lockner, 2013; Moore and Rymer, 2012, 2007), rainfall will cause the shallow fault to expand as the clay moistens and contract when dry, forcing the piers that anchor the creepmeter in place in random directions adding noise (Bilham et al., 2004). Creep events are also affected by rainfall with episodic slip induced following periods of heavy rain (Roeloffs, 2001) and retardation of slip in dryer periods (Schulz et al., 1983). Creep events that are closely timed with rainfall could be a result of the rainfall providing a 'kick' to a shallow portion of the fault that has nominally stable rheology and low resistance to slip at near-surface low-stress conditions (Helmstetter and Shaw, 2009; Kanu and Johnson, 2011; Perfettini and Ampuero, 2008). As this mechanism for creep events does not represent a tectonically driven process, we need to assess to what extent these longer events are driven by rainfall.

Alternatively, if the fault is impermeable, rainfall will increase the normal stress on the fault by providing a load to the surface. This increase in normal stress would actively move the fault further away from failure, stablising slip. The close relationship between rainfall and the onset of creep events (e.g., Roeloffs, 2001; Schulz et al., 1983) would suggest that the former response for rainfall may be more likely.

Here, we probe the shorter-timescale influence of rainfall to interpret our results in light of rainfall being a possible source of our longer multi-creepmeter events.

To probe the rainfall effect, we again recomputed our closely timed event percentages (Section 2.4.1), but with few modifications. We used rainfall records from the four

NOAA weather stations to identify creep events at the main creepmeter preceded by a 3, 7 (orange in Figure 2.8) or 14-day (red in Figure 2.8) interval that included rainfall. Previous work on the relationship between rainfall and creep events has found that creep events that are associated with rainfall tend to occur within 24 hours of rainfall (Roeloffs, 2001; Schulz et al., 1983). The range of thresholds we used is longer than this to allow for varying timescales of rain infiltration, as this is not a well-known quantity. Although fairly arbitrary, these timescales provide an ability to look at the broad overview of the effect of rainfall on the propagation of creep events within our statistical framework. Despite not being an in-depth analysis of this topic, we believe these timescales are sufficient to interpret our findings in the light of rainfall.

Events with rainfall before them were then removed from the main creepmeter before bootstrapping (Figure 2.8a) and shifting (Figure 2.8b) of the creep event record at the main creepmeter. We then computed the subtraction as before to determine the percentage of physically related creep events in following wet and dry periods (Figure 2.8c).

In this reanalysis, we do not use all creepmeter pairs. We consider only pairs that showed significant correlation to one another before rainfall considerations. If both creepmeters in the pair are triggered by rainfall, we would expect to see a reduction in correlation when we remove events that follow rainfall. Often, however, we see a minimal change in the correlation. For instance, the similarity of the blue to red histograms in Figure 2.8c suggests that the closely timed creep events at XMM and XMD are caused by something other than rainfall.

We summarise how excluding rainy intervals influences or does not influence the percentage of closely timed creep events for more pairs of creepmeters in Section 2.5. Those quantified influences are enough to determine the significance or lack of significance in the closely timed event percentages. Here, however, we also briefly consider how rainfall influences creep event timing. To slightly better understand the influence of short-timescale rainfall, we probed the number of creep events at "random" times at the second creepmeter (Figure 2.8d). To preserve the seasonality, we created random times by shifting the times of the main creepmeter events by multiples of a year. We then excluded events preceded by 3, 7, or 14-day intervals with rainfall before computing the percentage of times within 24 hours of a creep event at the second creepmeter (Figure 2.8d). These new time-shifted distributions allowed us to determine if certain creepmeters preferred to slip in wet or dry conditions (given the seasonality of the main creepmeter). For instance, it appears from Figure 2.8d that the creepmeter at Middle Ridge (XMD) prefers to slip in wet conditions; the percentage of times with creep events decreases when rainy intervals are removed. We do not discuss this further; however, the relevant results are presented in the supplement (Figures A.26-A.32).

2.4.3 Detecting Long Creep Events by Visual Inspection

Having determined the frequency of multi-creepmeter events and assessed the affects of rainfall, We next use our event detections to inspect coincidently timed creep events at multiple creepmeters visually. Using our creep event catalogue, we identify all the creep events at each creepmeter that occur within 24 hours of a creep event at any other creepmeter to produce a subsection of our catalogue that only contains these events. This subsection of events contains 306 potentially large creep events that rupture two or more creepmeters within 24 hours, made up of 719 different individual detections from our creep event catalogue. We present examples of different sized creep events in Section 2.5 and provide figures illustrating all of the multi-creepmeter events in the second supplementary creep booklet.

Visual inspection also allowed us to probe where slip happens in a creep event: on the surface or at depth. If a creep event was rupturing along the surface, we would expect to observe an event at every creepmeter along the way between two end-member creepmeters. However, we do not always find this to be the case, which would suggest that these creep events are rupturing at some depth below the surface(Evans et al., 1981). Examples of these events are discussed in Section 2.5.4.

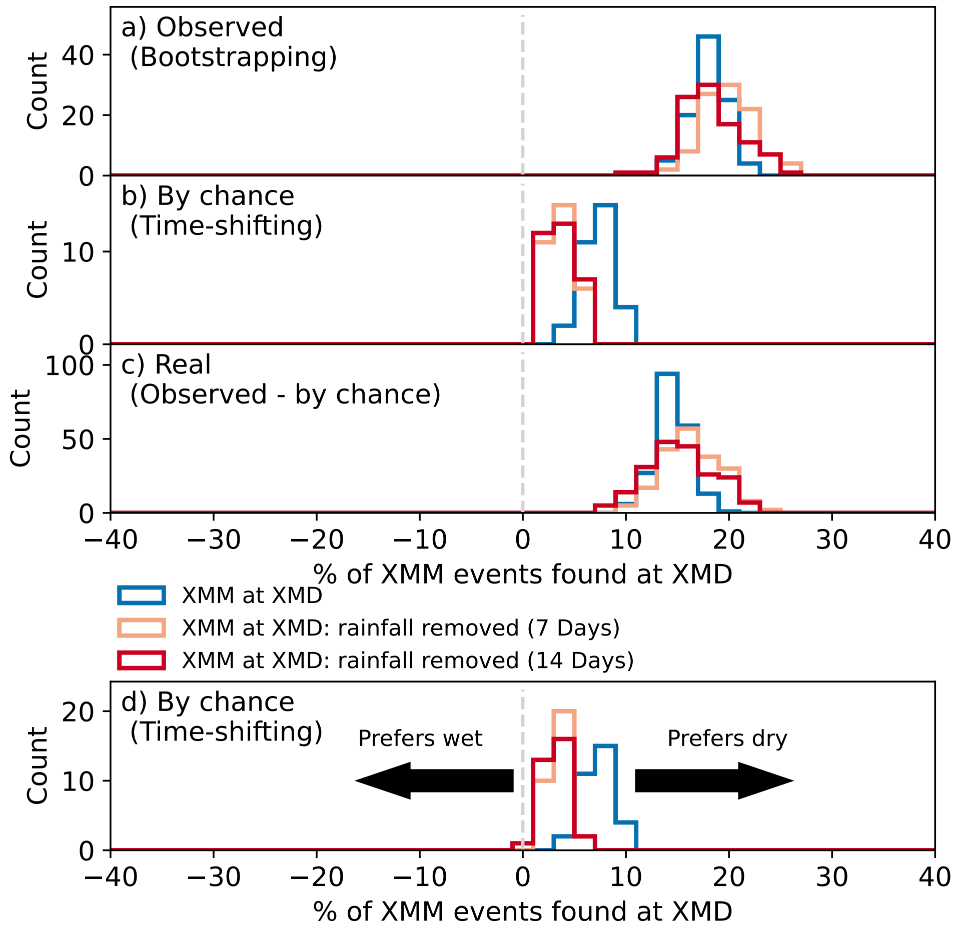

Figure 2.8: (a-c) Probability distributions on the percentage of XMM events observed at XMD. Panels a-c are as in Figure 2.7, with the observed, by chance, and real percentages, but the three histograms in each panel illustrate the effect of removing rainy intervals. The blue histograms use all XMM events in the comparison, while the orange and red histograms use only XMM events that follow 7 or 14-day periods without rain. d) The percentage of XMM events observed at XMD by chance, as in panel b, but when XMD events preceded by rainfall are removed. The reduced percentage suggests that XMD events are more common in rainy intervals.

2.5 Summary of Creep Event Behaviours

The creep event correlation described above reveals that many creep events rupture several kilometres along the fault strike. But other creep events appear short, perhaps less than 1 km long. By analysing over 2000 creep events found in our catalogue, we are able to identify a variety of creep event behaviours. Here we describe the five most common creep event types: (1) isolated events (Figure 2.9a), (2) small (<2 km) events recorded at two creepmeters (Figure 2.9b), (3) 5 km events recorded at multiple creepmeters(Figure 2.9c), (4) long (10 to 30 km) propagating events (Figure 2.9d), and (5) multi-strand ruptures.

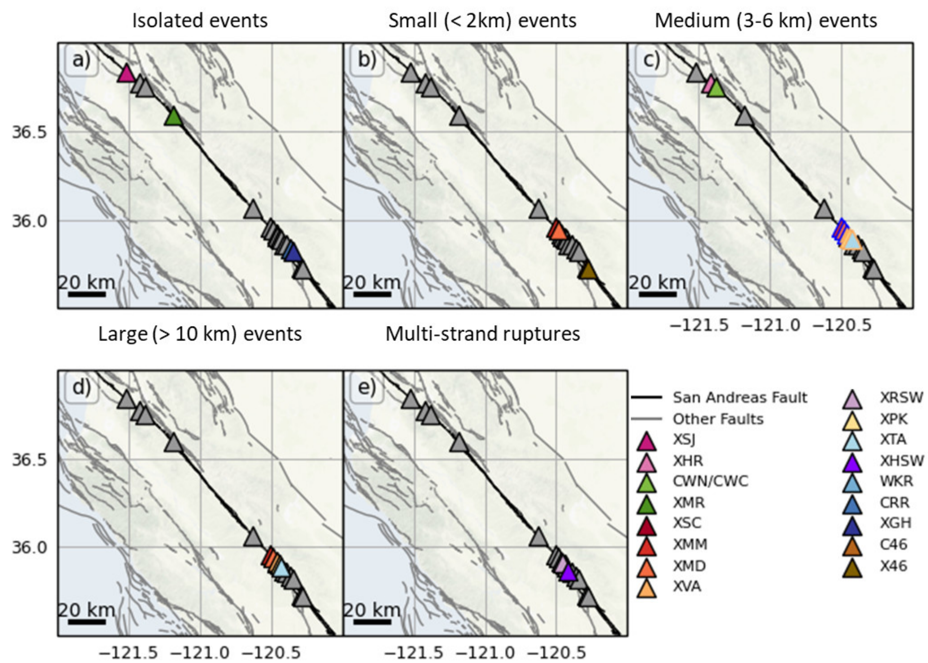

Figure 2.9: Maps of the creeping section of the central San Andreas Fault (black) showing the location of different creep event behaviours. The creepmeters are shown as coloured triangles, and greyed-out triangles are creepmeters not involved in events. a) Location of isolated events. b) Location of (<2 km) events recorded at two creepmeters. c) Location of 5 km events recorded at multiple creepmeters. d) Location of long (10 to 30 km) propagating events.

2.5.1 Isolated Events

A few creepmeters in this study appear to show only isolated creep events: events that are recorded at no other creepmeters. These locations are shown in Figure 2.9a.

2.5.1.1 San Juan Bautista (XSJ)

The creepmeter at San Juan Bautista (XSJ) displays isolated, repetitive 3 to 4 mm events every few months, which were previously analysed by Gladwin et al. (1994). One of these isolated events is shown in Figure 2.10a. The XSJ events show weak to minimal correlation in timing with the closest neighbouring creepmeters. Although 0.5 to 8.5% of XSJ events are recorded at Cienega Winery (CWN) 15.3 km southeast according to 70% confidence intervals, 70% confidence intervals overlap zero and have a maximum of 2.0% for a closer creepmeter located 11.2 km southeast (Figure 2.10b).

2.5.1.2 Melendy Ranch (XMR)

The creepmeter at Melendy Ranch (XMR) displays 2 mm events (Figure 2.10c) every few months that are recorded at no other creepmeter (Figure 2.10d). However, this creepmeter is far from its neighbours: 24.6 km southeast of Cienega Winery (CWN) and 77.32 km northwest of Slacks Canyon (XSC). Nevertheless, it is interesting to note that this creepmeter is situated above a locked patch identified by Jolivet et al. (2015). The locked patch could prevent creep events from rupturing into and out of the XMR area.

2.5.1.3 Gold Hill (XGH)

The creepmeter at Gold Hill (XGH) also displays isolated events (Figure 2.10e). These events are more intriguing than those at San Juan Bautista (XSJ) and Melendy Ranch (XMR) because XGH is just 2.2 km southeast of the Carr Ranch (CRR) creepmeter, yet there is no evidence of creep events that rupture both locations (Figure 2.10f). Indeed, on timescales of months to years, these locations seem to have anticorrelated slip rates. For instance, when the slip rate at CRR increased in September 1994, the slip rate at XGH decreased. Moreover, when the slip rate at CRR decreased between 2016 and 2017, the slip rate at XGH increased. This anti-correlation in slip was noted by Roeloffs (2001), who suggested that slip accumulates at one location before reaching a threshold that allows slip at the other location.

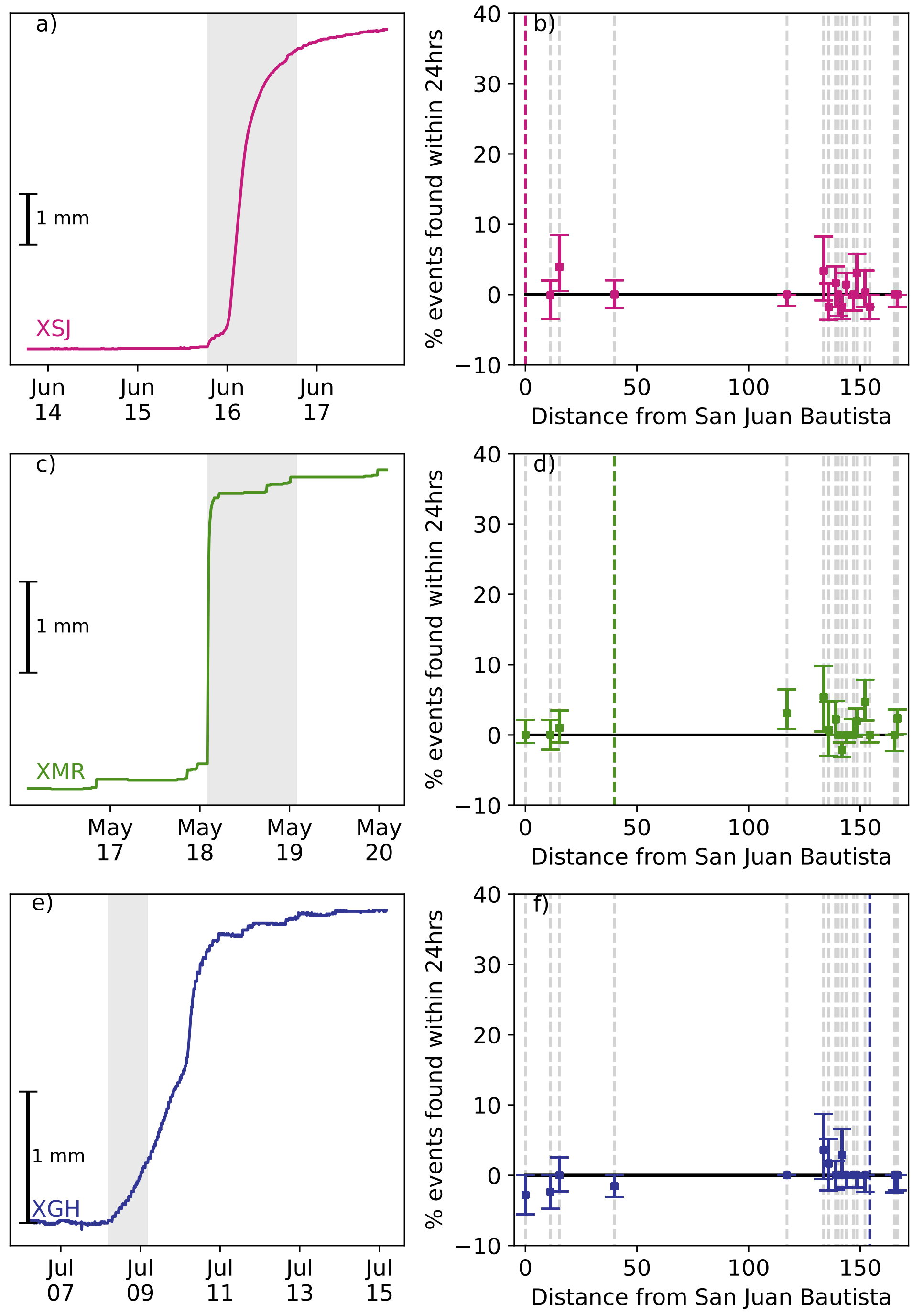

Figure 2.10: Creep events and percentage of events observed at other creepmeters for isolated creep events at XSJ, XMR, and XGH. a) Creep event at XSJ on 15th June 1993. c) Creep event at XMR on 18th May 1993. e) Creep event at XGH on 8th July 1991. b), d) and f) indicate the percentage of events XSJ, XMR, and XGH events found at other creepmeters, with 70% confidence intervals. Vertical coloured lines in b), d) and f) mark the location of the creepmeter.

2.5.2 Small Events (2 km or Less) Recorded at Two Creepmeters

Some creepmeters record events that coincide in time with events at creepmeters a short distance away. These locations are shown in Figure 2.9b.

2.5.2.1 Middle Mountain (XMM) - Middle Ridge(XMD)

The fault section between Middle Mountain (XMM) and Middle Ridge (XMD) is around 8 km north of Parkfield. These two creepmeters are 2.26 km from each other, 14.2 km from creepmeters farther north, and 2 km from creepmeters farther south. Both creepmeters record large numbers of <1 mm creep events, which occur every few weeks (see Figure 2.5a). Our analysis of coincidently timed events implies that many of these small creep events rupture both creepmeter locations (Figure 2.11a). 70% confidence intervals suggest that 12.9 to 16.3% of XMM events are also recorded at XMD, and 25.9 to 31.9% of XMD events are observed at XMM (Figure 2.11b).

When creep events with rainfall in the 7-14 days before the event are removed, the percentage of XMM events found at XMD and vice versa does not change significantly. When events preceded by a 14-day interval with rainfall are removed, 11.8 to 19.0% of XMM events are observed at XMD, and 24.4 to 34.7% of XMD events are observed at XMM. Combining these percentages with the observation that XMM and XMD have opposite responses to rainfall (Figure A.26g & A.26h) implies that correlated events recorded at these two creepmeters are not due to atmospheric effects; instead, their correlation is due to a slip at depth on the fault.

2.5.2.2 Highway 46 creepmeters (C46 - X46)

The southernmost pair of creepmeters is situated near Highway 46, 10 km south of the cluster of creepmeters around Parkfield. Creepmeters C46 and X46 are 1.27 km apart and record fewer events than Middle Mountain (XMM) and Middle Ridge (XMD); 0.4 to 1.6 mm events occur around 1-2 times a year. However, many of the recorded creep events rupture both locations (Figure 2.11c). 70% confidence intervals suggest 50.0 to 66.7% of creep events at C46 are observed at X46, and 47.1 to 64.8% of X46 events are observed at C46 (Figure 2.11d). When creep events with rainfall in the 7-14 days before the event are removed, the percentage of C46 events at X46 increases. When events with rainfall in the 14 days prior are removed, 40 to 80% of C46 events are found at X46, and 100% of X46 events are found at C46 (Figure A.27), which may arise from slip at depth. The picture of this section is not fully clear as both C46 and X46 prefer to slip in wet conditions (Figure A.27g & A.27h). This would suggest that some of the correlation here is rainfall-induced; however, there is still some evidence for slip at depth, given the percentage of correlated events goes up when rainfall is removed.

2.5.3 Medium-sized Events (3-6 km) Recorded at Two or Three Creepmeters

The next most frequently observed type of creep events are 3 to 6 km long and are typically observed at two or three creepmeters. These 5 km-long events are found at multiple locations along the fault, from Cienega Winery in the north to Highway 46 in the south. These locations are shown in Figure 2.9c.

2.5.3.1 Harris Ranch (XHR) - Cienega Winery (CWN)

The northern end of the creeping section between Harris Ranch (XHR) and Cienega Winery (CWN) hosts a series of creep events that have an along-strike length of at least 4 km (Figure 2.12a). Events at CWN and XHR are typically 2-2.5 mm and occur every few months. 70% confidence intervals suggest that 17.4 to 26.6% of creep events recorded at XHR are also recorded at CWN, and 21.3 to 29.1% of CWN events are observed at XHR (Figure 2.12b).

When creep events with rainfall in the 7 days before the event are removed, the percentage of XHR events observed at CWN and vice versa does not change significantly, with 16.3 to 28.5% of XHR events recorded at CWN and 20.8 to 32.0% of CWN

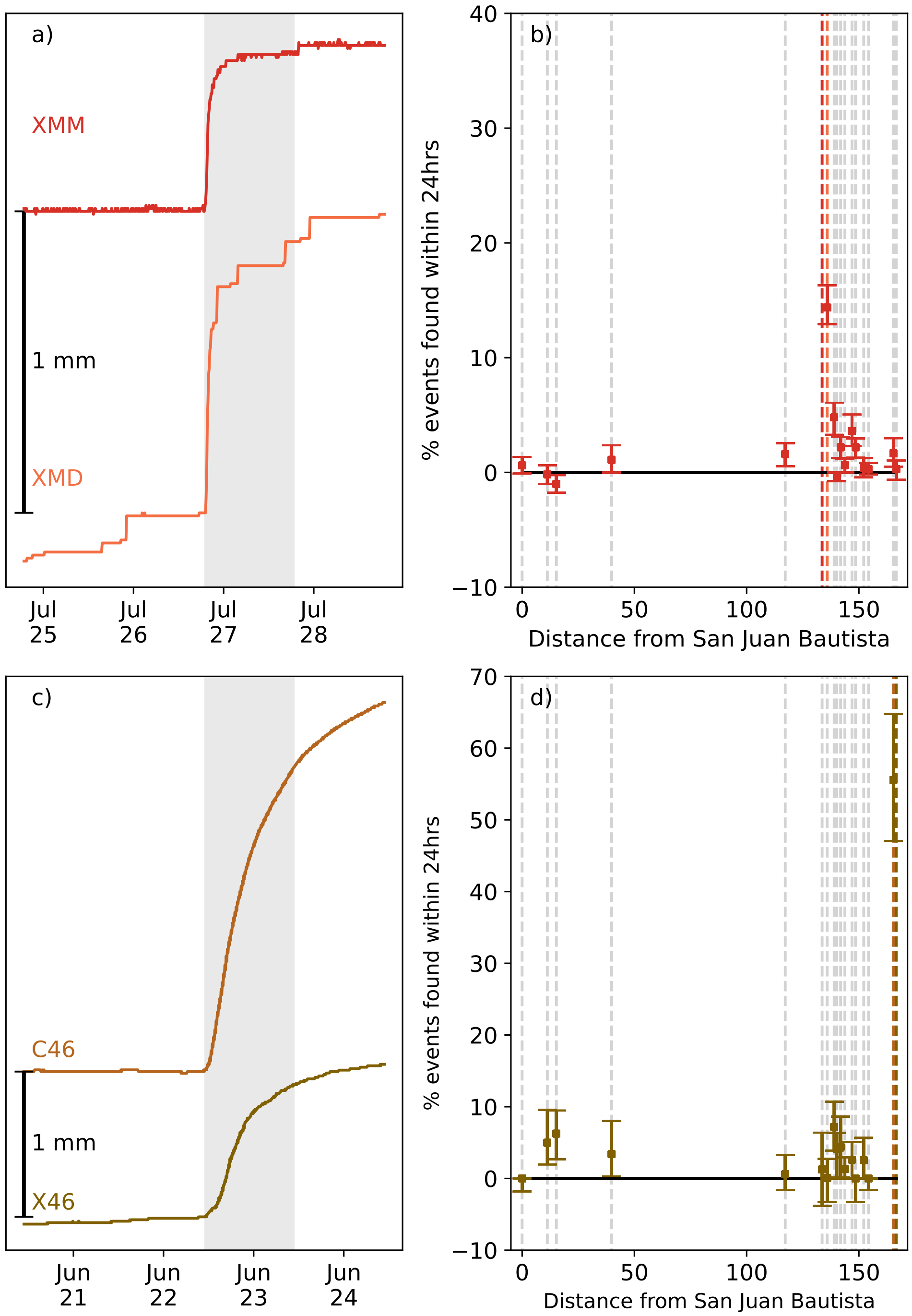

Figure 2.11: Small creep events from the XMM - XMD and Highway 46 (X46 & C46) areas and percentage of events observed at other creepmeters for XMM and X46. a) Creep event at XMM and XMD on 26th July 1991. c) Creep event at X46 and C46 on 22st June 2015.b) and d) indicate the percentage of XMM and X46 events found at other creepmeters, with 70% confidence intervals. Vertical coloured lines in b) and d) mark the location of the creepmeters in a) and c).

events observed at XHR. And if creep events with rainfall in the previous 14 days are excluded, the percentage of events rupturing both stations actually increases. If events with rainfall in the 14 days before the event are removed, 29.6 to 47.6% of XHR events are observed at CWN, and 28.0 to 48.7% of CWN events are observed at XHR (Figure A.28). The relationship between XHR, CWN and rainfall is discussed in more detail in Section 2.6.3.

2.5.3.2 Middle Mountain (XMM) - Middle Ridge (XMD) - Varian (XVA)

Farther south, the fault section between Middle Mountain (XMM) and Varian (XVA) also hosts 5 km-long events. As noted in Section 2.5.2.1, creep events rupture between XMM and XMD frequently. However, not all of the events in this fault section are simple, 2 km ruptures. Some events continue rupturing farther south to reach XVA (Figure 2.12c). 70% confidence intervals suggest that XVA events coincide with events at both XMM and XMD. 3.3 to 6.1% of events at XMM are observed at XVA, and 12.9 to 23.3% of XVA events are observed at XMM (Figure 2.12d). Further, 5.3 to 9.8% of XMD events are observed at XVA, and 11.0 to 18.8% of XVA events are observed at XMD (Figure 2.12d). Three-creepmeter ruptures can start at any of these stations. However, ruptures are most commonly seen first at XMD; the creep events may preferentially nucleate near XMD (Roeloffs et al., 1989; Rudnicki et al., 1993).

We note, however, that some apparent XMM-XVA or XMD-XVA rupture could arise because coincident creep events are triggered by rainfall. When creep events that are preceded by a 7-day interval that includes rainfall are removed, the percentage of XVA events observed at XMM decreases to 6.6 to 21.8%, and the percentage of XMM events observed at XVA decreases to 1.3 to 5.1%. The percentage of closely timed XMD-XVA events also decreases. 4.9 to 17.5% of XVA events observed at XMD and 3.2 to 7.3% of XMD events observed at XVA. When events with rainfall in the 14 days prior are removed, the percentage of XVA events at XMM reduces to 1.0 to 16.7%. The percentage of XMM events at XVA becomes 0 to 4.4%, implying that they may be unrelated. However, the percentages for XMD and XVA remain roughly constant when 7 or 14 days of rainfall are removed. These reductions in percentages imply that XMM and XVA events may be unrelated when longer-term rainfall is considered; however, the relation between XMD and XVA remains. These relations suggest that there are often events that rupture from XMD to XVA (a distance of 3.1 km) but do not always rupture up to XMM and may require atmospheric perturbations to do so.

2.5.3.3 Varian (XVA) - Parkfield (XPK) - Taylor Ranch (XTA)

In the last subsection, we discussed creepmeters that observed creep events to the north of Varian (XVA). However, XVA also hosts events that are only observed to the south, at the Parkfield creepmeter (XPK, 2.9 km away) and potentially at the Taylor Ranch creepmeter (XTA, 4.8 km away) (Figure 2.12e). 70% confidence intervals suggest that between 13.2 and 20.5% of XVA events are observed at XPK, and 15.5 to 25.3% of XPK events are observed at XVA (Figure 2.12f). These numbers imply that many events rupture the 2.9 km from XVA to XPK. Many events also rupture the 1.9 km from XPK to XTA; 70% confidence intervals suggest that 5.1 to 10.0% of XPK events are recorded at XTA and that 20.3 to 34.9% of XTA events are observed at XPK (Figures A.17–A.18). These percentages are minimally affected by removing times with rainfall.

However, even though XVA-XPK and XPK-XTA events are common, few to zero events rupture the entire 4.8 km from XVA to XTA; 70% confidence intervals suggest that 0 to 2.6% of XVA events are found at XTA and that 0 to 9.1% of XTA events are found at XVA (Figure 2.12f). When rainfall is removed, the percentages of XVA events at XTA and vice versa are reduced slightly, with the lower bound remaining at 0%, meaning that the coincidently timed XVA and XTA events may either be unrelated or driven by rainfall. The lack of closely timed events at XVA and XTA suggests that creep events along this region prefer to slip in two sections: XVA to XPK (2.9 km) or XPK to XTA (1.9km). Creep events rupture the 4.8 km from XVA to XTA less frequently or perhaps not at all.

2.5.3.4 Roberson Southwest (XRSW) - Hearst Southwest (XHSW)

Medium-sized multi-creepmeter ruptures may also be present on secondary strands of the San Andreas Fault: in a 6.4 km stretch between Roberson Southwest (XRSW) and Hearst Southwest (XHSW). Events on this secondary strand are less frequent than on the main strand, but we still observe closely timed creep events (Figure 2.12g). 70% confidence intervals suggest that 4.3 to 31.2% of XRSW events are observed at XHSW, and 0.0 to 10.3% of XHSW events are observed at XRSW (Figure 2.12h). The statistics are somewhat difficult to interpret because XRSW displays just 11 creep events, and that number is reduced by 50% when we remove creep events preceded by rainfall (Figure A.25). So, we simply note here that the XHSW-XRSW statistics marginally suggest that several creep events could rupture the 6 km between these creepmeters.

2.5.4 Large Events (10 km or more), Sometimes Skipping Creepmeters

The potential 6 km creep events between XHSW and XRSW are not the longest creep events we observe. Some closely timed creep events suggest ruptures that span 10 or even 30 km. These locations are shown in Figure 2.9d.

2.5.4.1 10 km Events

The 10 km events occur in the region we discussed in sections 2.5.3.2 and 2.5.3.3, between Middle Mountain (XMM) and Taylor Ranch (XTA), including XMD, XVA, and XPK. Two-creepmeter 2 to 5 km events are frequently observed in this region. But in September 2000, a large creep event was recorded at all five creepmeters (Figure 2.13a). Such closely timed slip at these creepmeters seems unlikely to be a coincidence or rainfall-induced; the September event was preceded by 104 days without rainfall. However, we only observe this 10 km XMM to XTA events once, suggesting such events are rare; 70% confidence intervals suggest that 0 to 1.2% of XMM events are observed

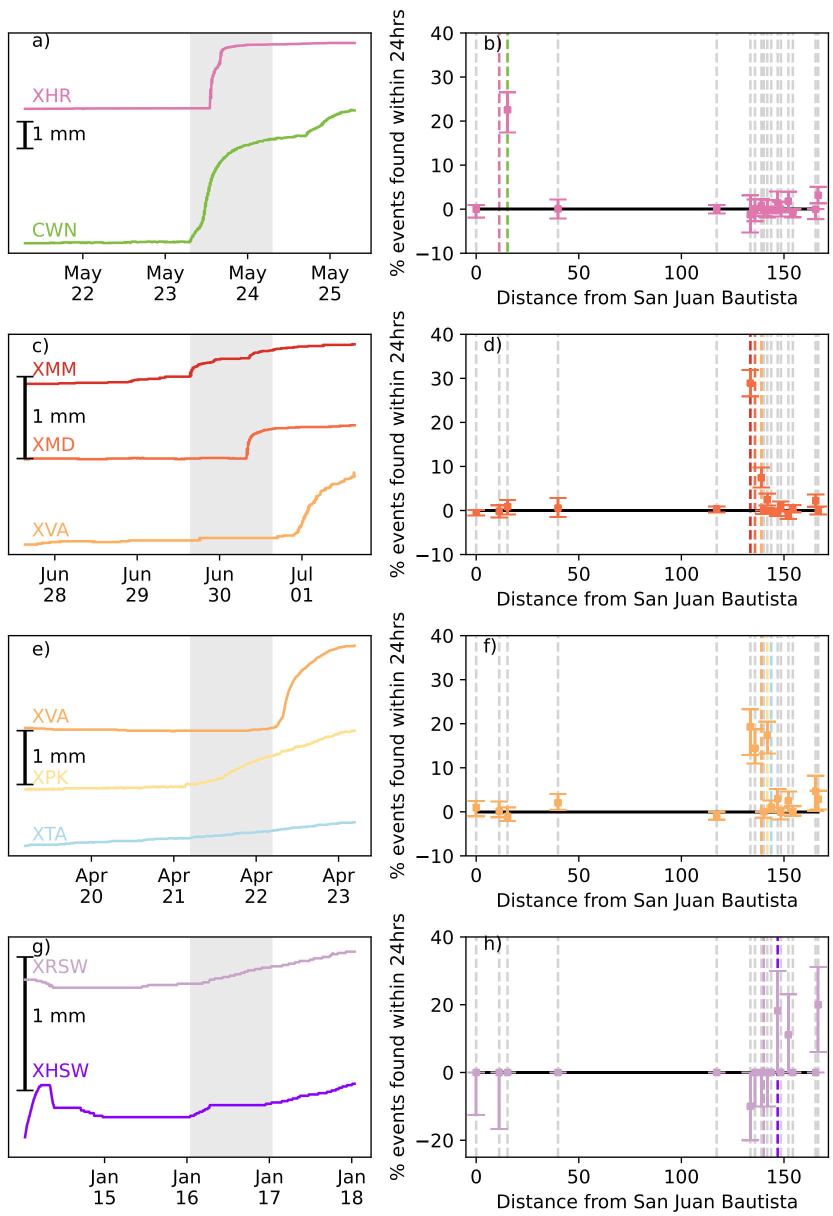

Figure 2.12: Medium-sized creep events from the XHR - CWN, XMM - XVA, XVA - XTA areas and the Southwest trace (XRSW - XHSW) and percentage of events observed at other creepmeters for XHR, XMD, XVA, and XRSW. a) Creep event at XHR and CWN on 11th–12th February 1994. c) Creep event at XMM, XMD and XVA on 29th–30th June 2014. e) Creep event at XVA, XPK and XTA on 21st–22st April 2008. g) Creep event at XRSW and XHSW on 16th January 1993. b), d), f), and h) indicate the percentage of XHR, XMD, XVA, and XRSW events found at other creepmeters, with 70% confidence intervals. Vertical coloured lines in b), d), f), and h) mark the location of the creepmeters in a), c), e) and g) respectively.

at XTA, and 0 to 15.3% of XTA events are observed at XTA.

The 8.2 km-long XMM to Parkfield (XPK) section ruptures more frequently. 70% confidence intervals for this section suggest that 1.2 to 3.1% of XMM events are observed at XPK, and 5.1 to 14.6% of XPK events observed at XMM (Figure 2.13b). Some of the closely timed events could be induced by rainfall, however. When creep events with rainfall in the 7 days prior are removed, 0.4 to 3.8% of XMM events are observed at XPK, and 3.9 to 18.4% of XPK events are observed at XMM. Moreover, if events with rainfall in the 14 days prior are removed, the relationship between XMM and XPK has at least a 15% chance of being explained by atmospheric perturbations.

Assuming that the closely timed slip at XMM and XPK do reflect 8 km-long creep events, it is interesting to note that even when creep events appear to rupture from XMM to XPK, they sometimes do not appear at the creepmeters in the middle (XMD and XVA). The lack of intermediate surface rupture suggests that the creep events commonly rupture at depth and sometimes do not reach the surface.

2.5.4.2 Potential 31 km Events: Slacks Canyon (XSC) - Work Ranch (WKR)

Some of the largest creep events that we seem to observe are those that propagate between Slacks Canyon (XSC) and Work Ranch (WKR), an along-strike distance of 31.2 km. 70% confidence intervals suggest that 15.8 to 27.0% of creep events observed at XSC are observed at WKR, and 10.2 to 19.6% of WKR events are observed at XSC (Figure 2.13d). These potentially long events are also observed at some of the creepmeters between them but not at all of the intermediate creepmeters. For instance, in Figure 2.13c, we have not plotted slip at XMD, XVA, and XTA because they displayed no creep event. Further, the percentage of XSC events observed at XMM and XPK is lower than the percentage of XSC events observed at WKR (Figure 2.13d).

We note, however, that much of the WKR-XSC correlation could be due to rainfall. If we remove events preceded by a 7-day interval with rainfall, 0.0 to 15.5% of XSC events are observed at WKR, and 0.0 to 13.0% of WKR events are observed at

XSC. Those percentages imply a 15% chance that the closely timed events result from hydrological forcing. If events with rainfall in the 14 days prior are removed, there are no closely timed events at XSC and WKR. Further, both XSC and WKR show a strong seasonal signal (Roeloffs, 2001); all of the closely timed creep events between these stations occur between December and March, showing a strong seasonal signal for these long events. Given both XSC and WKR prefer to slip in wet conditions (Figure A.29), one might expect that these potential long events may instead be small local events that occurred at similar times due to atmospheric perturbations and rainfall.

2.5.5 Multi-strand Ruptures?

The coincidence of creep events on creepmeters separated by 8 km or perhaps even 30 km suggests that widely separated fault locations can communicate with each other on 24-hour timescales. However, the last set of closely timed creep events we examine suggests that creep event slip may spread not just over 8 km distances but also over multiple strands of the San Andreas Fault.

The two instrumented strands of interest are at the southern end of the creeping section, from Varian (XVA) to Carr Ranch (CRR). The main San Andreas Fault has creepmeters installed at Varian (XVA), Parkfield (XPK), Taylor Ranch (XTA), Work Ranch (WKR), and Carr Ranch (CRR). The southwest trace has two creepmeters, one at Roberson Southwest (XRSW) and another at Hearst Southwest (XHSW). We will focus on correlations with XHSW here because XRSW has too few events to allow robust statistics.

2.5.5.1 Hearst Southwest (XHSW) and the Main San Andreas Fault Creepmeters

Events at XHSW, on the southwest trace, display several creep events that are coincident with events on the main fault trace. 70% confidence intervals that suggest XHSW events are observed at many different creepmeters: Slacks Canyon (XSC) observes 2.7

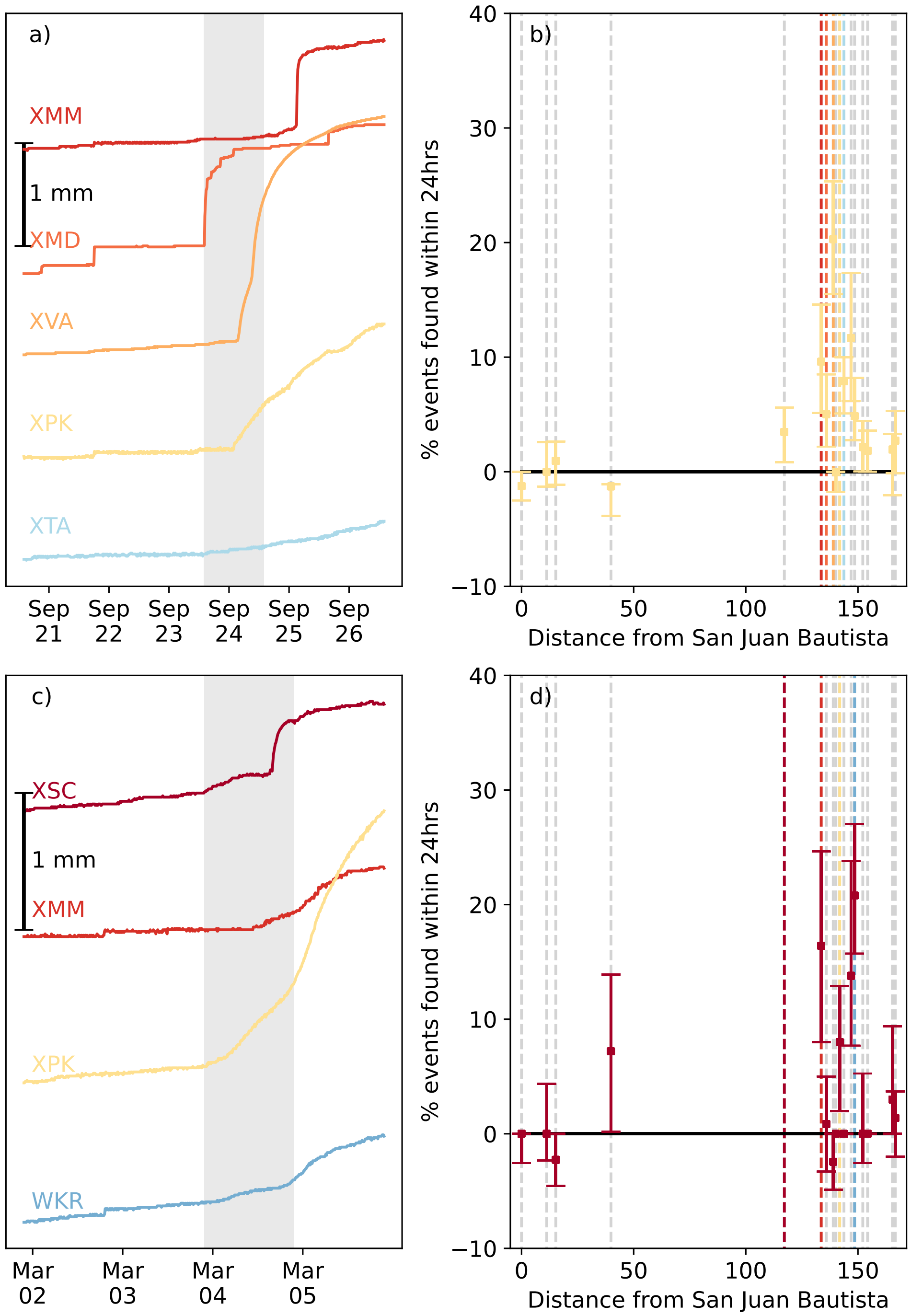

Figure 2.13: Potential large creep events from XSC - WKR section and percentage of events observed at other creepmeters for XPK and XSC. a) Creep event on the XMM - XTA section on 23st–25th September 2000. c) Creep event along the XSC - WKR section on 3st–4th March 1991. b) and d) indicate the percentage of XPK and XSC events found at other creepmeters, with 70% confidence intervals. Vertical coloured lines in b) and d) mark the location of the creepmeters in a) and c).

to 13.3% of XHSW events, Middle Mountain (XMM) observed 23.7 to 45.2% of XHSW events, Varian (XVA) observes 0.2 to 12.0% of XHSW events, Parkfield (XPK) observes 11.9 to 31.7% of XHSW events; Work Ranch (WKR) observes 13.4 to 25.9% of XHSW events; and Carr Ranch (CRR) observes 0.3 to 11.4% of XHSW events (Figure 2.14a).

Some of these percentages decrease to zero when we remove creep events preceded by rainfall. The correlations between XHSW, XVA and XPK could simply reflect a similar preference for slipping in wet conditions (Figures A.31-A.32). However, other correlations remain even when rainy intervals are removed (Figure 2.14b). XSC, XMM, WKR, and CRR all show evidence for coincident creep events, with XSC observing 0.0 to 27.3% of XHSW events, XMM observing 16.7 to 66.7% of XHSW events, WKR observing 16.7 to 50.0% of XHSW events, and CRR observing 0.0 to 44.4% of XHSW events. Both the XHSW at XSC and XHSW at CRR percentages intersect 0%, suggesting that their relationship may be arising by chance despite not being driven by rainfall. XMM and WKR still observe a percentage of creep events from XHSW that is significant. WKR and XHSW are 2.12 km apart and are the closest creepmeters from each strand to one another. Their relationship remains even after rainfall effects are considered, implying that there might be an interaction between the two strands of the San Andreas Fault in this region, which appear to connect at >6 km depth (Waldhauser and Schaff, 2008; NCEDC, 2014).

2.6 Short-term Rainfall Influence on Creep Events

The main goal of this study was to catalogue creep events to identify creep event behaviours described in Section 2.5 — to determine if creep events routinely rupture several or tens of km along strike. To do so, we examined the percentage of closely timed events at various pairs of creepmeters.

We compared our percentages with those expected for randomly timed creep events in a way that preserved any seasonality in the creep event records. However, creepmeters and creep events can also be triggered by hydrological variations on shorter timescales

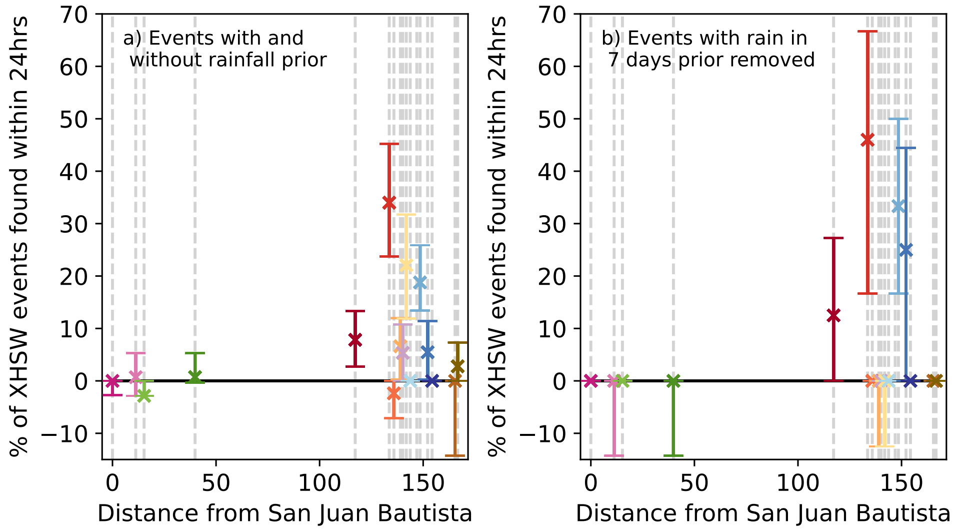

Figure 2.14: Scatter plots of the median percentage of creep events found at XHSW. In panel (a), all XHSW events are included. In panel (b), XHSW events with rainfall in the 7 days prior are removed.

(Roeloffs, 2001; Schulz, 1989). To assess whether the closely timed events observed at relatively distant creepmeters come from long along-strike ruptures or from a coincident response to rainfall, we redid our analysis after excluding creep events preceded by 3-, 7-, or 14-day intervals that included rainfall. We summarised the implications of those results for inferring creep event sizes in Section 2.5. However, a more thorough investigation of rainfall responses could teach us more about creep event behaviours. We do not attempt a thorough investigation here, but we briefly discuss why excluding rainfall could leave inter-creepmeter correlations in creep event timing decreased, unchanged, or increased.

2.6.1 Percentage of Correlated Events Decreases

For some creepmeter pairings, the percentage of closely timed creep decreases when we remove events preceded by rainy intervals. Figure 2.15a shows this effect for the XSC and WKR pair. Both creepmeters are seasonally modulated, with more events in the winter months (Roeloffs, 2001). When we preserve this seasonality but randomise times on shorter timescales (see Section 2.4.2), we can assess the local creep events' preference for rainfall, and we find that both creepmeters display more events in wet conditions (Figure A.29).

When two creepmeters have a common response to rainfall, we expect that some closely timed events coincide because they both respond to rainfall, not because a larger creep event connects the creepmeters. By removing times preceded by rainfall, we remove the largest amplitude forcing and expect a reduction in the correlated response. For the XSC-WKR pair, the reduction is significant. When we remove events with rainfall in the 7 days prior, the lower bound of the 70% confidence interval is 0. There is a 15% chance that none of the closely timed creep events reflect spatially expansive creep events. All of them could be coincidental responses to hydrological perturbations.

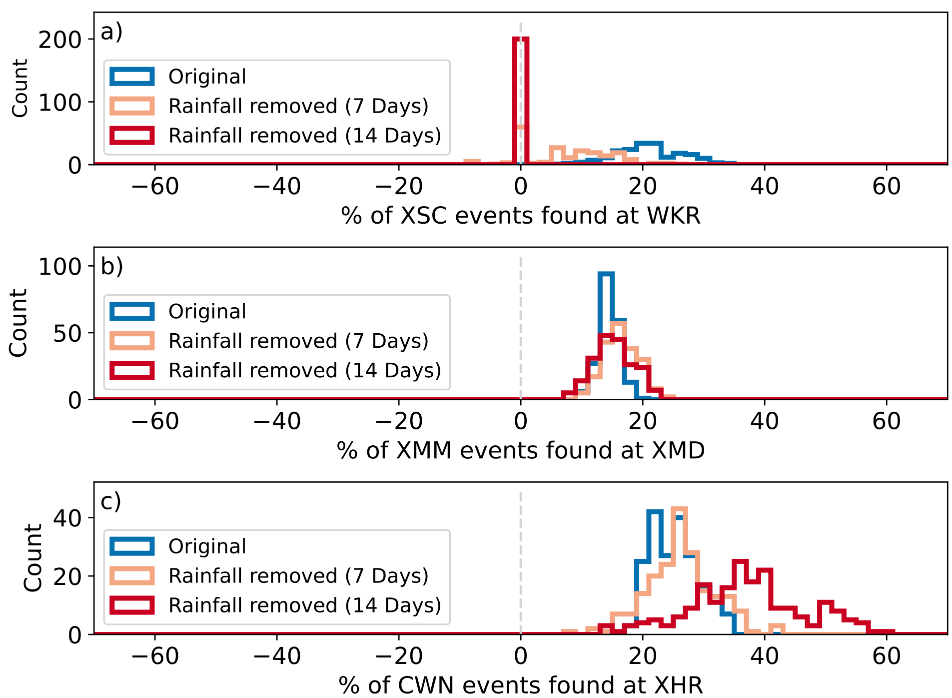

Figure 2.15: Percentage of creep events observed at pairs of creepmeters accounting for rainfall. a) Percentage of XSC events observed at WKR. b) Percentage of XMM events observed at XMD. c) Percentage of CWN events observed at XHR. In a), b), and c), the original percentages are in blue, and the percentage of events after accounting for rainfall in the previous 7- or 14-days are orange and red, respectively.

2.6.2 Percentage of Correlated Events Remains Unchanged

Intriguingly, however, we most commonly find that the percentage of closely timed events remains unchanged when we remove rainy intervals. The median percentage for the XMM-XMD pair, for instance, remains around 14.5%, increasing marginally to 15.9%, as we remove intervals with rainfall(Figure 2.15b). The lack of change in closely spaced events implies that the creep events respond minimally to short-timescale variations in rainfall or that the responses are uncorrelated at the two creepmeters. While it seems somewhat surprising that short-timescale rainfall responses are commonly uncorrelated between creepmeter locations, it makes many interpretations simple. Since the closely timed creep events are unaffected by rainfall, the correlations must be driven by something else, most likely slip at depth.

2.6.3 Percentage of Correlated Events Increases

However, for one creepmeter pair (XHR-CWN), we find a more dramatic *increase* in the percentage of closely timed events, from 25 to 40%, when we remove events preceded by a 14-day interval that includes rainfall(Figure 2.15c). The significant percentage change observed when rainfall events are removed from the XHR and CWN events suggests that small single-creepmeter events respond differently to rainfall than larger, multi-creepmeter events. Mortensen et al. (1977) noted that short and shallow creep events occurred at CWN, and longer and deeper creep events would rupture both CWN and XHR. Perhaps the small, shallow events at XHR and CWN are often triggered by rain, and by removing these small events when we remove rainy intervals, we retain only the deeper creep events that span both creepmeters.

2.7 Discussion

We have identified over 2000 long and short creep events along the San Andreas Fault using cross-correlation, slip thresholding, and manual inspection. The catalogue reveals a variety of creep event behaviours. Some creep events are observed only at individual creepmeters, while others appear to rupture to neighbouring creepmeters. Most of the multi-creepmeter events appear independent of rainfall; evidence for 2, 5 and 10 km long creep events remains robust when rainfall influences are excluded.

2.7.1 What Drives Creep Events?

Since the discovery of creep events in the 1960s, several mechanisms have been proposed to drive creep events. Here, we discuss different models for the driving of creep events and discuss their plausibility in light of our observed rupture lengths.

Perturbations by rainfall are often thought of as a driving mechanism for creep events through the close association between rainfall and creep (Roeloffs, 2001; Schulz et al., 1983). Creep events could arise on a stable slip-rate strengthening fault that has been 'kicked by a rainfall perturbation (Helmstetter and Shaw, 2009; Kanu and Johnson, 2011; Perfettini and Ampuero, 2008). Examples of rainfall-triggered events occur at XSC and WKR, both of which are seasonally modulated (Roeloffs, 2001). Most of the kilometre-long events observed, however, appear indifferent to rainfall, with the relationship between some creepmeters even strengthening when rainfall is removed (XHR — CWN). Therefore, it seems hard to explain how small, near-surface stress perturbations would drive creep events that are more than 5 km long. On the other hand, groundwater-driven perturbations could occur later than rainfall, and the fault could accelerate with a time lag, so a lack of timing with rainfall does not exclude this perturbed rate-strengthening model.

Having established that rainfall perturbations are not driving all observed creep events, we must consider other driving mechanisms for creep events. To fully assess these driving mechanisms would require information about the depths that creep events occur, which is difficult to determine from creepmeters alone, requiring data from other sources (e.g., strainmeters or tiltmeters). Therefore, we only briefly discuss possible driving mechanisms for creep events and the criteria that our observations provide when assessing these different models.

Given that our observed longer multi-creepmeter events are unlikely to respond to rainfall stress perturbations in the shallow crust, it would seem plausible to consider creep events being driven by frictional weakening of the fault, which drives accelerating albeit aseismic slip. Creep events can be created by patches or layers of slip-rate weakening material that have a particular size, which is large enough to accelerate into creep events but too small to grow into a seismic rupture (Liu and Rice, 2005, 2007; Rubin, 2008; Wei et al., 2013). Such layered rheologies could help explain some of the kinematics and size distribution of creep events (Bilham and Behr, 1992; Bilham et al., 2016; Gladwin et al., 1994), including the tendency of some creep events to skip creepmeters, as observed in events that rupture between XMM - XTA. Such events may rupture continuously at depth but discontinuously along the surface. They may not rupture all surface locations because the fault locally has low stress or a stable rheology (e.g., Luo and Ampuero, 2018).

Models of creep events based on rate-weakening patches do have one major issue: tuning. The patches of rate-weakening material must be close enough together to allow aseismic rupture propagation but far enough apart to prevent dynamic rupture (Ando et al., 2010; Luo and Ampuero, 2018; Rubin, 2008; Skarbek et al., 2012; Yabe and Ide, 2017). Our observations provide one more constraint on the patch tuning; creep events must be able to rupture 1 km regions in some instances and to expand 5 or 10 km along strike in other instances.

Given the apparent tuning issues involved in heterogeneity, one might prefer to explain creep events using a different fault zone process: something that promotes initial acceleration but eventually limits slip speeds at a local scale, such as shear-induced fault dilatancy and pore pressure changes (Iverson, 2005; Segall and Rice, 1995; Segall et al., 2010). Some limited support for dilatancy comes from an indication that pore pressure changes during creep events; the well water level rises or falls during creep events between Middle Mountain (XMM) and Middle Ridge (XMD) (Roeloffs et al., 1989; Rudnicki et al., 1993). However, as rainfall does not trigger or preclude many of our events, dilatancy might not be important to consider, as rainfall cannot be providing the pore pressure feedback for dilatant stabilisation.

2.7.2 Moment Accommodated by Creep Events?

Though we cannot directly constrain the depth of slip using creepmeter data, the skipped creepmeters noted in Section 2.7.1, along with the relatively large along-strike extents of some events, suggest that creep events could extend to significant depth—to depths of kilometres to rather than 100s of meters. And if creep events extend to significant depth (perhaps up to 6 km in the case of the parallel fault traces that connect at depth near Parkfield), they could have significant moment. Groups of creep events might modulate the moment budget of the San Andreas Fault on decadal or centennial timescales.

Such modulation is interesting to consider because geodetic and repeating earthquake observations have been used to observe variations in the faults' creep rate, with some suggesting this variation occurs on decadal timescales. (Khoshmanesh et al., 2015; Khoshmanesh and Shirzaei, 2018a,b; Nadeau and McEvilly, 2004; Sammis et al., 2016; Templeton et al., 2009). Further, large creep events have been reported on the San Andreas Fault and elsewhere (Linde et al., 1996; Martínez-Garzón et al., 2019; Roeloffs, 2001). And a few creepmeters display differently shaped, longer creep events. While most of the creepmeters we examined accumulate 50 to 75% of their slip in the small creep events examined here, creepmeters XSC and XTA creepmeters accumulate only 5 to 10% of their slip in small events. Much of the remaining slip accumulates in longer surges of slip, which have an indistinct onset but last weeks to months.

Current geodetic estimates suggest the San Andreas Fault's central creeping section is currently slipping slightly more slowly ($\approx$ 30 mmyr^{-1}) than its long-term rate (33 mmyr^{-1}) below the seismogenic zone (Ryder and Bürgmann, 2008). The low slip rate could lead to a M_w 5.2 – 7.2 earthquake every 150 (Maurer and Johnson, 2014; Michel et al., 2018; Ryder and Bürgmann, 2008). Such a large earthquake along the creeping section would be possible through dynamic weakening (Noda and Lapusta, 2013) yet no major (M $\geq$ 7) earthquake has ever been reported along the entire length of the creeping section (Toppozada et al., 2002) so it seems unlikely that this will be the mechanism to release this moment deficit. Alternatively, if creep events play an important role in reducing the creeping region's slip deficit, the low slip rate could lead to a cluster of 30 $M_w 4$ creep events rather than a $M_w 5$ earthquake. To give that moment context, $M_w 4$ creep event could be a 4 km long, 4 km deep event with 2 mm of slip. A 4 km long, 1 km deep event with 2 mm would have a moment equivalent to a M_w 3.6 earthquake.

We note, of course, that estimating the possible moments of creep events does not tell us whether clusters of tens or hundreds of creep events can occur. To assess the plausible variability of creep events, we would need to better understand the driving physics (Section 2.7.1). These physics may eventually help us assess whether creeping regions can also rupture in earthquakes and pose a seismic hazard (e.g., Harris, 2017). Many creeping faults appear to be barriers to seismic propagation (e.g., Nocquet et al., 2017; Ryder and Bürgmann, 2008; Thomas et al., 2014; Titus, 2006)), but laboratory-based faults often display strong weakening at ms^{-1} slip rates, and that dynamic weakening could allow a normally creeping region to rupture in an earthquake (Noda and Lapusta, 2013).

2.8 Conclusion

In this study, we have identified and correlated 2120 creep events recorded on creepmeters along the creeping section of the San Andreas Fault between 1985 and 2020. Some of these creep event detections occur simultaneously at two or more creepmeters; we identify 306 potential events that could rupture multiple creepmeters. Our analysis allows us to identify five groups of creep events: (1) isolated events, (2) small (<2km) events, (3) medium-sized (3-6 km) events, (4) large events (>10 km), and (5) events that rupture multiple strands. The vast majority of these events are not affected by rainfall.

Correlations between creepmeters persist when rainfall influences are excluded. The length of the creep events observed helps us assess the plausibility of different driving models for creep events; local frictional weakening, perhaps with a complex rheology, seems most possible. The creep event lengths, when coupled with the kinematics of slip at various creepmeters, also suggest that creep events rupture both at the surface and at depth. Determining the depth of this slip, and thus of creep events, is an essential next step in understanding the role of creep events in the overall slip dynamics of the creeping section.

3

Are Creep Events Big 2? Estimations of Rupture Location, Depth, and Magnitude

3.1 Introduction 93
3.2 Data 95
3.2.1 Processing and correcting the strainmeter data 97
3.3 Identifying strain offsets associated with creep events 98
3.4 Identifying the location and magnitude of slip 100
3.4.1 Forward model 100
3.4.2 Matching the observed strain data 101
3.4.3 Location of the slip creating creep-event associated strain offsets 105
3.4.4 Propagation of the slip creating creep-event associated strain offsets 111
3.4.5 Depth of the slip creating creep-event associated strain offsets . 111
3.4.6 Magnitude of the slip creating creep-event associated strain offsets 114
3.5 Discussion 115
3.5.1 How many locations produce creep events? 116
3.5.2 What are the implications of patches at depth? 116
3.5.3 What is the role of creep events in accommodating the moment budget of the region? 117
3.6 Conclusion 119

Abstract

We have observed aseismic creep events along the creeping section of the San Andreas Fault since the 1960s. Despite this, we do not know how they grow spatially or how much moment they release. To address this uncertainty, we identify strain offsets associated with creep events and estimate the location, depth, and magnitude of a slip patch producing them. We first identify 71 strain offsets associated with creep events at the northern end of the creeping section of the San Andreas Fault. We then grid search for slip locations and magnitudes by modelling rectangular slip patches in a homogeneous elastic half-space. Using these grid search results, we identify the location, depth, and magnitude of slip that caused these strain offsets. We find that creep events do not originate from the same place; instead, they are produced by a range of along-strike locations at depths typically greater than 4 km. We also find that the magnitude of the slip creating the observed strain offsets is generally between M_w 3–4. These findings suggest that creep events are not small shallow events but larger events that begin at significant depths and can potentially play a prominent role in the slip dynamics of the creeping section.

Plain language summary

We have observed bursts of slip, or creep events, along the creeping section of the San Andreas Fault since the 1960s. Despite this, we still need to learn how they grow spatially or how much energy they release. We identify strain offsets associated with creep events and estimate where the fault has slipped to produce these strain offsets and the event's magnitude. We identify 71 strain offsets associated with creep events at the northern end of the creeping section of the San Andreas Fault. We then grid search for the slip locations that cause the observed strain offsets and estimate their magnitude. We find a range of along-strike locations where slip occurs, most of which are below 4 km and have a magnitude of 3–4. These findings suggest that creep events are much larger and deeper than previous estimates and may play an important role in the slip dynamics of the creeping section of the San Andreas Fault.

3.1 Introduction

The northern end of the creeping section of the San Andreas Fault (Figure 3.1), near San Juan Bautista, CA, was one of the first places where aseismic slip was observed (Steinbrugge and Zacher, 1960; Tocher, 1960; Whitten and Claire, 1960). The fault here slips in bursts known as creep events, with a small amount of stable, steady background creep between events (e.g., Gittins and Hawthorne, 2022a; Gladwin et al., 1994; Nason et al., 1974; Schulz, 1989). In each creep event, the fault slips a few millimetres over several hours to days (Figure 3.2 d), e) & f)). Creep events here have a recurrence time of a few weeks to months (e.g., Gittins and Hawthorne, 2022a; Nason et al., 1974; Schulz, 1989).

Despite these small displacements, creep events along the San Andreas Fault can span large distances, often extending several kilometres along strike (e.g., Gittins and Hawthorne, 2022a; Mortensen et al., 1977). However, those along-strike extents are based primarily on observations of surface slip. What happens at depth remains a mystery. For instance, some models suggest that creep events represent repeated slip at a single shallow location (e.g., Gladwin et al., 1994; Goulty and Gilman, 1978; Mchugh and Johnston, 1976). Alternatively, other models suggest that the location of slip varies from event to event (e.g., Evans et al., 1981; Mortensen et al., 1977). Each of these scenarios has a different implication for the rupture dynamics of creep events, especially when considering creep events have been known to have more than one phase of slip (e.g., Schulz, 1989) as shown in Figure 3.2 d), e) & f). Whether each slip phase in the creep event represents slip in one or multiple locations remains ambiguous.

Creep events accommodate >50 % of the surface slip along the San Andreas Fault (Gittins and Hawthorne, 2022a). However, we do not know how much creep events slip at depth. Suppose creep events accommodate a significant amount of slip. In that

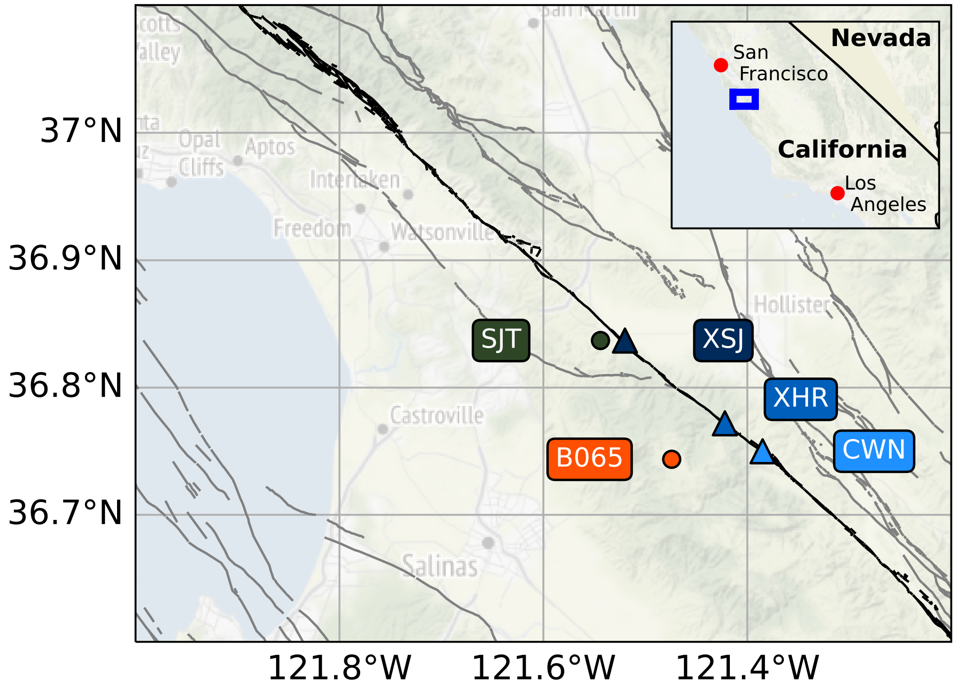

Figure 3.1: Map of the northern end of the creeping section of the San Andreas Fault (black). Other faults in central California are shown in grey. The USGS creepmeters are coloured triangles (XSJ: dark blue, XHR: medium blue, CWN: light blue), and the USGS (green) and PBO (orange) strainmeters are coloured circles. Faults plotted are from the USGS/California Geological Survey Quaternary Faults and Folds database (USGS and CGS, 2020).

case, they may play a key role in reducing the moment deficit of the San Andreas Fault that arises from the difference between the shallow creep rate ($\approx$ 30 mmyr^{-1}) and the long-term slip rate (33 mmyr^{-1}) below the seismogenic zone. Current estimates of this moment deficit suggest it is equivalent to a M_w 5.2–7.2 earthquake on average every 150 years (Maurer and Johnson, 2014; Michel et al., 2018; Ryder and Bürgmann, 2008). A burst of creep events could reduce some of this moment deficit (Khoshmanesh and Shirzaei, 2018b), yet a burst of M_w 1.0 events would do far less to reduce the deficit than a burst of M_w 4.0 events.

Therefore, a lack of a clear understanding of where creep events occur, how they grow spatially, and how much moment they release leaves us unable to adequately evaluate the role of creep events in the slip dynamics of the creeping section of the San Andreas Fault.

Using data from two strainmeters and three creepmeters, we investigate the spatiotemporal evolution of creep events at the northern end of the creeping section of the San Andreas Fault and estimate their magnitude. We process strainmeter data in Section 3.2, identify 71 strain offsets created by short bursts of slip within longer creep events in Section 3.3, and determine the location and magnitude of the slip creating these strain offsets in Section 3.4. We find that the slip creating the observed strain offsets originate from a range of along strike locations at depths below 4 km with a M_w between M_w 3–4. Finally, in Section 3.5, we discuss the implications of these results for the dynamics of creep events and the San Andreas Fault as a whole.

3.2 Data

We focus on creep events recorded between 2009 and 2019 on the USGS creepmeters at Harris Ranch (XHR) and Cienega Winery (CWN), located at the northern end of the creeping section of the San Andreas Fault (Figure 3.1). Here, we combine the creep event observations from XHR and CWN with data from two borehole strainmeters: B065, a nearby PBO instrument, and SJT, a USGS instrument 11 km north, near San Juan Bautista. We also use data from a third creepmeter near San Juan Bautista (XSJ) to validate our grid search results (see Section 3.4.3.6 for details). Figure 3.2 shows data from three creep events as recorded on the strainmeters (top panels) and the creepmeters (bottom panels). These instruments allow us to investigate the depth, horizontal location, and magnitude of slip during creep events.

The creepmeters XSJ, XHR, and CWN all have the same sampling rate of one sample per 10 minutes. Each creepmeter has a different operating duration. The most recent iteration of XSJ operated between 2007 and 2016, while the most recent iteration of XHR and CWN have operated since 2009 and 1991, respectively.

The two strainmeters have different sampling intervals. SJT, which operated from 1983 to 2016, has a sampling frequency of 18 minutes, whereas the B065, operating since 2007, can record 20 samples per second. Here, we use the resampled 10-minute

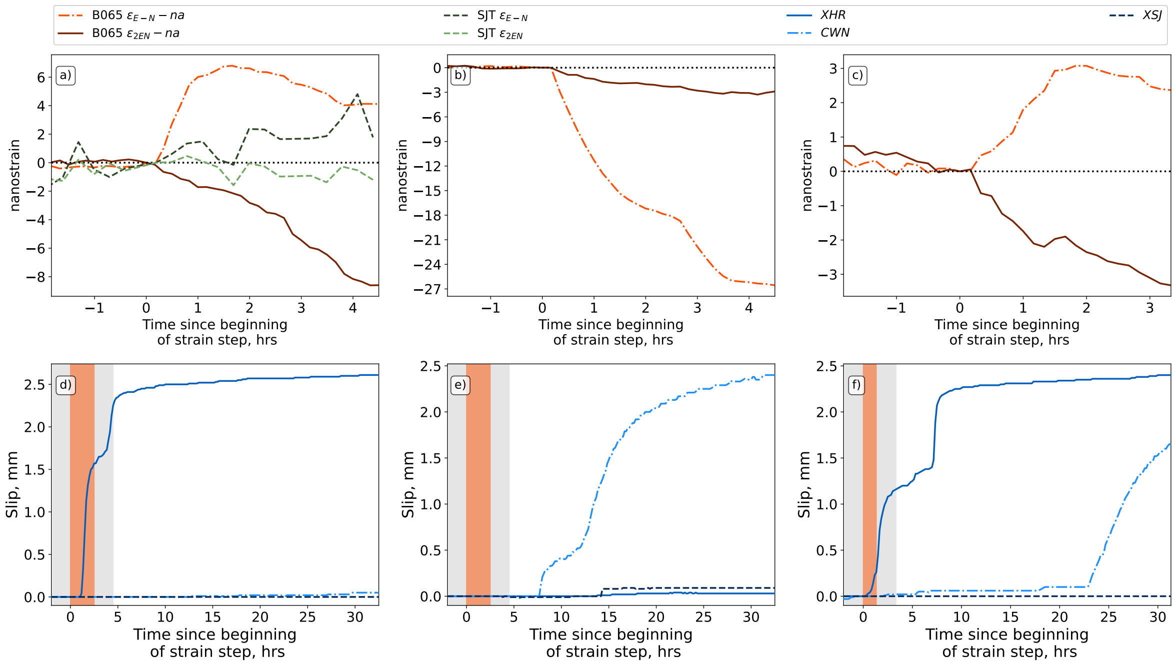

Figure 3.2: Strain offsets associated with creep events. a) & d) XHR082, b) & e) CWN080 and c) & f) XHR084. In a) to c), the orange and brown lines represent the ϵ_{E-N}-na and ϵ_{2EN}-na components at B065, respectively. The dark green and medium green lines represent the ϵ_{E-N} and ϵ_{2EN} components at SJT when it was operational. In d) to f), creep records from XSJ (dark blue dashed line), XHR (medium blue solid line), and CWN (light blue dot-dashed line) are plotted. The grey vertical bar represents the time shown in the corresponding panel above for the strain offset, with the orange vertical bar representing the duration and timing of the associated strain offset.

B065 data. Both instruments can detect nanostrain variations in strain, but B065 has a slightly better instrument resolution with fewer data gaps (Gladwin, 1984; Gladwin et al., 1987; Hodgkinson et al., 2013; Roeloffs, 2010).

Although the selection of instruments available leads to only a few spatial data points, these instruments provide time-series data with a temporal resolution much higher than other instruments used to monitor fault creep (i.e., InSAR). Therefore, they provide a unique opportunity to monitor bursts of slip on time scales of a few hours to days (Gittins and Hawthorne, 2022a; Gladwin et al., 1994; Schulz, 1989).

3.2.1 Processing and correcting the strainmeter data

We begin our strainmeter analysis by calibrating the data to horizontal strain; the strainmeter time series are recorded on four horizontal gauges, and we map these into the three components of horizontal strain using the calibration of Hodgkinson et al. (2013) for B065 and the calibration of J. Langbein and others at the USGS for the SJT. We thereby obtain three strain time series at each strainmeter: areal strain ϵ_{E+N}, differential extension ϵ_{E-N}, and engineering shear ϵ_{2EN}.

The sub-nanostrain resolution of the borehole strainmeters means they often record 'noise' from non-tectonic sources, such as borehole settling, tidal loading, and atmospheric pressure (Hodgkinson et al., 2013; Roeloffs, 2010). These signals dominate the record and make observing the typically very small strain offsets ($\leq$ 10 nanostrain, Figure 3.2) associated with creep events challenging. Therefore, we correct for these non-tectonic signals following the approach of Hawthorne et al. (2016a).

We use the corrected SJT strainmeter data from Hawthorne et al. (2016b). They removed the effects of tidal loading, atmospheric pressure, and a spurious 3-hour instrument signal. Hawthorne et al. (2016b) describes the processing of SJT in full detail.

To begin processing B065, we first estimate and remove the long-term exponential trend associated with the long-term settling of the borehole (Gladwin, 1984).

Next, we identify the strain components at B065 that respond minimally to loading by atmospheric pressure. These non-atmospheric components appear to have a smaller amount of hydrological noise (Hawthorne et al., 2016a) and are relatively close in orientation to the original three strain components. These new non-atmospheric components (denoted by the -na suffix) are a linear combination of ϵ_{E+N}, ϵ_{E-N} and ϵ_{2EN} such that:

$$\epsilon_{E-N}\text{-}na = 0.9526\epsilon_{E-N} - 0.0164\epsilon_{2EN} - 0.3037\epsilon_{E+N}, \tag{3.1}$$

$$\epsilon_{2EN}\text{-}na = 0.9987\epsilon_{2EN} - 0.0490\epsilon_{E+N} - 0.0157\epsilon_{E-N}. \tag{3.2}$$

Now that we have these non-atmospheric components, we remove the last non-tectonic signal: tidal loading. We fit a set of sinusoids to the remaining data with periods equivalent to the different tidal periods. We subsequently remove these from the data.

3.3 Identifying strain offsets associated with creep events

Having processed the strainmeter data to remove non-tectonic signals, we visually inspect the strainmeter data and find that there are often abrupt offsets in strain, which are associated with the timing of creep events (Figure 3.2). The strain offsets we find at B065 are typically small (few nanostrain) and last for a couple of hours (Figures 3.2 a) to c)). These offsets are caused by slip somewhere on the fault and may represent shorter bursts of slip within a larger creep event.

To better characterise the strain offsets we observe, we systematically search for strain offsets associated with creep events. We search in windows around the timing of surface creep events that span from 10 hours before the onset of the event to its end, based upon the event catalogue of Gittins and Hawthorne (2022a). By removing a long-term trend (based upon a linear trend from the previous seven days), the strain offsets we are searching for become deviations from zero or changes in the gradient of the strain record, making them easier to identify. We identify 92 potential strain offsets associated with creep events; however, we will only focus on the 71 clear offsets associated with 44 surface creep events. Sometimes, two or more strain offsets are associated with each creep event.

Figure 3.3 summarises the identified strain offsets. The strain offsets at B065 are typically $< \pm$ 10 nanostrain (Figure 3.3 a) & b)). These strain offsets are typically 1–3 hours in duration (Figure 3.3 c)) and occur predominantly in the 3 hours before the surface creep event recording (Figure 3.3 d)).

The magnitude of the strain offsets we observe are not the same, nor are their signs.

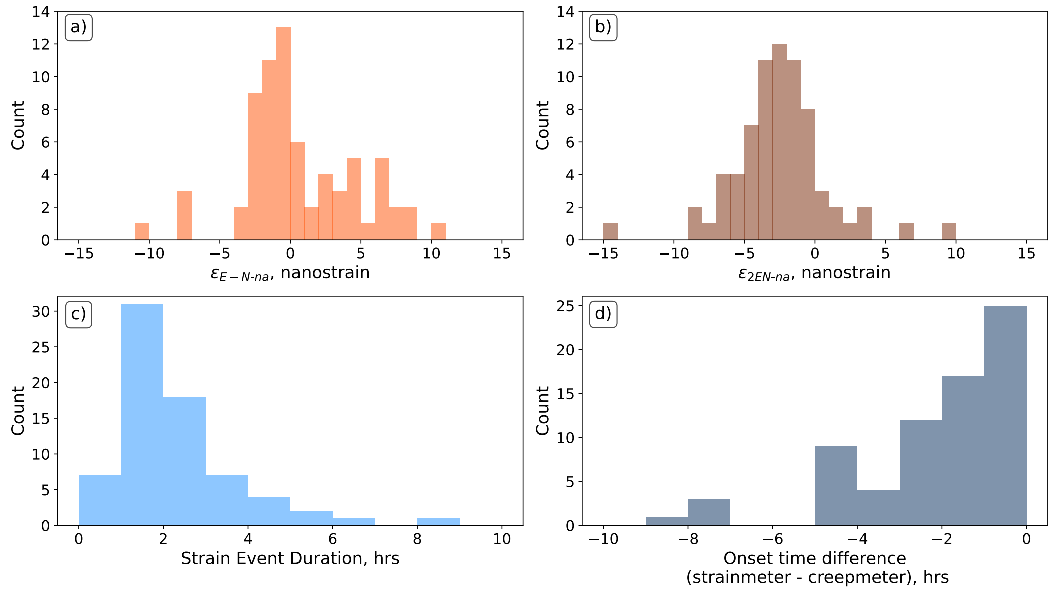

Figure 3.3: Histograms showing the size of the observed strain offsets on the non-atmospheric components of a) ϵ_{E-N}-na, and b) ϵ_{2EN}-na, as well as c) their duration and d) onset time difference to creep events recorded on creepmeters.

The size of a strain offset is controlled by the dimensions of the patch of fault that slipped, its depth (Figure B.1 a) to c)) and M_w (Figure B.1 d) to f)). The sign of the strain offset is predominantly controlled by the along-strike location of slip relative to the strainmeter (Figure B.1 g) to i)).

If these offsets were all produced by slip on the same patch of fault, we could have strain offsets of different sizes resulting from varying amounts of slip from creep event to creep event. Yet, we would expect the strain offsets to all have the same sign. Gladwin et al. (1994) observed this scenario for creep event-associated strain offsets on the SJT strainmeter in San Juan Bautista, 11 km north of our study region. Here, in the Harris Ranch - Cienega Winery region, we observe strain offsets of equal magnitude that are both positive and negative (Figure 3.3 a) & b)), so it seems likely that more than one location is producing these strain offsets.

3.4 Identifying the location and magnitude of slip

Having suggested that the different signs of the strain offsets we observe likely arise from distinct locations, we now try to identify these locations. Here, we describe the forward model we use to produce predicted strain offsets from various grid points. We then illustrate how we match these predicted offsets to the observed strain data.

3.4.1 Forward model

We need to reproduce the strain offsets observed to determine the region of the fault that slipped to create them. To do this, we perform a grid search varying depth, location, and M_w of a patch of slip, assuming the fault lies within a homogeneous elastic half-space (Okada, 1985, 1992; Thompson, 2015).

It should be noted that the grid search outputs strain in ϵ_{E+N}, ϵ_{E-N} and ϵ_{2EN}. As we observe strain in the non-atmospheric components, we use Equations 3.1 & 3.2 to convert between the grid search output components and the components we observe.

We calculate the strain offsets we would observe from slip on a range of patch locations. We assume these patches are square and have conducted the grid search on 500 m and 1000m squares, which show similar results. From this point, we focus on the results of the 500 m square patches.

We vary depth between 250 m and 9750 m at 500 m intervals. Figure 3.4 shows the strain offsets observed along the vertical depth cross-section for the ϵ_{E-N}-na (panel b)) and ϵ_{2EN}-na (panel e)) components of strain. Here, we can see that as the depth of the patch gets deeper, the amplitude of the strain offset decreases.

We also vary the along-strike location between 13 km north to 17 km south of XHR at 500 m intervals. Figure 3.4 shows how the strain offsets observed vary with different along-strike locations of slip for the ϵ_{E-N}-na (panel c)) and ϵ_{2EN}-na (panel f)) components of strain. By moving along the strike of the fault, we can change both the amplitude of the strain offset and, potentially more crucially, the sign of the strain offset.

We also change the fault's strike according to the along strike location. We use a strike of 126° between 13 km north and 7 km south of XHR, 133° between 7–10.3 km south of XHR, and 137° from 10.3 km south of XHR onwards.

In Figure 3.4 a) & d), we plot the Green's function of the different gird locations. This Green's function represents the strain change at the surface resulting from the displacement at point x0, a 500×500 m fault patch.

Using the strain offset sign, we identify regions of the fault where the slip patch may be located. For instance, if the strain offset we observe is negative, the slip patch should be within the unshaded region in Figure 3.4 a) or c), depending on which component you use. For example, the strain offset presented in Figure 3.4 has a negative offset on both components. Therefore, from Figure 3.4 a) and d), we can see that there are only two regions of the fault where both strain components are negative: the far north of the section or just to the south of XHR. The patch that slipped, therefore, is more likely to be located in one of those two regions over locations within the shaded positive regions. The contours in Figure 3.4 a) and d) illustrate how the Green's function evolves within the shaded and unshaded regions. If the strain offset is small, the slip location will be close to the boundary between the shaded and unshaded areas. Conversely, if the offset is large, the slip location will be closer to the inner contours.

We also vary magnitude between M_w 1–6, at $0.1M_w$ intervals. This range allows for the possibility that creep events are larger at depth than one would expect from just looking at the creepmeter recordings. Increasing the M_w of the patch increases the strain offset produced, with a major increase occurring above M_w 4.0 (Figure B.2).

3.4.2 Matching the observed strain data

To see which locations and M_w match the observed data the best, we need to assign each scenario in our grid search a probability based on how well it can reproduce the strain offset.

We first make simple estimates of accumulated strain during each strain offset by

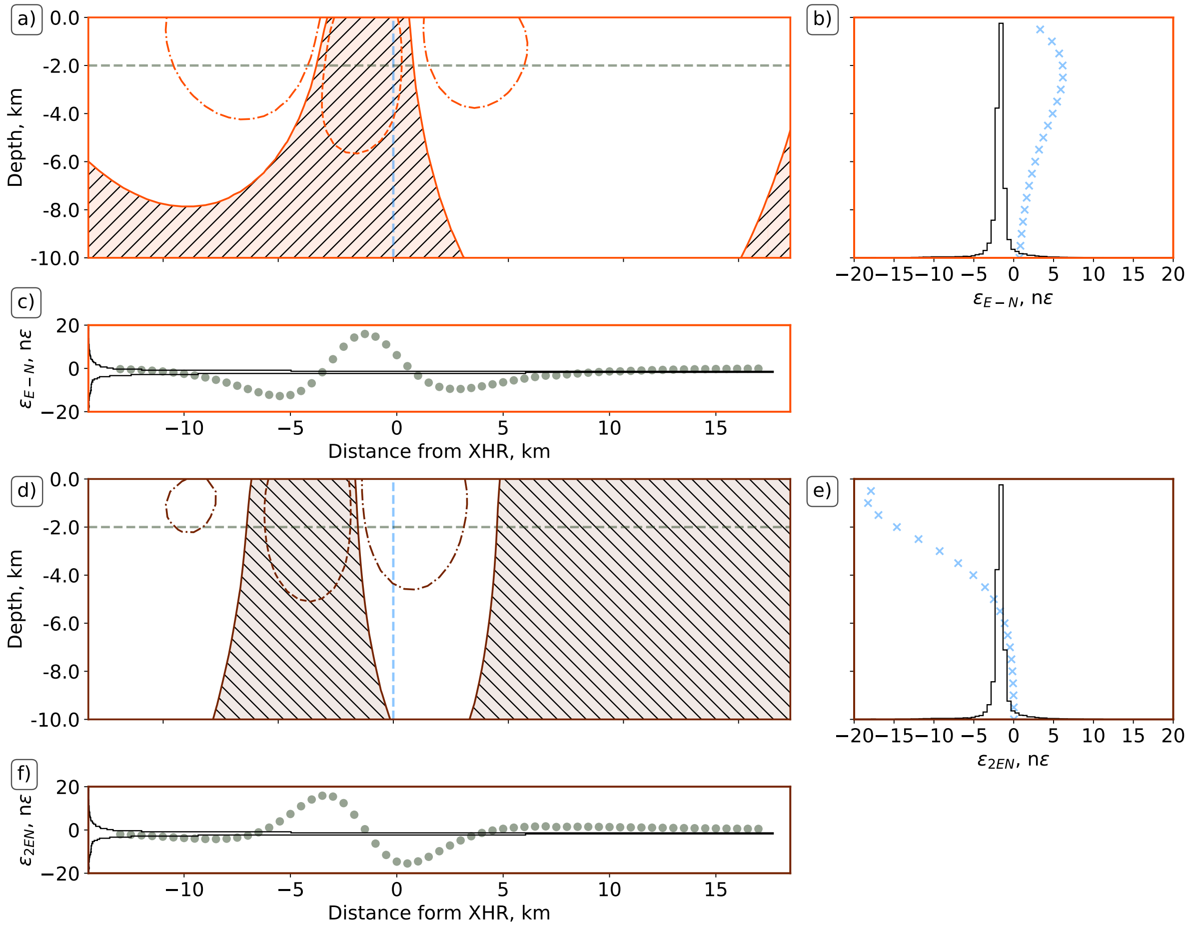

Figure 3.4: Green's functions of a) ϵ_{E-N}-na and d) ϵ_{2EN}-na components showing how strain changes at the surface as a result of displacements in different locations. The shaded region of panels a) & d) represent regions that produce positive strain offsets. In contrast, the unshaded represent the regions that produce a negative strain offset. The contours in both the shaded and unshaded regions illustrate how the strain offsets change within the regions, with locations further away from the boundary between shaded and unshaded having larger strain offsets. The vertical dashed blue line is the depth cross-section in b) or e). The horizontal dashed green line is the along-strike cross-section in c) & f). b) & e) show the effects of varying depth at one location (blue crosses) compared to the observed offset and associated uncertainty (black shifted histogram) for the ϵ_{E-N}-na and ϵ_{2EN}-na respectively. c) & f) show the effects of varying along-strike location at one depth (green circles) compared to the observed offset and associated uncertainty (black shifted histogram) for the ϵ_{E-N}-na and ϵ_{2EN}-na respectively.

subtracting the strain at the end of the identified offset from the strain at the beginning. Next, we calculate the uncertainties in these strain offsets. We compute the change in strain during 50,000 2-hour-long windows at random times during the strain time series. We add the distribution of random offsets to each observed offset to obtain probability distributions on the actual offsets (see black distribution in Figure 3.4 b), c), e) & f)). The uncertainties in the strain offset measurements are small. Of the 50,000 random strain offsets taken at B065, 70% lie between -0.63–0.59 nanostrains for the ϵ_{E-N}-na component and -0.75–0.49 nanostrains for the ϵ_{2EN}-na component. At SJT, 70% of the random strain offsets we calculate lie between -2.47–0.67 nanostrains for the ϵ_{E-N} component and -1.88–1.23 nanostrains for the ϵ_{2EN} component.

We normalise the distributions of uncertainty into a density function and use the difference between the observed and modelled strain offsets to assign each grid search scenario a probability. We assign a probability to each grid search scenario by multiplying the probability estimated for each component.

Changing the M_w of a particular patch makes certain locations more or less probable. This means specific locations on the fault have more than one probability, each based upon the M_w we assign it. We, therefore, select the scenario with the highest probability for each location.

Now that each part of the fault only has one grid search scenario, we plot the distribution of M_w and probability to identify the location of slip producing the observed strain offset.

3.4.2.1 Is it possible to use other geodetic instruments to study the slip bursts that create the observed strain offsets?

In this analysis, we do not use other types of geodetic data to constrain the depths of the slip bursts associated with creep events. InSAR and GNSS are often used to identify slip along the creeping section of the San Andreas Fault from the surface to several kilometres depth (e.g., Jolivet et al., 2015; Ryder and Bürgmann, 2008). However, they cannot identify slip bursts on the order of a millimetre, as is the case for creep events. InSAR also has a recurrence time that is too long to study bursts of slip that are only a few hours long.

Creepmeters sample creep at high temporal rates (every 10 minutes) with a resolution of 10^{-3}–10^{-2} mm. To use creepmeters to determine the depth of slip bursts, there would need to be slip at the surface associated with these deeper slip bursts. Say we consider a slip burst with a moment equivalent to a M_w 3.6 earthquake at 4 km depth directly below XHR. Considering $\epsilon = \frac{\Delta l}{l}$, where ϵ is strain along the creepmeter, Δl is the slip recorded on the creepmeter, and l is the length of the creepmeter, we can estimate the amount of slip that would be recorded at XHR. If we assume a homogeneous elastic half-space, we can estimate the strain that XHR would experience associated with the M_w 3.6 slip burts at 4 km depth directly below XHR (Okada, 1985, 1992; Thompson, 2015). The resulting strain we calculate will be in terms of ϵ_{E+N}, ϵ_{E-N} and ϵ_{2EN}. To convert the strain into the orientation of XHR, we need to rotate the strain field such that:

$$\epsilon_{XHR} = \epsilon_{EE} cos^2\alpha + 2\epsilon_{EN} sin\alpha cos\alpha + \epsilon_{NN} sin^2\alpha, \tag{3.3}$$

where

$$\epsilon_{EE} = \frac{\epsilon_{E+N} + \epsilon_{E-N}}{2}, \tag{3.4}$$

$$\epsilon_{NN} = \frac{\epsilon_{E+N} - \epsilon_{E-N}}{2} \tag{3.5}$$

(Jaeger et al., 2007). Here ϵ_{XHR} is the strain along the XHR creepmeter, ϵ_{E+N}, ϵ_{E-N} and ϵ_{2EN} are the areal, differential and engineering components of strain and α is the counterclockwise rotation to orient the east axis with the orientation of XHR which is installed at 22 ° to the fault strike of 126 °. Calculating ϵ_{XHR} and using $l = 30$ m (the length of XHR (Schulz, 1989)), we can estimate that the associated slip that XHR would record is $\approx 2 \times 10^{-4}$ mm. The estimated slip is below the resolution of XHR.

Creepmeters are also known to be noisy instruments, with white noise characterising the noise up to a period of 1 hr with random walk dominating at longer periods (Langbein et al., 1993; Langbein and Johnson, 1997). In reality, this means that any slip at the surface associated with slip at depth in the slip bursts that create the observed strain offsets would likely need to be an order of magnitude higher than the resolution of the creepmeters.

More work is required on processing other geodetic data and understanding how to incorporate them into constraining the depth of creep event-associated slip bursts. Therefore, we focus on the strainmeter observations as they appear to be the most viable dataset given our current processing techniques.

3.4.3 Location of the slip creating creep-event associated strain offsets

Here, we will discuss the range of possible along-strike locations based on the strain offsets' sign. For the rest of the analysis, we consider only locations between 7 km north and 12 km south of XHR, removing the region beneath XSJ for reasons explained in Section 3.4.3.6.

3.4.3.1 Positive offset on both components

The least common strain combination we observe is where both strain components are positive (Figure 3.5 b)). The patch of slip that produces these strain offsets lies in a narrow region about 3 km north of XHR that expands with depth (Figure 3.5 c)). Slip in this region only produces ≈ 4 % of the strain offsets.

3.4.3.2 Positive ϵ_{2EN}-na offset and a negative ϵ_{E-N}-na offset

The next least common strain combination we observe is a positive ϵ_{2EN}-na offset and a negative ϵ_{E-N}-na offset (Figure 3.6 b)) The patch of slip that produces these strain offsets lies either 5 km north of XHR or >5 km south of CWN (Figure 3.6 c)). Slip in these regions only produces ≈ 10 % of the strain offsets. While both regions are equally probable, we discriminate between them based on which creep event is associated with this strain offset, i.e., whether XHR or CWN records the creep event.

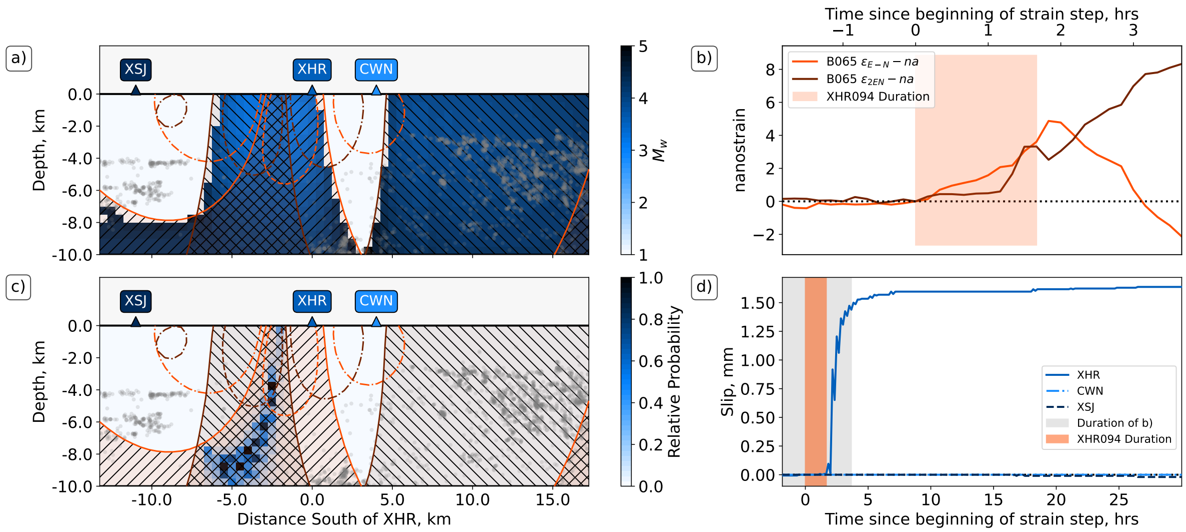

Figure 3.5: XHR094 observed at B065 and associated with a creep event at XHR. a) Magnitude of the best fitting scenarios for each 500×500m grid square. b) Strain records of B065 (ϵ_{E-N}-na orange line and ϵ_{2EN}-na brown line). The vertical orange bar shows the duration of the strain offset. c) Relative probability of the best fitting scenarios for each 500×500m grid square. d) Creepmeter record of XSJ (dark blue dashed line), XHR (medium blue solid line), and CWN (light blue dot-dashed line). The grey vertical bar represents the time shown in b), with the orange vertical bar representing the duration and timing of the associated strain offset. In a) & c), the grey dots are seismicity from the Northern California Earthquake Data Center catalogue (NCEDC, 2014), the brown and orange lines are contours of the Green's function of the ϵ_{2EN}-na and ϵ_{E-N}-na components of strain respectively. The hatching shows where the Green's function is positive.

3.4.3.3 Positive ϵ_{E-N}-na offset and negative ϵ_{2EN}-na offset

The second most common combination of strain we observe is a positive ϵ_{E-N}-na offset and a negative ϵ_{2EN}-na offset (Figure 3.7 b)). The patch of slip that produces these strain offsets is located in a narrow band just north of XHR that sweeps subtly southwards with depth (Figure 3.7 c)). Slip in this region produces ≈ 39 % of the strain offsets.

3.4.3.4 Negative offset on both components

The most common combination of strain offsets we observe is where both strain components are negative (Figure 3.8 b)). The patch of slip that produces these strain offsets

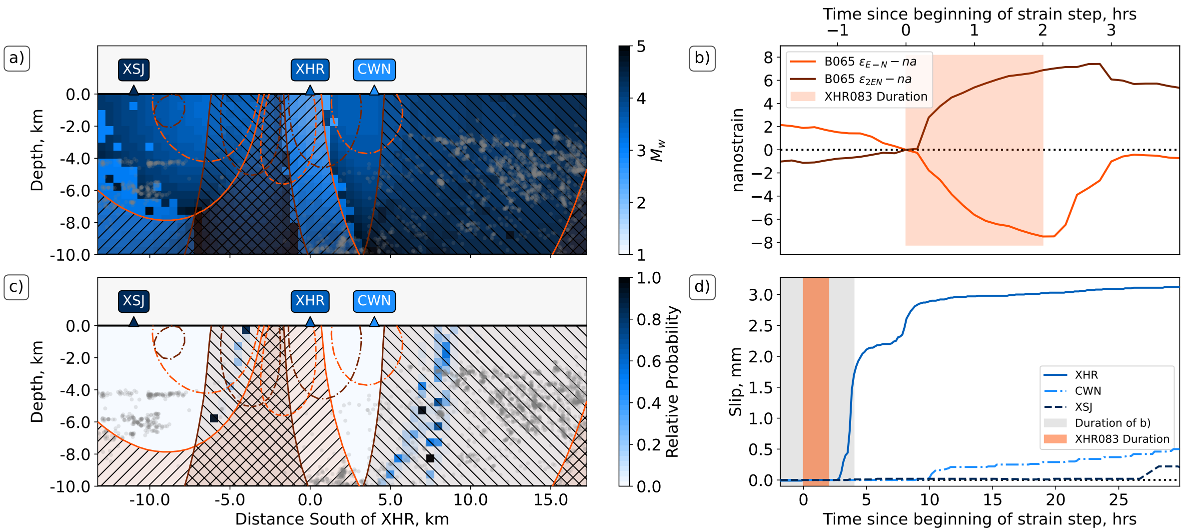

Figure 3.6: XHR083 observed at B065 and associated with a creep event at XHR, panels as in 3.5.

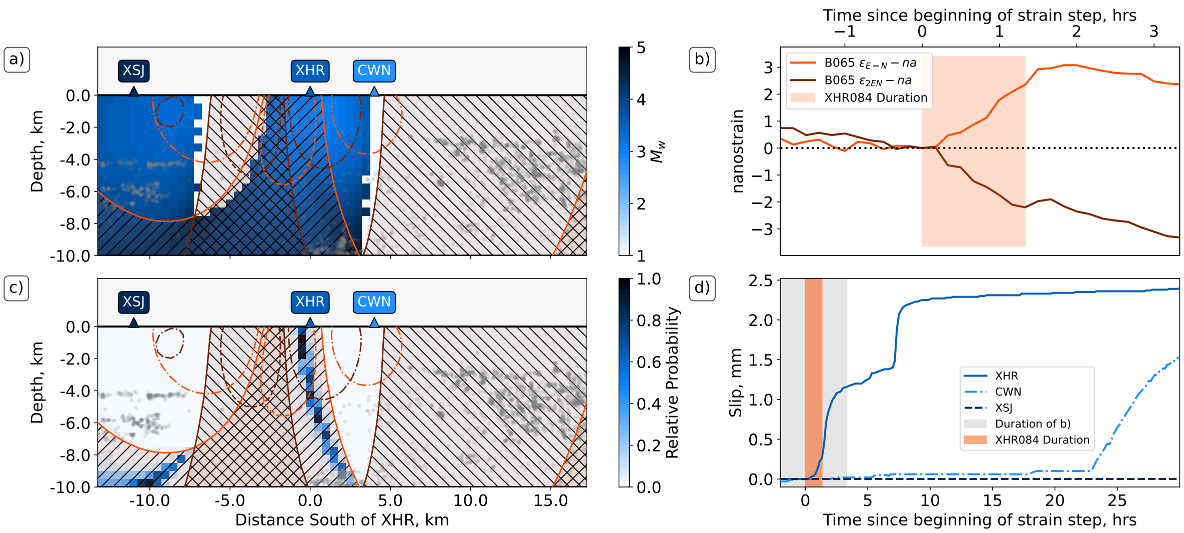

Figure 3.7: XHR084 observed at B065, associated with a creep event at XHR, panels as in 3.5.

lies either >7 km north of XHR or between XHR and CWN (Figure 3.8 c)). For reasons set out in section 3.4.3.6, we believe that if both components are negative (Figure 3.8 b)), then the slip will be located between XHR and CWN (Figure 3.8 c)). Slip in this region produces ≈ 46 % of the strain offsets.

One double negative strain offset event worth noting is CWN080, whose location is subtly different from all other events with double negative offsets (Figure B.3). This

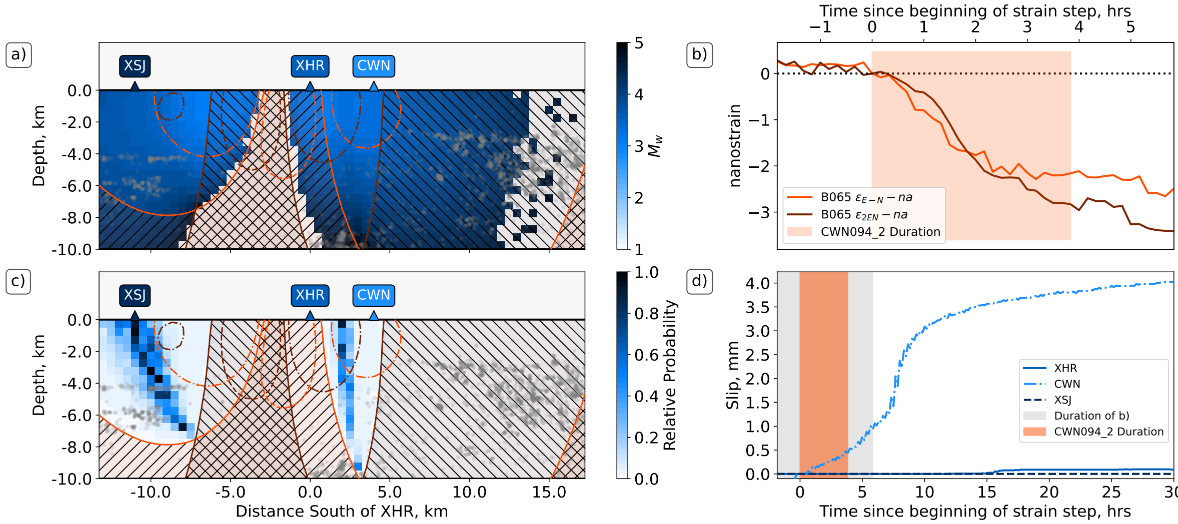

Figure 3.8: CWN094_2 observed at B065 and associated with a creep event at CWN, panels as in 3.5.

event has a large negative offset on the ϵ_{E-N}-na component and is located directly below CWN. CWN080 is the only event located here.

3.4.3.5 Are events in these four locations from the same patch?

The relative signs of the strain offsets identify four groups of locations where slip can occur. However, as Figure 3.9 a) shows, considering only the best five scenarios for each event, instead of four discrete locations, there appears to be a spread of locations within each group from with slip originates. Crucially, however, whether considering the four distinct locations based upon the signs of the strain offsets (Figures 3.5–3.8) or the best five scenarios of each event (ordered by distance along the fault) (Figure 3.9 a)), it is clear that the slip locations creating these strain offsets associated with creep events are *not* all originating from the same place.

3.4.3.6 Excluding scenarios under XSJ

Figure 3.8 c) shows two locations where our grid search suggests the slip could be. One location is just north of the CWN, and the other is under XSJ (Figure 3.8 c)). Both of these locations appear equally likely, given the observations at B065.

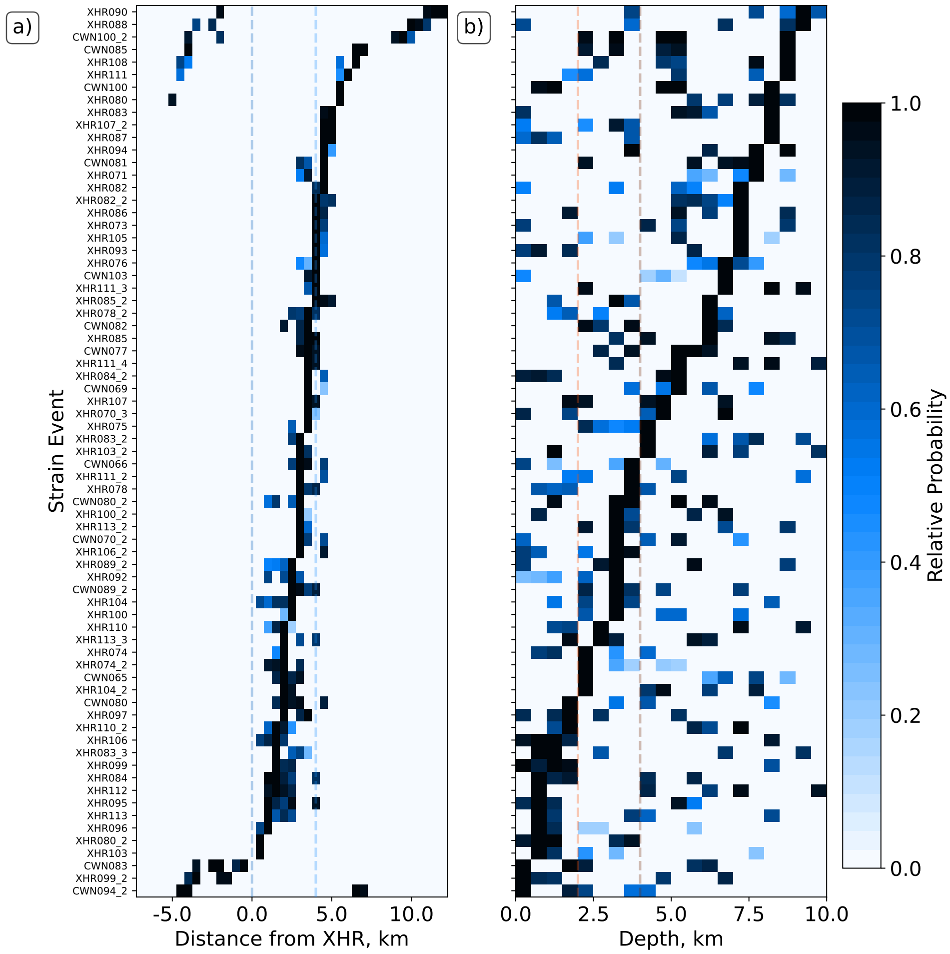

Figure 3.9: a) Distance from XHR horizontally of the five best-fitting scenarios for each strain event, ordered by the distance of each event's best-fitting scenario and coloured by each scenario's relative probability. The vertical dashed blue lines represent the location of XHR (dark blue) and CWN (light blue). b) The depth of the five best-fitting scenarios for each strain event, ordered by the depth of each event's best-fitting scenario and coloured by each scenario's relative probability. The vertical dashed orange line represents 2 km depth, and the vertical dashed brown line represents 4 km depth.

To investigate whether the region of fault under XSJ will likely produce the observed stain offset or if this northern location results from a data availability issue, we investigate the five most probable slip locations that create each strain offset. By comparing the five most probable slip locations that produced strain offsets that occurred when SJT was operational (Figure 3.10 a)) against those for all events regardless of SJT's operational status (Figure 3.10 b)), we find that when data from SJT is present, the best-fitting scenarios predominantly do not localise below SJT.

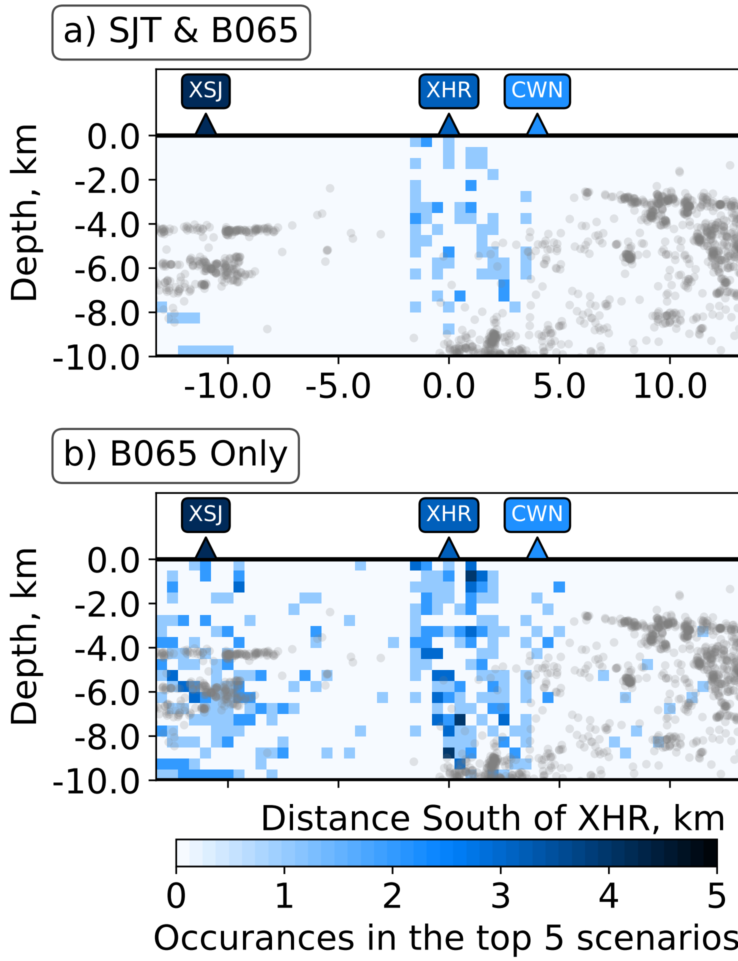

Figure 3.10: a) Location of the five best-fitting scenarios for slip location creating strain offsets when data is available from SJT. b) Location of the five best-fitting scenarios for all slip locations creating strain offsets. The grey dots are seismicity from the Northern California Earthquake Data Center catalogue (NCEDC, 2014).

Another factor against the slip locating under XSJ is the lack of slip at the XSJ creepmeter at the time of these strain offsets (Figure 3.8 d)). This lack of surface slip when a strain event is located directly below XSJ is a different behaviour than we observe at both XHR (Figure 3.7) and CWN (Figure B.3).

Therefore, the combination of (1) very few scenarios under XSJ having a high probability when SJT is operational and (2) a lack of surface slip at XSJ for events directly underneath it could rule out these locations.

3.4.4 Propagation of the slip creating creep-event associated strain offsets

The details within the strain record allow us to identify slip location variations over a series of strain offsets associated with creep events. For instance, in November 2012, there were three sequential strain offsets (Figure 3.11 a)), each associated with a phase of slip at either XHR or CWN (Figure 3.11 b)).

The first strain offset we observe has a positive ϵ_{E-N}-na and negative ϵ_{2EN}-na component of strain (see the dark green stripe in Figure 3.11 a)). This combination of strain components places the slip location $\approx$ 2 km north of XHR (Figure 3.11 c)). About 8 hours later, we observe a second strain offset with negative offsets on both strain components (see the medium green stripe in Figure 3.11 a)). This combination of strain offsets places the slip location between XHR and CWN (Figure 3.11 d)).

Finally, we observe a third strain offset about 20 hours after the first one. In this strain offset, both strain components have negative offsets. This combination of strain offsets places the slip location between XHR and CWN. As the ϵ_{2EN}-na component is close to zero, the location of slip here lies closer to CWN than XHR (Figure 3.11 e)). One could then imagine that this sequence of events is sequential and a result of a single propagating slip front triggering patches in three locations.

Other examples of such behaviour exist within our strain offsets, but how these creep events evolve remains unclear.

3.4.5 Depth of the slip creating creep-event associated strain offsets

Having assessed where the slip that produces our observed strain offsets is located along the fault's strike, the next challenge is determining at what depth the slip occurs. Looking directly at the relative probability distributions (e.g., Figure 3.7 c)), it is clear that there is some apparent uncertainty in the depth of strain offset. This uncertainty

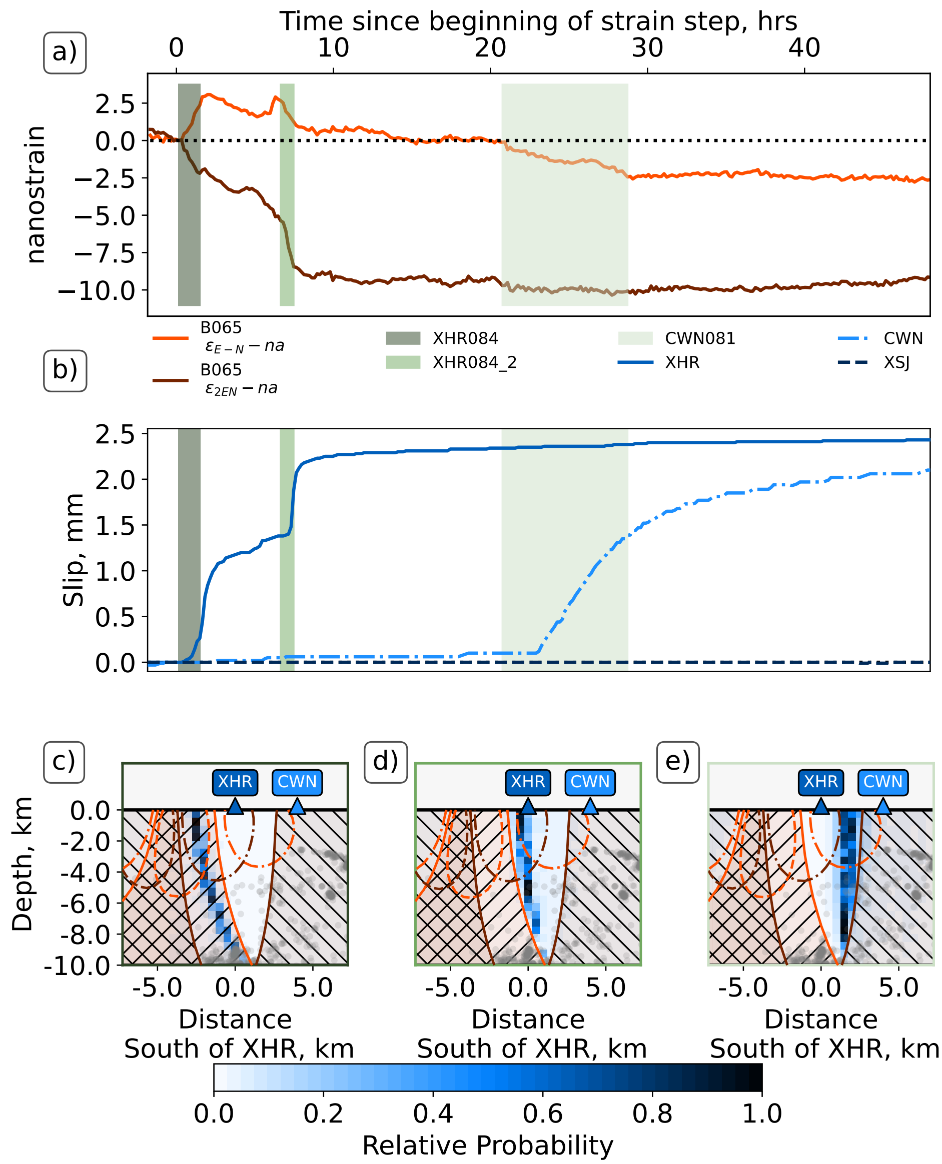

Figure 3.11: a) Strainmeter record spanning XHR084, XHR084_2, and CWN081, with ϵ_{E-N}-na shown as the orange line and ϵ_{2EN}-na as the brown line. b) Creepmeter record of the same time as in a), showing the creepmeter records of XSJ (dashed dark blue), XHR (solid medium blue), and CWN (dot-dashed light blue). In both a) and b), the durations of strain offsets XHR084, XHR084_2, and CWN081 are shown as dark, medium, and light green vertical bands, respectively. c), d) & e) Probability distributions for XHR084, XHR084_2 and CWN081 respectively. c), d) & e) are as in 3.5 c).

leads to some events not having well-resolved depths, even considering only the best five locations (Figure 3.9 b)).

Rather than determine the exact depth at which the slip occurred, we instead focus on whether the slip is shallow (0–2 km, blue histogram in Figure 3.12), intermediate (2–4 km, orange histogram in Figure 3.12) or deep (>4 km, green histogram in Figure 3.12). We chose these depths as they represent distinct horizons in the region's seismicity (Figure B.4).

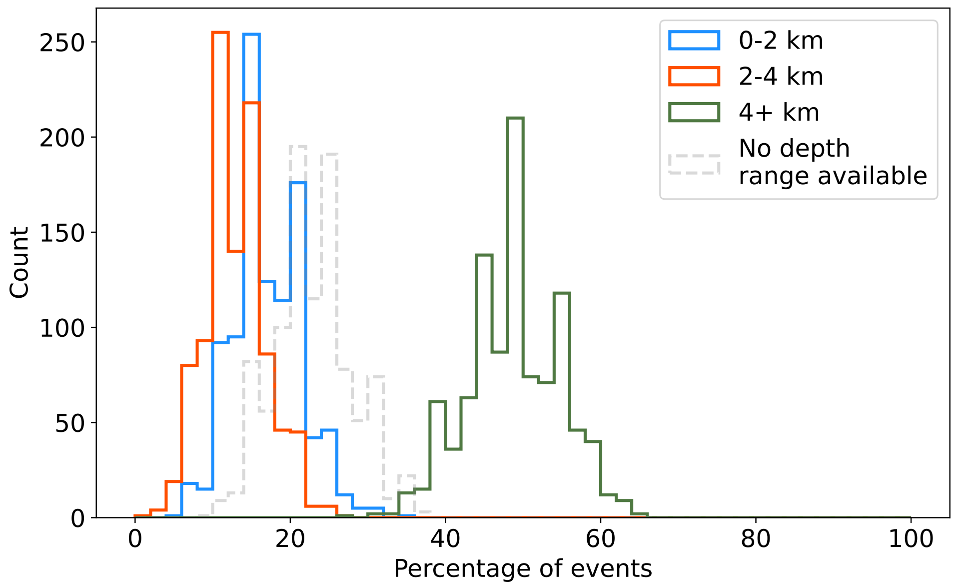

Figure 3.12: Histograms of the percentage of slip locations in each depth range following bootstrapping. The blue histogram shows the 0 - 2 km depth range, the orange histogram shows the 2 - 4 km depth range, and the green histogram shows the 4+ km range. The grey histogram represents the slip location group with an inconclusive depth range.

We assign each strain offset we observe to one of these depth ranges based on whether three out of five of the best fitting locations are within each depth range (Figure 3.9 b)). Suppose a creep event associated strain offset does not have three scenarios in one of the ranges but is instead spread across them. In that case, we do not assign it a depth classification.

Once we have assigned each creep event associated strain offset to a depth range, we conduct bootstrapping with replacement to calculate the 70% confidence interval for each depth range. Most slip locations occur below 4 km, with 42–55% of offsets requiring slip below this depth (green histogram in Figure 3.12). In the remaining two depth ranges, we find that 8–17% of offsets require slip between 2–4 km deep (orange histogram in Figure 3.12), and 13–21% of offsets require slip above 2 km (blue histogram in Figure 3.12). We cannot assign a depth to 17–28% of offsets (grey dashed histogram in Figure 3.12).

3.4.6 Magnitude of the slip creating creep-event associated strain offsets

We take a similar approach to classifying the M_w of the slip patch, producing the strain offsets as we did with the depth classification. Rather than assigning each event a M_w, we included all five of its best-fitting scenarios in the classification. By plotting the best five scenarios for each event (Figure 3.13), we find that the majority of scenarios lie between M_w 3–4 (Figure 3.13 between the blue and orange vertical lines), with the rest made up of events above M_w 4 (Figure 3.13 right of the orange vertical line).

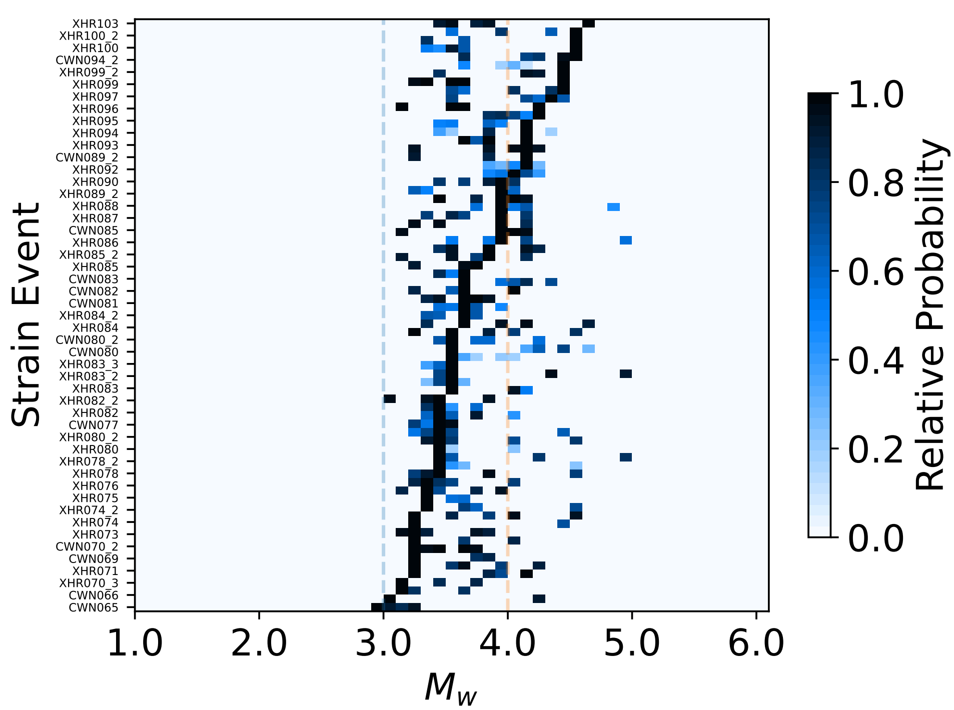

Figure 3.13: Magnitude of the top five scenarios for each strain event. Each square is coloured based on the top 5 events and their relative probability. The blue and orange vertical lines represent M_w 3 and 4 respectively.

To more robustly constrain the magnitude range of the slip patch which produces the strain offsets, we conduct bootstrapping with replacement to calculate the 70% confidence interval of the percentage of events that are $<M_w$ 3, between M_w 3–4 and $>M_w$ 4. We find, as through visual inspection of Figure 3.13 would suggest, that the majority of scenarios are between M_w 3–4, with 77–81% of the top five best fitting scenarios having a magnitude in this range (Figure 3.14, orange histogram). The remaining scenarios predominantly have a M_w >4, accounting for 19–23% of scenarios (Figure 3.14, green histogram). Next to none of the top five best fitting scenarios have a M_w <3 (0–1% of scenarios, Figure 3.14, blue histogram).

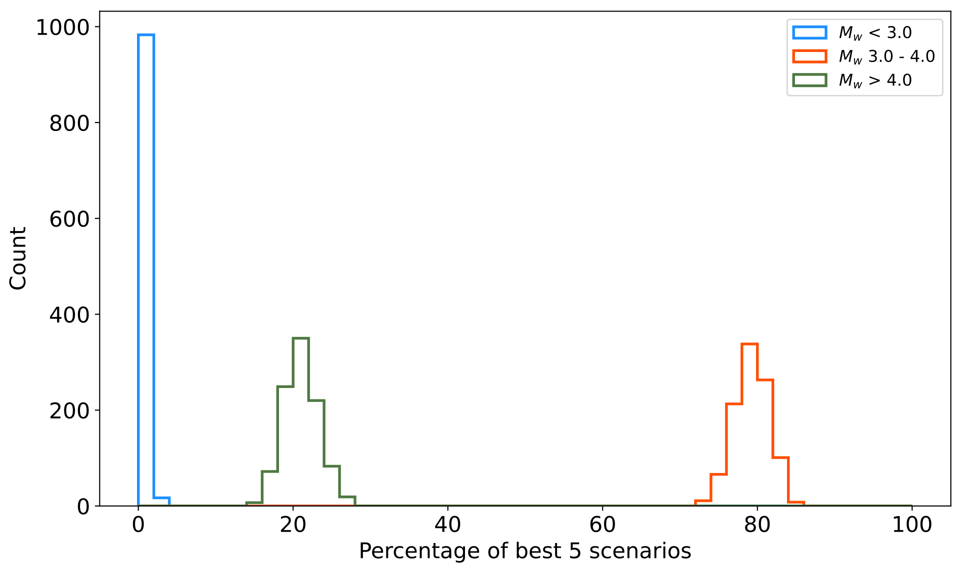

Figure 3.14: Histograms of the percentage of creep events in each M_w range following bootstrapping. The blue histogram shows the creep events with M_w <3.0, the orange histogram shows creep events with M_w 3.0 - 4.0, and the green histogram shows events with M_w >4.0.

3.5 Discussion

Our grid search provides interesting information about the (1) location and depth, (2) propagation, and (3) magnitude of a fault patch that creates strain offsets that are associated with creep events. Here, we will discuss the implications of these findings, focussing on (1) the number of patches of slip, (2) the depth of these patches of slip, and (3) how these slip patches in creep events are affecting the moment accumulation on the San Andreas Fault.

3.5.1 How many locations produce creep events?

It is important to know whether creep events are the result of slip at a single location (e.g., Gladwin et al., 1994; Goulty and Gilman, 1978) or if different creep events are originating from different locations, e.g., (Evans et al., 1981; Mortensen et al., 1977). These two scenarios have different implications for how creep events begin, grow spatially, and propagate.

If creep events result from slip in one location, this would suggest a relatively simple mechanism where a single fault patch repeatedly fails. If this is the case, creep events will originate from the same location and depth. The strain offsets we would observe from this slip patch would also have the same sign. This scenario appears to be the case for creep events near San Juan Bautista (Gladwin et al., 1994).

This one-patch scenario does not appear to be the case in the Harris Ranch–Cienega Winery area. Instead, we observe a range of slip locations producing strain offsets associated with creep events (Figure 3.9). Therefore, in this region, there are many different patches from which creep events can arise. These patches appear to be able to be triggered independently from one another or in sequence as a propagating slip front passes through the area (Figure 3.11). This suggests that several discrete fault patches can slip to produce creep events.

3.5.2 What are the implications of patches at depth?

The depth of creep events is an important factor as events originating in the shallow crust could have a different mechanism to those that occur deeper.

Suppose creep events originate in the shallow portion of the fault. In that case, they will likely arise from a slip rate-strengthening location with a relatively stable frictional rheology. These shallow creep events could then be produced by a 'kick' in stress due to pore pressure changes induced by rainfall or atmospheric pressure (Helmstetter and Shaw, 2009; Kanu and Johnson, 2011) or from slip below. This mechanism would only be plausible at locations with low normal stress that provided limited resistance to acceleration.

On the other hand, deep creep events may result from slip on rate weakening sections of the fault (e.g., Scholz, 1998; Wei et al., 2013). Here, a conditionally stable layer of the fault would slip at depth (creating the observed strain offset) and trigger slip in an upper surface layer later, which would be recorded by surface creepmeters. This scenario would represent a two-layer model for creep events (e.g., Bilham and Behr, 1992; Slater and Burford, 1979; Wei et al., 2013) and would explain the observed delay between the strain offset and the onset of surface creep.

The best-fitting depths we observe are mostly more than 4 km deep. Although there is significant uncertainty, it appears clear that some slip locations are deep, and it seems plausible that only some events are within the uppermost kilometre. This result would lend evidence to that later mechanism for creep events.

If creep events originate under the deeper mechanism related to a conditionally stable layer, the depth of this layer would be much deeper than previous estimates (e.g., Bilham and Behr, 1992; Wei et al., 2013). At 4 km depth, this layer would be comparable to the depth of the base of the unconsolidated sedimentary sequence (2–3 km) deposited in the Hollister region since the Early Pliocene (Allen et al., 1946; Dibblee, 2006; Rogers, 1980). However, the lack of a distinct depth layer (Figure 3.9 b)) would suggest that these events do not originate from a specific layer within the crust but rather from several discrete patches of fault.

3.5.3 What is the role of creep events in accommodating the moment budget of the region?

Our analysis suggests that the median moment released in a slip burst is 3.6. If each of the 71 slip bursts has this moment, they will account for 2.2–6.7% of the moment released by a 10×10 km section of the fault over a 10-year period, assuming a background creep rate of 10–30 mmyr^{-1}. This background creep rate is based on the creep rates reported for Harris Ranch–Cienega Winery stretch of fault with the lower estimate from creepmeters and alignment arrays (10 mmyr^{-1} (e.g., Burford and Harsh, 1980; Schulz, 1989)) and the upper estimate from GNNS and InSAR (30 mmyr^{-1}(e.g., Jolivet et al., 2015; Ryder and Bürgmann, 2008; Titus, 2006)). This percentage is much lower than that suggested from looking at surface recordings of creep events, where >50% of slip is accommodated in creep events Gittins and Hawthorne (2022a).

However, the percentage could be a dramatic underestimate. We have only considered the 71 clearest slip bursts and ignored less distinct events. If we include the less distinct events, we can visually identify at least 92 bursts of slip at XHR and CWN between 2009 and 2019. Further, we may have excluded many slip bursts because we have only examined the strain records during creep events recorded at the surface. Slip bursts could occur independent of surface slip; propagating deeper slip does not always trigger slip at the surfaceEvans et al. (1981); Gittins and Hawthorne (2022a). This would mean we could miss even more strain offsets associated with creep events that do not rupture the surface, further increasing their importance.

Geodetic estimates of the San Andreas Fault currently have its rate of movement below the long-term slip rate. This low slip rate produces a moment deficit equivalent to a M_w 5.2 to 7.2 earthquake every 150 years (Maurer and Johnson, 2014; Michel et al., 2018; Ryder and Bürgmann, 2008). Alternatively, a burst of aseismic creep events could reduce the moment deficit of the creeping section (e.g., Khoshmanesh and Shirzaei, 2018b).

The median M_w of the strain offsets we observe is a M_w 3.6. Accommodating the slip deficit of a M_w 5.2 earthquake would require us to have ≈ 250 more M_w 3.6 slip events in 150 years. In the worst-case scenario that the moment deficit is equivalent to a M_w 7.2 earthquake every 150 years, we would require almost 1700 more M_w 3.6 slip events every year, over 75 % of the total number of creep events identified by (Gittins and Hawthorne, 2022a) between 1985–2020. If instead, we consider a moderate value for the moment deficit closer to the middle of the estimated range, such that a M_w 6.2 earthquake is required every 150 years, then we would require a burst of almost 800 more M_w 3.6 slip events every 15 years.

It is worth assessing how the excess number of creep events required to account for this moderate estimate of the moment deficit compares to the number of creep events observed along the San Andreas Fault in 10 years. Between 1991 and 2001, Gittins and Hawthorne (2022a) observed 630 creep events on 17 creepmeters along the San Andreas Fault. To accommodate the moment deficit equivalent to a M_w 6.2 earthquake would require an increase of ≈ 85 % in the number of creep events observed across those 10 years, assuming all creep events have a M_w of 3.6. However, this is a maximum estimated increase given the heterogeneous distribution of creepmeters, with an almost 80 km stretch of fault between Melendy Ranch and Slacks Canyon lacking any measurement of creep events due to a lack of suitable instrumentation. Given that aseismic slip is known to occur in larger bursts of fault slip rate (Khoshmanesh and Shirzaei, 2018b), this does not appear outside the realms of possibility, if somewhat unlikely.

3.6 Conclusion

In this study, we identified 71 strain offsets associated with 44 surface rupturing creep events at the northern end of the creeping section of the San Andreas Fault between 2009 and 2019. We have modelled these offsets using rectangular patches of slip varying along strike locations, depths, and M_w to determine the location and M_w of the slip patch creating these offsets. We identify a range of along-strike locations relative to the surface creepmeters. This suggests that these events do not all rupture the same fault location. We categorise these events into three potential depth ranges, with the $\approx$ 42–55 % of the slip locations producing strain offsets originating below 4 km depth. Slip patches with a M_w of 3–4 produce most creep event-associated strain offsets. Compared to a 10×10 km fault section, the slip producing these strain offsets accommodates 2–6% of the moment budget of the fault. This suggests that creep events play a significant role in accommodating part of the slip budget in this region. Determining the physical process by which creep events nucleate and assessing their rupture dynamics is an essential next step in understanding creep events' role in the creeping section's overall slip dynamics.

4

Determining the rheology of creep events using their temporal evolution

4.1 Introduction . . . 123
4.2 Data . . . 124
4.3 Rheological Laws . . . 126
4.3.1 Spring-Block slider model . . . 128
4.3.2 Rate and state models . . . 129
4.3.3 Power-law and Linear Flow . . . 133
4.4 Fitting the shape of the events . . . 135
4.4.1 Forward Model . . . 135
4.4.2 Noise Estimates . . . 136
4.4.3 Parameter Search . . . 137
4.5 Results . . . 138
4.5.1 Power-law flow . . . 138
4.5.2 Rate and state friction below steady state: the healing regime ($\dot{\theta} \approx 1$) . . . 139
4.5.3 Rate and state friction above steady state: decreasing state regime ($\dot{\theta} < 0$) . . . 139
4.5.4 Linear flow model . . . 139
4.5.5 Rate and state friction at constant state rate near steady state ($\dot{\theta} \approx 0$) . . . 140
4.5.6 Fit parameters . . . 140
4.6 Discussion . . . 141
4.6.1 Option 1: Power-law flow . . . 142
4.6.2 Option 2: Rate and state friction below steady state in a velocity-weakening regime (the healing regime, $\dot{\theta} \approx 1$ . . . 143
4.6.3 Option 3: More complex model required? . . . 143

4.7 Conclusion 145

Abstract

We have known about aseismic creep events along the San Andreas Fault since the 1960s, yet we still need to determine their driving mechanisms. To address this uncertainty, we use creepmeter data from Harris Ranch at the northern end of the creeping section of the San Andreas Fault to asses how well different rheological models can describe the displacement time evolution of surface rupturing creep events. Using a basin-hopping approach, we minimise the misfit between the observed creepmeter data and five rheological models: 1) rate and state friction at a constant state rate near steady state ($\dot{\theta} \approx 0$), (2) rate and state friction above steady state (decreasing state regime, $\dot{\theta} < 0$), (3) rate and state friction below steady state (healing regime $\dot{\theta} \approx 1$), (4) power-law flow, and (5) linear flow. We find that most events are best fit by either a power-law flow model or a rate and state friction below steady state model. These surprising results suggest additional work is required to understand the driving physics behind creep events, potentially incorporating more complex physical models that allow for other fault zone processes such as dilatancy and rupture front propagation.

Plain language summary

We have observed bursts of slip, or creep events, along the San Andreas Fault since the 1960s, yet we still need to understand what is causing them to occur. To try and determine this, we compare the shape of creep events to five different models: (1) a frictional model near steady state, (2) a frictional model above steady state (decreasing state regime), (3) a frictional model below steady state (healing regime), (4) power-law flow, and (5) linear flow. Most creep events have their shape best described by power-law flow or a frictional model below steady state. These surprising results suggest additional work is required to understand the driving physics behind creep events, potentially incorporating more complex physical models than tested here.

4.1 Introduction

Aseismic creep along the 175 km-long central San Andreas Fault has been observed since the 1960s (Steinbrugge and Zacher, 1960; Tocher, 1960; Whitten and Claire, 1960). The aseismic slip along this creeping section occurs via slow, steady slip punctuated by few-mm bursts of slip known as creep events (e.g., Gittins and Hawthorne, 2022a; Gladwin et al., 1994; Nason et al., 1974; Schulz, 1989). These creep events last a few hours to days and recur every few weeks or months (e.g., Gittins and Hawthorne, 2022a; Gladwin et al., 1994; Schulz, 1989; Wei et al., 2013; Wesson, 1988).

Since Tocher (1960) first observed creep events, there have been various attempts to understand their behaviour. Researchers have estimated creep events' rupture extents (e.g., Bilham and Behr, 1992; Bilham et al., 2016; Burford, 1977; Evans et al., 1981; Gittins and Hawthorne, 2022a; Gladwin et al., 1994; Goulty and Gilman, 1978; King, 2019; King et al., 1973; Nason and Weertman, 1973; Mchugh and Johnston, 1976; Mortensen et al., 1977; Slater and Burford, 1979). They have also examined creep events' associations to rainfall (e.g., Roeloffs, 2001; Roeloffs et al., 1989; Schulz et al., 1983) and seismicity (e.g., Harris, 2017; Hirao et al., 2021; Khoshmanesh et al., 2015;

Lyons and Sandwell, 2003; Nadeau and McEvilly, 2004; Thurber and Sessions, 1998).

Researchers have proposed some physical and rheological models to address the fundamental mystery of creep events: why slip accelerates but then quickly stalls at low slip rates (e.g., Bilham and Behr, 1992; Nason and Weertman, 1973; Scholz, 1998; Slater and Burford, 1979; Wei et al., 2013; Wesson, 1988).

Of particular interest here are some proposed rheological laws — relationships between fault slip rate and fault strength — that could explain why creep events are always slow (e.g., Crough and Burford, 1977; Nason and Weertman, 1973; Scholz, 1998; Wei et al., 2013; Wesson, 1988).

In this study, we assess five proposed rheological models by examining the temporal evolution of slip during creep events. We assess whether the proposed rheological models predict slip evolution similar to that observed on surface creepmeter recordings.

The rheological models we test are (1) rate and state friction at a constant state rate near steady state ($\dot{\theta} \approx 0$), (2) rate and state friction above steady state (a decreasing state regime, $\dot{\theta} < 0$), (3) rate and state friction below steady state (a healing regime, $\dot{\theta} \approx 1$), (4) power-law flow, and (5) linear flow.

We describe the creepmeter data and event selection in Section 4.2, discuss the five rheological laws in Section 4.3, and describe how we fit these models in Section 4.4. We determine the percentage of events each rheology explains in Section 4.5 and find that the two best fitting rheological laws are a power-law flow model and rate and state friction below steady state (in a healing regime). Both of these rheologies turn out to be surprising, given our physical intuition. In Section 4.6, we discuss the implications of these rheologies for the driving mechanisms of creep events.

4.2 Data

We use creepmeter data from two iterations of the USGS creepmeter XHR at Harris Ranch, 11 km south of San Juan Bautista, CA (Figure 4.1), to investigate the driving rheology for creep events. The XHR2 iteration operated between 1991 and 2005 and was replaced by XHR3, which operated between 2009 and 2019. Each of these creepmeter iterations records at a sampling frequency of 10 minutes.

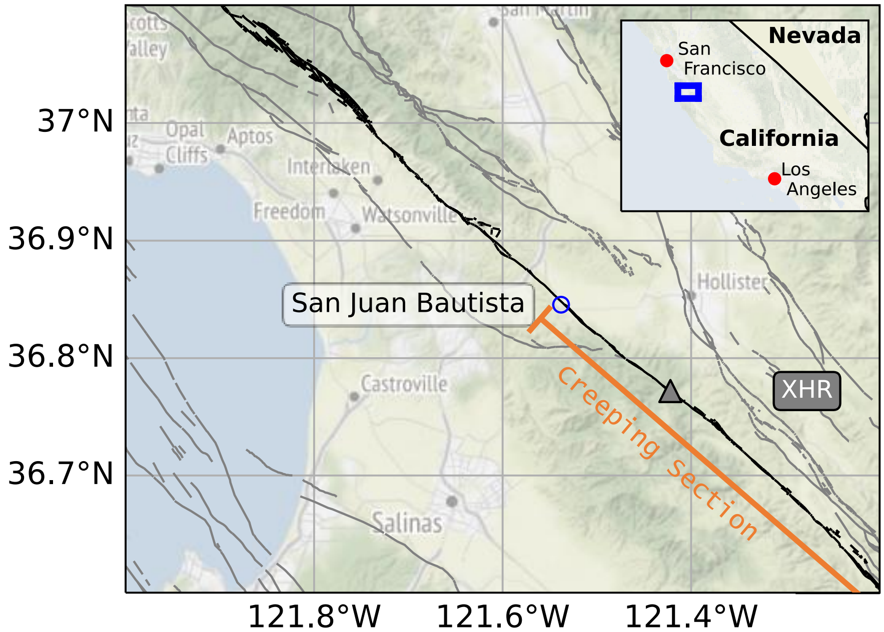

Figure 4.1: Map of the northern end of the creeping section of the central San Andreas Fault (black). Other faults in central California are shown in grey. The USGS creepmeter XHR is the grey triangle. Faults plotted are from the USGS/California Geological Survey Quaternary faults and folds database (USGS and CGS, 2020).

We use the creep event catalogue of Gittins and Hawthorne (2022a) to identify and extract 113 creep events within the creepmeter record at XHR. These creep events typically last a few hours to days and have displacements of a few millimetres (Gittins and Hawthorne, 2022a; Schulz, 1989). Figure 4.2 shows an example of a creep event recorded in December 1997, illustrating some of the key characteristics of creep events recorded at XHR. The majority of creep events at XHR have a sharp onset with little preamble (e.g., Bilham et al., 2004; Wesson, 1988). The gradient of the displacement-time curve is quite steep following this sharp onset but then rapidly decreases around the 'bend' of the creep event. After this sharp bend, little to no slip is recorded on the creepmeter, indicating the end of the creep event.

Many of the creep events recorded at XHR have multiple phases of slip — multiple steps in the record (Bilham and Behr, 1992; Gladwin et al., 1994; Schulz, 1989; Wesson,

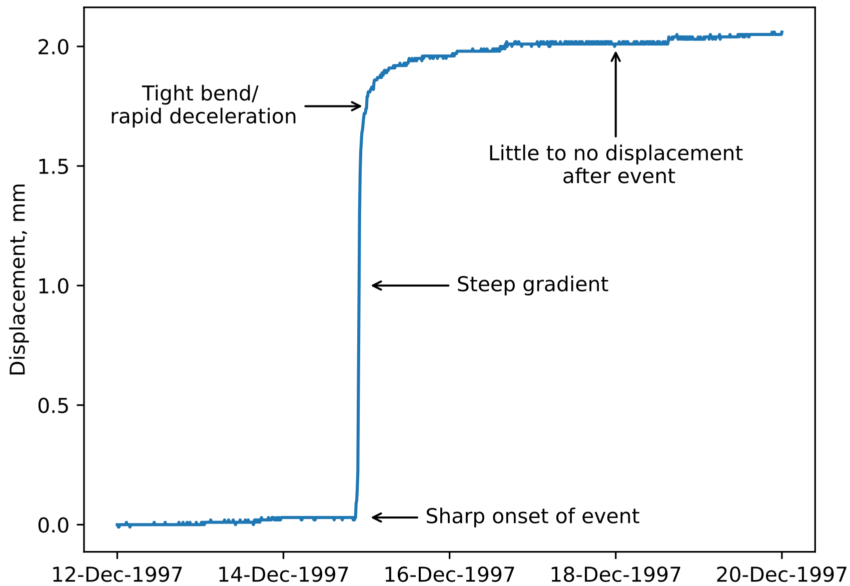

Figure 4.2: Example creep event recorded at XHR2 on 15$^{\text{th}}$ December 1997. Key features of the creep events recorded at XHR are highlighted.

1988), but for simplicity, we model only the 50 events that have one phase of slip.

4.3 Rheological Laws

Surface properties of faults are often found to be velocity-strengthening (e.g., Marone et al., 1991; Scholz, 1990; Wei et al., 2013). Here, the fault is nominally stable and will resist slip. The fault may slip stably at the surface for a time at a slip rate $\approx 10^{-9}$ ms^{-1}, slightly below plate rate.

Suppose the stably sliding portion of the fault receives an increase in stress from elsewhere, perhaps from above, in the form of rainfall-induced pore-pressure changes (e.g., Helmstetter and Shaw, 2009; Kanu and Johnson, 2011) or below from some slip at depth (e.g., Bilham and Behr, 1992; Slater and Burford, 1979). In this case, the fault will accelerate to slip rates of $\approx 10^{-7}$–10^{-6} ms^{-1} before stalling, resulting in a creep event. The velocity-strengthening nature of the fault causes this stalling. As the fault slips faster, its strength will increase, leading to a higher resistance to slip and causing the fault to slow down. This acceleration and subsequent relaxation of the fault following a step increase in stress forms the basis of the 'kick' hypothesis for creep events.

The displacement in a creep event that arises from the 'kick' hypothesis depends on the fault zone rheology and the state of stress, i.e., how well healed the fault is. Therefore, we aim to determine which rheology and stress state best describes the displacement evolution of creep events.

We model the displacement evolution of creep events produced through different combinations of rheological laws and stress states. Here, we test three rheological laws: (1) rate and state friction, (2) power-law flow and (3) linear flow. Using the rate and state friction law, we consider three scenarios with different stress states: (1) a relatively abrupt change in stress that leaves the fault close to steady state, (2) an abrupt increase in stress that takes the fault above steady state into a decreasing state regime ($\dot{\theta} < 0$), and (3) a decrease in stress during deceleration that takes the fault below steady state and into a healing regime ($\dot{\theta} \approx 1$).

These combinations of rheological law and stress state provide us with a total of five rheological models in which to try and explain the displacement evolution of creep events: (1) rate and state friction at a constant state rate near steady state ($\dot{\theta} \approx 0$), (2) rate and state friction above steady state ($\dot{\theta} < 0$), and (3) rate and state friction below steady state ($\dot{\theta} \approx 1$) (4) power-law flow, and (5) linear flow.

These rheological models are simple scenarios that could produce creep events. More complex models may better describe the evolution of slip in creep events; however, they do not have simple analytical solutions. Therefore, we test these simple models to see if any can describe the displacement evolution of creep events, providing a foundation for testing more complex models in the future.

4.3.1 Spring-Block slider model

The rheology of the patch is not the only determining factor controlling how the slip rate evolves with time. The elastic interactions of neighbouring fault patches also affect the slip rate.

If one patch of the fault moves, it will apply stress to neighbouring patches through the elasticity between the patches. When the adjacent patches move towards the moved patch, the stress on the adjacent patch is reduced. This concept can be considered a simple spring-block slider model (Figure 4.3) where a spring of stiffness k represents the elasticity between patches. The size of the fault patch is inversely proportional to the stiffness, such that large patches experience less stress than small patches when neighbouring patches of the fault move (Dieterich, 1992; Scholz, 1998).

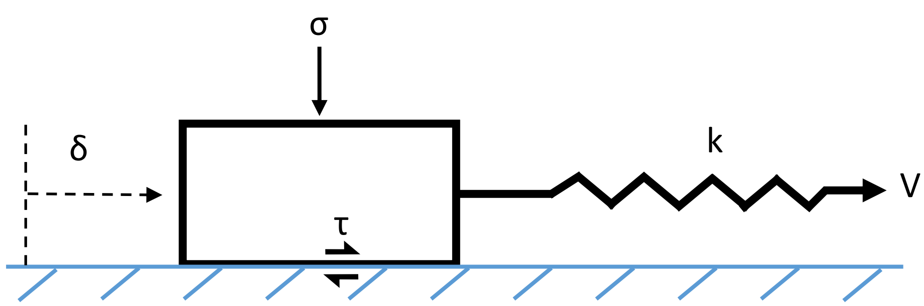

Figure 4.3: Spring block slider model.

How fast the fault patch slips is related to the stress applied by the movement of the adjacent patches such that:

$$\tau_d = k(Vt - \delta), \tag{4.1}$$

where τ_d is the driving stress acting on the patch, k is the spring stiffness, V is the slip rate, t is time and δ is the displacement of the block.

This simple spring-block slider model demonstrates the importance of elasticity by providing an additional relationship between stress and slip rate. Therefore, we need both elasticity and the rheology of the patch to describe how the slip rate evolves with time.

4.3.2 Rate and state models

Given that creep events occur at shallow depths (e.g., Bilham and Behr, 1992; Gladwin et al., 1994; Wei et al., 2013), it is plausible that frictional processes drive them. Here, we use the rate and state friction formulation of Ruina (1983), based upon Dieterich (1979) to try and explain the displacement evolution of creep events.

In the rate and state framework, the shear stress, τ, is a function of the slip rate, V, and the 'state' variable, θ:

$$\tau = \sigma\Big[\mu^* + Aln\frac{V}{V^*} + Bln\frac{V^*\theta}{D_c}\Big], \tag{4.2}$$

where σ is the normal stress, D_c is the characteristic sliding distance, μ^* and V^* are reference values of friction and slip rate, and A and B are the coefficients of the direct and evolution effect, respectively.

The state variable, θ, changes with time and slip. Two evolution laws were proposed by Ruina (1983) to describe the rate of change of θ with time depending upon the slip rate, V, and the critical slip distance, D_c. The first of these is the aging law

$$\dot{\theta} = 1 - \frac{V\theta}{D_c}, \tag{4.3}$$

which explains the observation of fault surfaces strengthening on stationary contact (e.g., Marone et al., 1991). The second state evolution law is the slip law

$$\dot{\theta} = -\frac{V\theta}{D_c}ln\frac{V\theta}{D_c}, \tag{4.4}$$

which is able to explain large changes in slip rate (Beeler et al., 1994) and may be well suited to explaining the nucleation phase of slip (Ampuero and Rubin, 2008).

A fault patch governed by rate and state friction can respond to a step in stress in several ways. If the step in stress is relatively abrupt, but the slip rate evolves slowly compared to the timescale for state to evolve, the fault patch will slip close to steady state (Section 4.3.2.1). Alternatively, if the step in stress is abrupt so the fault patch slips faster than state can evolve, the fault patch will slip above steady state in a decreasing state regime (Section 4.3.2.2). However, if the fault patch accumulates most of its slip during a decrease in stress while decelerating, it will slip below steady state in a healing regime (Section 4.3.2.3).

We will use several analytical approximations for each of these stress states that only exist for the aging law (e.g., Helmstetter and Shaw, 2009), despite the slip law describing behaviour above steady state better.

4.3.2.1 Constant state rate near steady state ($\dot{\theta} \approx 0$)

Suppose the change in slip rate following an increase in stress occurs slowly enough relative to the timescale for the state evolution. In that case, the fault will remain close to steady state. Here, the state rate remains constant but not zero (Helmstetter and Shaw, 2009).

In this scenario, creep events at the surface record the relaxation following a step change in stress. This process is similar to that of afterslip. Within studies of afterslip, the system is often approximated to steady state (e.g., Helmstetter and Shaw, 2009; Montési, 2004). In this steady state approximation, state is inversely proportional to the slip rate. The displacement occurring following a step change in stress evolves logarithmically with time under the steady state approximation (Helmstetter and Shaw, 2009; Marone et al., 1991; Scholz, 1990) such that

$$\delta(t) = V_0 t_{ss} ln\Big(1 + \frac{t - t_0}{t_{ss}}\Big), \tag{4.5}$$

where

$$t_{ss} = \frac{\sigma(A - B)}{kV_0}. \tag{4.6}$$

Here δ is the displacement, t is time, V_0 is the initial slip rate, t_{ss} is the characteristic time for displacement decay, t_0 is the initial time, A and B are the coefficients of the direct and evolution effects, σ is normal stress, and k is the spring stiffness (Helmstetter and Shaw, 2009).

4.3.2.2 Above steady state: a decreasing state regime ($\dot{\theta} < 0$)

A step in stress causes a near-instantaneous change in slip rate. However, the "state" of the fault — the size and number of asperities — cannot change instantaneously. So, a large step in stress causes a step in slip rate with little change in state. Subsequently, state decreases, and asperities get smaller. The decrease in state causes a decrease in frictional resistance, which helps drive slip. Following this sequence of events, the fault ends up above steady state, with state decreasing with time ($\dot{\theta} < 0$).

Although the slip law (Equation 4.4) is better at describing how the system behaves well above steady state, in this work, we use the aging law (Equation 4.3) following previous work to define how displacement evolves following a large step increase in stress (e.g., Helmstetter and Shaw, 2009; Rubin and Ampuero, 2005).

In the rate and state friction above steady state regime, $\dot{\theta} = -\frac{V\theta}{D_c} < 0$, resulting in $\mu(V) >> \mu_{ss}(V)$ (Dieterich, 1992; Helmstetter and Shaw, 2009). If creep events occur in this regime and the loading rate from the surrounding material, $\dot{\tau}_l$, does not equal zero, then their slip will evolve as

$$\delta(t) = V_0 t_1 ln\Big(1 - \Big(\frac{t_a}{t_1}\Big)\Big(1 - e^{\frac{t-t_0}{t_a}}\Big)\Big), \dot{\tau}_l \neq 0, \tag{4.7}$$

where t_1 is given by

$$t_1 = \frac{A\sigma}{V_0(k - k_B)}, \tag{4.8}$$

with $k_B = \frac{B\sigma}{D_c}$ and t_a is given by

$$t_a = \frac{A\sigma}{\dot{\tau}_l}. \tag{4.9}$$

In Equations 4.7–4.9, δ is the displacement, t is time, V_0 is the initial slip rate, t_0 is the initial time, t_a is the characteristic time of loading, t_1 is the characteristic time of decay,

$\dot{\tau}_l$ is the loading rate from the surrounding material, A and B are the coefficients of the direct and evolution effects, D_c is the critical slip distance, and k_B is the characteristic spring stiffness (Helmstetter and Shaw, 2009).

The above steady state (decreasing state) regime does have a significant drawback when describing the slip evolution of creep events. As the fault slows down and state rate increases, the fundamental assumption that $\dot{\theta} \ll 0$, used to derive Equation 4.7 no longer holds (Helmstetter and Shaw, 2009). This means that Equation 4.7 is only valid when the slip rate is much greater than the loading rate from the surrounding material.

In Figure 4.2, the slip rate following the bend of the creep event is low at $\approx 10^{-9}$ms^{-1}, similar to the loading rate. Therefore, the above steady state (decreasing state) regime may only be valid in the early stages of the creep event and poorly describe the displacement evolution at the end of the event, where slip rates are low.

4.3.2.3 Below steady state: a healing regime ($\dot{\theta} \approx 1$)

In the above steady state (decreasing state) regime, the fault is accelerating. However, it is also possible that significant slip occurs while the fault slows down and state is increasing with time — when the fault is healing.

During this healing phase, state increases as asperities get bigger. However, if the fault slows down faster than asperities can grow, the fault will be below steady state. One possible way that the surface ends up below steady state is if we only observe the end of a larger slip event that has propagated from depth. A velocity-weakening patch could nucleate the creep event at depth, which then propagates to the surface. By the time it reaches the surface, most of the moment release in the event has occurred. The whole system then decelerates together below steady state with only modest changes in stress.

We consider a particular case of fault healing when the slip rate decreases quickly enough that the fault is far below steady state so that $\dot{\theta} \approx 1$. Coupling this constraint with the modest changes in stress and a negligible loading rate, the slip in a creep event will evolve as

$$\delta(t) \approx \frac{V_0\theta_0}{B/A-1}\left[1-\left(1+\frac{t-t_0}{\theta_0}\right)^{1-B/A}\right], \tag{4.10}$$

where δ is the displacement, t is time, t_0 is the initial time, V_0 is the initial slip rate, θ_0 is the characteristic time, and A and B are the direct and evolution effect coefficients, respectively (Helmstetter and Shaw, 2009).

4.3.3 Power-law and Linear Flow

We now attempt to model the displacement during creep events using flow laws. At first, describing creep events using flow laws may seem counter-intuitive. Flow laws are typically associated with deformation at high temperatures and pressures in a ductile regime within the crust at depths near the brittle-ductile transition (Montési, 2004; Passchier and Trouw, 2005), unlike the shallow, cool conditions in which creep events occurs.

Experiments on rocks that deform in a ductile manner at depth often find that slip rate $\propto$ applied stress^n, where the motion of intercrystalline dislocations gives a value of n between 3–5 (Hirth and Kohlstedt, 2004; Montési, 2004). In this n = 3–5 regime, deformation occurs through grain boundary sliding accommodated by dislocation creep (Hirth and Kohlstedt, 2004; Montési, 2004). On the other hand, if $n = 1$, deformation occurs through grain boundary sliding accommodated by diffusion creep (Evans and Kohlstedt, 1995; Hirth and Kohlstedt, 2004; Montési, 2004).

Empirically derived laws for the displacement evolution of creep events by Crough and Burford (1977) and later modified by Wesson (1988) have a similar functional form to the ductile flow laws at depth. This leads us to include flow laws in our analysis, and we suggest a possible way to explain the occurrence of ductile deformation at the shallow, brittle depths where creep events occur.

Creep events often occur at depths which correspond to diagenetic conditions. At these diagenetic conditions where fluids are abundant, ductile deformation can occur through pressure solution creep, a stress-driven fluid-assisted mass transfer process (Passchier and Trouw, 2005). During pressure solution creep, localised stress heterogeneities result in variations in chemical potential. In areas of high chemical potential, soluble minerals are progressively dissolved and subsequently precipitated elsewhere (Gratier et al., 2013; Passchier and Trouw, 2005; Richard et al., 2014). The pressure solution creep process has a net effect of removing soluble minerals such as quartz and feldspar and leads to a higher percentage of phyllosilicate minerals (Gratier et al., 2011; Richard et al., 2014). Pressure solution creep also results in a slip rate $\propto$ stress^n relationship similar to those of deeper ductile deformation mechanisms.

Evidence for pressure solution creep has been observed on rock samples collected from the San Andreas Fault Observatory at Depth (SAFOD) (Gratier et al., 2011; Richard et al., 2014). Here, microstructural analysis gives evidence for stress-driven dissolution of quartz and feldspars at quartz-feldspar grain impingements along pressure solution seams (Gratier et al., 2011). In contrast, phyllosilicates are passively concentrated along these pressure solution seams, leading to up to 50–70 % phyllosilicates in rock samples from the actively creeping zone of the SAFOD drill core (Gratier et al., 2011; Richard et al., 2014) compared to 10 % in the surrounding rocks outside of the actively creeping zone (Richard et al., 2014; Solum et al., 2006). These phyllosilicates are predominantly saponite, a frictionally weak mineral used to explain the low frictional strength of the San Andreas Fault (Lockner et al., 2011; Moore and Rymer, 2012). At the SAFOD site, diffusion-accommodated grain boundary sliding alone is able to accommodate the 20 mmyr^{-1} creep rate (Gratier et al., 2011). The process of grain sliding accommodating active creep illustrates that a steady state ductile behaviour may be a viable mechanism to explain creep events given their relatively slow creep rates of $\approx 10^{-7}$–10^{-6} ms^{-1}.

In the general case that the near-surface fault is governed by power-law flow, if the fault segment then experiences a 'kick' from a change in stress, slip at the surface will evolve as:

$$\delta(t) = \delta_0 + V_0 t_c n \Big[1 - \Big\{1 + \Big(1 - \frac{1}{n}\Big)\Big(\frac{t - t_0}{t_c}\Big)\Big\}^{\frac{1}{1-n}}\Big], \tag{4.11}$$

where δ is the displacement, t is time, δ_0 is the initial displacement at time t_0, V_0 is the initial slip rate, t_c is the time constant and n is the power-law exponent (Montési, 2004).

When $n = 1$, Equation 4.11 reduces to the linear flow model

$$\delta(t) = \delta_0 + V_0 t_c \Big(1 - e^{\frac{t - t_0}{t_c}}\Big), \tag{4.12}$$

where δ is the displacement, t is time, δ_0 is the initial displacement at time t_0, V_0 is the initial slip rate and t_c is the time constant (Montési, 2004). This linear flow model is often used in fluid mechanics as it is appropriate for water (Montési, 2004). Rock behaviour is likely more complicated than this simple Newtonian flow (Montési, 2004), but we include it as an end member model of power-law flow.

4.4 Fitting the shape of the events

4.4.1 Forward Model

We determine the best-fitting parameters for each rheological model using a two-part fit. This two-part fit includes a straight line and the displacement described by the rheological model, such that

$$\delta = \begin{cases} \delta(t) = V_b t + Q, & t \leq T_{01} \\ \delta(t) = V_b t + Q + \delta_r(t), & t > T_{01} \end{cases}. \tag{4.13}$$

In Equation 4.13, δ is the displacement, t is time, $\delta_r(t)$ represents the rheology-dependant displacement evolution (Equations 4.5, 4.7, 4.10, 4.11, & 4.12), V_b is the slip rate in the few hours before the creep event, Q is a constant allowing for a straight line to be fit to the time T_{01}. T_{01} is a fitting parameter dictating the time at which the rheological model begins to be incorporated, i.e., the start of the creep event.

The fit prior T_{01} accommodates any initial displacement that may occur before the main phase of slip in the creep event. This initial displacement accounts for any preamble before the creep event. This preamble represents an increase in the creep rate at the creepmeter included in the creep event catalogue of Gittins and Hawthorne (2022a), yet does not constitute the main phase of slip in the creep event. Often, we find that both V_b and Q are both 0 as there is no preamble and, therefore, no displacement before most of the events we model.

4.4.2 Noise Estimates

We needed to determine the best fit for the data to discriminate between the different rheological laws.

When assessing whether the modelled slip matches the data, it is important to account for the temporal covariance in the creepmeter noise: the relationship between creep at one time and creep later. To estimate the temporal covariance, we select 50,000 segments of creepmeter data that are four days long. We calculate the covariance of these samples, producing a data covariance matrix, C, where C_{nm} is the average value of $(\delta(t_n) - \delta(t_0)) \times (\delta(t_m) - \delta(t_0))$. We calculate one data covariance matrix per creepmeter iteration.

The covariance matrices are shown in Figure 4.4; they capture the largest uncertainties in the data. From these covariance matrices, we can see that both white noise and random walk noise are present in the data as we do not have a constant value on the diagonal (indicative of white noise), and the uncertainty also gets larger further away from the origin, indicative of random walk. This result is not surprising given previous work on characterising the noise of creepmeters (e.g., Langbein et al., 1993; Langbein and Johnson, 1997).

However, even an average of 50,000 segments misses small details of the covariance matrix. Noise in our estimates means that the calculated covariance matrices have a few negative eigenvalues. To regularise the covariance matrices and make them invertible, we add a component of white noise to the covariance matrices, with an amplitude of $0.1 \times C_{22}$.

To determine which rheological law was best, we optimised the parameters for each creep event, minimising the misfit between the observed and predicted creep event displacement defined as:

$$\text{Misfit} = \frac{(\delta_{obs} - \delta_{pred})^T \cdot C^{-1} \cdot (\delta_{obs} - \delta_{pred})}{\delta_{obs} \cdot C^{-1} \cdot \delta_{obs}}, \tag{4.14}$$

where δ_{obs} and δ_{pred} are the observed and modelled slips, respectively, and C is the data covariance matrix.

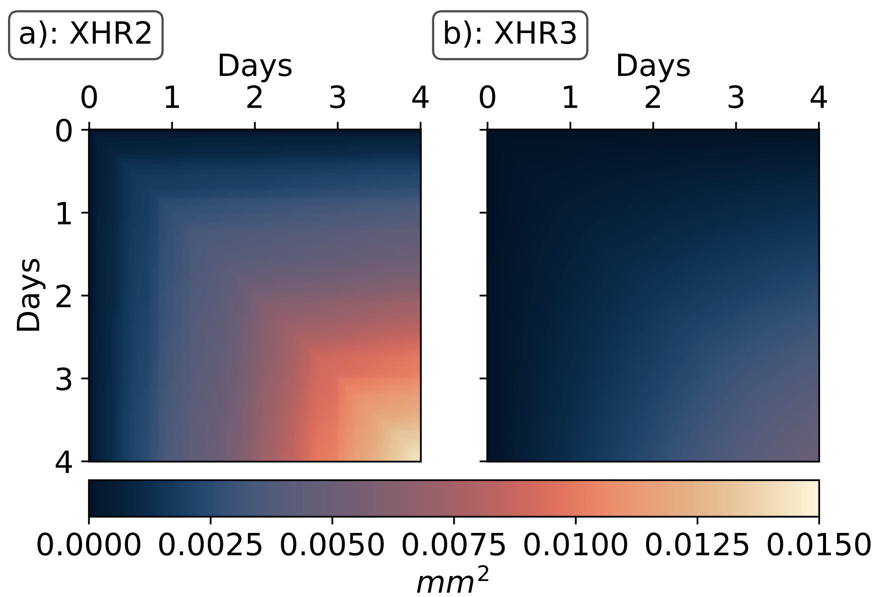

Figure 4.4: a) The covariance matrix of the earlier XHR2 creepmeter (1992 to 2005). b) The covariance matrix of the later XHR3 creepmeter (2009 to 2019). Note that XHR3 has lower noise than XHR2.

4.4.3 Parameter Search

To minimise the misfit, we use a two-step approach utilising basin-hopping. We first fit the data with a rapid Sequential Least Squares Programming (SLSQP) algorithm.

This SLSQP algorithm allows us to get a reasonable result quickly without needing a good initial guess for the parameters. This initial fitting converges and does well for the power-law flow, linear flow and rate and state friction below steady state (the healing regime). However, for both rate and state friction at a constant state rate near steady state ($\dot{\theta} \approx 0$) and rate and state friction above steady state (decreasing state, ($\dot{\theta} < 0$)), the SLSQP algorithm converges to a poor fit, failing to match the middle of the creep event. The output of the SLSQP algorithm is then used as an initial guess for a more precise fitting using a Nelder-Mead algorithm. We use this two-stage approach because using Nelder-Mead alone leads to unsatisfactory fitting due to poorly constrained initial conditions prior to the inclusion of the SLSQP fitting.

4.5 Results

All of the rheologies can match the rough shape of the creep events. Figure 4.5 shows six examples of the modelled slip. However, some rheologies tend to give a better match to the data: a smaller misfit. We use a bootstrapping approach to determine the 70% confidence interval on the percentage of events each rheological model best describes, based on their misfits (Figure 4.6).

We first discuss how well each rheology explains the shape of creep events, followed by discussing some individual fitting parameters.

4.5.1 Power-law flow

A simple analysis of the misfits suggests that power-law flow is the best model. It has the lowest misfit for 68–80% of the creep events (Figure 4.6, dark blue histogram). This model can capture the initial steep gradient of the creep event and its transition through the relatively sharp bend into the relatively flat portion at the end of the events (Figure 4.5 a), d) & e)).

4.5.2 Rate and state friction below steady state: the healing regime ($\dot{\theta} \approx 1$)

A second rheological model may be just as good — rate and state friction below steady state, in a healing regime. This model is the best fitting for 10–22% of events (Figure 4.6, yellow histogram).

It is difficult to interpret the misfits as the fit of the rate and state friction below steady state (the healing regime) model often overlap with the power-law flow model (compare the dark blue and yellow lines in Figure 4.5). Much like the power-law flow model, the rate and state friction below steady state model can capture the creep event's steep initial gradient, bend, and deceleration.

4.5.3 Rate and state friction above steady state: decreasing state regime ($\dot{\theta} < 0$)

The third best fitting is the rate and state friction above steady state (decreasing state) model, which best describes 4–12% of events (Figure 4.6, orange histogram).

Despite capturing the first few hours of the event well, the rate and state friction above steady state model fails to capture the bend of the creep event (i.e., the transition from accelerating to decelerating), which is often much sharper than these fits can turn. This failure to turn also results in an inability to flatten quickly enough. There are exceptions to this (e.g., Figure 4.5 c)), but this is the predominant drawback of this model.

4.5.4 Linear flow model

The fourth best fitting is the linear flow model, which can explain only 0–4% of events (Figure 4.6, light blue histogram).

This rheology has the opposite problem to the rate and state friction above steady state model in which it turns too sharply around the bend (e.g., Figure 4.5 c), d) & e)).

4.5.5 Rate and state friction at constant state rate near steady state ($\dot{\theta} \approx 0$)

The worst fitting model is the rate and state friction at a constant state rate near steady state model ($\dot{\theta} \approx 0$), which is the best fitting rheology for 0% of events (Figure 4.6, red histogram).

This model suffers from the same drawbacks as the rate and state friction above steady state (decreasing state) model, whereby it fails to turn sharply and flatten off quickly enough to match the data.

4.5.6 Fit parameters

To get a further plausibility check and to learn more about the properties of the system, we investigate the individual parameters of the fit (Figure 4.7).

The first column of Figure 4.7 shows the distribution of the initial slip rate for each rheological model: a) linear flow, c) power-law flow, f) rate and state friction at a constant state rate near steady state ($\dot{\theta} \approx 0$), h) rate and state friction above steady state (decreasing state) & k) rate and state friction below steady state (the healing regime). Although not identical, they all show a similarly flat distribution, which peaks at 0.1–0.2x10^{-7} ms^{-1}. The similarity of these distributions may also explain why most of the fits in Figure 4.5 do a relatively good job of explaining the initial acceleration of the creep event.

The second column in Figure 4.7 shows the distribution of the various 'time constants' present in each of the rheological models: b) linear flow, d) power-law flow, g) rate and state friction at a constant state rate near steady state ($\dot{\theta} \approx 0$), i) rate and state friction above steady state (decreasing state) & l) rate and state friction below steady state (the healing regime). These time constants control the rate at which the laws can turn and flatten off during deceleration. Most of these time constants are below 1 hour, except for rate and state below steady state (the healing regime), which has time constants up to 10 hours (note the change in x-axis limits in Figure 4.7 l)).

The remaining panels in Figure 4.7 show the distributions of any other fitting parameters used, notably n for the power-law flow law (panel e)) and B/A for the rate and state friction below steady state (panel m)).

The median value of the power-law constant, n, that we fit is 0.99, lower than the value estimated by Crough and Burford (1977) for their empirical power-law fit. However, our mean value is identical to the value of 1.6 proposed by Crough and Burford (1977). The median value being so close to 1 suggests that some of these fits may be linear flow, given that this is a special case of the power-law flow model with n = 1. This closeness of the two flow laws is also seen in Figure 4.5, where they occasionally lie on top of one another.

The rate and state friction below steady state model (Equation 4.10) contains the ratio of the two rate and state coefficients, B/A. If this ratio is below 1, the fault is velocity-strengthening, whereas if it is above 1, it is velocity-weakening. From Figure 4.7 m), we can see that the majority of scenarios lie above 1 (vertical grey dashed line). This suggests that the best fitting rate and state friction below steady state model (the healing regime) for most events is within the velocity-weakening regime.

4.6 Discussion

We fit five rheological models to creepmeter data from XHR. Several models fit the data poorly, particularly those associated with relaxation following a kick. However, we find two best-fitting scenarios that may be within error of one another: (1) power-law flow and (2) rate and state friction below steady state (the healing regime) in a velocity-weakening setting.

In Sections 4.6.1 & 4.6.2, we discuss each model's implications for the dynamics of creep events. In Section 4.6.3, we recognise that the rheological models we test are simple and that more complex models may be more suited to describing the displacement in creep events. We then discuss some of the potential origins of this complexity.

4.6.1 Option 1: Power-law flow

In the power-law flow model, slip rate $\propto$ applied stress^n. This relationship would suggest that the shallow fault follows this relation, typically reserved for studying ductile behaviour at depth (Montési, 2004; Passchier and Trouw, 2005). This is surprising given that the depths at which creep events occur (e.g., Bilham and Behr, 1992; Gladwin et al., 1994; Mortensen et al., 1977; Wei et al., 2013) are much shallower than the brittle-ductile transition (e.g., Sibson, 1977). Therefore, one would expect them to occur from a brittle process.

However, ductile deformation can occur in diagenetic conditions if fluids are abundant through a process called pressure solution creep where stress variations drive mass transfer (Passchier and Trouw, 2005). During this process, material is dissolved from grain boundaries at sites of high solubility. It diffuses down a stress-induced chemical potential gradient to be redeposited at nearby sites of low solubility (Passchier and Trouw, 2005). Pressure solution creep accommodates creep by grain-boundary sliding through diffusion creep (Gratier et al., 2011). This process concentrates weak phyllosilicates such as the saponite found in the SAFOD samples (**?**) and increases the percentage of these phyllosilicates from 10% to 50–70% in the creeping zone of the San Andreas Fault (Gratier et al., 2011). This concentration of phyllosilicate minerals, in particular saponite (Lockner et al., 2011), can help to explain the frictional weakness of the creeping section of the San Andreas Fault (Gratier et al., 2011).

Pressure solution creep is able to explain the 20 mmyr^{-1} creep rate at the SAFOD drill site (Gratier et al., 2011). However, at higher slip speeds, pressure solution creep will need to compete with other deformation mechanisms, such as dilation due to granular flow (Niemeijer and Spiers, 2006). Dilatancy has been observed during creep events using a series of orthogonal creepmeters along the San Andreas Fault (Bilham, 2022) and is thought to be accommodated by the rotation of large lens-shaped clay clasts found along the creeping faults (Bilham, 2022). This dilation should not be surprising given that shear strain results in dilatancy of granular materials (Kruyt and Rothenburg, 2016). More work is required to assess the interplay of pressure solution creep and dilation due to granular flow in the context of accommodating the slip occurring during creep events.

4.6.2 Option 2: Rate and state friction below steady state in a velocity-weakening regime (the healing regime, $\dot{\theta} \approx 1$

To explain the fit by rate and state friction below steady state (the healing regime), we propose a simple scenario whereby we only observe the end of a larger creep event at surface creepmeters. One could then imagine a sequence of events that produces such a scenario. A small-velocity-weakening fault patch at depth nucleates slip into a creep event, initially creating the strain offsets discussed in Chapter 3. This slip then propagates, and by the time it reaches the surface, we are near the end of the event. Here, the surface slip follows the slip at depth, with the whole fault slowing down everywhere with a modest change in stress.

This scenario represents a simple system. Here, there is slip at depth in the form of a creep event. When this slip reaches the surface, the upper parts of the fault follow along with what is happening at depth. The upper surface layer in question would require a low enough normal stress to provide only a modest resistance to acceleration. Further insight needs to be gained into the implications of this model and whether the assumption of a zero change in stress is truly plausible.

4.6.3 Option 3: More complex model required?

The scenario above for rate and state friction below steady state (the healing regime) differs from the previous two-layer models for creep events. Here, creep events occur in a lower layer and provide a 'kick' to an upper surface layer that then responds accordingly (Bilham and Behr, 1992; Scholz, 1998; Slater and Burford, 1979; Wei et al., 2013). These two-layer models can explain different aspects of aseismic fault behaviour, such as multi-year afterslip, creep events, and stable background slip, all occurring at the same location (Wei et al., 2013). This suggests that perhaps we need a more complex model to understand the mechanisms behind creep events.

4.6.3.1 Does the fit need more parts?

We have attempted to model the acceleration and deceleration in a creep event with a single approximation. However, we have neglected the full slip cycle and instead should have used a two-part fit to explain the acceleration and deceleration phases.

The accelerating portion of the creep may be modelled better using rate and state friction above steady state (in a decreasing state regime) up to the point of maximum slip rate. This would be similar to the observation that this regime does a good job explaining the nucleation of slow earthquakes (Helmstetter and Shaw, 2009). As we transition into a deceleration phase, we would cross over to below steady state (the healing regime) and, therefore, we should have modelled the end of the creep event using the rate and state below steady state regime.

This two-part fit may better explain the physical mechanisms behind creep events. Here, the upper surface would receive an increase in stress as slip propagates from depth, causing the surface to accelerate. Then, the whole fault system would decelerate together and cross below steady state and into the healing regime. The whole system would then continue to slow down while experiencing minimal changes in stress.

4.6.3.2 Does the fit require more complex physical models?

We have used the simplest analytical solutions for all five rheologies in our fitting approach, ignoring several fault zone processes.

One important fault zone process we have neglected is dilatancy, which is known to modulate fault slip rates (Iverson, 2005; Segall and Rice, 1995; Segall et al., 2010). Dilatancy could significantly change the functional form of some of the rate and state friction laws, making them able to fit the data better.

There is evidence for fault zone dilation during creep events in the form of water well level changes when creep events propagate past (Roeloffs et al., 1989; Rudnicki et al., 1993), measurements from orthogonal creepmeter setups (Bilham, 2022), and the proposed rotation during creep events of lens-shaped clay clasts found within the core of creeping faults at the surface (Bilham, 2022). One might even expect dilation to occur during creep events, given the depths of creep events (see Chapter 3), which places them at similar depths to the extent of the unconsolidated sedimentary sequence deposited since the Early Pliocene (Allen et al., 1946; Dibblee, 2006; Rogers, 1980) and that shear strain results in dilatancy of granular materials (Kruyt and Rothenburg, 2016).

Additional work is required to (1) incorporate more complex rheologies, (2) develop models that fit different parts of the full creep event cycle, and (3) determine the stress-slip rate relationships of cataclastic flow to assess its validity as a mechanism for creep events.

4.7 Conclusion

In this study, we have used the displacement time evolution of surface rupturing creep events to determine the physical process driving them. Using creepmeter data from Harris Ranch, we have minimised the misfit between the observed data and the displacement time evolution of five rheological models: (1) rate and state friction at a constant state rate near steady state ($\dot{\theta} \approx 0$), (2) rate and state friction above steady state (decreasing state regime), (3) rate and state friction below steady state (the healing regime), (4) power-law flow, and (5) linear flow. We find that a power-law flow model or rate and state friction below steady state model best fits the displacement evolution creep events. These two rheological models are often within error of one another and are both surprising. Additional work is required to understand the physical models these rheologies suggest or whether a more complex approach involving other fault zone processes, such as dilatancy and rupture front propagation, is required to explain the driving physics behind creep events better.

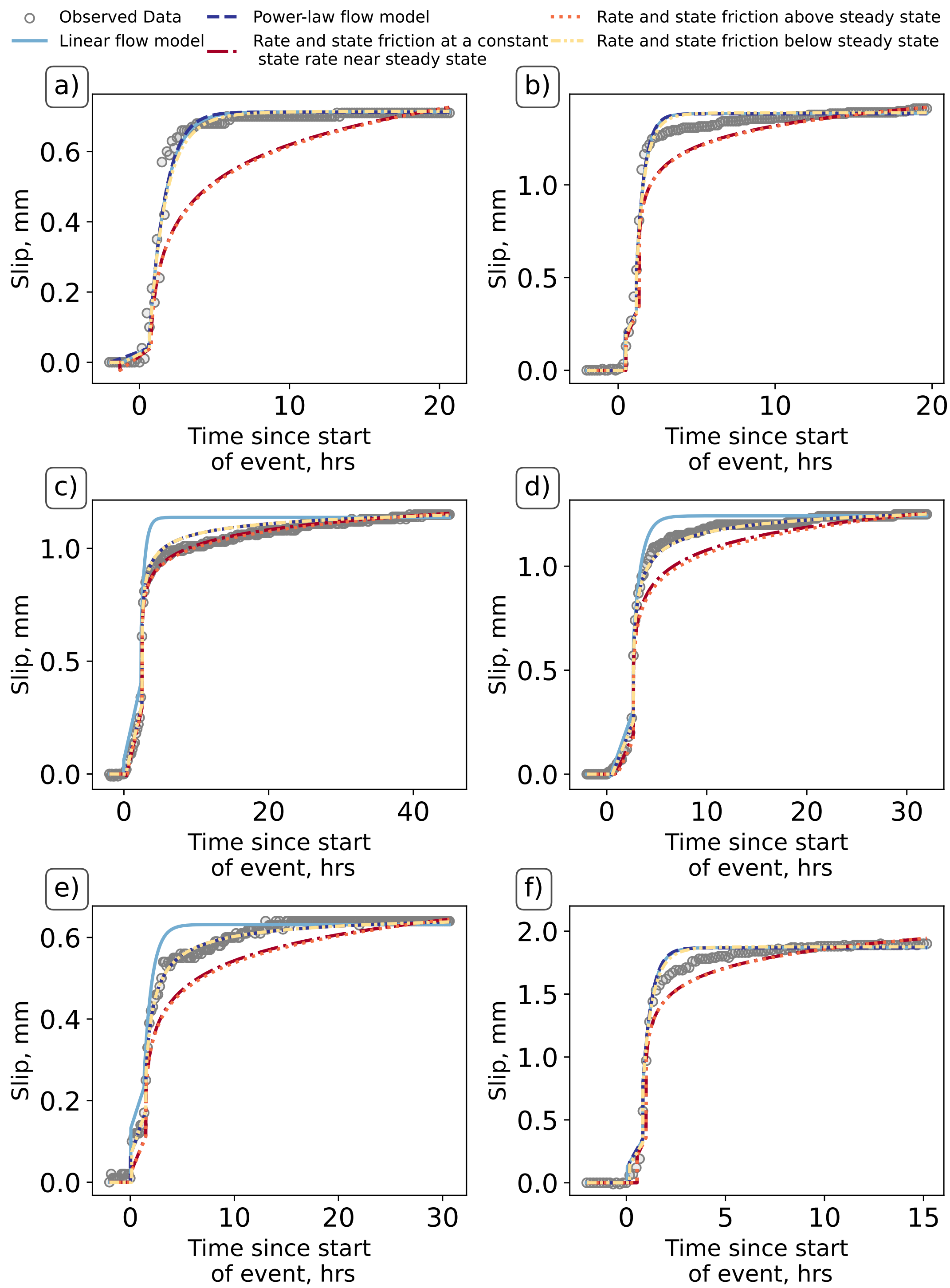

Figure 4.5: Six example events showing the five rheological fits. a) XHR 004, b) XHR 030, c) XHR 064, d) XHR 072, e) XHR 088 & f) XHR 105. Note that event codes refer to the events in the catalogue of Gittins and Hawthorne (2022a). The observed creepmeter data are grey circles. Linear flow and power-law flow are in light and dark blue, respectively. For the rate and state friction laws, the constant state rate near the steady state ($\dot{\theta} \approx 0$) is in red, the above steady state (decreasing state) is in orange, and the below steady state (healing regime) is in yellow.

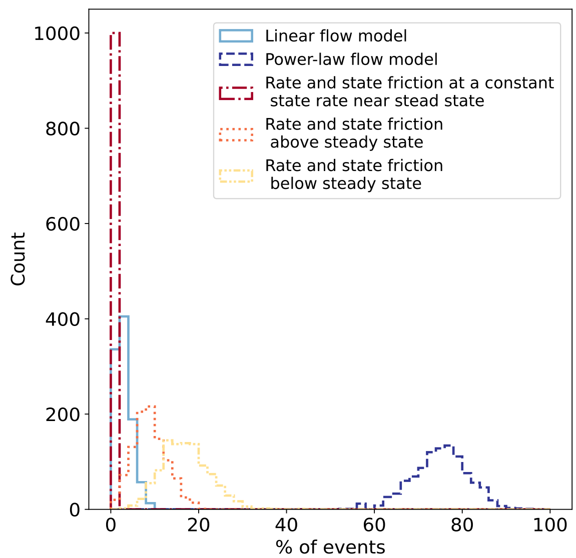

Figure 4.6: Histograms showing the percentage of events best fit by each rheology. Linear flow and power-law flow are in light and dark blue, respectively. For the rate and state friction laws, the constant state rate near steady state ($\dot{\theta} \approx 0$) is in red, the above steady state (decreasing state) is in orange, and the below steady state (healing regime) is in yellow.

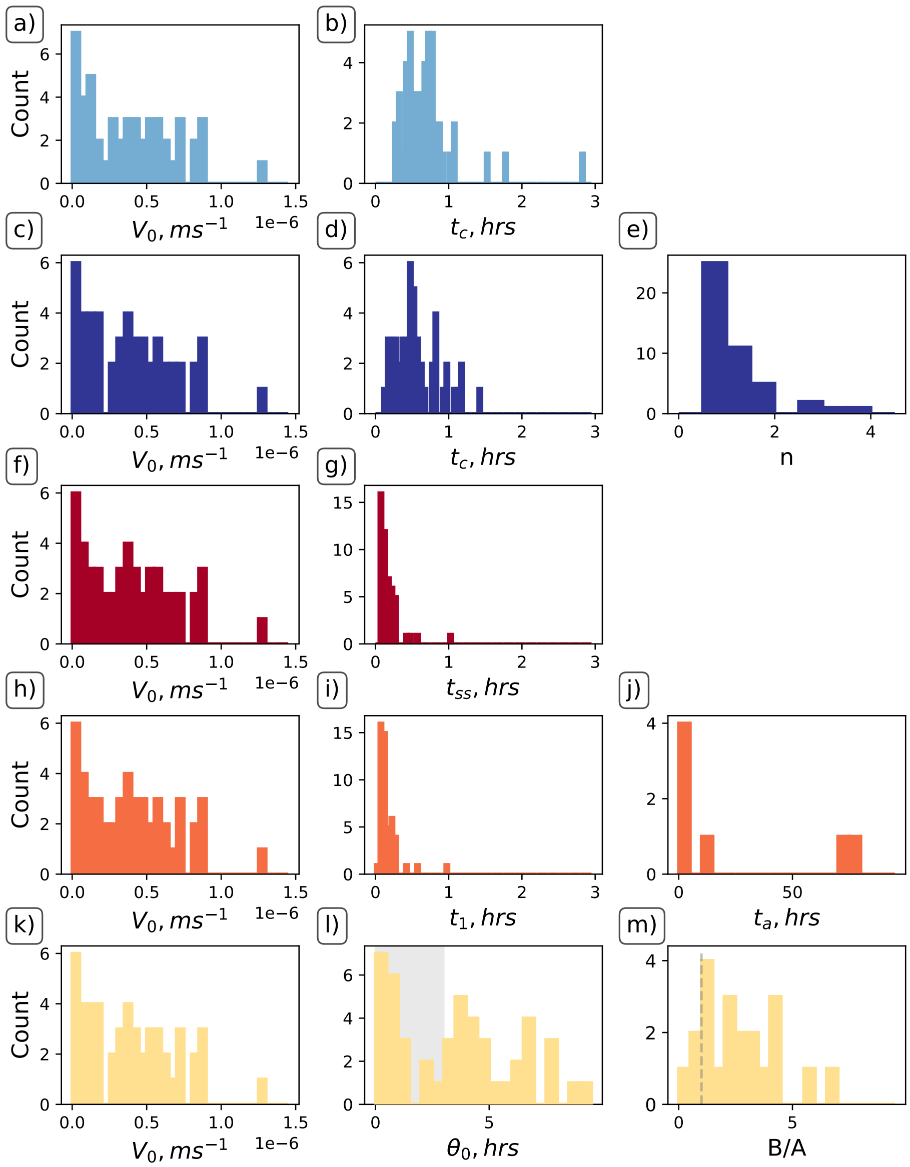

Figure 4.7: Distributions of the fitting parameters. a) & b) are the initial slip rate and time constant of the linear flow law. c), d), and e) are the power-law flow law's initial slip rate, time constant, and power-law exponent. f) & g) are the initial slip rate and time constant of the rate and state friction at a constant state rate near steady state ($\dot{\theta} \approx 0$). h), i) & j) are the initial slip rate, time constant, and time of tectonic loading in the rate and state friction law above steady state (decreasing state). k), l), and m) are the initial slip rate, time constant, and the ratio of the rate and state coefficients B/A of the rate and state friction law below the steady state (healing regime).

5

General conclusions and perspectives

5.1 Chapter aims 150
5.1.1 Chapter 2: Are Creep Events Big? Estimations of Along-strike Rupture Lengths 150
5.1.2 Chapter 3: Are Creep Events Big 2? Estimations of Rupture Location, Depth, and Magnitude 152
5.1.3 Chapter 4: Rheology of creep events 154
5.2 Future Work 155
5.3 Broader Outlook 157
5.4 Concluding remarks 159

In this thesis, I have used creepmeter and strainmeter observations to identify and characterise aseismic creep events along the creeping section of the San Andreas Fault and investigate possible driving mechanisms behind them. In this concluding chapter, I reflect on the work conducted in this thesis, present future avenues of research, and explore the implications for the broader field of aseismic creep events. In Section 5.1, I discuss the aims set out in Chapter 1. In Section 5.2, I present some possible avenues for advancing the work presented in this thesis. In Section 5.3, I explore where this may lead the field of aseismic creep events. Finally, in Section 5.4, I will present my final concluding remarks.

5.1 Chapter aims

In the introduction, I outlined the five main aims of this thesis. Here, I will reflect on these aims.

5.1.1 Chapter 2: Are Creep Events Big? Estimations of Along-strike Rupture Lengths

In Chapter 2, I use creepmeter data from 18 USGS creepmeters to understand some of the fundamental features of aseismic creep events along the San Andreas Fault. Despite knowing about these creep events since the 1960s (Steinbrugge and Zacher, 1960; Tocher, 1960; Whitten and Claire, 1960), we still did not know how far creep events extend along strike. Knowing how spatially large creep events are is important as it changes how significant they are in the slip dynamics of the San Andreas Fault.

It is well reported that the central San Andreas Fault is accumulating a moment deficit equivalent to a M_w 5.2–7.2 earthquake every 150 years (Maurer and Johnson, 2014; Michel et al., 2018; Ryder and Bürgmann, 2008). Alternatively, a burst of aseismic slip may further reduce the moment deficit (Khoshmanesh and Shirzaei, 2018b). Therefore, we must establish how large creep events are to determine what role a burst of creep events would have in further reducing the moment deficit.

Before estimating how large creep events are, we must know when they occur. There are global up-to-date seismic catalogues in seismology, yet no such catalogues for creep events exist. The most recent catalogue of creep events along the San Andreas Fault was published 25 years ago (Thurber and Sessions, 1998). Knowing when these creep events occur underpins all other work on them. Therefore, the first aim of this chapter was to:

> *Identify creep events in the creepmeter record from the central San Andreas Fault and produce the first open-access catalogue of creep events.*

Using a manually picked template event, I applied a cross-correlation approach to find creep events on 18 USGS creepmeters along the central San Andreas Fault. With this approach, I identified 2120 creep events between 1985 to 2020. These creep events varied in size, duration, and frequency across the creepmeter network. Some locations have frequent, small, short-duration events, and others have infrequent, large, long-duration events (compare XMM and XSJ in Figure 2.5). Using this catalogue, I observe that the fault accumulates over 50% of its slip in creep events near the surface. Even without further analysis, this catalogue showed the relative importance of creep events to the overall slip dynamics of the fault at shallow crustal levels.

With a catalogue of events now produced, I was able to complete the second aim of this chapter, which was to:

> *Determine the along-strike length of creep events along the San Andreas Fault.*

To determine the along-strike length of creep events, I compared the onset times of every creep event at one creepmeter to those at all others. I identified the percentage of events that occurred within 24 hours of each other.

Next, I conducted a bootstrapping and time-shifting analysis to test the null hypothesis that creep events at two creepmeters are coincidental. I rejected the null hypothesis if the bootstrapped distribution minus the shifted distribution lay above zero (see Figure 2.7). After comparing each creepmeter pair, I determined the rupture lengths of creep events.

I was able to find five distinct groups of events: (1) isolated events (Figure 2.9a), (2) small (<2 km) events recorded at two creepmeters (Figure 2.9b), (3) medium-sized (3-6 km) events recorded at multiple creepmeters (Figure 2.9c), (4) long (10 to 30 km) propagating events (Figure 2.9d), and (5) multi-strand ruptures (Figure 2.9e).

One common drawback often cited when studying creep events is their close association with rainfall (e.g., Roeloffs, 2001; Schulz et al., 1983). Therefore, I repeated the above analysis, removing events closely associated with rainfall. By doing this, I established if this removed the likelihood of any of the correlations found. I found that only the longest events had their correlations removed (see Figure 2.15a), and in fact, some creepmeters saw their correlations increase at the 70 % confidence level (see Figure 2.15c).

Within Chapter 2, I have produced a data product in the form of a catalogue of events and have demonstrated that creep events are not small isolated events. Instead, creep events propagate along-strike for several kilometres, rupturing multiple creepmeters at the surface.

5.1.2 Chapter 3: Are Creep Events Big 2? Estimations of Rupture Location, Depth, and Magnitude

I have used creepmeters to identify when creep events are occurring and give estimates of the horizontal rupture extent of creep events. However, creepmeters alone cannot tell us (1) the depth extent of creep events, (2) whether they occur all in the same location as repeated ruptures of the same fault patch, or (3) the moment released in each creep event.

Gladwin et al. (1994) identified strain offsets in borehole strainmeter data associated with creep events. Using these strain offsets, they determined the depth extent of creep events, noting that they originated from one fault location. Gladwin et al. (1994) illustrated how it was possible to use strainmeters to determine features of creep events not possible with creepmeters.

In Chapter 3, I used data from three USGS creepmeters and two borehole strainmeters (one USGS and one PBO) to investigate strain offsets associated with creep events in the Harris Ranch–Cienega Winery region of the San Andreas Fault.

Just as there was no catalogue of creep events, no catalogue of strain offsets associated with creep events exists. The first task in Chapter 3 was identifying strain offsets within the strainmeter data. I processed the strainmeter data to remove the 'noise' signals of borehole settling, tides, and atmospheric perturbations. I then manually picked the strain offsets associated with the observed surface creep events. I was able to identify 71 strain offsets associated with creep events.

The first aim of this chapter, once I identified strain offsets, was to:

Estimate the along-strike rupture location and depth extent of creep events.

To achieve this aim, I conducted a grid search analysis that modelled the strain offset produced by a slip patch at various fault locations and moments. Using the strain offsets observed, I could identify a range of along-strike regions from which these strain offsets originated. Using this finding, I inferred that creep events do not repeatedly rupture the same fault patch but rather that creep events rupture several different patches.

The second part of this aim was to constrain the depth of creep events. Using the five best grid search scenarios for each strain offset, I identified that the slip producing these creep event-associated strain offsets was not confined to shallow depths but happened over a range of depths. Following a bootstrapping approach, I found that most strain offsets originated from a depth of >4 km. This finding puts these strain offsets deeper than previous creep event depth estimates in the region (e.g., Mortensen et al., 1977).

The second aim of this chapter was to:

Estimate the M_w of creep events.

Using the grid search results, I identified the five best-fitting scenarios and thus M_w of the fault patch that produced each strain offset. Following a bootstrapping approach, I found that most events had a M_w between M_w 3–4, with a median M_w of 3.6.

The results of both Chapters 2 & 3 illustrate that creep events are not small repeated ruptures of the same fault patch but display a rich array of behaviours. These events can propagate several kilometres along-strike, occasionally triggering slip at several locations as they do so. Creep events also appear to be associated with strain offset produced by slip from much deeper in the fault system than previously estimated. These findings suggest that these creep events, although associated with rainfall at the surface, reflect a much deeper process. Creep events most likely play a more important role in the slip dynamics of the creeping section than previously they may have been assigned.

5.1.3 Chapter 4: Rheology of creep events

Having established that creep events arise from slip on fault patches at various depths and locations, the final piece to the puzzle is to understand what is causing them to occur. A variety of models have been previously proposed for how creep events originate from flow-law models in the 1970s/80s (e.g., Wesson, 1988) to more recent frictional models based upon rate and state friction (e.g., Scholz, 1998; Wei et al., 2013). Both of these groups of models have different implications for the driving physics behind creep events. Therefore, the aim of this chapter was to:

> *Determine the rheological model best capable of describing the displacement evolution of a creep event.*

I modelled the displacement evolution of creep events recorded at the Harris Ranch creepmeters to determine the rheological model capable of reproducing the shape of creep events. I aimed to minimise the misfit between the predicted displacement evolution of five rheological laws and the observed creepmeter data: (1) rate and state friction at a constant state rate near steady state ($\dot{\approx}0$), (2) rate and state friction above steady state (decreasing state regime, $\dot{<}0$), (3) rate and state friction below steady state (the healing regime, ≈ 1), (4) power-law flow, and (5) linear flow.

To do this, I used a two-stage basin-hopping approach. First, I minimised the misfit using a Sequential Least Squares Programming (SLSQP) algorithm, which allowed me to determine better initial conditions. Following this, I fitted the data again, this time with a Nelder-Mead algorithm, using the initial conditions calculated from the SLSQP fitting.

After assigning each creep event a rheological model based upon the misfit of each rheological law, I conducted a bootstrapping approach, which allowed me to calculate the 70 % confidence intervals of the total percentage of events best described by each rheological model. The two best-fitting models were power-law flow and rate and state friction below steady state. These rheologies were often within error of one another.

A power-law flow model would suggest that the shallow crust is adhering to the slip rate $\propto$ applied stress$^{\mathrm{n}}$ relationship implied by power-law flow. One possible mechanism for accommodating this ductile flow law at diagenetic conditions is through pressure solution creep, a stress-driven fluid-assisted mass transfer process. Pressure solution creep is able to accommodate aseismic slip through grain boundary sliding accommodated by diffusion creep. A rate and state friction below steady state model in a velocity weakening setting would suggest that creep events are caused by slip on patches at depth and that creepmeters only observe the end of the event as it reaches the surface. They then follow the slip at depth as the whole fault decelerates with minimum changes in stress.

The rheological models I have used are relatively simple. Therefore, the work in Chapter 4 provides the first step towards understanding what is causing creep events. Further investigations are needed into the rheological model for creep events, incorporating more complex rheologies such as shear-induced dilatancy or a combination of different rheological models.

5.2 Future Work

The research presented in this thesis has some natural extensions, some of which I detail below:

- **Apply the grid search approach described in Chapter 3 to creep event-associated strain offsets in other fault locations, i.e., Parkfield, CA.** In Chapter 3, I used a grid search method at the northern end of the creeping section. I identified the depths, moments, and along-strike locations of several strain offsets associated with creep events. This methodology could be applied to the Parkfield region, where greater instrument density and complex along-strike rupture behaviours of creep events exist. One potential drawback is that the creep events in the Parkfield region have an amplitude of <1 mm. Therefore, their associated strain offsets may be smaller than those observed at the northern end of the creeping section. Identifying them within the strainmeter records would likely require more close attention. Incorporating the nearby dilatometer data would also add a new constraint on any model produced.

- **Combine the event detection outlined in Chapter 2 with the rheological modelling in Chapter 4 to produce a more robust event detection algorithm.** One of the main issues with the detection algorithm in Chapter 2 is that it is poor at constraining the end of a creep event, leading to overestimates of the duration of creep events. To improve on the estimate of creep event duration, we could incorporate the rheology fitting methodology. The best fitting rheology I found was the power-law flow model, which has a similar functional form to the one proposed by Crough and Burford (1977) and Wesson (1988) for describing the shape of a creep event. The main difference, however, is that the model of Wesson (1988) contains the parameter representing the creep event's final displacement. By modelling the creep event forward and continually adjusting the fit of the rheological model each time, we should approach a minimum in the misfit function around the end of the creep event.

- **Apply the rheological modelling approach in Chapter 4 to other instruments.** In Chapter 4, I only applied the rheological modelling to one creepmeter with a clearly defined consistent shape. Other creepmeters record creep events that have different shapes and gradients that different rheological models may better explain than those that worked best for XHR. Therefore, a logical next step would be to apply this rheological modelling to all other creep events identified in Chapter 2. The fitting framework set out in Chapter 4 also does not need to be confined to just creepmeter data and could also be applied to the strain offsets described in Chapter 3.

- **More advanced rheological modelling of creep events.** In Chapter 4, I outlined a methodology for determining the driving rheology of creep events based on their functional form. This approach, however, concentrated on events from one creepmeter location (XHR). Even at this location, rheological modelling was only attempted for events with one slip phase, when many creep events often show two or more slip phases. One could repeat the process by modifying Equation 4.13 each time, adding additional rheological fits per phase of the creep event. But this leads to a question as to whether the misfit for both phases should be calculated together or whether each phase of the creep event is a separate phase of slip and needs to be treated separately. Another additional complexity not introduced into this rheological fitting is shear-induced dilatancy, which is known to stabilise slip (e.g., Iverson, 2005; Segall and Rice, 1995; Segall et al., 2010). Possible evidence for dilatancy has been observed during creep events along the San Andreas Fault. Firstly, changes in water well levels are reported during the passing of creep events caused by the deformation of aquifers (Roeloffs et al., 1989; Rudnicki et al., 1993). Secondly, dilatancy may also be caused by the rotation of lens-shaped clay clasts within the fault zone. These lens-shaped clay clasts are synonymous with creeping faults and have been found during creepmeter installations on the Charman, Anatolian, and San Andreas Faults (Bilham, 2022).

5.3 Broader Outlook

At the beginning of this thesis, I introduced the idea that creep events may be a shallow analogue for slow-slip events and be part of the slow-earthquake family. By completing the future work laid out in the first two points above, we will be in a situation where we can determine the moment duration scaling of creep events and see if they lie within the $M_0 \propto T$ scaling of the slow earthquake family.

If this is the case, creep events could form the foundation for discriminating between driving models for the slow earthquake family. They could provide a unique opportunity to study this family of events. As creep events extend to the surface, the faults producing them are easily accessible for direct sampling and measurements. We could directly sample the fault material to test different rheological models and continuously monitor them using geodetic instruments. We would also not have to wait long for events, given that creep events occur regularly compared to subduction zone slow slip events.

If they are found to lie elsewhere within moment-duration space, then more work needs to be conducted to understand the driving physics behind these events and why they are occurring.

More locally to the San Andreas Fault, I believe that with the proposal of the Near-Fault Observatory (also known as the Rupture and Fault Zone Observatory) (Aderhold et al., 2022), the interest in understanding the full spectrum of fault slip along the San Andreas Fault will increase. The San Andreas Fault has such a diverse spectrum of fault slip from slow slip events and tremor at the base (e.g., Rousset et al., 2019a; Shelly, 2017), to repeating earthquakes in the middle (e.g., Waldhauser and Schaff, 2021), the regular M_w 6 Parkfield earthquakes (e.g., Bakun and Lindh, 1985) and its associated afterslip (e.g., Langbein, 2006) near the surface, and the aseismic creep events that form the basis of this thesis (e.g., Schulz, 1989). With such a variety of fault behaviours occurring atop one another, it seems unlikely that these phenomena do not interact on some time scales. Slater and Burford (1979) proposed that a deeper slip of weeks to months may trigger several surface creep events. With the ability to observe deep, slow slip (e.g., Rousset et al., 2019a) combined with a comprehensive repeating earthquake catalogue (e.g., Waldhauser and Schaff, 2021) and a consistent way to observe and model creep events and their associated strain offsets (built upon the work in this thesis) in the next 10-15 years we may be able to unify all these processes on the fault to gain a deeper understanding of the overall slip dynamics of the creeping region of the San Andreas Fault.

5.4 Concluding remarks

I have analysed creepmeter and strainmeter data in this thesis to investigate surface rupturing creep events along the central San Andreas Fault, CA. Using a cross-correlation approach on creepmeter data, I have identified 2120 creep events between 1985 and 2020. I correlated these events across creepmeters and identified five distinct length scale behaviours for creep events: (1) isolated events, (2) small (<2 km) events recorded at two creepmeters, (3) medium-sized (3-6 km) events recorded at multiple creepmeters, (4) long (10 to 30 km) propagating events, and (5) multi-strand ruptures. By assessing these correlations in light of rainfall, I have shown that creep events can propagate several kilometres along strike without the aid of rainfall triggering and thus must be driven by a process at depth.

For the creep events observed at the Harris Ranch and Cienega Winery, I have identified 71 strain offsets associated with the various slip phases of surface rupturing creep events. I have modelled these strain offsets using a homogeneous elastic half-space within a grid search approach to identify the along-strike location, depth, and magnitude of the patch of fault that created these strain offsets. By doing this, I found that these strain offsets result from a slip in at various locations, indicating that these creep events do not arise from a repeated slip on one fault patch. The depth of the patch of slip that causes these strain offsets is much deeper than previous estimates for creep events in the area, with many likely originating from below 4 km depth. Most of the magnitudes of the slip producing these strain offsets are between M_w 3–4. Combining all these, I have shown that creep events are not small, shallow events induced by rainfall. Instead, creep events result from slip with a magnitude similar to that of nearby earthquakes, occurring below 4 km that can propagate several kilometres along-strike, potentially triggering other fault patches along the way.

Finally, I conducted rheological modelling on the shape of creep events to constrain their driving rheology. By minimising the misfit of various rheological laws, I was able to show that two potential models can fit the shape of creep events relatively well: (1)

a power law flow model or (2) rate and state friction below steady state within the velocity weakening regime. These surprising rheologies have different consequences for the driving mechanisms behind creep events.

In this thesis, I have reanalysed an underutilised dataset to answer some fundamental questions about creep events that we have been asking since the 1970s. By conducting new careful analysis and applying more modern techniques than previously used on this dataset, this thesis has generated new insight into one of the longest continuously monitored fault phenomena observed globally — the aseismic creep event.

APPENDIX A

Supporting Material for 'Are Creep Events Big? Estimations of Along-strike Rupture Lengths'

A.1 Supplementary Text S1 162
A.2 Creep Catalog 166
A.3 Creep Booklets 168
A.4 Supplementary Figures 169

Contents of this file

1. Supplementary Text S1

2. Figures A1 to A32

Additional Supporting Information (Files uploaded separately)

1. Creep catalogue

2. Creep Booklet: Scaled to event

3. Creep Booklet: Scaled to all creepmeters

Introduction This supplementary information consists of four parts. In part 1, we provide a more detailed methodology of our creep event detections. Part 2 consists of CSV files containing our various creep event catalogues used in our multi-creepmeter event detections. Part 3 is the two creep booklets used in this study. Part 4 includes all the supplementary figures referenced in the main text and figures of each creepmeter's percentages with every other creepmeter used in this study.

A.1 Supplementary Text S1

To study creep events in greater detail requires knowing when creep events occur in the creepmeter record. To detect creep events, we have used cross-correlation techniques to reduce the bias found in manual detections and produce more consistent start and end times. Before proceeding with the cross-correlation, we interpolated the creepmeter record to ensure that the data were spaced evenly at 10-minute intervals, except for Melendy Ranch (XMR) creepmeter, whose sampling frequency changed to 1-minute on 6^{th} September 2018. We, therefore, split the XMR record into two based on sampling frequency before proceeding.

Creep events at each creepmeter have different characteristic shapes; therefore, we picked a creep event for each creepmeter that captured the creepmeter's characteristic creep event shape that acted as a template for cross-correlation. We identified each template's start and end times before pre-processing to remove any error in the start time introduced during these processes. Then, the templates were extracted from the processed creep record using their start and end times before conducting the cross-correlation.

We removed a background trend from each creepmeter record so that creep events are easier to isolate within the creep record. In addition, we applied a zero-phase Butterworth bandpass filter at periods of 2 hours and 5 days to remove short- and long-period noise in the creepmeter record. Filtering the creepmeter data improved detection accuracy as it reduced error in the start time of the creep event and removed long-period non-creep event-related trends.

Using our template timings, we conducted a rough cross-correlation for each creepmeter on the filtered creep event record. We identified peaks in the cross-correlation that exceeded a creepmeter dependant threshold between 0.05 and 0.2, allowing only one peak per 40 minutes. These thresholds were set relatively low, allowing for many false positives so that creep events that had a different shape could still be identified. These peak times were treated as potential creep events; however, their star times needed improvement. We estimated the start time of these potential events by examining the running average of the slip in hourly windows just before and after the cross-correlation peak. For the creepmeters north of Slacks Canyon (XSC), this time window varied from 1–5 days before the potential start time and 12 hours afterwards. Creepmeters south of XSC required a shorter variable window of 6 hours to 3 days before and 12 hours after the potential start time. The change in the length of the time window from north to south accounted for the difference in creep styles between the northern and southern ends of the creeping section. The creep event start time is identified as the first time the slip rate exceeds the background slip rate within the examined window. This threshold value varies from creepmeter to creepmeter but is always the value of the 99th percentile of the average slip in hourly windows for the entire creepmeter record.

To improve the start time further, we also used a method involving the shape of a bandpass-filtered creep event. When a creep event is bandpass filtered, it develops a characteristic shape in which it has a large trough where the event begins. We used this to improve the detection start time by shifting the start time to the bottom of the nearest trough to our previous start time estimate.

Once we identified the start time, we used a similar approach to find the end of the creep event. To estimate the end time of our potential events, we examined the running average of the slip in overlapping daily windows following the start time. We estimated the end time to be the first time after the start time that the slip rate fell below a threshold value that represented the average slip per day at the background slip rate. This threshold was different for events affected by 28^{th} September 2004 Parkfield earthquake. For those creepmeters unaffected by the afterslip following the earthquake, the threshold was set at the 90^{th} percentile of the daily slip for all of the windows used. However, a lower 80^{th} percentile was used for events affected by this earthquake. This 80th percentile overestimates the length of creep events in the first nine months after the 2004 Parkfield earthquake. To better isolate the end time of creep events in these first nine months, we extract the daily slip windows for these nine months and determine the end time of events in these nine months at the 90^{th} percentile of the daily slip windows.

Once the start and end times were deduced, we calculated the slip that occurred during the creep event by differencing the measured values of the slip from the start and end of the creep event. To validate the approach used in calculating the slip values, we conducted a power spectral analysis. For this approach to be valid, the noise on the creepmeter is required to be a form of random walk noise as opposed to white noise. At long periods, the power spectrum for each has a slope of -1.98 ± 0.005. The only exception to this is creepmeter X461, which has a slope closer to -1.87 ± 0.005. We believe this creepmeter does not have the same power spectrum slope. Its location is more problematic than the other creepmeters (steeper slope, rainfall influenced, and soil relaxation towards a nearby pipeline) (Roeloffs, 2001)). At shorter periods (<1 hour), the power spectra become frequency-independent and more characteristic of white noise. If the slope of the power spectra is equal to 2, then the noise is classified as random-walk noise and is caused by small random motions of the geodetic instrument (Langbein et al., 1993; Langbein and Johnson, 1997). We have concluded that the majority of noise seen in the creepmeter data is in the form of random walk noise. This validated the approach of taking slip measurements as the difference between a start and end-points as the error in the data between these two points is incorporated in the error of the slip measurement.

The initial set of detection includes very short-duration detections that are steps between data points. These steps are caused by earthquakes or stick-slip instrumental artefacts (Bilham and Castillo, 2020). We remove these steps by including the criteria that our creep event detections must be longer than 10 minutes in duration.

To make the detections more robust, we also removed some detections based on their slip. We find detections with tiny slip values are often found at times when the data is particularly noisy. To remove these, we isolated the top 10% largest slip values from each creepmeter's detections and identified a minimum slip threshold for the detection to be classified as a creep event. This threshold is set at 1% of the slip of the median value of the largest 10% of creep event detections at each creepmeter.

Creep events may have one or more steps within them, leading to double detections via the detection algorithm. The detection process distinguishes between multiple humped creep events and temporally close single hump creep events by determining if the daily slip value at the end of the first hump is small enough to fall below the creep event end threshold value. If the creep event has multiple humps, it will have two detections within the creep record (one for each hump), which will have the same end time. Therefore, we remove duplicate events based on their end times as well as their start times. Following on from this, we have flagged any detections that have a start or end time that lies within the creep record that was filled in by interpolation. These detections are unreliable as their large slip values may be due to either the temporally short steps mentioned above or due to a creep event.

Once the detections have been through this process, they are plotted and checked manually to ensure only real creep events are carried forward into further work based on these creep events. These detections we remove usually consist of steps in the data surrounded by noise, meaning their start times are detected early, which increases their duration above the 10-minute duration cut-off designed to remove them.

A final manual correction was then completed on each real creep event detection to achieve the best possible pick for the start of the creep event guided by the start time detected using the above approach. As a result, we have produced a finalized creep event catalogue for each creepmeter, which included 2120 creep events.

A.2 Creep Catalog

Here, we provide a brief description of our creep event catalogue. The 18 creepmeters used in this study have a creep event catalogue, provided here as 18 CSV files (available from Gittins and Hawthorne (2022b); **?**. These catalogues include information on the start time of the creep event and its corresponding displacement. We have also included estimates of the end time, end displacement, and the slip and duration of the creep event. It is important to note that the end of a creep event is less well-defined than the beginning; therefore, these end times are only to be used as a guide. The reader should determine the end of the creep event themselves if using these catalogues for future work.

Our catalogue of multi-creepmeter events is also provided as a CSV file. This catalogue is split into creepmeter columns. If an event is within 24 hours of another event at another creepmeter, then the start time of that event is included in the creepmeter column, with potential multi-creepmeter events lying on the same row. Thus, this catalogue does include all events within 24 hours of one another. It, therefore, should be interpreted and used after consultation of the relevant Figures S1-S17, which provide the percentage of creep events observed at each creepmeter pair, indicating if the relationship between these events is genuine or likely to have occurred by chance.

Data Set S1. Catalogue of creep events recorded at the San Juan Bautista (XSJ2/XSJ3) creepmeter as a CSV file.

Data Set S2. Catalogue of creep events recorded at the Harris Ranch (XHR2/XHR3) creepmeter as a CSV file.

Data Set S3. Catalogue of creep events recorded at the Cienega Winery Central (CWC3) creepmeter as a CSV file.

Data Set S4. Catalogue of creep events recorded at the Cienega Winery North

(CWN1) creepmeter as a CSV file.

Data Set S5. Catalogue of creep events recorded at the Melendy Ranch (XMR1) creepmeter as a CSV file.

Data Set S6. Catalogue of creep events recorded at the Slacks Canyon (XSC1) creepmeter as a CSV file.

Data Set S7. Catalogue of creep events recorded at the Middle Mountain (XMM1) creepmeter as a CSV file.

Data Set S8. Catalogue of creep events recorded at the Middle Ridge (XMD1) creepmeter as a CSV file.

Data Set S9. Catalogue of creep events recorded at the Varian (XVA1) creepmeter as a CSV file.

Data Set S10. Catalogue of creep events recorded at the Roberson, SW trace (XRSW) creepmeter as a CSV file.

Data Set S11. Catalogue of creep events recorded at the Parkfield (XPK1/XPK2) creepmeter as a CSV file.

Data Set S12. Catalogue of creep events recorded at the Taylor Ranch (XTA1) creepmeter as a CSV file.

Data Set S13. Catalogue of creep events recorded at the Hearst, SW trace (XHSW) creepmeter as a CSV file.

Data Set S14. Catalogue of creep events recorded at the Work Ranch (WKR1) creepmeter as a CSV file.

Data Set S15. Catalogue of creep events recorded at the Carr Ranch (CRR1) creepmeter as a CSV file.

Data Set S16. Catalogue of creep events recorded at the Gold Hill (XGH1) creepmeter as a CSV file.

Data Set S17. Catalogue of creep events recorded at the Highway 46 (C46) creepmeter as a CSV file.

Data Set S18. Catalogue of creep events recorded at the Highway 46 (X46) creepmeter as a CSV file.

Data Set S19. Catalogue of creep events recorded within 24 hours of a creep event at another creepmeter as a CSV file.

A.3 Creep Booklets

Here, we include two booklets depicting creep events; one scaled to the creep event itself and another scaled to the maximum slip of all of the records. Each page of the booklet includes one creep event, with the time of the event and the creepmeter that recorded it, noted at the top of the page. We have stacked the creepmeter records one on top of another, with the most northern creepmeter (XSJ) at the top and the most southern creepmeter (X46) at the bottom. The start and end times of the creep event are shown as vertical dashed lines across all plots, and the event is shown in colour. If another event at another creepmeter occurs in the window plotted, we highlight this by giving that trace a faint colour with vertical dashed grey lines to highlight the event on that plot only. All of the plots are rescaled so that the creep event's start time is when all of the creepmeter traces will cross the x-axis.

Data Set S20. Booklet of creep events scaled to the event itself.

Data Set S21. Booklet of creep events scaled to the maximum slip in the window of all of the 18 creepmeters.

A.4 Supplementary Figures

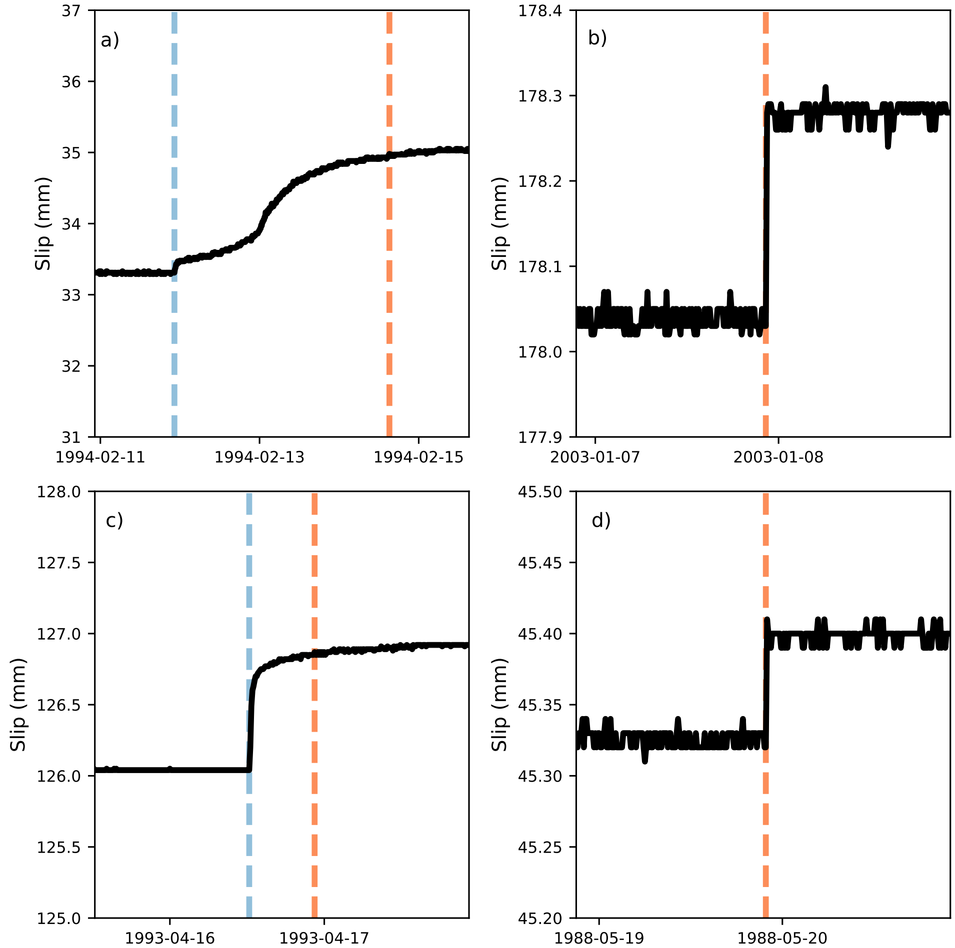

Figure A.1: Examples of creep event and non-creep event-related signals at both CWN and XMM. The blue vertical dashed lines indicate the start of the event, and the orange dashed line is the end of the event. a) Example of creep event at CWN. b) Example of a non-creep event-related step at CWN. c) Example of creep event at XMM. d) Example of a non-creep event-related step at XMM.

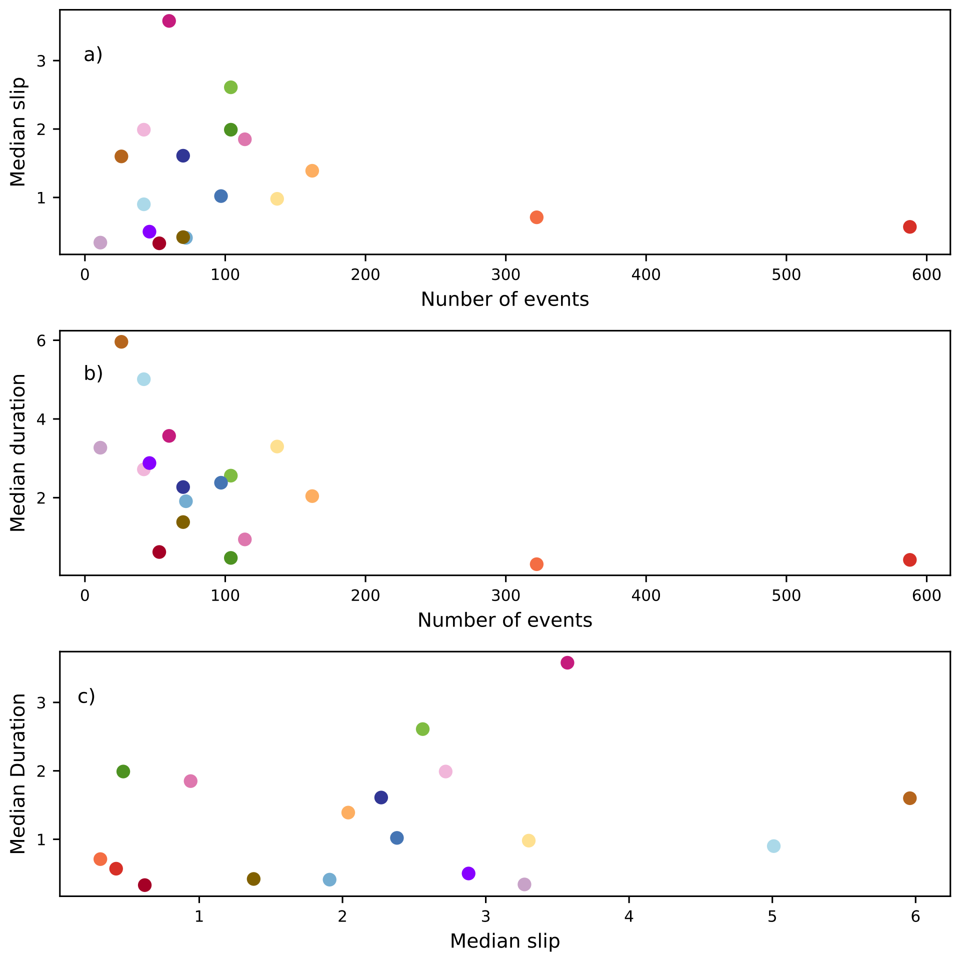

Figure A.2: Scatter plots plotting slip, duration and number of events against one another. a) Median slip vs. number of events at each creepmeter. b) Median duration vs. number of events at each creepmeter. c) Median slip vs. medium duration of events at each creepmeter.

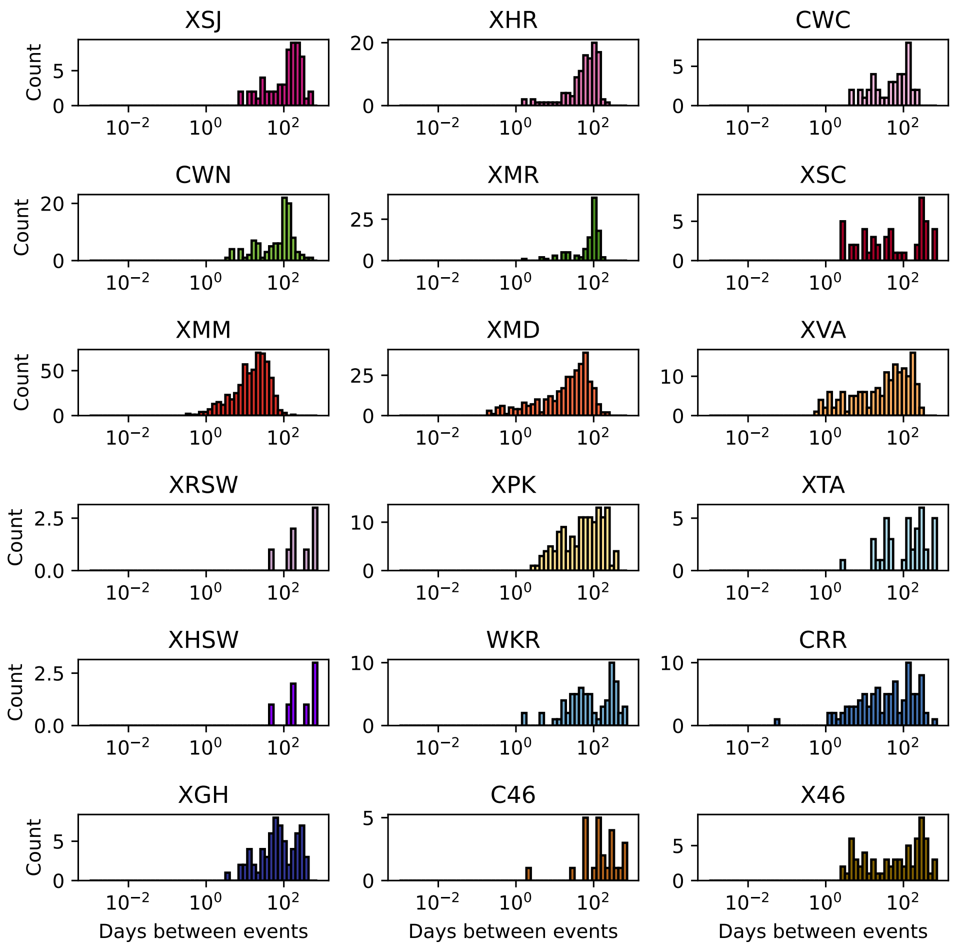

Figure A.3: Recurrence intervals of creep events at the 18 USGS creepmeters used in this study.

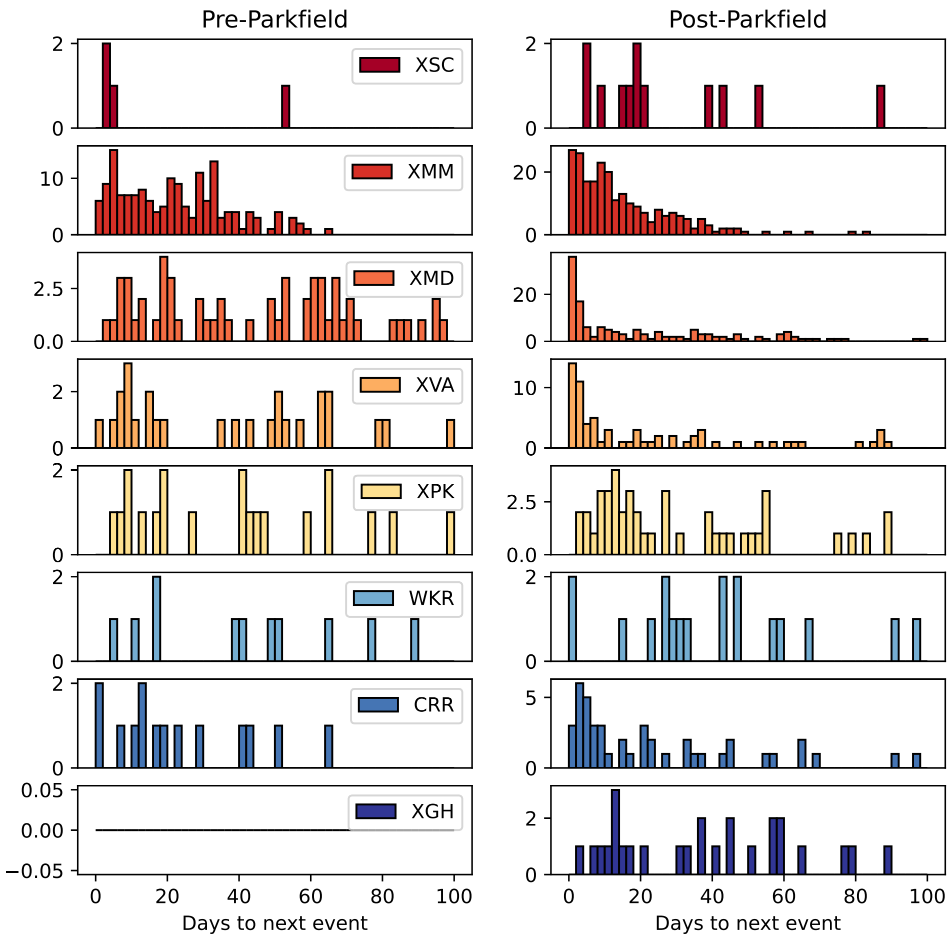

Figure A.4: Recurrence intervals of creep events at southern creepmeters before and after the 2004 Parkfield earthquake.

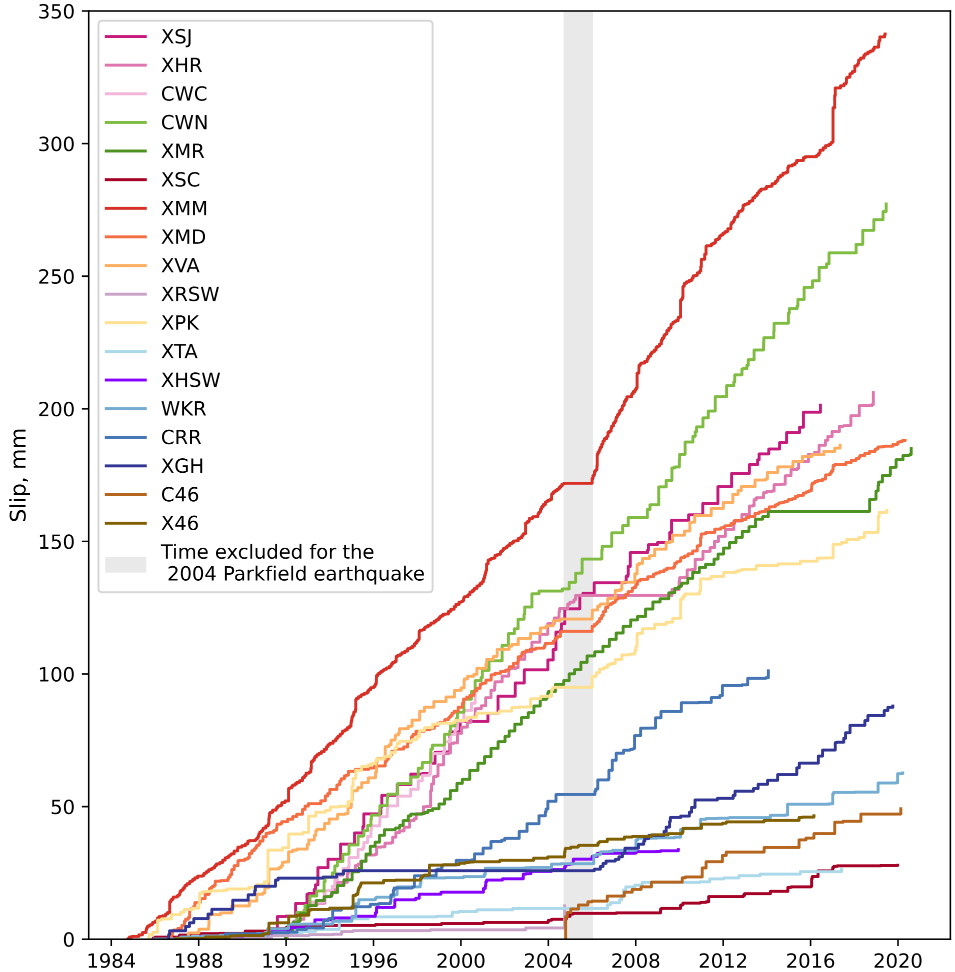

Figure A.5: Creep records from 18 USGS creepmeters showing the timing of creep events. The inter-event slip has been set to 0. The grey vertical band shows the times when creep events were removed from our analysis of southern creepmeters due to the 2004 Parkfield Earthquake.

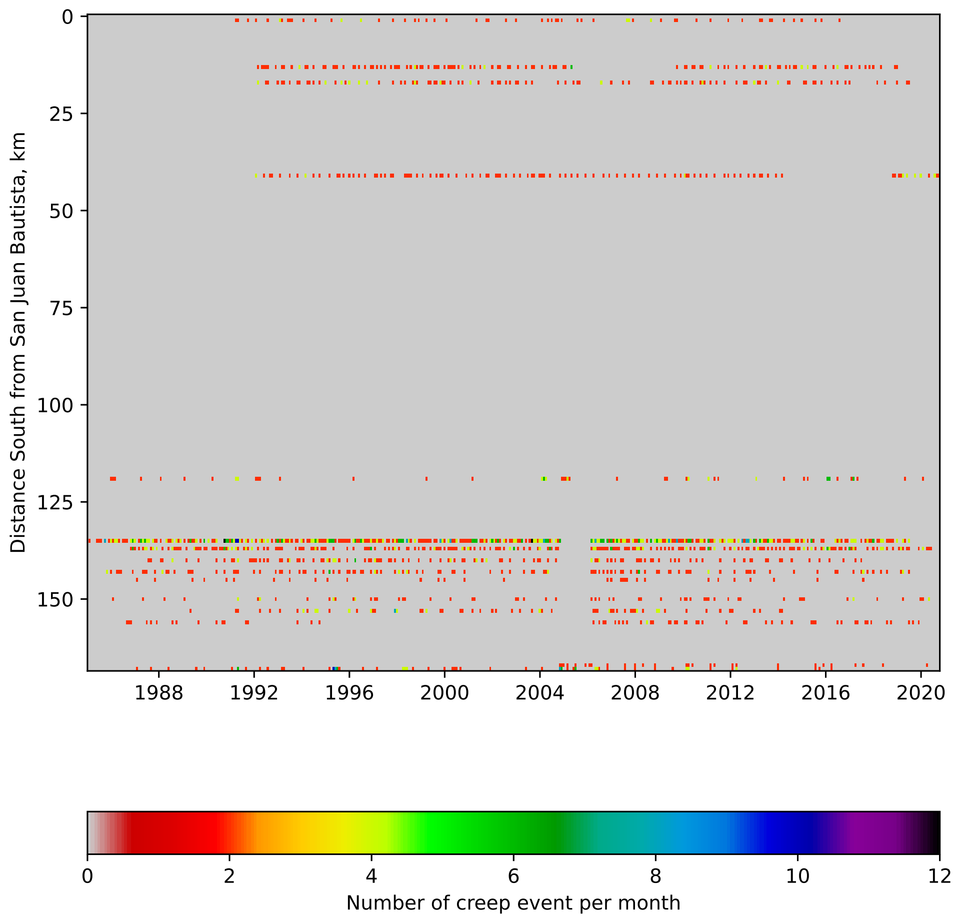

Figure A.6: Spatio-temporal plot of the number of creep events per month at each of the 18 USGS creepmeters, ordered by distance from San Juan Bautista. 28/Sep/2004 - 01/Jan/2006 excluded for southern creepmeters.

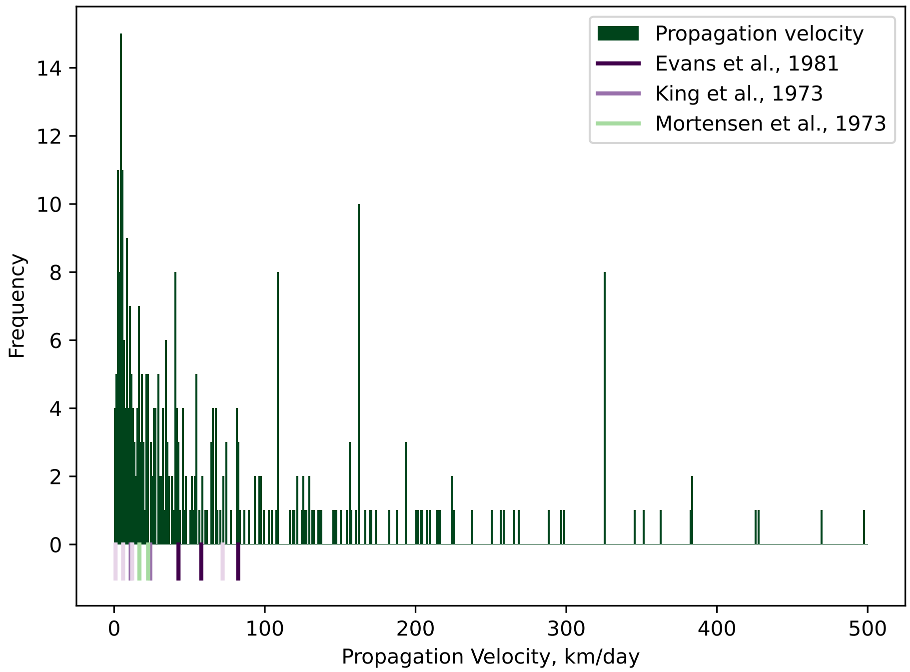

Figure A.7: Propagation velocities of all creep events found within 24 hours of a creep event at any other creepmeter. The vertical coloured lines below 0 indicate the propagation velocities reported by Evans et al. (1981) (dark purple), King et al. (1973) (light purple) and Mortensen et al. (1977) (light green).

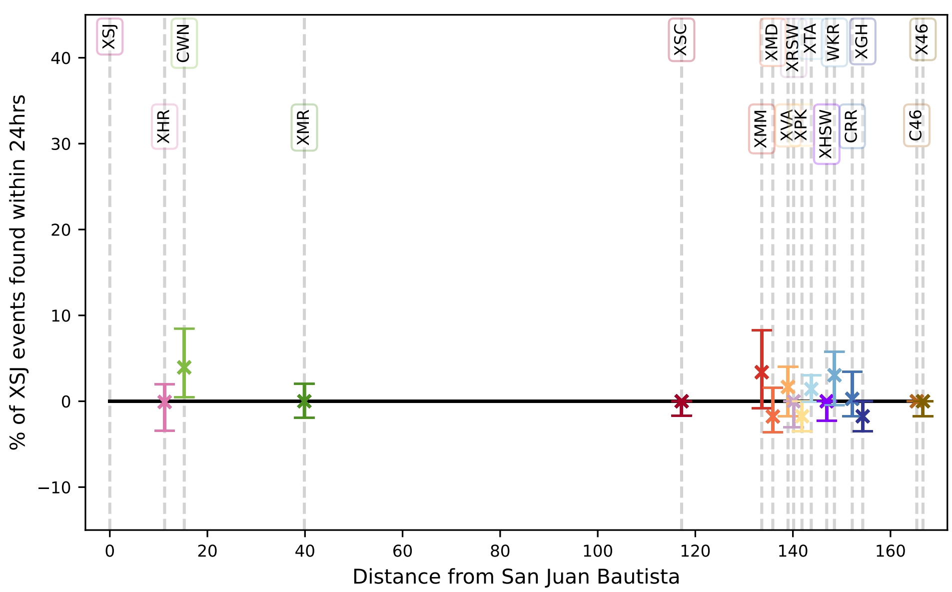

Figure A.8: Percentage of XSJ events observed at all other creepmeters, scaled with distance.

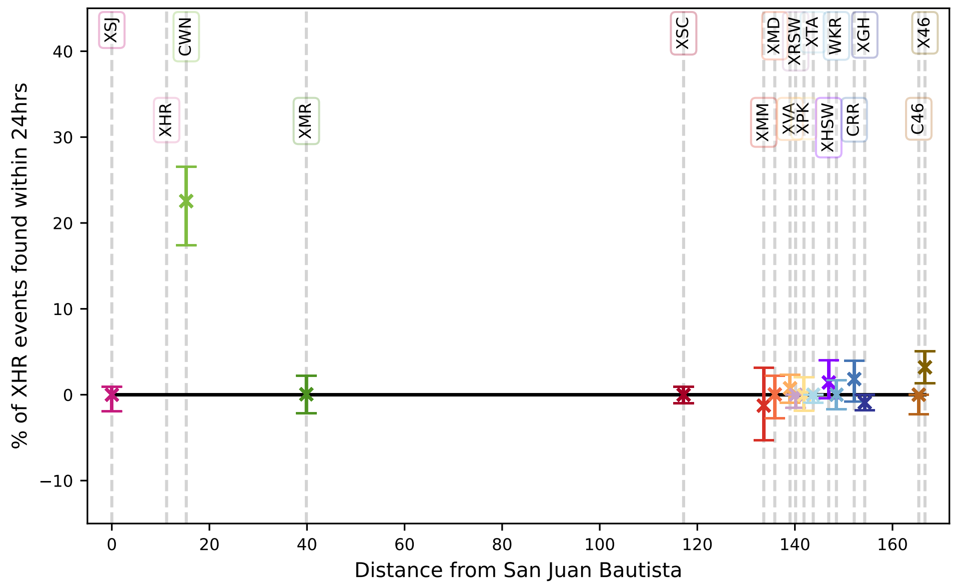

Figure A.9: Percentage of XHR events observed at all other creepmeters, scaled with distance.

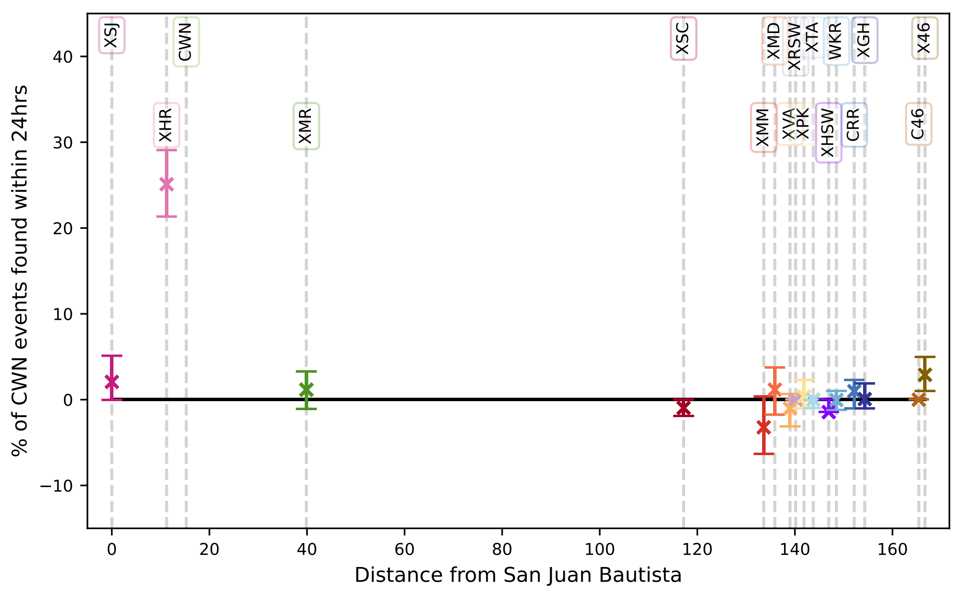

Figure A.10: Percentage of CWN events observed at all other creepmeters, scaled with distance.

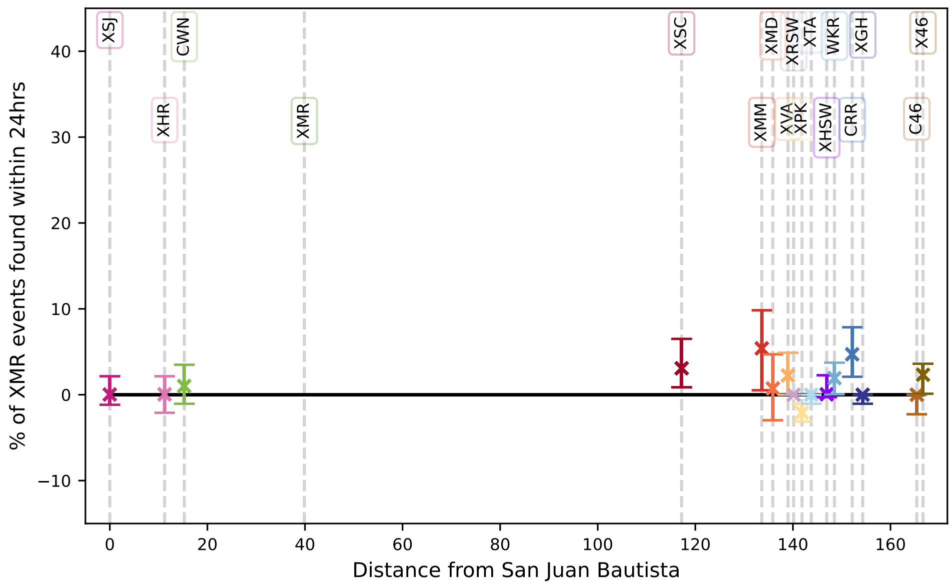

Figure A.11: Percentage of XMR events observed at all other creepmeters, scaled with distance.

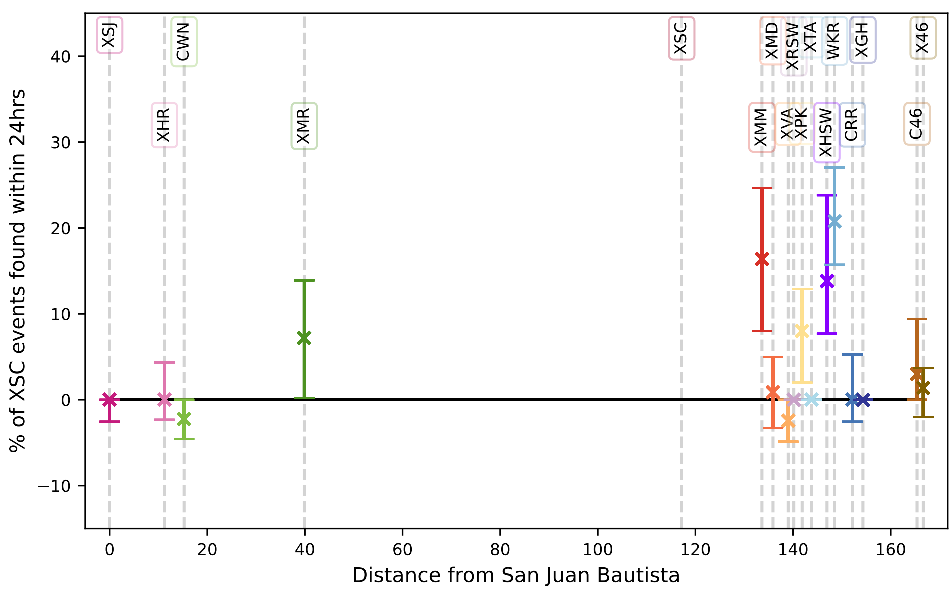

Figure A.12: Percentage of XSC events observed at all other creepmeters, scaled with distance.

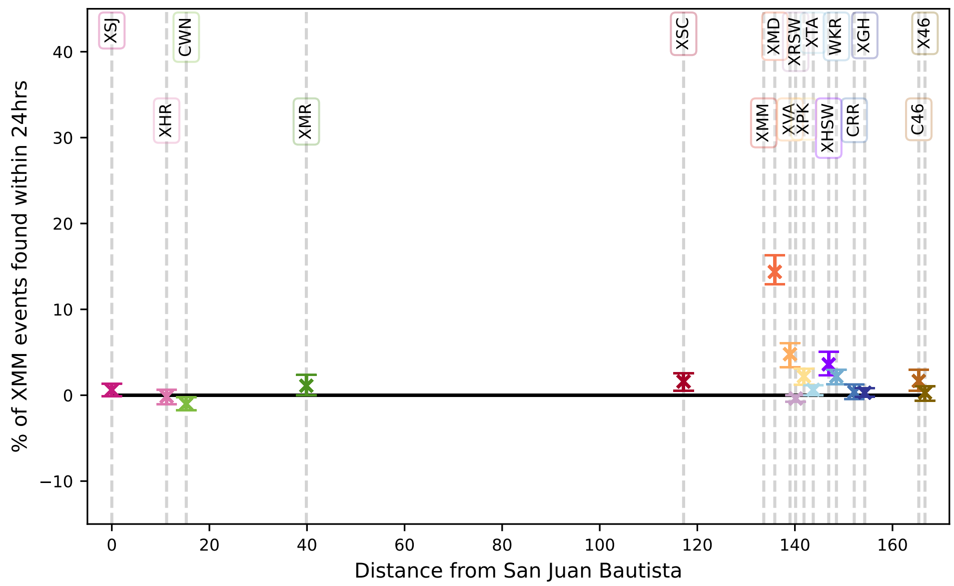

Figure A.13: Percentage of XMM events observed at all other creepmeters, scaled with distance.

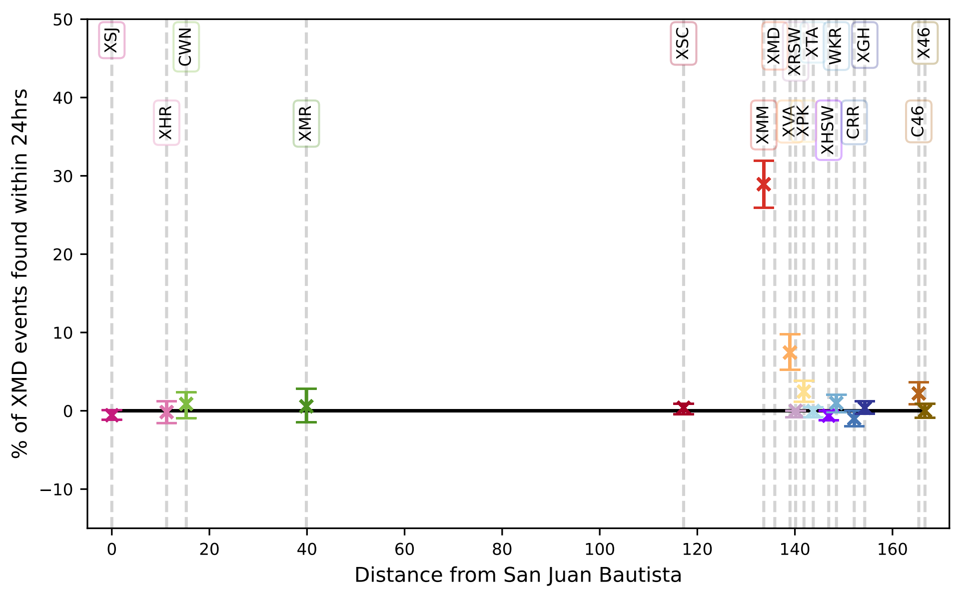

Figure A.14: Percentage of XMD events observed at all other creepmeters, scaled with distance.

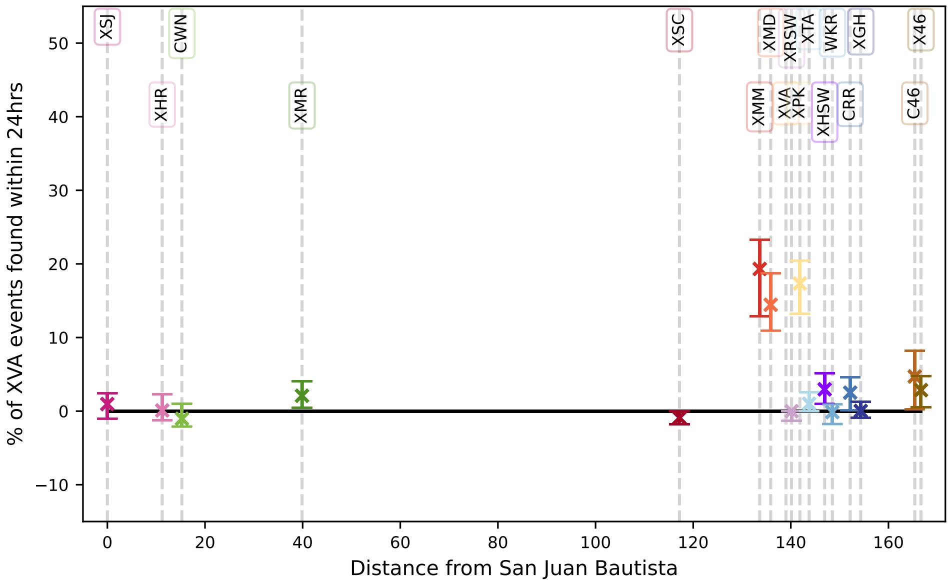

Figure A.15: Percentage of XVA events observed at all other creepmeters, scaled with distance.

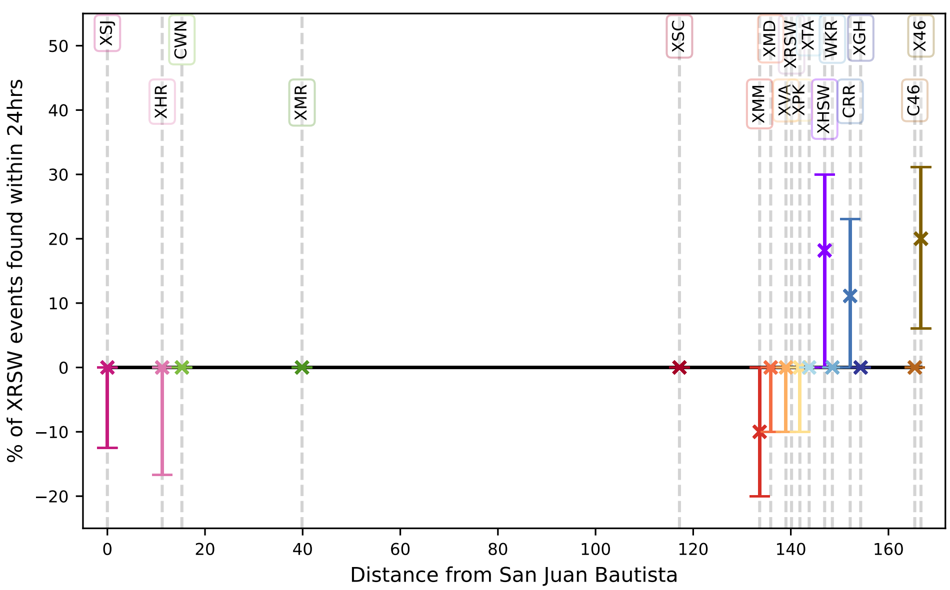

Figure A.16: Percentage of XRSW events observed at all other creepmeters, scaled with distance.

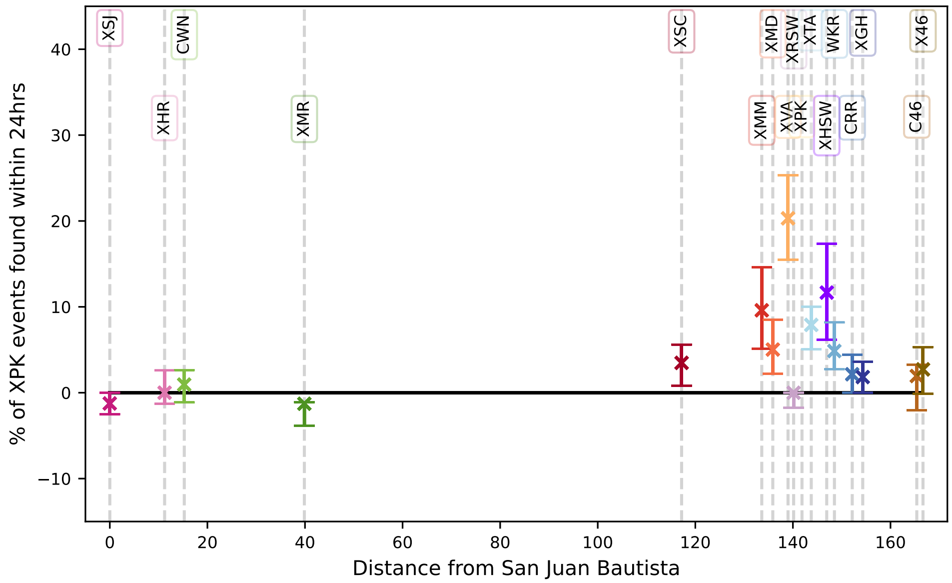

Figure A.17: Percentage of XPK events observed at all other creepmeters, scaled with distance.

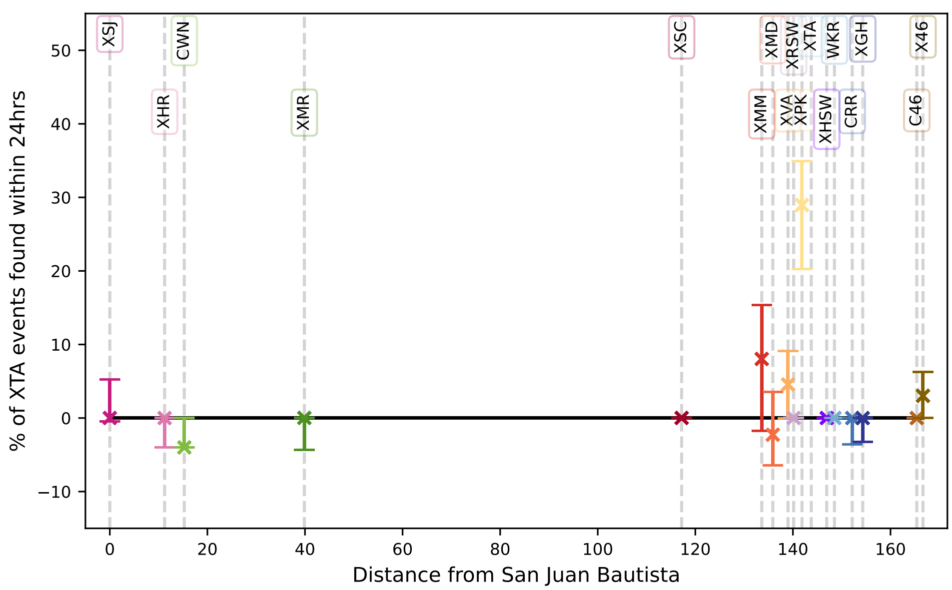

Figure A.18: Percentage of XTA events observed at all other creepmeters, scaled with distance.

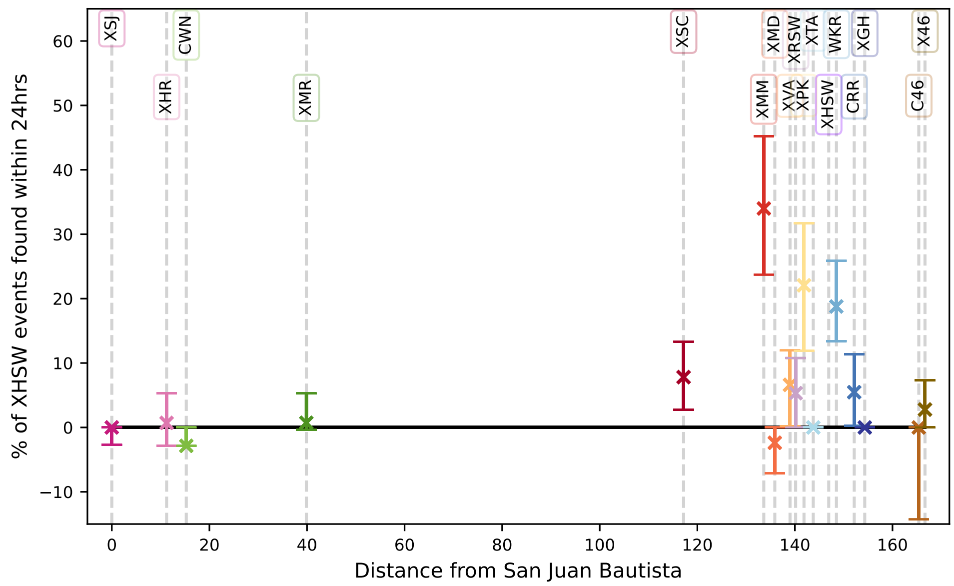

Figure A.19: Percentage of XHSW events observed at all other creepmeters, scaled with distance.

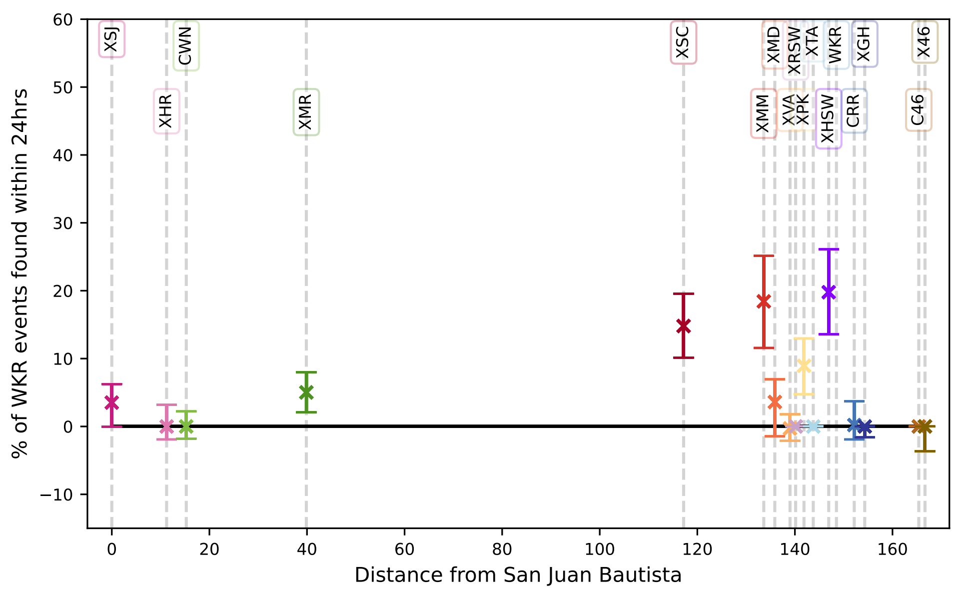

Figure A.20: Percentage of WKR events observed at all other creepmeters, scaled with distance.

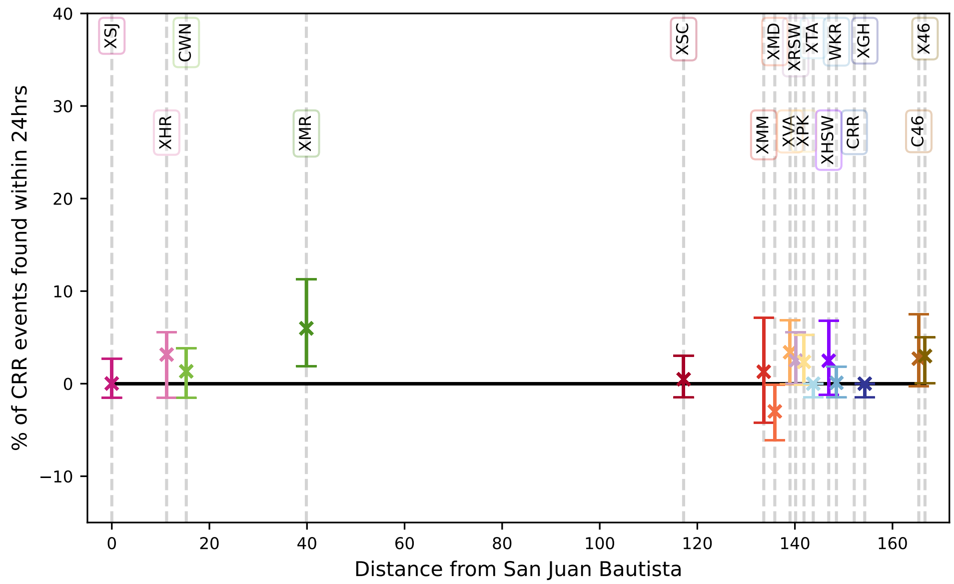

Figure A.21: Percentage of CRR events observed at all other creepmeters, scaled with distance.

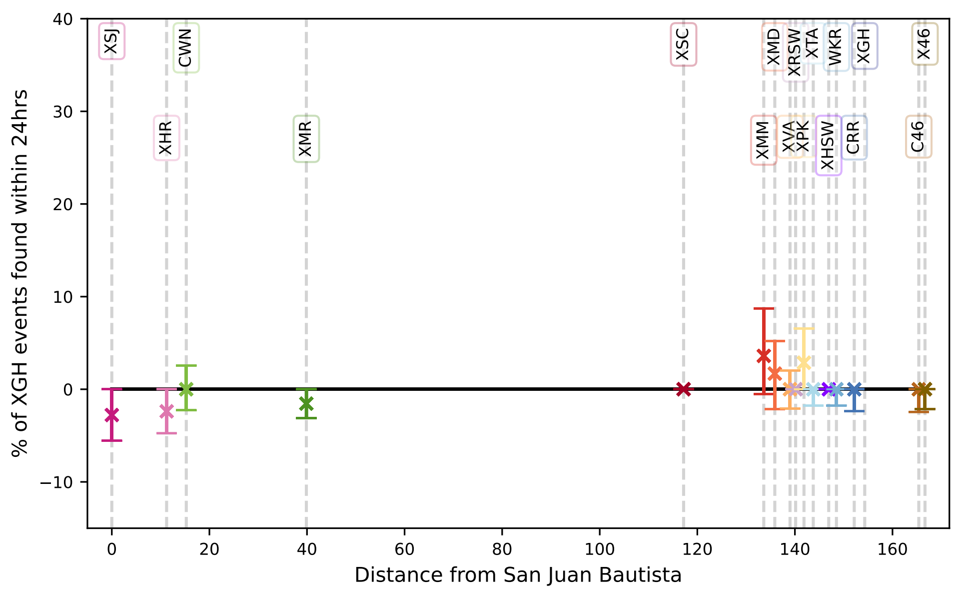

Figure A.22: Percentage of XGH events observed at all other creepmeters, scaled with distance.

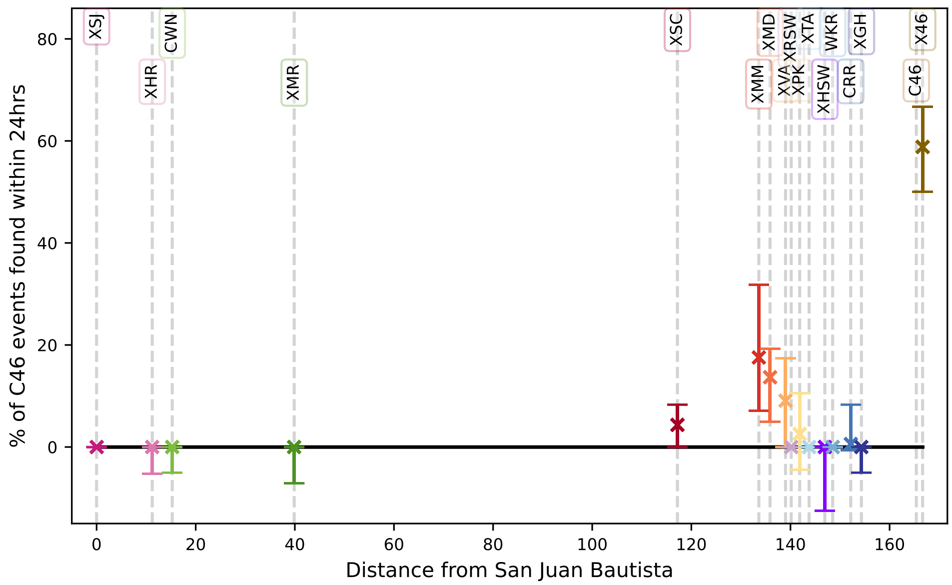

Figure A.23: Percentage of C46 events observed at all other creepmeters, scaled with distance.

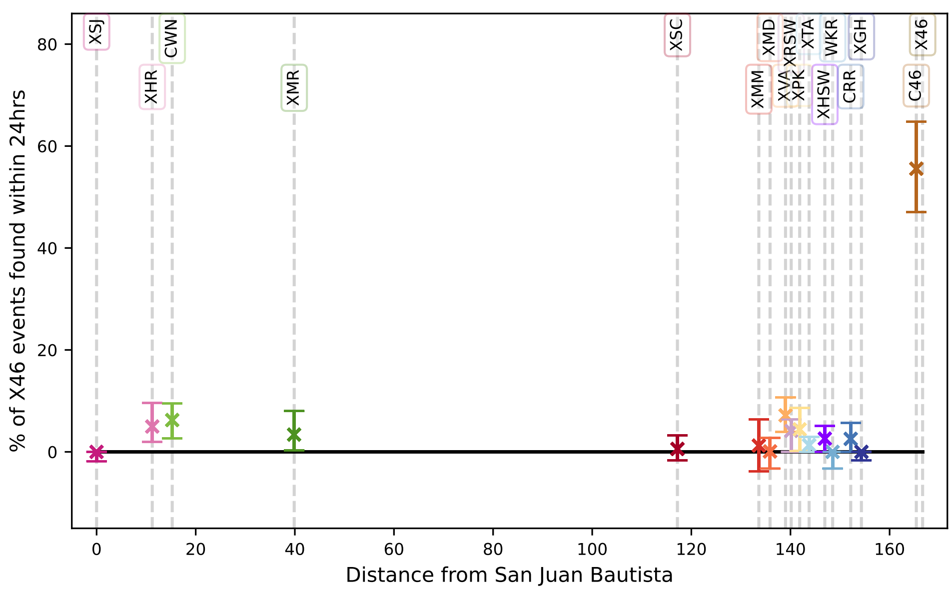

Figure A.24: Percentage of X46 events observed at all other creepmeters, scaled with distance.

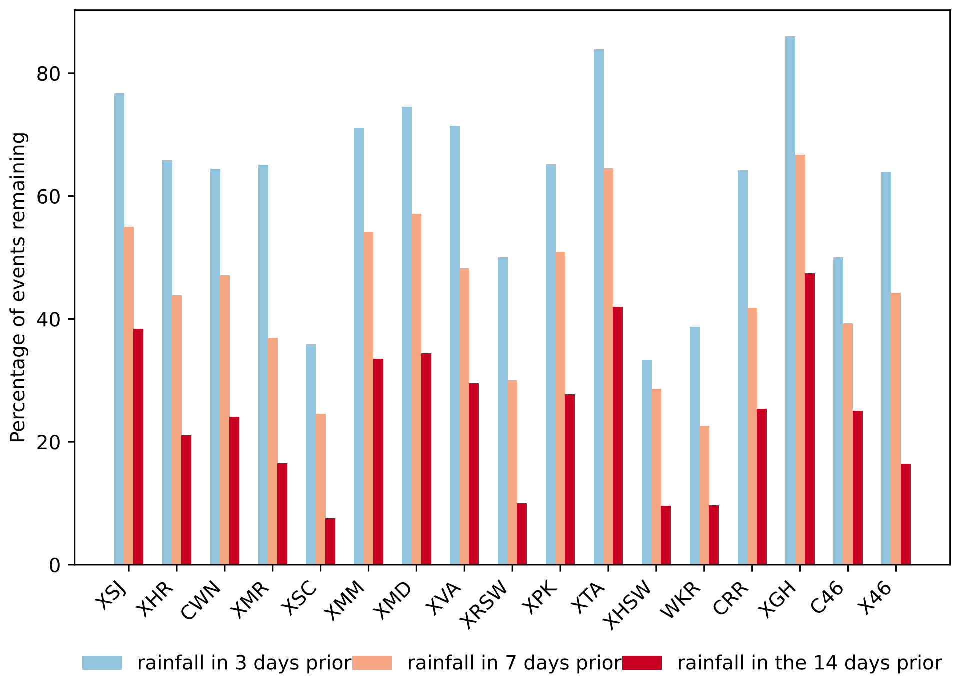

Figure A.25: Percentage of creep events remaining when events with rainfall in the 3- (light blue), 7- (orange), and 14-days (red) before the event are removed.

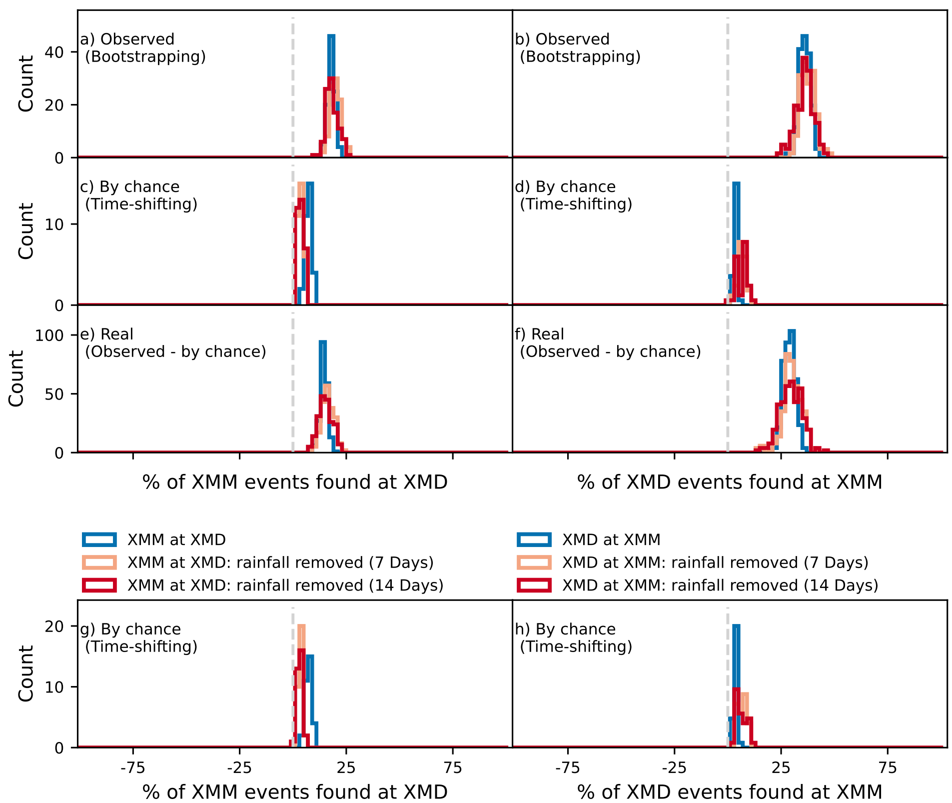

Figure A.26: Rainfall analysis histograms for Middle Mountain (XMM) and Middle Ridge (XMD). Blue histograms are the original analysis before rainfall was removed, and orange and red histograms are for when events with rainfall in the 7 or 14 days prior are removed, respectively. a) and b) are the bootstrapped distributions of the percentage of events with different amounts of rainfall accounted for. c) and d) show the percentage of time-correlated events that are occurring by chance. e) and f) are the percentage of events that are detected at both creepmeters when by chance occurrences are removed. g) and h) show the percentage of events that are observed at one creepmeter given seasonality and rain at the other.

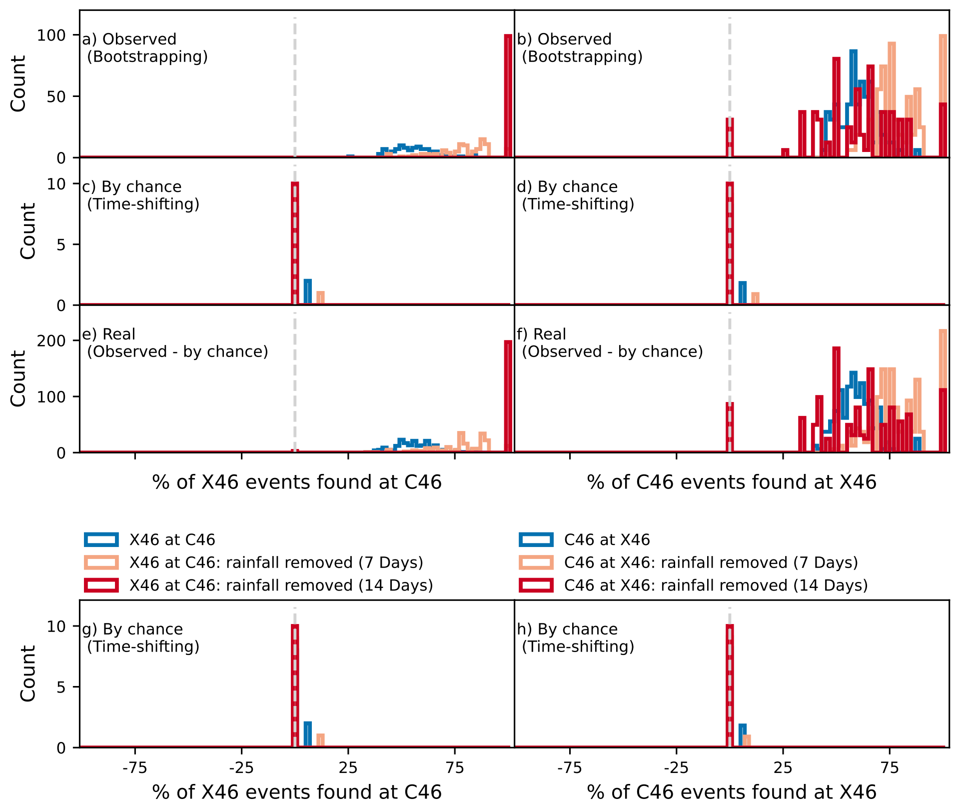

Figure A.27: Rainfall analysis histograms for Highway 46 (X46/C46). Blue histograms are the original analysis before rainfall was removed, and orange and red histograms are for when events with rainfall in the 7 or 14 days prior are removed, respectively. a) and b) are the bootstrapped distributions of the percentage of events with different amounts of rainfall accounted for. c) and d) show the percentage of time-correlated events that are occurring by chance. e) and f) are the percentage of events that are detected at both creepmeters when by chance occurrences are removed. g) and h) show the percentage of events that are observed at one creepmeter given seasonality and rain at the other.

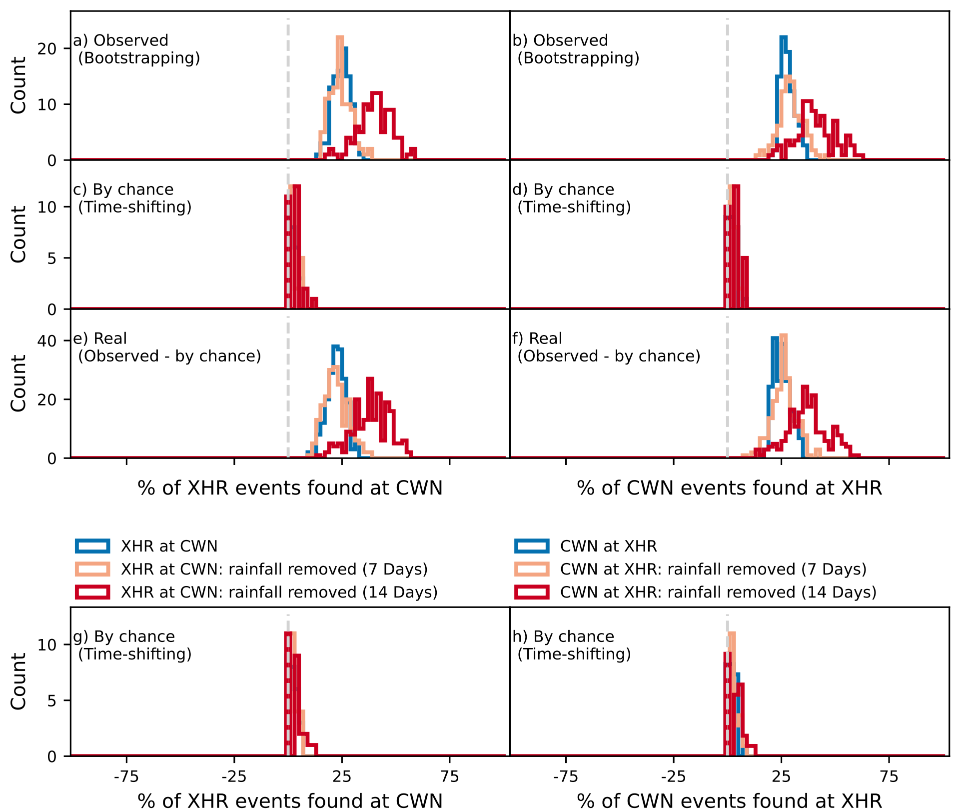

Figure A.28: Rainfall analysis histograms for Harris Ranch (XHR) and Cienega Winery (CWN). Blue histograms are the original analysis before rainfall was removed, and orange and red histograms are for when events with rainfall in the 7 or 14 days prior are removed, respectively. a) and b) are the bootstrapped distributions of the percentage of events with different amounts of rainfall accounted for. c) and d) show the percentage of time-correlated events that are occurring by chance. e) and f) are the percentage of events that are detected at both creepmeters when by chance occurrences are removed. g) and h) show the percentage of events that are observed at one creepmeter given seasonality and rain at the other.

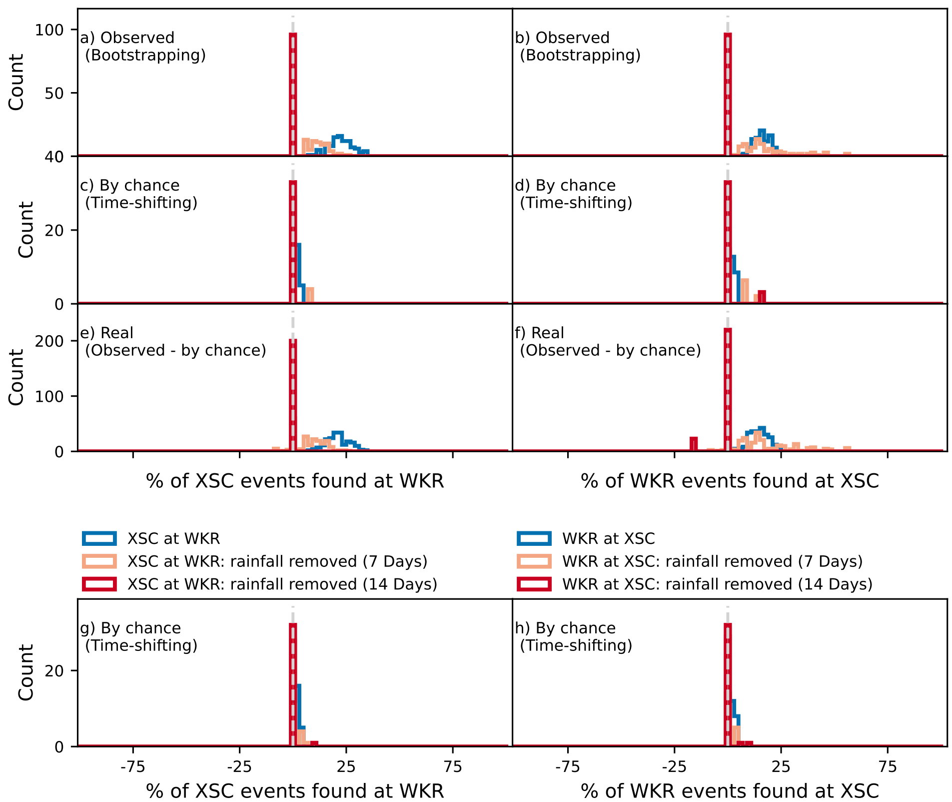

Figure A.29: Rainfall analysis histograms for Slacks Canyon (XSC) and Work Ranch (WKR). Blue histograms are the original analysis before rainfall was removed, and orange and red histograms are for when events with rainfall in the 7 or 14 days prior are removed, respectively. a) and b) are the bootstrapped distributions of the percentage of events with different amounts of rainfall accounted for. c) and d) show the percentage of time-correlated events that are occurring by chance. e) and f) are the percentage of events that are detected at both creepmeters when by chance occurrences are removed. g) and h) show the percentage of events that are observed at one creepmeter given seasonality and rain at the other.

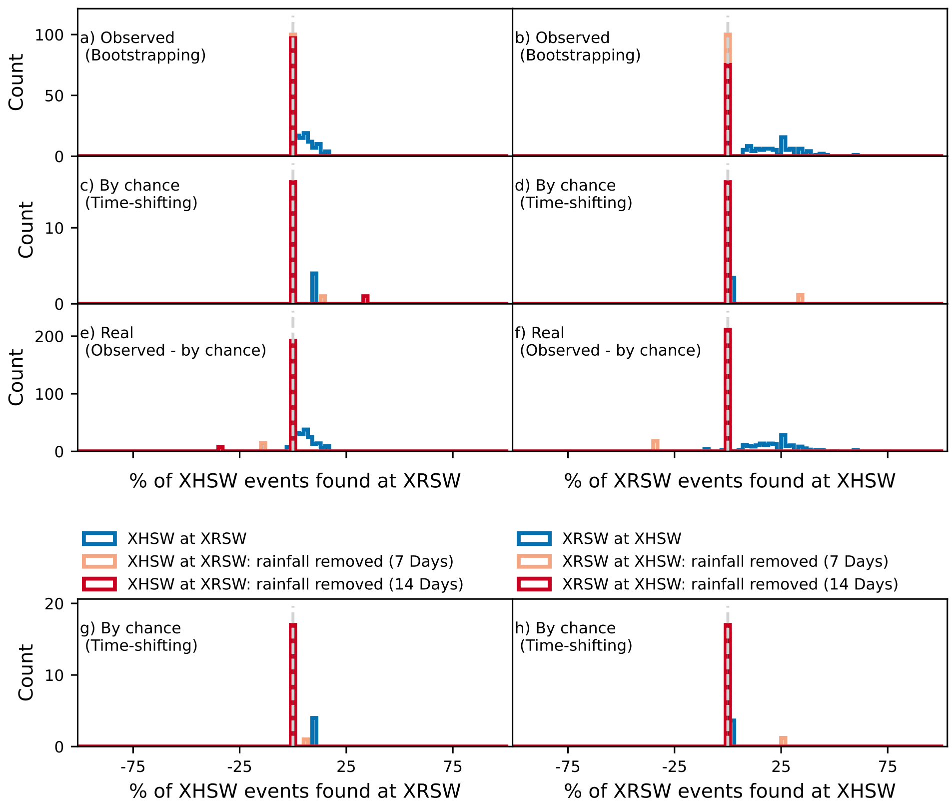

Figure A.30: Rainfall analysis histograms for Roberson Southwest (XRSW) and Hearst Southwest (XHSW). Blue histograms are the original analysis before rainfall was removed, and orange and red histograms are for when events with rainfall in the 7 or 14 days prior are removed, respectively. a) and b) are the bootstrapped distributions of the percentage of events with different amounts of rainfall accounted for. c) and d) show the percentage of time-correlated events that are occurring by chance. e) and f) are the percentage of events that are detected at both creepmeters when by chance occurrences are removed. g) and h) show the percentage of events that are observed at one creepmeter given seasonality and rain at the other.

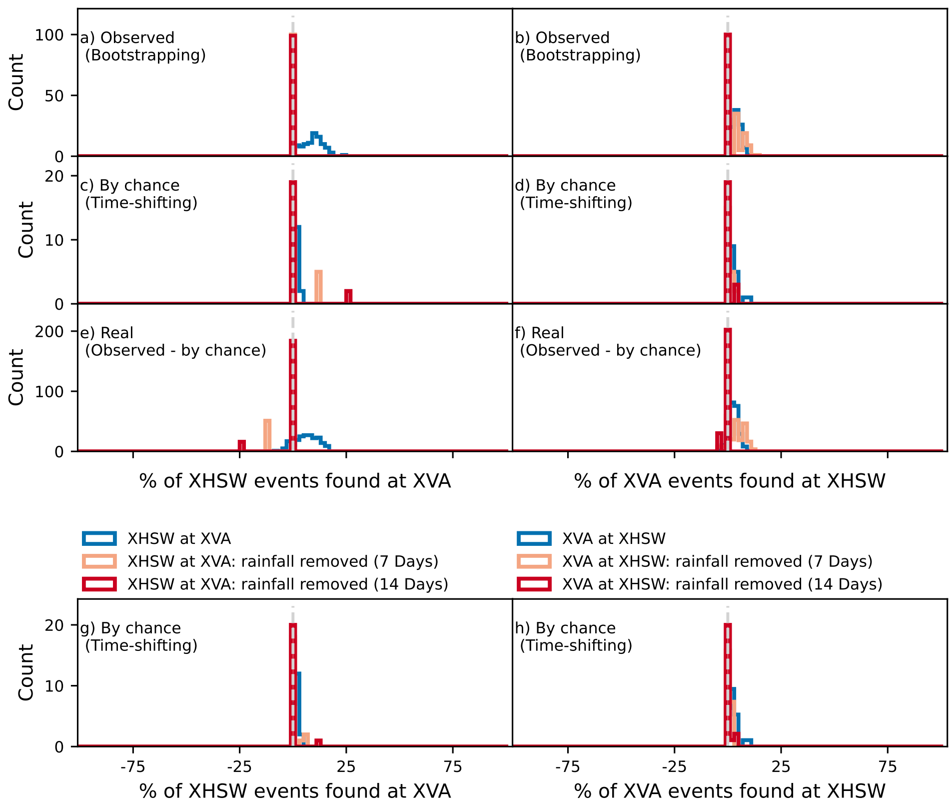

Figure A.31: Rainfall analysis histograms for Hearst Southwest (XHSW) and Varian (XVA). Blue histograms are the original analysis before rainfall was removed, and orange and red histograms are for when events with rainfall in the 7 or 14 days prior are removed, respectively. a) and b) are the bootstrapped distributions of the percentage of events with different amounts of rainfall accounted for. c) and d) show the percentage of time-correlated events that are occurring by chance. e) and f) are the percentage of events that are detected at both creepmeters when by chance occurrences are removed. g) and h) show the percentage of events that are observed at one creepmeter given seasonality and rain at the other.

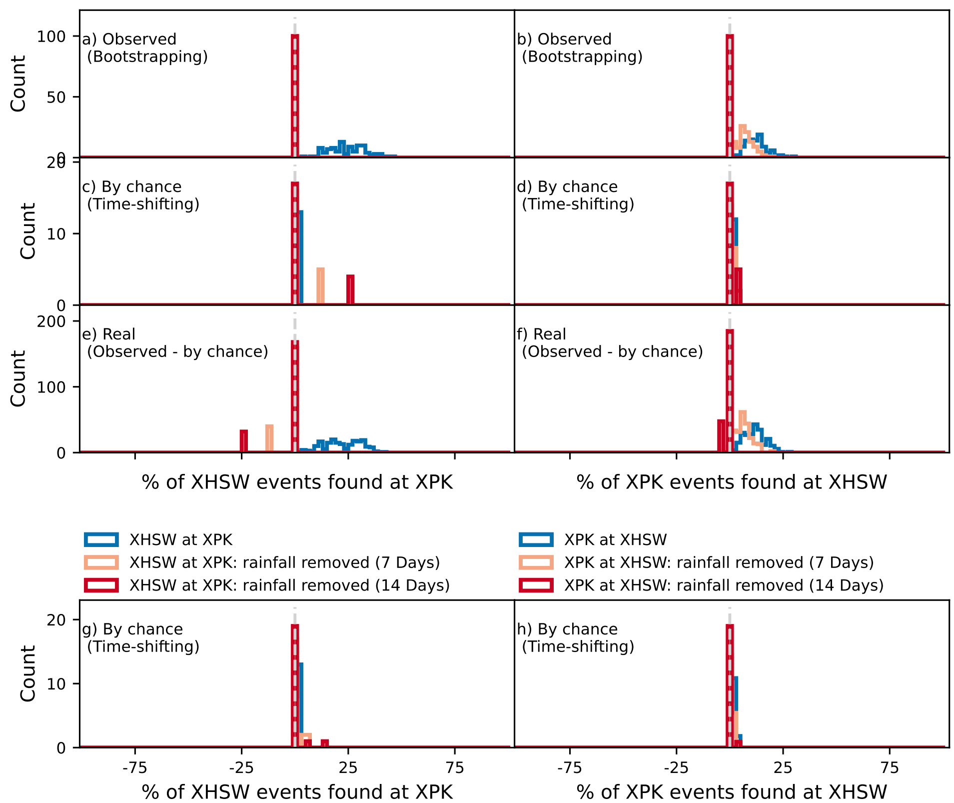

Figure A.32: Rainfall analysis histograms for Hearst Southwest (XHSW) and Parkfield (XPK). Blue histograms are the original analysis before rainfall was removed, and orange and red histograms are for when events with rainfall in the 7 or 14 days prior are removed, respectively. a) and b) are the bootstrapped distributions of the percentage of events with different amounts of rainfall accounted for. c) and d) show the percentage of time-correlated events that are occurring by chance. e) and f) are the percentage of events that are detected at both creepmeters when by chance occurrences are removed. g) and h) show the percentage of events that are observed at one creepmeter given seasonality and rain at the other.

APPENDIX B

Supporting Material for 'Are Creep Events Big 2? Estimations of Rupture Location, Depth, and Magnitude'

B.1 Supplementary Figures 192

Contents of this file

1. Figures B.1 to B.4

Introduction This supplementary information consists of one part, which includes all the supplementary figures referenced in the main text.

B.1 Supplementary Figures

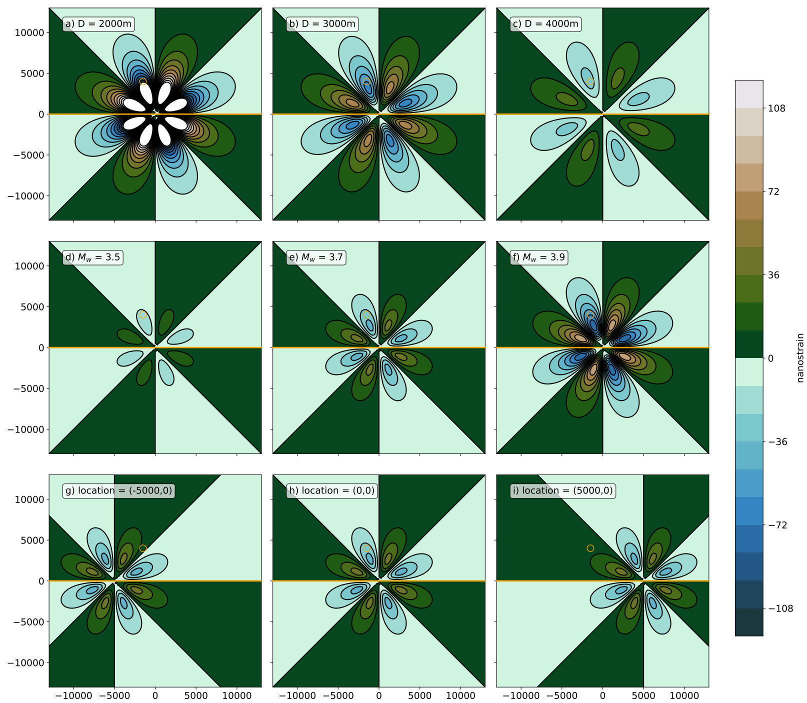

Figure B.1: How ϵ_{E-N} strain offsets changes for a 500×500 m patch of fault slipping at different depths (panels a) - c)), having different magnitudes (panels d) - f)) or changing along-strike location (panels g) - i)). The orange horizontal line represents the fault plane, and the orange circle is the location of a hypothetical strainmeter.

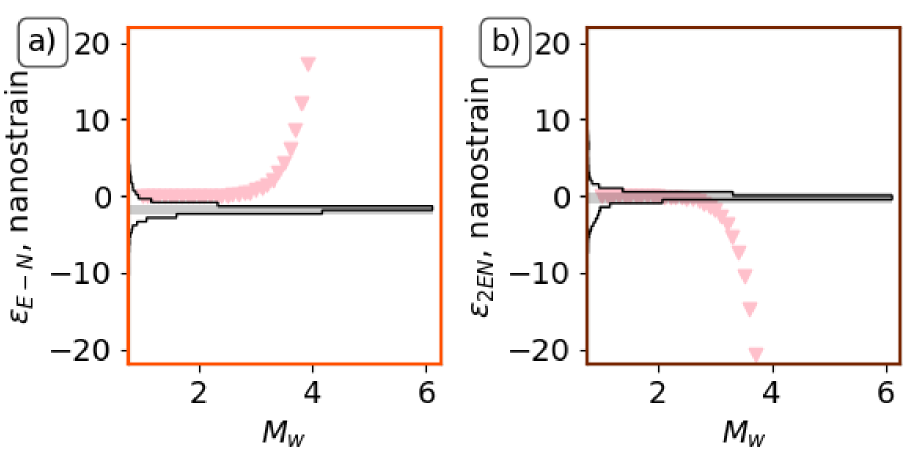

Figure B.2: Affect of changing the magnitude of the rectangular patch in the grid search on both the ϵ_{E-N} (a)) and ϵ_{2EN} (b)) components of strain.

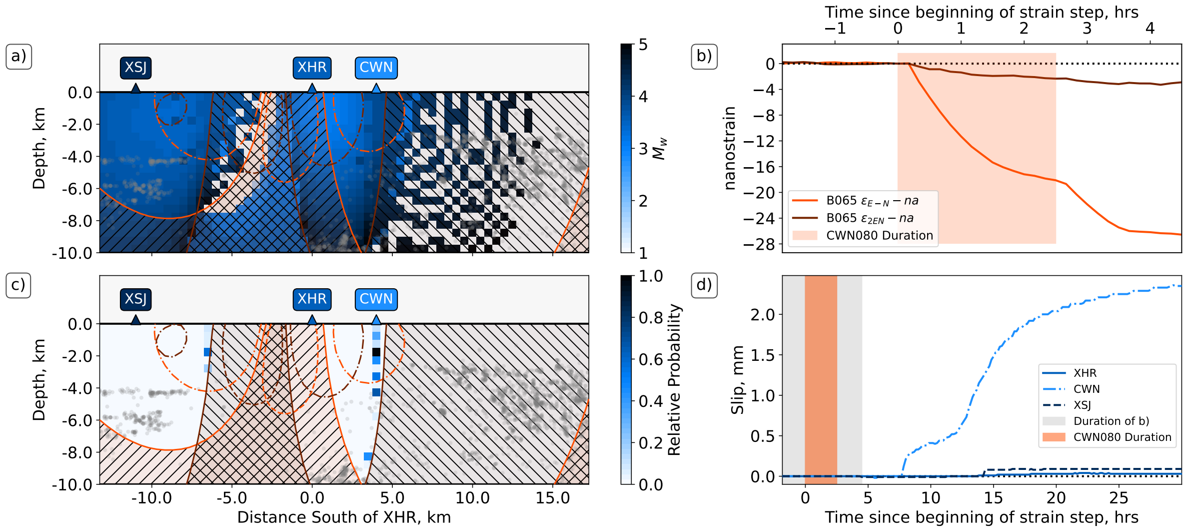

Figure B.3: CWN080 observed at B065, associated with a creep event at CWN, panels as in 3.5.

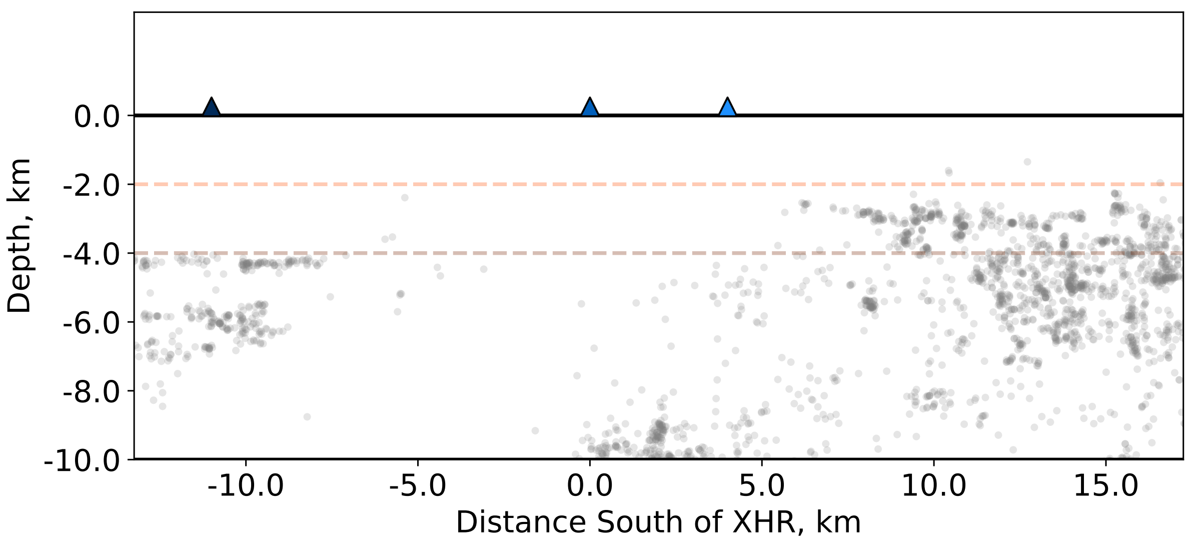

Figure B.4: Seismicity at the northern end of the creeping section of the San Andreas Fault (grey circles). Creepmeter locations are plotted at the surface (XSJ, dark blue; XHR, medium blue; and CWN, light blue). Horizontal orange and brown lines represent 2 and 4 km depths, respectively, and mark the depths used for categorising the depth of the slip patches producing strain offsets.

References

Aderhold, K., Arrowsmith, R., Atkinson, G., Ben-Zion, Y., Elbanna, A., Grifith, W., Share, P.-E., Steidl, J., Trugman, D., Vernon, F., and Woodwood, R. (2022). Shaping of the Rupture and Fault Zone Observatory. https://www.scec.org/article/930.

Allen, C. R. (1982). Comparisons Between the North Anatolian Fault of Turkey and the San Andreas Fault of California. In Işikara, A. M. and Vogel, A., editors, *Multidisciplinary Approach to Earthquake Prediction: Proceedings of the International Symposium on Earthquake Prediction in the North Anatolian Fault Zone held in Istanbul, March 31–April 5, 1980*, Progress in Earthquake Prediction Research, pages 67–85. Vieweg+Teubner Verlag, Wiesbaden.

Allen, J. E., Fowle, R. E., and California, Division of Mines (1946). *Geology of the San Juan Bautista quadrangle, California*. Number 112 p. California Division of Mines, Geologic Branch, San Francisco.

Altay, C. and Sav, H. (1991). Continuous creep measurement along the North Anatolian Fault zone, Bull. Geol. Congress Turkey. In *Abstracts of the Geological Congress of Turkey*, page 21.

Ambraseys, N. (1970). Some characteristic features of the Anatolian fault zone. *Tectonophysics*, 9(2-3):143–165.

Ampuero, J.-P. and Rubin, A. M. (2008). Earthquake nucleation on rate and state faults – Aging and slip laws. *Journal of Geophysical Research*, 113(B1):B01302.

Anderlini, L., Serpelloni, E., and Belardinelli, M. E. (2016). Creep and locking of a low-angle normal fault: Insights from the Altotiberina fault in the Northern Apennines (Italy): Creep and Locking of Altotiberina Fault. *Geophysical Research Letters*, 43(9):4321–4329.

Anderson, G., Hodgkinson, K., Herring, T., and Agnew, D. C. (2006). Plate Boundary Observatory Data Management System Critical Design Review Version 1.2. https://www.unavco.org/projects/past-projects/pbo/lib/docs.

Ando, R., Nakata, R., and Hori, T. (2010). A slip pulse model with fault heterogeneity for low-frequency earthquakes and tremor along plate interfaces. *Geophysical Research Letters*, 37(10):n/a–n/a.

Argus, D. F. and Gordon, R. G. (2001). Present tectonic motion across the Coast Ranges and San Andreas fault system in central California. *GSA Bulletin*, 113(12):1580–1592.

Aslan, G., Lasserre, C., Cakir, Z., Ergintav, S., Özarpaci, S., Dogan, U., Bilham, R., and Renard, F. (2019). Shallow Creep Along the 1999 Izmit Earthquake Rupture (Turkey) From GPS and High Temporal Resolution Interferometric Synthetic Aperture Radar Data (2011–2017). *Journal of Geophysical Research: Solid Earth*, 124(2):2218–2236.

Aytun, A. (1982). Creep Measurements in the Ismetpaşa Region of the North Anatolian Fault Zone. In Işikara, A. M. and Vogel, A., editors, *Multidisciplinary Approach to Earthquake Prediction: Proceedings of the International Symposium on Earthquake Prediction in the North Anatolian Fault Zone held in Istanbul, March 31–April 5, 1980*, Progress in Earthquake Prediction Research, pages 279–292. Vieweg+Teubner Verlag, Wiesbaden.

Bakun, W. H. and Lindh, A. G. (1985). The Parkfield, California, Earthquake Prediction Experiment. *Science*, 229(4714):619–624. Publisher: American Association for the Advancement of Science.

Bakun, W. H. and McEvilly, T. V. (1984). Recurrence models and Parkfield, California, earthquakes. *Journal of Geophysical Research: Solid Earth*, 89(B5):3051–3058.

Barnhart, W. D. (2017). Fault creep rates of the Chaman fault (Afghanistan and Pakistan) inferred from InSAR. *Journal of Geophysical Research: Solid Earth*, 122(1):372–386.

Bartlow, N. M., Miyazaki, S., Bradley, A. M., and Segall, P. (2011). Space-time correlation of slip and tremor during the 2009 Cascadia slow slip event. *Geophysical Research Letters*, 38(18):n/a–n/a.

Beeler, N. M., Tullis, T. E., and Weeks, J. D. (1994). The roles of time and displacement in the evolution effect in rock friction. *Geophysical Research Letters*, 21(18):1987–1990.

Behr, J., Bilham, R., Bodin, P., Breckenridge, K., and Sylvester, A. G. (1997). Increased surface creep rates on the San Andreas Fault southeast of the Loma Prieta Main Shock. In Reasenberg, P. A., editor, *The Loma Prieta, California, Earthquake of October 17, 1989 - Aftershocks and Postseismic Effects*, pages 179–192. U.S. Government Printing Office.

Belardinelli, M. E. (1997). Increase of creep interevent intervals: a conceptual model. *Tectonophysics*, 277(1-3):99–107.

Beyreuther, M., Barsch, R., Krischer, L., Megies, T., Behr, Y., and Wassermann, J. (2010). ObsPy: A Python Toolbox for Seismology. *Seismological Research Letters*, 81(3):530–533.

Bilham, R. and Behr, J. (1992). A two-layer model for aseismic slip on the Superstition Hills fault, California. *Bulletin of the Seismological Society of America*, 82(3):1223–1235.

Bilham, R. and Castillo, B. (2020). The July 2019 Ridgecrest, California, Earthquake Sequence Recorded by Creepmeters: Negligible Epicentral Afterslip and Prolonged Triggered Slip at Teleseismic Distances. *Seismological Research Letters*, 91(2A):707–720.

Bilham, R., Ozener, H., Mencin, D., Dogru, A., Ergintav, S., Cakir, Z., Aytun, A., Aktug, B., Yilmaz, O., Johnson, W., and Mattioli, G. (2016). Surface creep on the North Anatolian Fault at Ismetpasa, Turkey, 1944–2016. *Journal of Geophysical Research: Solid Earth*, 121(10):7409–7431.

Bilham, R., Suszek, N., and Pinkney, S. (2004). California Creepmeters. *Seismological Research Letters*, 75(4):481–492.

Bilham, R. G. (2022). The surface signature of subsurface fault creep: episodic dilation and gas emission. https://earthquake.usgs.gov/contactus/menlo/seminars/1372.

Bostock, M. G., Thomas, A. M., Savard, G., Chuang, L., and Rubin, A. M. (2015). Magnitudes and moment-duration scaling of low-frequency earthquakes beneath southern Vancouver Island. *Journal of Geophysical Research: Solid Earth*, 120(9):6329–6350.

Brodsky, E. E., Kirkpatrick, J. D., and Candela, T. (2016). Constraints from fault roughness on the scale-dependent strength of rocks. *Geology*, 44(1):19–22.

Brown, R. D. and Wallace, R. E. (1968). Current and historical fault movement along the San Andreas fault between Paicines and Camp Dix. In Dickinson, W. R. and Grantz, A., editors, *Proceedings, Conference on Geologic Problems of the San Andreas Fault System*, volume 11, pages 23–39. Stanford University Publications, Geological Sciences.

Burford, R. O. (1977). Bimodal distribution of creep event amplitudes on the San Andreas fault, California. *Nature*, 268(5619):424–426. Number: 5619 Publisher: Nature Publishing Group.

Burford, R. O. (1988). Retardations in fault creep rates before local moderate earthquakes along the San Andreas fault system, central California. *pure and applied geophysics*, 126(2):499–529.

Burford, R. O. and Harsh, P. W. (1980). Slip on the San Andreas fault in central California from alinement array surveys. *Bulletin of the Seismological Society of America*, 70(4):1233–1261.

Candela, T., Renard, F., Klinger, Y., Mair, K., Schmittbuhl, J., and Brodsky, E. E. (2012). Roughness of fault surfaces over nine decades of length scales. *Journal of Geophysical Research: Solid Earth*, 117(B8).

Carpenter, B., Mollo, S., Viti, C., and Collettini, C. (2015). Influence of calcite decarbonation on the frictional behavior of carbonate-bearing gouge: Implications for the instability of volcanic flanks and fault slip. *Tectonophysics*, 658:128–136.

Cetin, E., Cakir, Z., Meghraoui, M., Ergintav, S., and Akoglu, A. M. (2014). Extent and distribution of aseismic slip on the Ismetpaşa segment of the North Anatolian Fault (Turkey) from Persistent Scatterer InSAR. *Geochemistry, Geophysics, Geosystems*, 15(7):2883–2894.

Crameri, F. (2018). Geodynamic diagnostics, scientific visualisation and StagLab 3.0. *Geoscientific Model Development*, 11(6):2541–2562. Publisher: Copernicus GmbH.

Crameri, F. (2023). Scientific colour maps. https://zenodo.org/record/8035877 DOI: 10.5281/zenodo.8035877.

Crameri, F., Shephard, G. E., and Heron, P. J. (2020). The misuse of colour in science communication. *Nature Communications*, 11(1):5444.

Crough, S. T. and Burford, R. O. (1977). Empirical law for fault-creep events. *Tectonophysics*, 42(1):T53–T59.

d'Alessio, M. A., Williams, C. F., and Bürgmann, R. (2006). Frictional strength heterogeneity and surface heat flow: Implications for the strength of the creeping San Andreas fault. *Journal of Geophysical Research: Solid Earth*, 111(B5).

Dianala, J. D. B., Jolivet, R., Thomas, M. Y., Fukushima, Y., Parsons, B., and Walker, R. (2020). The Relationship Between Seismic and Aseismic Slip on the Philippine Fault on Leyte Island: Bayesian Modeling of Fault Slip and Geothermal Subsidence. *Journal of Geophysical Research: Solid Earth*, 125(12).

Dibblee, T. W. (2006). Geologic map of the Hollister quadrangle, Monterey & San Benito Counties, California. https://ngmdb.usgs.gov/Prodesc/proddesc_77440.htm.

Dieterich, J. H. (1979). Modeling of rock friction: 1. Experimental results and constitutive equations. *Journal of Geophysical Research: Solid Earth*, 84(B5):2161–2168.

Dieterich, J. H. (1992). Earthquake nucleation on faults with rate-and state-dependent strength. *Tectonophysics*, 211(1):115–134.

Dragert, H., Wang, K., and James, T. S. (2001). A Silent Slip Event on the Deeper Cascadia Subduction Interface. *Science*, 292(5521):1525–1528. Publisher: American Association for the Advancement of Science.

Duffield, W. A. and Burford, R. (1973). An accurate Invar-wire extensometer. *Journal of Research of the U.S. Geological Survey*, 1(5):569577.

Duquesnoy, T., Barrier, E., Kasser, M., Aurelio, M., Gaulon, R., Punongbayan, R. S., and Rangin, C. (1994). Detection of creep along the Philippine Fault: First results of geodetic measurements on Leyte Island, central Philippine. *Geophysical Research Letters*, 21(11):975–978.

Evans, B. and Kohlstedt, D. L. (1995). Rheology of Rocks. In Ahrens, T. J., editor, *Rock Physics and Phase Relations: A Handbook of Physical Constants*, volume 3 of *AGU reference shelf*, pages 148–165. American Geophysical Union.

Evans, K. F., Burford, R. O., and King, G. C. P. (1981). Propagating episodic creep and the aseismic slip behavior of the Calaveras Fault north of Hollister, California. *Journal of Geophysical Research*, 86(B5):3721.

Fang, Z. and Dunham, E. M. (2013). Additional shear resistance from fault roughness and stress levels on geometrically complex faults. *Journal of Geophysical Research: Solid Earth*, 118(7):3642–3654. _eprint: https://agupubs.onlinelibrary.wiley.com/doi/pdf/10.1002/jgrb.50262.

Farge, G., Shapiro, N. M., and Frank, W. B. (2020). Moment-Duration Scaling of Low-Frequency Earthquakes in Guerrero, Mexico. *Journal of Geophysical Research: Solid Earth*, 125(8):e2019JB019099.

Fattahi, H. and Amelung, F. (2016). InSAR observations of strain accumulation and fault creep along the Chaman Fault system, Pakistan and Afghanistan: Strain Accumulation at Chaman Fault. *Geophysical Research Letters*, 43(16):8399–8406.

Fukushima, Y., Hashimoto, M., Miyazawa, M., Uchida, N., and Taira, T. (2019). Surface creep rate distribution along the Philippine fault, Leyte Island, and possible repeating of Mw ˜ 6.5 earthquakes on an isolated locked patch. *Earth, Planets and Space*, 71(1):118.

Funning, G. J., Bürgmann, R., Ferretti, A., Novali, F., and Fumagalli, A. (2007). Creep on the Rodgers Creek fault, northern San Francisco Bay area from a 10 year PS-InSAR dataset. *Geophysical Research Letters*, 34(19):L19306.

Furuya, M. and Satyabala, S. P. (2008). Slow earthquake in Afghanistan detected by InSAR. *Geophysical Research Letters*, 35(6):L06309.

GAGE (2023). Borehole Strainmeter Data | Data | GAGE. https://www.unavco.org/data/strain-seismic/bsm-data/bsm-data.html.

Ghosh, A., Vidale, J. E., Sweet, J. R., Creager, K. C., Wech, A. G., Houston, H., and Brodsky, E. E. (2010). Rapid, continuous streaking of tremor in Cascadia. *Geochemistry, Geophysics, Geosystems*, 11(12):n/a–n/a.

Gittins, D. B. and Hawthorne, J. C. (2022a). Are Creep Events Big? Estimations of Along-Strike Rupture Lengths. *Journal of Geophysical Research: Solid Earth*, 127(1):e2021JB023001.

Gittins, D. B. and Hawthorne, J. C. (2022b). Supporting Information for "Are creep events big? Estimations of along-strike rupture lengths?". https://ora.ox.ac.uk/objects/uuid:e0922f91-0224-41cc-b895-8e4effa5d46a.

Gladwin, M. T. (1984). High-precision multicomponent borehole deformation monitoring. *Review of Scientific Instruments*, 55(12):2011–2016.

Gladwin, M. T., Gwyther, R. L., Hart, R., Francis, M., and Johnston, M. J. S. (1987). Borehole tensor strain measurements in California. *Journal of Geophysical Research*, 92(B8):7981.

Gladwin, M. T., Gwyther, R. L., Hart, R. H. G., and Breckenridge, K. S. (1994). Measurements of the strain field associated with episodic creep events on the San Andreas Fault at San Juan Bautista, California. *Journal of Geophysical Research: Solid Earth*, 99(B3):4559–4565.

Gombert, B. and Hawthorne, J. C. (2023). Rapid Tremor Migration During Few Minute-Long Slow Earthquakes in Cascadia. *Journal of Geophysical Research: Solid Earth*, 128(2):e2022JB025034.

Goulty, N. R. and Gilman, R. (1978). Repeated creep events on the San Andreas Fault near Parkfield, California, Recorded by a strainmeter array. *Journal of Geophysical Research*, 83(B11):5415.

Gratier, J.-P., Dysthe, D. K., and Renard, F. (2013). The Role of Pressure Solution Creep in the Ductility of the Earth's Upper Crust. In *Advances in Geophysics*, volume 54, pages 47–179. Elsevier.

Gratier, J.-P., Richard, J., Renard, F., Mittempergher, S., Doan, M.-L., Di Toro, G., Hadizadeh, J., and Boullier, A.-M. (2011). Aseismic sliding of active faults by pressure solution creep: Evidence from the San Andreas Fault Observatory at Depth. *Geology*, 39(12):1131–1134.

Hamiel, Y., Piatibratova, O., and Mizrahi, Y. (2016). Creep along the northern Jordan Valley section of the Dead Sea Fault. *Geophysical Research Letters*, 43(6):2494–2501.

Harris, C. R., Millman, K. J., van der Walt, S. J., Gommers, R., Virtanen, P., Cournapeau, D., Wieser, E., Taylor, J., Berg, S., Smith, N. J., Kern, R., Picus, M., Hoyer, S., van Kerkwijk, M. H., Brett, M., Haldane, A., del Río, J. F., Wiebe, M., Peterson, P., Gérard-Marchant, P., Sheppard, K., Reddy, T., Weckesser, W., Abbasi, H., Gohlke, C., and Oliphant, T. E. (2020). Array programming with NumPy. *Nature*, 585(7825):357–362.

Harris, R. A. (2017). Large earthquakes and creeping faults. *Reviews of Geophysics*, 55(1):169–198.

Hawthorne, J. C., Bostock, M. G., Royer, A. A., and Thomas, A. M. (2016a). Variations in slow slip moment rate associated with rapid tremor reversals in Cascadia. *Geochemistry, Geophysics, Geosystems*, 17(12):4899–4919.

Hawthorne, J. C. and Rubin, A. M. (2013). Short-time scale correlation between slow slip and tremor in Cascadia. *Journal of Geophysical Research: Solid Earth*, 118(3):1316–1329.

Hawthorne, J. C., Simons, M., and Ampuero, J. (2016b). Estimates of aseismic slip associated with small earthquakes near San Juan Bautista, CA. *Journal of Geophysical Research: Solid Earth*, 121(11):8254–8275.

Hawthorne, J. C., Thomas, A. M., and Ampuero, J.-P. (2019). The rupture extent of low frequency earthquakes near Parkfield, CA. *Geophysical Journal International*, 216(1):621–639.

Hay, E. A., Hall, N. T., and Cotton, W. R. (1989). Rapid creep on the San Andreas fault at Bitterwater Valley. In Sylvester, A. G., Crowell, J. C., Galehouse, J. S., Hay, E. A., Hall, N. T., Cotton, W. R., Prentice, C. S., and Sims, J. D., editors, *The San Andreas Transform Belt: Long Beach to San Francisco, California July 20–29, 1989*, pages 36–39. American Geophysical Union, Washington, D. C.

Helmstetter, A. and Shaw, B. E. (2009). Afterslip and aftershocks in the rate-and-state friction law. *Journal of Geophysical Research: Solid Earth*, 114(B1).

Hirao, B., Savage, H., and Brodsky, E. E. (2021). Communication Between the Northern and Southern Central San Andreas Fault via Dynamically Triggered Creep. *Geophysical Research Letters*, 48(13):e2021GL092530.

Hirth, G. and Kohlstedt, D. (2004). Rheology of the Upper Mantle and the Mantle Wedge: A View from the Experimentalists. In *Inside the Subduction Factory*, Geophysical Monograph Series, pages 83–105. American Geophysical Union (AGU).

Hodgkinson, K., Langbein, J., Henderson, B., Mencin, D., and Borsa, A. (2013). Tidal calibration of plate boundary observatory borehole strainmeters. *Journal of Geophysical Research: Solid Earth*, 118(1):447–458.

Hreinsdottir, S. and Bennett, R. A. (2009). Active aseismic creep on the Alto Tiberina low-angle normal fault, Italy. *Geology*, 37(8):683–686.

Huang, H. and Hawthorne, J. C. (2022). Linking the scaling of tremor and slow slip near Parkfield, CA. *Nature Communications*, 13(1):5826. Number: 1 Publisher: Nature Publishing Group.

Huggett, G. R., Slater, L. E., and Langbein, J. (1977). Fault slip episodes near Hollister, California: Initial results using a multiwavelength distance-measuring instrument. *Journal of Geophysical Research (1896-1977)*, 82(23):3361–3368.

Hunter, J. D. (2007). Matplotlib: A 2D Graphics Environment. *Computing in Science & Engineering*, 9(3):90–95. Conference Name: Computing in Science & Engineering.

Hussain, E., Wright, T. J., Walters, R. J., Bekaert, D., Hooper, A., and Houseman, G. A. (2016). Geodetic observations of postseismic creep in the decade after the 1999 Izmit earthquake, Turkey: Implications for a shallow slip deficit. *Journal of Geophysical Research: Solid Earth*, 121(4):2980–3001.

Ide, S., Beroza, G. C., Shelly, D. R., and Uchide, T. (2007). A scaling law for slow earthquakes. *Nature*, 447(7140):76–79.

Ide, S., Imanishi, K., Yoshida, Y., Beroza, G. C., and Shelly, D. R. (2008). Bridging the gap between seismically and geodetically detected slow earthquakes. *Geophysical Research Letters*, 35(10).

Ide, S. and Yabe, S. (2014). Universality of slow earthquakes in the very low frequency band: Ide and Yabe: Slow earthquakes in the VLF band. *Geophysical Research Letters*, 41(8):2786–2793.

Ikari, M. J., Marone, C., and Saffer, D. M. (2011). On the relation between fault strength and frictional stability. *Geology*, 39(1):83–86.

Itaba, S. and Ando, R. (2011). A slow slip event triggered by teleseismic surface waves. *Geophysical Research Letters*, 38(21).

Itaba, S., Kitagawa, Y., Koizumi, N., Takahashi, M., Matsumoto, N., and Takeda, N. (2013). Short-term slow slip events in the Tokai area, the Kii Peninsula and the Shikoku District, Japan (from November 2012 to April 2013). Coordinating Committee for Earthquake Prediction 90.

Ito, Y., Obara, K., Shiomi, K., Sekine, S., and Hirose, H. (2007). Slow Earthquakes Coincident with Episodic Tremors and Slow Slip Events. *Science*, 315(5811):503–506. Publisher: American Association for the Advancement of Science.

Iverson, R. M. (2005). Regulation of landslide motion by dilatancy and pore pressure feedback. *Journal of Geophysical Research: Earth Surface*, 110(F2).

Jaeger, J. C., Cook, N. G. W., and Zimmerman, R. W. (2007). *Fundamentals of Rock Mechanics*. Blackwell Publishing, Malden, Mass. ; Oxford, 4th edition.

Jolivet, R., Lasserre, C., Doin, M.-P., Guillaso, S., Peltzer, G., Dailu, R., Sun, J., Shen, Z.-K., and Xu, X. (2012). Shallow creep on the Haiyuan Fault (Gansu, China) revealed by SAR Interferometry. *Journal of Geophysical Research: Solid Earth*, 117(B6):n/a–n/a.

Jolivet, R., Lasserre, C., Doin, M.-P., Peltzer, G., Avouac, J.-P., Sun, J., and Dailu, R. (2013). Spatio-temporal evolution of aseismic slip along the Haiyuan fault, China: Implications for fault frictional properties. *Earth and Planetary Science Letters*, 377-378:23–33.

Jolivet, R., Simons, M., Agram, P. S., Duputel, Z., and Shen, Z.-K. (2015). Aseismic slip and seismogenic coupling along the central San Andreas Fault. *Geophysical Research Letters*, 42(2):297–306.

Jordahl, K., Bossche, J. V. d., Fleischmann, M., Wasserman, J., McBride, J., Gerard, J., Tratner, J., Perry, M., Badaracco, A. G., Farmer, C., Hjelle, G. A., Snow, A. D., Cochran, M., Gillies, S., Culbertson, L., Bartos, M., Eubank, N., maxalbert, Bilogur, A., Rey, S., Ren, C., Arribas-Bel, D., Wasser, L., Wolf, L. J., Journois, M., Wilson, J., Greenhall, A., Holdgraf, C., Filipe, and Leblanc, F. (2020). geopandas/geopandas: v0.8.1. https://zenodo.org/record/3946761 DOI: 10.5281/zenodo.3946761.

Jouanne, F., Audemard, F. A., Beck, C., Van Welden, A., Ollarves, R., and Reinoza, C. (2011). Present-day deformation along the El Pilar Fault in eastern Venezuela: Evidence of creep along a major transform boundary. *Journal of Geodynamics*, 51(5):398–410.

Kaduri, M., Gratier, J.-P., Renard, F., Çakir, Z., and Lasserre, C. (2017). The implications of fault zone transformation on aseismic creep: Example of the North Anatolian Fault, Turkey. *Journal of Geophysical Research: Solid Earth*, 122(6):4208–4236.

Kanu, C. and Johnson, K. (2011). Arrest and recovery of frictional creep on the southern Hayward fault triggered by the 1989 Loma Prieta, California, earthquake and implications for future earthquakes. *Journal of Geophysical Research*, 116(B4):B04403.

Karabacak, V., Altunel, E., and Cakir, Z. (2011). Monitoring aseismic surface creep along the North Anatolian Fault (Turkey) using ground-based LIDAR. *Earth and Planetary Science Letters*, 304(1-2):64–70.

Khoshmanesh, M. and Shirzaei, M. (2018a). Episodic creep events on the San Andreas Fault caused by pore pressure variations. *Nature Geoscience*, 11(8):610–614.

Khoshmanesh, M. and Shirzaei, M. (2018b). Multiscale Dynamics of Aseismic Slip on Central San Andreas Fault. *Geophysical Research Letters*, 45(5):2274–2282.

Khoshmanesh, M., Shirzaei, M., and Nadeau, R. M. (2015). Time-dependent model of aseismic slip on the central San Andreas Fault from InSAR time series and repeating earthquakes. *Journal of Geophysical Research: Solid Earth*, 120(9):6658–6679.

King, C.-Y. (1972). A Shallow-Faulting Model. *Bulletin of the Seismological Society of America*, 62(2):551–559.

King, C.-Y. (2019). Kinematics of Slow-Slip Events. In *Kinematics of Slow-Slip Events*. IntechOpen. Publication Title: Earthquakes - Impact, Community Vulnerability and Resilience.

King, C.-Y., Nason, R. D., and Tocher, D. (1973). Kinematics of Fault Creep. *Philosophical Transactions of the Royal Society of London. Series A, Mathematical and Physical Sciences*, 274(1239):355–360. Publisher: The Royal Society.

Kitagawa, Y., Itaba, S., Koizumi, N., Takahashi, M., Matsumoto, N., and Takeda, N. (2011). The variation of the strain, tilt and groundwater level in the Shikoku District and Kii Peninsula, Japan (from November 2010 to May 2011). Coordinating Committee for Earthquake Prediction 86.

Kruyt, N. P. and Rothenburg, L. (2016). A micromechanical study of dilatancy of granular materials. *Journal of the Mechanics and Physics of Solids*, 95:411–427.

Lam, S. K., Pitrou, A., and Seibert, S. (2015). Numba: A llvm-based python jit compiler. In *Proceedings of the Second Workshop on the LLVM Compiler Infrastructure in HPC*, pages 1–6.

Langbein, J. (2006). Coseismic and Initial Postseismic Deformation from the 2004 Parkfield, California, Earthquake, Observed by Global Positioning System, Electronic Distance Meter, Creepmeters, and Borehole Strainmeters. *Bulletin of the Seismological Society of America*, 96(4B):S304–S320.

Langbein, J., Borcherdt, R., Dreger, D., Fletcher, J., Hardebeck, J. L., Hellweg, M., Ji, C., Johnston, M., Murray, J. R., Nadeau, R., Rymer, M. J., and Treiman, J. A. (2005). Preliminary Report on the 28 September 2004, M 6.0 Parkfield, California Earthquake. *Seismological Research Letters*, 76(1):10–26.

Langbein, J. and Johnson, H. (1997). Correlated errors in geodetic time series: Implications for time-dependent deformation. *Journal of Geophysical Research: Solid Earth*, 102(B1):591–603.

Langbein, J., Quilty, E., and Breckenridge, K. (1993). Sensitivity of crustal deformation instruments to changes in secular rate. *Geophysical Research Letters*, 20(2):85–88.

Lavier, L. L., Bennett, R. A., and Duddu, R. (2013). Creep events at the brittle ductile transition: Creep Events at BDT. *Geochemistry, Geophysics, Geosystems*, 14(9):3334–3351.

Lavier, L. L., Tong, X., and Biemiller, J. (2021). The Mechanics of Creep, Slow Slip Events, and Earthquakes in Mixed Brittle-Ductile Fault Zones. *Journal of Geophysical Research: Solid Earth*, 126(2):e2020JB020325.

Lee, J.-C., Angelier, J., Chu, H.-T., Hu, J.-C., and Jeng, F.-S. (2005). Monitoring active fault creep as a tool in seismic hazard mitigation. Insights from creepmeter study at Chihshang, Taiwan. *Comptes Rendus Geoscience*, 337(13):1200–1207.

Leeman, J. R., Marone, C., and Saffer, D. M. (2018). Frictional Mechanics of Slow Earthquakes. *Journal of Geophysical Research: Solid Earth*, 123(9):7931–7949.

Li, Y., Nocquet, J.-M., Shan, X., and Song, X. (2021). Geodetic Observations of Shallow Creep on the Laohushan-Haiyuan Fault, Northeastern Tibet. *Journal of Geophysical Research: Solid Earth*, 126(6):e2020JB021576.

Lienkaemper, J. J. (2006). Surface Slip Associated with the 2004 Parkfield, California, Earthquake Measured on Alinement Arrays. *Bulletin of the Seismological Society of America*, 96(4B):S239–S249.

Lienkaemper, J. J., McFarland, F. S., Simpson, R. W., Bilham, R. G., Ponce, D. A., Boatwright, J. J., and Caskey, S. J. (2012). Long-Term Creep Rates on the Hayward Fault: Evidence for Controls on the Size and Frequency of Large Earthquakes. *Bulletin of the Seismological Society of America*, 102(1):31–41.

Linde, A. T., Gladwin, M. T., Johnston, M. J. S., Gwyther, R. L., and Bilham, R. G. (1996). A slow earthquake sequence on the San Andreas fault. *Nature*, 383(6595):65–68. Number: 6595 Publisher: Nature Publishing Group.

Lisowski, M. and Prescott, W. H. (1981). Short-range distance measurements along the San Andreas fault system in central California, 1975 to 1979. *Bulletin of the Seismological Society of America*, 71(5):1607–1624.

Liu, Y. and Rice, J. R. (2005). Aseismic slip transients emerge spontaneously in three-dimensional rate and state modeling of subduction earthquake sequences. *Journal of Geophysical Research: Solid Earth*, 110(B8).

Liu, Y. and Rice, J. R. (2007). Spontaneous and triggered aseismic deformation transients in a subduction fault model. *Journal of Geophysical Research*, 112(B9):B09404.

Lockner, D. A., Morrow, C., Moore, D., and Hickman, S. (2011). Low strength of deep San Andreas fault gouge from SAFOD core. *Nature*, 472(7341):82–85. Number: 7341 Publisher: Nature Publishing Group.

Luo, Y. and Ampuero, J.-P. (2018). Stability of faults with heterogeneous friction properties and effective normal stress. *Tectonophysics*, 733:257–272.

Lyons, S. and Sandwell, D. (2003). Fault creep along the southern San Andreas from interferometric synthetic aperture radar, permanent scatterers, and stacking. *Journal of Geophysical Research: Solid Earth*, 108(B1).

Lyons, S. N., Bock, Y., and Sandwell, D. T. (2002). Creep along the Imperial Fault, southern California, from GPS measurements. *Journal of Geophysical Research: Solid Earth*, 107(B10):ETG 12–1–ETG 12–13.

Mariniere, J., Nocquet, J.-M., Beauval, C., Champenois, J., Audin, L., Alvarado, A., Baize, S., and Socquet, A. (2020). Geodetic evidence for shallow creep along the Quito fault, Ecuador. *Geophysical Journal International*, 220(3):2039–2055.

Marone, C. J., Scholtz, C. H., and Bilham, R. (1991). On the mechanics of earthquake afterslip. *Journal of Geophysical Research: Solid Earth*, 96(B5):8441–8452.

Martínez-Garzón, P., Bohnhoff, M., Mencin, D., Kwiatek, G., Dresen, G., Hodgkinson, K., Nurlu, M., Kadirioglu, F. T., and Kartal, R. F. (2019). Slow strain release along the eastern Marmara region offshore Istanbul in conjunction with enhanced local seismic moment release. *Earth and Planetary Science Letters*, 510:209–218.

Massonnet, D., Rossi, M., Carmona, C., Adragna, F., Peltzer, G., Feigl, K., and Rabaute, T. (1993). The displacement field of the Landers earthquake mapped by radar interferometry. *Nature*, 364(6433):138–142.

Matsuzawa, T., Obara, K., and Maeda, T. (2009). Source duration of deep very low frequency earthquakes in western Shikoku, Japan. *Journal of Geophysical Research: Solid Earth*, 114(B11).

Maurer, J. and Johnson, K. (2014). Fault coupling and potential for earthquakes on the creeping section of the central San Andreas Fault: Fault coupling on the creeping SAF. *Journal of Geophysical Research: Solid Earth*, 119(5):4414–4428.

Maury, J., Ide, S., Cruz-Atienza, V. M., Kostoglodov, V., González-Molina, G., and Pérez-Campos, X. (2016). Comparative study of tectonic tremor locations: Characterization of slow earthquakes in Guerrero, Mexico. *Journal of Geophysical Research: Solid Earth*, 121(7):5136–5151.

Mchugh, S. and Johnston, M. J. S. (1976). Short-period nonseismic tilt perturbations and their relation to episodic slip on the San Andreas Fault in central California. *Journal of Geophysical Research (1896-1977)*, 81(35):6341–6346.

McHugh, S. and Johnston, M. J. S. (1978). Dislocation modeling of creep-related tilt changes. *Bulletin of the Seismological Society of America*, 68(1):155–168.

McKinney, W. (2010). Data Structures for Statistical Computing in Python. pages 56–61, Austin, Texas.

Mencin, D. (2018). *PERIODIC AND STATIC STRAIN INVESTIGATIONS WITH BOREHOLE STRAINMETERS AND GPS*. PhD thesis, University of Colorado.

Met Office (2010). *Cartopy: a cartographic python library with a Matplotlib interface*. Exeter, Devon.

Michel, S., Avouac, J.-P., Jolivet, R., and Wang, L. (2018). Seismic and Aseismic Moment Budget and Implication for the Seismic Potential of the Parkfield Segment of the San Andreas FaultSeismic and Aseismic Moment Budget and Implication for the Seismic Potential of the Parkfield Segment of the SAF. *Bulletin of the Seismological Society of America*, 108(1):19–38.

Michel, S., Gualandi, A., and Avouac, J.-P. (2019). Similar scaling laws for earthquakes and Cascadia slow-slip events. *Nature*, 574(7779):522–526.

Montési, L. G. J. (2004). Controls of shear zone rheology and tectonic loading on postseismic creep. *Journal of Geophysical Research: Solid Earth*, 109(B10).

Moore, D. E. and Lockner, D. A. (2013). Chemical controls on fault behavior: Weakening of serpentinite sheared against quartz-bearing rocks and its significance for fault creep in the San Andreas system. *Journal of Geophysical Research: Solid Earth*, 118(5):2558–2570.

Moore, D. E., Lockner, D. A., Ma, S., Summers, R., and Byerlee, J. D. (1997). Strengths of serpentinite gouges at elevated temperatures. *Journal of Geophysical Research: Solid Earth*, 102(B7):14787–14801.

Moore, D. E., McLaughlin, R. J., and Lienkaemper, J. J. (2018). Serpentinite-Rich Gouge in a Creeping Segment of the Bartlett Springs Fault, Northern California: Comparison With SAFOD and Implications for Seismic Hazard. *Tectonics*, 37(12):4515–4534.

Moore, D. E. and Rymer, M. J. (2007). Talc-bearing serpentinite and the creeping section of the San Andreas fault. *Nature*, 448(7155):795–797.

Moore, D. E. and Rymer, M. J. (2012). Correlation of clayey gouge in a surface exposure of serpentinite in the San Andreas Fault with gouge from the San Andreas Fault Observatory at Depth (SAFOD). *Journal of Structural Geology*, 38:51–60.

Morrow, C. A., Moore, D. E., and Lockner, D. A. (2000). The effect of mineral bond strength and adsorbed water on fault gouge frictional strength. *Geophysical Research Letters*, 27(6):815–818.

Mortensen, C. E., Lee, R. C., and Burford, R. O. (1977). Observations of creep-related tilt, strain, and water-level changes on the central San Andreas fault. *Bulletin of the Seismological Society of America*, 67(3):641–649.

Murray, J. R., Minson, S. E., and Svarc, J. L. (2014). Slip rates and spatially variable creep on faults of the northern San Andreas system inferred through Bayesian inversion of Global Positioning System data: N. California fault creep and slip rates. *Journal of Geophysical Research: Solid Earth*, 119(7):6023–6047.

Murray, J. R. and Svarc, J. (2017). Global Positioning System Data Collection, Processing, and Analysis Conducted by the U.S. Geological Survey Earthquake Hazards Program. *Seismological Research Letters*, 88(3):916–925.

Nadeau, R. M. and McEvilly, T. V. (2004). Periodic Pulsing of Characteristic Microearthquakes on the San Andreas Fault. *Science*, 303(5655):220–222.

Nason, R. and Weertman, J. (1973). A dislocation theory analysis of fault creep events. *Journal of Geophysical Research (1896-1977)*, 78(32):7745–7751.

Nason, R. D., Philippsborn, F. R., and Yamashita, P. A. (1974). Catalog of creepmeter measurements in central California from 1968 to 1972. Technical Report 74-31, U.S. Geological Survey. ISSN: 2331-1258 Publication Title: Open-File Report.

NCEDC (2014). Northern California Earthquake Data Center. *UC Berkeley Seismological Laboratory. Dataset.* http://ncedc.org.

Niemeijer, A. R. and Spiers, C. J. (2006). Velocity dependence of strength and healing behaviour in simulated phyllosilicate-bearing fault gouge. *Tectonophysics*, 427(1):231–253.

NOAA (2021). Climate Data Online: Dataset Discovery. https://www.ncdc.noaa.gov/cdo-web/datasets.

Nocquet, J.-M., Jarrin, P., Vallée, M., Mothes, P. A., Grandin, R., Rolandone, F., Delouis, B., Yepes, H., Font, Y., Fuentes, D., Régnier, M., Laurendeau, A., Cisneros, D., Hernandez, S., Sladen, A., Singaucho, J.-C., Mora, H., Gomez, J., Montes, L., and Charvis, P. (2017). Supercycle at the Ecuadorian subduction zone revealed after the 2016 Pedernales earthquake. *Nature Geoscience*, 10(2):145–149.

Noda, H. and Lapusta, N. (2013). Stable creeping fault segments can become destructive as a result of dynamic weakening. *Nature*, 493(7433):518–521.

Ochi, T., Itaba, S., Koizumi, N., Takahashi, M., and Kitagawa, Y. (2016). Short-term slow slip events in the Tokai area, the Kii Peninsula and the Shikoku District, Japan (from May 2015 to October 2015). Coordinating Committee for Earthquake Prediction 95.

Ohzono, M., Sagiya, T., Hirahara, K., Hashimoto, M., Takeuchi, A., Hoso, Y., Wada, Y., Onoue, K., Ohya, F., and Doke, R. (2011). Strain accumulation process around the Atotsugawa fault system in the Niigata-Kobe Tectonic Zone, central Japan: Strain field around the Atotsugawa fault system. *Geophysical Journal International*, 184(3):977–990.

Okada, Y. (1985). Surface deformation due to shear and tensile faults in a half-space. *Bulletin of the Seismological Society of America*, 75(4):1135–1154.

Okada, Y. (1992). Internal deformation due to shear and tensile faults in a half-space. *Bulletin of the Seismological Society of America*, 82(2):1018–1040.

Oohashi, K., Hirose, T., Kobayashi, K., and Shimamoto, T. (2012). The occurrence of graphite-bearing fault rocks in the Atotsugawa fault system, Japan: Origins and implications for fault creep. *Journal of Structural Geology*, 38:39–50.

Oohashi, K., Hirose, T., and Shimamoto, T. (2011). Shear-induced graphitization of carbonaceous materials during seismic fault motion: Experiments and possible implications for fault mechanics. *Journal of Structural Geology*, 33(6):1122–1134.

Pacheco, M., Martín-Barajas, A., Elders, W., Cardena, J., Helenes, J., and Segura, A. (2006). Stratigraphy and structure of the Altar basin of NW Sonora: Implications for the history of the Colorado River delta and the Salton Trough. *Revista mexicana de ciencias geológicas, ISSN 1026-8774, Vol. 23, Nº. 1, 2006, pags. 1-22*, 23.

pandas development team, T. (2023). pandas-dev/pandas: Pandas. https://zenodo.org/record/8301632 DOI: 10.5281/zenodo.8301632.

Passchier, C. W. and Trouw, R. A. J. (2005). *Microtectonics*. Springer, Berlin ; New York, 2nd rev. and enl. ed. edition.

Peng, Y. and Rubin, A. M. (2017). Intermittent tremor migrations beneath Guerrero, Mexico, and implications for fault healing within the slow slip zone. *Geophysical Research Letters*, 44(2):760–770.

Peng, Z. and Gomberg, J. (2010). An integrated perspective of the continuum between earthquakes and slow-slip phenomena. *Nature Geoscience*, 3(9):599–607.

Perfettini, H. and Ampuero, J.-P. (2008). Dynamics of a velocity strengthening fault region: Implications for slow earthquakes and postseismic slip. *Journal of Geophysical Research*, 113(B9):B09411.

Pousse Beltran, L., Pathier, E., Jouanne, F., Vassallo, R., Reinoza, C., Audemard, F., Doin, M. P., and Volat, M. (2016). Spatial and temporal variations in creep rate along the El Pilar fault at the Caribbean-South American plate boundary (Venezuela), from InSAR. *Journal of Geophysical Research: Solid Earth*, 121(11):8276–8296. _eprint: https://onlinelibrary.wiley.com/doi/pdf/10.1002/2016JB013121.

Prescott, W. H., Lisowski, M., and Savage, J. C. (1981). Geodetic measurement of crustal deformation on the San Andreas, Hayward, and Calaveras Faults near San Francisco, California. *Journal of Geophysical Research: Solid Earth*, 86(B11):10853–10869.

Pérez, F. and Granger, B. E. (2007). IPython: a System for Interactive Scientific Computing. *Computing in Science and Engineering*, 9(3):21–29. Publisher: IEEE Computer Society.

Qiao, X. and Zhou, Y. (2021). Geodetic imaging of shallow creep along the Xianshuihe fault and its frictional properties. *Earth and Planetary Science Letters*, 567:117001.

Reinoza, C., Jouanne, F., Audemard, F. A., Schmitz, M., and Beck, C. (2015). Geodetic exploration of strain along the El Pilar Fault in northeastern Venezuela. *Journal of Geophysical Research: Solid Earth*, 120(3):1993–2013. _eprint: https://onlinelibrary.wiley.com/doi/pdf/10.1002/2014JB011483.

Richard, J., Gratier, J.-P., Doan, M.-L., Boullier, A.-M., and Renard, F. (2014). Rock and mineral transformations in a fault zone leading to permanent creep: Interactions between brittle and viscous mechanisms in the San Andreas Fault. *Journal of Geophysical Research: Solid Earth*, 119(11):8132–8153. fl.

Roeloffs, E. (2010). Tidal calibration of Plate Boundary Observatory borehole strainmeters: Roles of vertical and shear coupling. *Journal of Geophysical Research: Solid Earth*, 115(B6).

Roeloffs, E. A. (2001). Creep rate changes at Parkfield, California 1966-1999: Seasonal, precipitation induced, and tectonic. *Journal of Geophysical Research: Solid Earth*, 106(B8):16525–16547.

Roeloffs, E. A., Burford, S. S., Riley, F. S., and Records, A. W. (1989). Hydrologic effects on water level changes associated with episodic fault creep near Parkfield, California. *Journal of Geophysical Research: Solid Earth*, 94(B9):12,387–12,402.

Rogers, G. and Dragert, H. (2003). Episodic Tremor and Slip on the Cascadia Subduction Zone: The Chatter of Silent Slip. *Science*, 300(5627):1942–1943.

Rogers, T. (1980). Geology and seismicity at the convergence of the San Andreas and Calaveras fauft zones near Hollister, San Benito County, California. In Sherburne, R. W. and Streitz, R., editors, *Studies of the San Andreas Fault zone in Northern California*, pages 19–28. Sacramento CA : California Division of Mines and Geology.

Rossum, G. and Drake, F. L. (2009). *Python 3 Reference Manual*. CreateSpace, Scotts Valley, CA.

Rousset, B., Bürgmann, R., and Campillo, M. (2019a). Slow slip events in the roots of the San Andreas fault. *Science Advances*, 5(2):eaav3274.

Rousset, B., Campillo, M., Lasserre, C., Frank, W. B., Cotte, N., Walpersdorf, A., Socquet, A., and Kostoglodov, V. (2017). A geodetic matched filter search for slow slip with application to the Mexico subduction zone. *Journal of Geophysical Research: Solid Earth*, 122(12):10,498–10,514.

Rousset, B., Fu, Y., Bartlow, N., and Bürgmann, R. (2019b). Weeks-Long and Years-Long Slow Slip and Tectonic Tremor Episodes on the South Central Alaska Megathrust. *Journal of Geophysical Research: Solid Earth*, 124(12):13392–13403.

Rousset, B., Jolivet, R., Simons, M., Lasserre, C., Riel, B., Milillo, P., Çakir, Z., and Renard, F. (2016). An aseismic slip transient on the North Anatolian Fault. *Geophysical Research Letters*, 43(7):3254–3262.

Royer, A. A., Thomas, A. M., and Bostock, M. G. (2015). Tidal modulation and triggering of low-frequency earthquakes in northern Cascadia. *Journal of Geophysical Research: Solid Earth*, 120(1):384–405.

Rubin, A. M. (2008). Episodic slow slip events and rate-and-state friction. *Journal of Geophysical Research*, 113(B11):B11414.

Rubin, A. M. and Ampuero, J.-P. (2005). Earthquake nucleation on (aging) rate and state faults. *Journal of Geophysical Research: Solid Earth*, 110(B11).

Rubin, A. M. and Armbruster, J. G. (2013). Imaging slow slip fronts in Cascadia with high precision cross-station tremor locations. *Geochemistry, Geophysics, Geosystems*, 14(12):5371–5392.

Rudnicki, J. W., Yin, J., and Roeloffs, E. A. (1993). Analysis of water level changes induced by fault creep at Parkfield, California. *Journal of Geophysical Research: Solid Earth*, 98(B5):8143–8152.

Ruina, A. (1983). Slip instability and state variable friction laws. *Journal of Geophysical Research: Solid Earth*, 88(B12):10359–10370.

Ryder, I. and Bürgmann, R. (2008). Spatial variations in slip deficit on the central San Andreas Fault from InSAR. *Geophysical Journal International*, 175(3):837–852.

Sammis, C. G., Smith, S. W., Nadeau, R. M., and Lippoldt, R. (2016). Relating Transient Seismicity to Episodes of Deep Creep at Parkfield, California. *Bulletin of the Seismological Society of America*, 106(4):1887–1899.

Savage, J. C. and Prescott, W. H. (1973). Precision of geodolite distance measurements for determining fault movements. *Journal of Geophysical Research (1896-1977)*, 78(26):6001–6008.

Schleicher, A., van der Pluijm, B., and Warr, L. (2012). Chlorite-smectite clay minerals and fault behavior: New evidence from the San Andreas Fault Observatory at Depth (SAFOD) core. *Lithosphere*, 4(3):209–220.

Scholz, C. H. (1990). *The Mechanics of Earthquakes and Faulting*. Cambridge University Press, New York.

Scholz, C. H. (1998). Earthquakes and friction laws. *Nature*, 391(6662):37–42.

Schulz, S. (1989). CATALOG OF CREEPMETER MEASUREMENTS IN CALIFORNIA FROM 1966 THROUGH 1988. U.S. Geol. Surv. Open File Rep 89-650. Series: Open-File Report.

Schulz, S. and Burford, R. O. (1978). Installation of an Invar Wire Creepmeter, Elkhorn Valley, California August 1977. Open-File Report 78-203, U.S. Geological Survey. Series: Open-File Report.

Schulz, S., Burford, R. O., and Mavko, B. (1983). Influence of seismicity and rainfall on episodic creep on the San Andreas Fault System in central California. *Journal of Geophysical Research: Solid Earth*, 88(B9):7475–7484.

Schulz, S. S., Burford, R. O., and Nason, R. D. (1976). Catalog of creepmeter measurements in central California from 1973 through 1975. Technical Report 77-31, U.S. Geological Survey,. ISSN: 2331-1258 Publication Title: Open-File Report.

Schulz, S. S., Mavko, G. M., Burford, R. O., and Stuart, W. D. (1982). Long-term fault creep observations in central California. *Journal of Geophysical Research: Solid Earth*, 87(B8):6977–6982.

Scott, C., Bunds, M., Shirzaei, M., and Toke, N. (2020a). Creep Along the Central San Andreas Fault From Surface Fractures, Topographic Differencing, and InSAR. *Journal of Geophysical Research: Solid Earth*, 125(10):e2020JB019762.

Scott, C. P., DeLong, S. B., and Arrowsmith, J. R. (2020b). Distribution of Aseismic Deformation Along the Central San Andreas and Calaveras Faults From Differencing Repeat Airborne Lidar. *Geophysical Research Letters*, 47(22).

Segall, P. and Rice, J. R. (1995). Dilatancy, compaction, and slip instability of a fluid-infiltrated fault. *Journal of Geophysical Research: Solid Earth*, 100(B11):22155–22171.

Segall, P., Rubin, A. M., Bradley, A. M., and Rice, J. R. (2010). Dilatant strengthening as a mechanism for slow slip events. *Journal of Geophysical Research*, 115(B12):B12305.

Sekine, S., Hirose, H., and Obara, K. (2010). Along-strike variations in short-term slow slip events in the southwest Japan subduction zone. *Journal of Geophysical Research: Solid Earth*, 115(B9).

Shelly, D. R. (2017). A 15 year catalog of more than 1 million low-frequency earthquakes: Tracking tremor and slip along the deep San Andreas Fault. *Journal of Geophysical Research: Solid Earth*, 122(5):3739–3753.

Shelly, D. R., Beroza, G. C., and Ide, S. (2007a). Complex evolution of transient slip derived from precise tremor locations in western Shikoku, Japan. *Geochemistry, Geophysics, Geosystems*, 8(10):n/a–n/a.

Shelly, D. R., Beroza, G. C., and Ide, S. (2007b). Non-volcanic tremor and low-frequency earthquake swarms. *Nature*, 446(7133):305–307.

Shelly, D. R., Beroza, G. C., Ide, S., and Nakamula, S. (2006). Low-frequency earthquakes in Shikoku, Japan, and their relationship to episodic tremor and slip. *Nature*, 442(7099):188–191.

Shibazaki, B. and Iio, Y. (2003). On the physical mechanism of silent slip events along the deeper part of the seismogenic zone. *Geophysical Research Letters*, 30(9).

Shreedharan, S., Ikari, M., Wood, C., Saffer, D., Wallace, L., and Marone, C. (2022). Frictional and Lithological Controls on Shallow Slow Slip at the Northern Hikurangi Margin. *Geochemistry, Geophysics, Geosystems*, 23(2):e2021GC010107.

Sibson, R. H. (1977). Fault rocks and fault mechanisms. *Journal of the Geological Society*, 133(3):191–213.

Sims, J. (1990). Geological Map of the San Andreas fault in the Parkfield 7.5-minute quadrangle, Monterey and Fresno Counties, Calironia.

Skarbek, R. M., Rempel, A. W., and Schmidt, D. A. (2012). Geologic heterogeneity can produce aseismic slip transients. *Geophysical Research Letters*, 39(21):n/a–n/a.

Slater, L. E. and Burford, R. O. (1979). A comparison of long-baseline strain data and fault creep records obtained near Hollister, California. *Tectonophysics*, 52(1):481–496.

Solum, J. G., Hickman, S. H., Lockner, D. A., Moore, D. E., van der Pluijm, B. A., Schleicher, A. M., and Evans, J. P. (2006). Mineralogical characterization of protolith and fault rocks from the SAFOD Main Hole. *Geophysical Research Letters*, 33(21). _eprint: https://onlinelibrary.wiley.com/doi/pdf/10.1029/2006GL027285.

Steinbrugge, K. V. and Zacher, E. G. (1960). FAULT CREEP AND PROPERTY DAMAGE. *Bulletin of the Seismological Society of America*, 50(3):389–396.

Steinbrugge, K. V., Zacher, E. G., Tocher, D., Whitten, C. A., and Claire, C. N. (1960). Creep on the San Andreas fault. *Bulletin of the Seismological Society of America*, 50(3):389–415.

Stiros, S. C. (2021). The 373 B.C. Helike (Gulf of Corinth, Greece) Earthquake and Tsunami, Revisited. *Seismological Research Letters*, 93(1):444–457.

Supino, M., Poiata, N., Festa, G., Vilotte, J. P., Satriano, C., and Obara, K. (2020). Self-similarity of low-frequency earthquakes. *Scientific Reports*, 10(1):6523. Number: 1 Publisher: Nature Publishing Group.

Swanson, K. R., Cashman, S. M., and Baldwin, J. N. (2004). Macro- and Micro-deformation Features of the Creeping Strand of the San Andreas Fault, and Evidence for Changes in Historic Creep Rate, Flook Ranch, Bitterwater Valley, CA. 2004:G11A–0764. Conference Name: AGU Fall Meeting Abstracts ADS Bibcode: 2004AGUFM.G11A0764S.

Takeo, A., Idehara, K., Iritani, R., Tonegawa, T., Nagaoka, Y., Nishida, K., Kawakatsu, H., Tanaka, S., Miyakawa, K., Iidaka, T., Obayashi, M., Tsuruoka, H., Shiomi, K., and Obara, K. (2010). Very broadband analysis of a swarm of very low frequency earthquakes and tremors beneath Kii Peninsula, SW Japan. *Geophysical Research Letters*, 37(6).

Templeton, D. C., Nadeau, R. M., and Bürgmann, R. (2009). Distribution of postseismic slip on the Calaveras fault, California, following the 1984 M6.2 Morgan Hill earthquake. *Earth and Planetary Science Letters*, 277(1):1–8.

Thom, C. A., Brodsky, E. E., Carpick, R. W., Pharr, G. M., Oliver, W. C., and Goldsby, D. L. (2017). Nanoscale Roughness of Natural Fault Surfaces Controlled by Scale-Dependent Yield Strength: Nanoscale Fault Roughness and Strength. *Geophysical Research Letters*, 44(18):9299–9307.

Thomas, A. M., Beroza, G. C., and Shelly, D. R. (2016). Constraints on the source parameters of low-frequency earthquakes on the San Andreas Fault. *Geophysical Research Letters*, 43(4):1464–1471.

Thomas, M. Y., Avouac, J.-P., Champenois, J., Lee, J.-C., and Kuo, L.-C. (2014). Spatiotemporal evolution of seismic and aseismic slip on the Longitudinal Valley Fault, Taiwan. *Journal of Geophysical Research: Solid Earth*, 119(6):5114–5139.

Thompson, B. (2015). okada_wrapper. https://github.com/tbenthompson/okada_wrapper.

Thurber, C. and Sessions, R. (1998). Assessment of Creep Events as Potential Earthquake Precursors: Application to the Creeping Section of the San Andreas Fault, California. *Pure and Applied Geophysics*, 152(4):685–705.

Tiampo, K. F., González, P. J., and Samsonov, S. S. (2013). Results for aseismic creep on the Hayward fault using polarization persistent scatterer InSAR. *Earth and Planetary Science Letters*, 367:157–165.

Titus, S. J. (2006). Thirty-Five-Year Creep Rates for the Creeping Segment of the San Andreas Fault and the Effects of the 2004 Parkfield Earthquake: Constraints from Alignment Arrays, Continuous Global Positioning System, and Creepmeters. *Bulletin of the Seismological Society of America*, 96(4B):S250–S268.

Titus, S. J., DeMets, C., and Tikoff, B. (2005). New slip rate estimates for the creeping segment of the San Andreas fault, California. *Geology*, 33(3):205–208.

Titus, S. J., Dyson, M., DeMets, C., Tikoff, B., Rolandone, F., and Burgmann, R. (2011). Geologic versus geodetic deformation adjacent to the San Andreas fault, central California. *Geological Society of America Bulletin*, 123(5-6):794–820.

Tocher, D. (1960). CREEP RATE AND RELATED MEASUREMENTS AT VINEYARD, CALIFORNIA. *Bulletin of the Seismological Society of America*, 50(3):396–404.

Toppozada, T. R., Branum, D. M., Reichle, M. S., and Hallstrom, C. L. (2002). San Andreas Fault Zone, California: M 5.5 Earthquake History. *Bulletin of the Seismological Society of America*, 92(7):2555–2601.

Tu, Y. and Heki, K. (2017). Decadal Modulation of Repeating Slow Slip Event Activity in the Southwestern Ryukyu Arc Possibly Driven by Rifting Episodes at the Okinawa Trough. *Geophysical Research Letters*, 44(18):9308–9313.

Tymofyeyeva, E., Fialko, Y., Jiang, J., Xu, X., Sandwell, D., Bilham, R., Rockwell, T. K., Blanton, C., Burkett, F., Gontz, A., and Moafipoor, S. (2019). Slow Slip Event On the Southern San Andreas Fault Triggered by the 2017 M_w 8.2 Chiapas (Mexico) Earthquake. *Journal of Geophysical Research: Solid Earth*, 124(9):9956–9975.

USGS (1991). Geodolite Trilateration Data Set. https://earthquake.usgs.gov/monitoring/deformation/geodolite/.

USGS (2005). Data from the Parkfield two-color EDM network. https://earthquake.usgs.gov/monitoring/deformation/edm/parkfield/data.php.

USGS (2023). Fault Creep, Borehole Strain, and Tiltmeter Monitoring Measurements. https://earthquake.usgs.gov/monitoring/deformation/data/download.php.

USGS and CGS (2020). Quaternary fault and fold database for the United States. https://www.usgs.gov/programs/earthquake-hazards/faults.

Virtanen, P., Gommers, R., Oliphant, T. E., Haberland, M., Reddy, T., Cournapeau, D., Burovski, E., Peterson, P., Weckesser, W., Bright, J., van der Walt, S. J., Brett, M., Wilson, J., Millman, K. J., Mayorov, N., Nelson, A. R. J., Jones, E., Kern, R., Larson, E., Carey, C. J., Polat, , Feng, Y., Moore, E. W., VanderPlas, J., Laxalde, D., Perktold, J., Cimrman, R., Henriksen, I., Quintero, E. A., Harris, C. R., Archibald, A. M., Ribeiro, A. H., Pedregosa, F., and van Mulbregt, P. (2020). SciPy 1.0: fundamental algorithms for scientific computing in Python. *Nature Methods*, 17(3):261–272. Number: 3 Publisher: Nature Publishing Group.

Waldhauser, F. and Schaff, D. P. (2008). Large-scale relocation of two decades of Northern California seismicity using cross-correlation and double-difference methods. *Journal of Geophysical Research: Solid Earth*, 113(B8).

Waldhauser, F. and Schaff, D. P. (2021). A Comprehensive Search for Repeating Earthquakes in Northern California: Implications for Fault Creep, Slip Rates, Slip Partitioning, and Transient Stress. *Journal of Geophysical Research: Solid Earth*, 126(11).

Wallace, L. M., Webb, S. C., Ito, Y., Mochizuki, K., Hino, R., Henrys, S., Schwartz, S. Y., and Sheehan, A. F. (2016). Slow slip near the trench at the Hikurangi subduction zone, New Zealand. *Science*, 352(6286):701–704. Publisher: American Association for the Advancement of Science.

Wallace, R. E. and Roth, E. F. (1967). Rates and patterns of progressive deformation. In *The ParkfieldCholame California Earthquakes of June-August 1966*, volume 579, pages 23–40. U.S. Geol. Surv., Profess. Paper.

Walter, J. I., Schwartz, S. Y., Protti, J. M., and Gonzalez, V. (2011). Persistent tremor within the northern Costa Rica seismogenic zone. *Geophysical Research Letters*, 38(1):n/a–n/a.

Warren-Smith, E., Fry, B., Wallace, L., Chon, E., Henrys, S., Sheehan, A., Mochizuki, K., Schwartz, S., Webb, S., and Lebedev, S. (2019). Episodic stress and fluid pressure cycling in subducting oceanic crust during slow slip. *Nature Geoscience*, 12(6):475–481.

Weber, J., Geirsson, H., La Femina, P., Robertson, R., Churches, C., Shaw, K., Latchman, J., Higgins, M., and Miller, K. (2020). Fault Creep and Strain Partitioning in Trinidad-Tobago: Geodetic Measurements, Models, and Origin of Creep. *Tectonics*, 39(1):e2019TC005530.

Wei, M., Kaneko, Y., Liu, Y., and McGuire, J. J. (2013). Episodic fault creep events in California controlled by shallow frictional heterogeneity. *Nature Geoscience*, 6(7):566–570.

Wesson, R. L. (1988). Dynamics of fault creep. *Journal of Geophysical Research*, 93(B8):8929.

Whitten, C. A. and Claire, C. N. (1960). ANALYSIS OF GEODETIC MEASUREMENTS ALONG THE SAN ANDREAS FAULT. *Bulletin of the Seismological Society of America*, 50(3):404–415.

Wilkinson, R., Daout, S., Parsons, B., Walker, R., Pierce, J., and Ischuk, A. (2021). A time series InSAR study of faulting around Dushanbe (Tajikistan). Fringe 2021, 11th international workshop on "advances in the science and applications of SAR interferometry and sentinel-1 InSAR", 31 May–4 June 2021. Retrieved from https://www.youtube.com/watch?v=u1-ok689wWw.

Wilmesher, J. F. and Baker, F. B. (1987). Catalog of alinement array measurements in Central and Southern California from 1983 through 1986. Technical Report 87-280, U.S. Geological Survey,. ISSN: 2331-1258 Publication Title: Open-File Report.

Yabe, S., Baba, S., Tonegawa, T., Nakano, M., and Takemura, S. (2021). Seismic energy radiation and along-strike heterogeneities of shallow tectonic tremors at the Nankai Trough and Japan Trench. *Tectonophysics*, 800:228714.

Yabe, S. and Ide, S. (2017). Slip-behavior transitions of a heterogeneous linear fault. *Journal of Geophysical Research: Solid Earth*, 122(1):387–410.

Yamashita, P. and Burford, R. (1973). Catalog of preliminary results from an 18-Station creepmeter network along the San Andreas fault system in central California for the time interval June 1969 to June 1973. USGS Numbered Series 73-366, U.S. Geological Survey, Reston, VA.